Detector Development and Analysis Techniques for Finding Leptoquarks with the ATLAS Detector at the LHC

Inauguraldissertation

der Philosophisch-naturwissenschaftlichen Fakultät
der Universität Bern

vorgelegt von

Roman Müller

von Seewen SO

Leiter der Arbeit:

Prof. Dr. Michele Weber

Laboratorium für Hochenergiephysik
Albert Einstein Center for Fundamental Physics
Physikalisches Institut

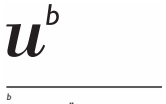
b
UNIVERSITÄT
BERN
AEC
ALBERT EINSTEIN CENTER
FOR FUNDAMENTAL PHYSICS


LABORATORIUM FÜR HOCHENERGIEPHYSIK
LHEP
UNIVERSITÄT BERN


ATLAS
EXPERIMENT

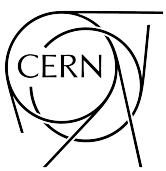
CERN

So lächelt der Physiker denn auch nachsichtig: Niemand sei sich klar darüber und könne sich klar darüber sein, was denn eigentlich, ausserhalb der physikalischen Fragestellung, «in Wirklichkeit» diese Teilchen seien, die man da erforsche, erforschen wolle oder zu erforschen hoffe – oder zu erfinden, weil es für den Physiker gar kein «ausserhalb» geben könne, dieses falle vielmehr in das Gebiet der philosophischen Spekulation und sei für die Physik irrelevant.

Gleichgültig.

Hauptsache, dass man forsche, überhaupt neugierig bleibe. So unwahrscheinlich und paradox das Ganze auch sei, fährt der Physiker schliesslich fort, es stelle bis jetzt das weitaus Sinnvollste dar, was Europa hervorgebracht habe, weil es das scheinbar Sinnloseste sei, im Spekulativen, Abenteuerlichen angesiedelt, in der Neugierde an sich. Thelen, sein Freund und ich entfernen uns beinahe stolz durch leerstehende Büros, auf den Tischen immer wieder Comics.

– Friedrich Dürrenmatt, after a visit to CERN 1974 [1]

Abstract

The LHC and its experiments at CERN constitute the largest particle physics research programme to date, allowing for extensive studies of the existing Standard Model and for potential evidence of physics beyond that of our current comprehension. This thesis presents an analysis technique to find third generation Leptoquarks in high mass $\tau^+\tau^-$ final states. The sensitivity on the coupling strength of a leptoquark with a chosen mass of 1.5 TeV (2 TeV) is $g^2 = 6.61^{+1.13}_{-0.95}$ ($g^2 = 10.98^{+1.92}_{-1.65}$). This is calculated using the total transverse mass of an event, $m_{\mathrm{T}}^{\mathrm{total}}$. In order to enhance the accuracy of tests on the Standard Model and to broaden the potential for uncovering new realms of physics such as leptoquarks, the LHC will be upgraded to the High-Luminosity LHC. This thesis presents the development of the Optoboard System – the part of the ATLAS new Inner Tracker (ITk) Pixel Detector readout system that handles the transfer of data, command and trigger between the modules and the backend. All ITk Pixel Detector modules are assigned and mapped to the Optoboard System with Twinax cables length between 3016 mm and 5776 mm. Compatible with requirements in data transmission reliability, the Optoboard System is validated first with jitter measurements and bit error rate tests, reaching the desired $BER_{95\%} < 2.7 \times 10^{-12}$ and second, with Sr-90 radiation at the ITk Pixel system test site with the Outer Barrel demonstrator.

Acknowledgements

This journey until now was by no means planned nor did I expect, many years ago, to end up here. I am forever grateful for the opportunities I had and still have. I am trying to commemorate, in chronological order, all the people along the way that brought me here.

I want to thank my parents, Karin and Beat, for the decision of having me and supporting me in every way possible throughout my life. Thank you to my brother Simon, my grandparents Hedy and Hasso, Erna and Beat, my godfather Roland and family, my godmother Hedi and family, Markus and Céline. My past, present and future would not be so rewarding without you Elena. Thank you as well Susanna and Rolf.

I want to thank teachers during primary and secondary school for making school not too much fun – I might never have considered doing an apprenticeship. I want to know Matthias M., Pädi, Pasci, Gabi, Flo, Marco, Fabio, Steven, Matthias B., Mänä, Renato, you all made these years much more fun.

Thank you to Schmidlin Elektro who delegated me after my trial week to Ramseyer Elektro. Thank you to Kurt for accepting me and being patient. A big thank you to Reto, Franz and Michi for taking me under your wings – I think you always saw potential. I also want to thank Andi, Marcel, Sandro, Arno, Mark, Dominik, Fredi, Noe, Priska and all the others – the camaraderie was second to none up until today.

I met some of the finest individuals during electrician school: Thank you Laurent and Manu – you are great friends and you have the best taste in music. Nils you have influenced me more than you might think and I learned a lot about life from you. Also shout out to Stefano, Strauss and the other electricians. I had the best teachers during vocational school: Andreas “Boogy” Burgherr, Peter Kurt, Andreas Ötterli and Kurt Lanz. I am grateful to have met Bütti, Sascha, Can, Jon, Chris during that time and thank you as well Michi and other GIBL friends. Thank you for the countless study sessions during the Passerelle Nicolas and Elia, I never learned more about cooking during that time. Thank you Christian Döbeli for that one coffee-chat in Basel and a first glimpse of what a PhD even is.

Thank you snowboarding – no “sport” is that beautiful and has given me so much! You connected me with so many great people and going to Whistler was without a doubt one

of the best decisions I have ever made. Shout out to Core Camps, Marijn, Lucas and all other people I have met there. Thank you Alex, Marc, Simu, Thierry, Bruno, Hendrik, Roman, Patrick, Benj and all the other instructors at Alpinzentrum, it never really was conventional work. Thank you Mellow Mountain Hostel Wolfie, Elias and the diverse people I have met while travelling.

Of course snowboarding connected me to some of the kindest humans I know and I am very grateful for calling them my friends: Dävu, Fabi, Silvan, Romina, Diana and of course Radiator Verband Zweisimmen with Marlies, Thomas, Tobias and the almighty Kronebar.

Thank you Laurin, Michi, Lukas and the other ETH people for dragging me along in a rough first year of physics. Finally thank you to my fellow students at University of Bern with a special thanks to Omar, I probably would not have survived the theoretical physics and maths classes without you. I am glad to have taken astronomy classes as I might have never met Nils – thank you for being a great friend.

To all the people I have met at CERN and through the ATLAS collaboration. You were helpful in every way and I truly believe this collaboration is more than just an experiment. Thank you especially to Ismet Siral, Brian Moser, Leyre Flores Sanz De Acedo, Vakhtang Tsiskaridze, Hans Joos, Benedikt Vormwald, Timon Heim, Sasha Paramonov, Abhishek Sharma, Ali Skaf, Leonardo Vannoli, Carlos Solans, Gerhard Brandt, Marius Wensing, Marco Trovato, Martin Janda, Jonas Schmeing, Daniel Hernandez Montesinos and the lpGBT support, Datao Gong and the GBCR people, Stephan Eisenhardt, Matthias Hamer, Diego Alvarez Feito, Sergio Gonzalez Sevilla, Piotr Rymaszewski and the Bonn people. Special thanks to Susanne Kühn for the continuing support and believing in me. Thank you to the SLAC people Andrew Young, Alex Wang, Zhi Zheng, Eric Miller, Zijun Xu, Matthias Wittgen, Adrienne Higashi for welcoming me. Also thank you James Sinclair for the support.

I also want to thank the analysis group for supporting a hardware-enthusiast and taking the time to answer all my silly questions. Special thanks go to Chris Pollard, Chris Gutschow, Simon Koch, Federico Morodei, Giovanni Padovano, Patrick Rieck, Chris Hays as well as the initial Leptoquark support at University of Bern – Admir Greljo.

Last but not least I want to thank the Bern ATLAS group, the other research groups and the connected workshops and secretary: I might have never considered doing a thesis with you if it were not for Antonello, thank you for introducing me to particle physics. I want to thank Ciro, Aki, Igor, Jan, Samuel, Svenja, Thierry, Igor, Livio, Dean, Yves, Armin, Thom, Marco, Gianfranco, Claudia and Kris. It was an honour to study and do research with my fellow PhD students Lea, Megh, Meinrad and Daniele. My most sincere thanks to the electronic workshop Camilla, Lino and Andri, I enjoyed every minute there and learned so much. Thank you as well to the mechanical workshop Roger, Lori, Jan and Silas, your opinions and expertise are such large assets to myself and the group. Nothing at LHEP would function without the patience and efforts of the

secretaries Ursula and Marcella, thank you so much. Thank you as well to the whole facility staff from cleaning personnel to facility managers.

Very special thanks to the best postdocs ever and for guiding me through every day of this PhD and in the end taking your time to correct this thesis: Laura, Isidre, Niklaus, John and Aaron! Thank you also Silke for jumping into the cold water and correcting this thesis. Thank you Gilberto Colangelo for being the referee at my PhD defence. Thank you to Su Dong for taking the time and effort to be my ATLAS qualification task supervisor and external evaluator of this thesis. All this work would not have been possible without Michele, thank you for giving me the opportunities I had and the support from the Bachelor until the completion of this PhD and beyond.

Contents

Introduction

The Standard Model (SM) of particle physics provides humanity with the most accurate description of subatomic processes to date. It describes processes along many orders of magnitudes in energies to a remarkable precision. It has predicted many particles, including the Higgs boson, discovered in 2012 with the two general purpose experiments ATLAS and CMS [2, 3] at the LHC at CERN.

Despite its success, the SM leaves questions unanswered: it neither includes gravity nor accounts for dark matter and dark energy, which are predicted by cosmology [4]. It does not predict neutrino masses, although they have been observed to be larger than zero [5]. Unexplained are also the matter-antimatter asymmetry and the hierarchy problem of the Higgs boson [6, 7]. Additionally, recent hints at lepton flavour violation have been observed [8]. There are several theories trying to overcome these limitations [6, 7, 9]. These theories extend the SM and predict new fundamental particles, such as leptoquarks, at energies that have not been reached with previous colliders.

In this thesis, sensitivity studies of a leptoquark interpretation of a $pp \to \tau\tau$ fiducial differential cross-section measurement are carried out. This analysis is motivated by the valuable insights obtained in previous studies and analyses of the $\tau^+\tau^-$ final state: ATLAS has conducted measurements on the differential cross sections and properties of $Z \to \tau\tau$ [10–12]. ATLAS has also observed and studied the properties of the $H \to \tau\tau$ decay mode [13–15], in addition to exploring the presence of new heavy resonances that decay into pairs of $\tau^+\tau^-$ [16].

The analysis has multiple goals driving its implementation. Notably, discrepancies of 3.4σ and 2.1σ in $b \to c\tau\nu$ rates have been observed in precision measurements of b-hadron decay fractions by both BaBar [17] and LHCb [18] experiments, respectively. These anomalies could potentially be explained by new physics phenomena at high-energy scales, featuring preferential interactions with third-generation fermions, particularly τ-leptons [19]. The presented analysis is sensitive to effects induced by such scenarios as well as more general, new high-energy physics with flavour-dependent coupling to quarks and leptons, namely Leptoquarks (LQ).

The studies presented in this analysis, which concentrate on final states incorporating τ-leptons, complete a vital component of the overall investigation into high-mass dilepton

production at the LHC. For ATLAS it is the first LQ search in the $\tau\tau$ final state [20]. Comparisons with measured cross sections allow for a direct assessment of the SM, including the assumption of lepton universality, in a new kinematic regime. Furthermore, a comparison to a similar third generation LQ search by CMS [21] is established.

To significantly extend the study of the above-mentioned SM limitations and to substantially improve statistics for small cross-section processes in searches for leptoquarks or many other signatures of new physics, the LHC will be upgraded to the High-Luminosity LHC (HL-LHC). The instantaneous luminosity will be increased by 5–7.5 times when compared to the design parameters of the current LHC. As a consequence, the average number of simultaneous collisions (pile-up) will increase from 55 to around 140 and the detector electronics will have to provide faster readout rates and cope with higher radiation levels. The experiments at the LHC will therefore also need to be upgraded in order to cope with the challenges posed by HL-LHC.

One of the major upgrades of the ATLAS experiment for the HL-LHC phase will be the Inner Tracker (ITk). The ITk replaces the complete current Inner Detector with an all-silicon-sensor detector and consists of a Pixel Detector surrounded by a Strip Detector. This will enlarge the coverage up to the pseudo-rapidity $|\eta|$ = 4.0 and increase the granularity for the tracking of charged particles.

To handle the increased data rate from the new modules, a new data transmission chain and backend for the read out is being developed. The optical-electrical conversion and aggregation stage of the Pixel Detector data transmission chain is the Optoboard System with a custom-designed PCB that regulates the transmission of data. The Optoboard System is a modular system that handles the transmission from the ITk Pixel modules inside the Pixel Detector to the backend network cards FELIX and vice versa control and command to the front end modules.

In this work, a detailed study of the interplay between the ITk Pixel Detector layout and the Optoboard System is conducted, culminating in a first estimate of the cable bundle lengths of the different ITk Pixel Detector subsystems, Inner System, Outer Barrel and End Caps. Additionally, the Optoboard version 2 was designed, developed and integrated into a prototype setup of the data transmission chain. Its performance was validated with jitter measurements and bit error tests. The major milestone of the thesis is the integration of the Optoboard System into the ITk Pixel System Tests. All necessary components, separately developed in many institutes, come together for the first time and are tested under close-to-real detector conditions. First results of the modules integrated in the full setup, which included the Optoboards, when exposed to β^- radiation from a Sr-90 source of the most advanced test site, the Outer Barrel demonstrator at CERN, are presented.

The thesis is structured as follows: Chapter 1 describes the physics of the SM and BSM theories. The collider and detector of the experiment are explained in Chapter 2,

including the planned upgrades. An analysis of collected data is presented in Chapter 3. Chapter 4 describes the Optoboard System with the estimation of the cable lengths and the arrangement of the sub-detector modules inside the Optoboard System. The validation of data transmissions with the Optoboard System is presented in Chapter 5.

Note: portions of the referenced content in this thesis have been rephrased with the assistance of an AI language model [22].

Chapter 1

The Standard Model of Particle Physics and Beyond

The Standard Model (SM) of particle physics describes the behaviour of subatomic particles and their interactions [23, 24]. It is currently the best description of how the universe works at the smallest scale. This chapter gives an overview of the SM with its successes and limitations, and describes how certain Beyond Standard Model (BSM) theories could overcome some of these limitations. This thesis uses *natural* units, setting both the speed of light and the reduced Planck constant to 1 ($c = \hbar = 1$) and using electron-volts (1 eV = 1 V $\cdot$ e).

1.1 The Standard Model

The SM is a theory that describes the fundamental particles and fundamental forces (except gravity) that govern their interactions. It is a Quantum Field Theory (QFT) that is based on the principles of special relativity and quantum mechanics. In QFT the most fundamental units are the quantum fields that pervade the entire universe and elementary particles are quantisations of those fields. Figure 1.1 provides an overview of the model, which consists of two main categories of these elementary particles: fermions and bosons. Fermions are particles that make up matter, while bosons are particles that mediate the fundamental forces.

1.1.1 Fermions

Fermions, the first three columns on the left in Figure 1.1, obey Fermi-Dirac statistics and are half-integer spin particles. They are further divided into two categories: quarks and leptons.

Quarks are particles that interact with all fundamental forces in the SM carrying all

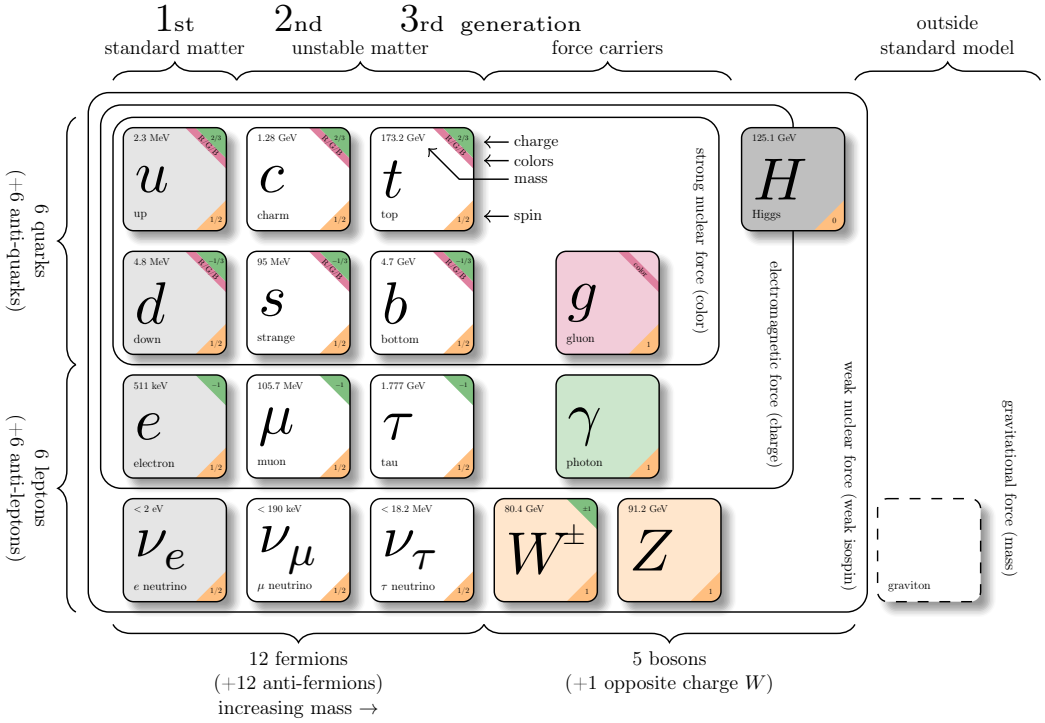

Figure 1.1: Schematic overview of the Standard Model with its particles and interactions. The charge is given in units of the electron charge $|e|$. Figure taken from [25].

charges: the electromagnetic and weak charges, and the strong charge (the only SM fermions to do so). There are six quarks known[1] as up u, down d, charm c, strange s, top t and bottom b that are grouped into three generations of flavour doublets:

$$\begin{pmatrix} u \\ d \end{pmatrix} \quad \begin{pmatrix} c \\ s \end{pmatrix} \quad \begin{pmatrix} t \\ b \end{pmatrix}$$

Each type of quark has a corresponding anti-particle (or anti-quark) with the opposite charge. Quarks have several interesting properties. One of the most notable is their "colour" charge, which is not related to the colours of light we see in everyday life, but rather a property of the strong force interaction between quarks (see Section 1.1.2). Quarks can have one of three colour charges red, green, or blue (or colour indexes 1, 2 and 3) and anti-quarks have the corresponding anti-colours anti-red, anti-green, and anti-blue.

Unlike quarks, leptons [26] do not experience the strong nuclear force and therefore do not combine to form hadrons. They also are a set of six fermions, sorted by increasing mass into three generations that all feel the weak force:

$$\begin{pmatrix} \nu_e \\ e \end{pmatrix} \quad \begin{pmatrix} \nu_\mu \\ \mu \end{pmatrix} \quad \begin{pmatrix} \nu_\tau \\ \tau \end{pmatrix}$$

While the electron e, muon μ and tau τ can interact also through the electromagnetic

[1] The top and bottom are also sometimes (historically) called *truth* and *beauty*.

force, the neutrinos electron-neutrino ν_e, muon-neutrino ν_μ and tau-neutrino ν_τ are a unique type of lepton as they only interact weakly and do not carry any electric charge. In the frame of the SM, the neutrinos are massless (see Section 1.2). Just as for the quarks, each lepton has a corresponding anti-particle (or anti-lepton) with the opposite charge.

1.1.2 Bosons

Bosons are responsible for transmitting the fundamental forces of nature between the particles and are characterised by having integer values of spin. Three out of four of the fundamental forces – the electromagnetic force, the weak nuclear force and the strong nuclear force – are mediated by known bosons. An overview can be found on the right hand side columns of Figure 1.1. The last fundamental force, gravity, is also theorised to be mediated by a boson, the graviton, but has not been experimentally confirmed and is also not part of the SM. In the SM, the fundamental forces are described by gauge theories, which are based on local symmetries. These symmetries are associated with certain Lie groups, which are mathematical structures that capture the concept of symmetry transformations.

The gauge group of the electromagnetic force is U(1), which represents the symmetry associated with the conservation of electric charge. This U(1) symmetry is related to the electromagnetic interaction mediated by the photon γ, which is a massless boson [27]. When charged particles interact with each other, they exchange photons to create the attractive or repulsive force between them. The electromagnetic interaction can be described by Quantum Electrodynamics [28].

The weak nuclear force is described by the gauge group SU(2), which represents the symmetry associated with the weak isospin. This group has three generators, which results in the W^+, W^- and Z bosons [27, 29] that mediate the weak interactions. Particles with weak isospin can exist in different "flavours" or states, for example, there are left-handed and right-handed states for fermions, such as electrons and neutrinos. The SU(2) symmetry of the weak force requires the existence of left-handed doublets of particles (shown above), they have weak isospin $+\frac{1}{2}$ and $-\frac{1}{2}$. The W bosons in the SU(2) group are responsible for the change of weak isospin between the particles in the left-handed doublets. For example, in the β^-decay, a d quark changes into a u quark by emitting a W^- boson:

$$d \rightarrow u e^- \bar{\nu}_e$$

The Z boson, being electrically neutral, does not change the weak isospin of particles but is involved in neutral weak interactions. The weak interaction is unique in that it violates parity (P) and charge conjugation (C) symmetry, but it conserves their combination known as CP symmetry. This violation of parity and charge conjugation was experimentally observed [30–32] in processes involving the weak force. This is a

unique feature of the weak interaction, as the other fundamental forces do not distinguish between particles and antiparticles [33].

The electroweak theory [34] postulates that the electromagnetic and weak forces are actually two aspects of a single, unified force that become distinct only at high energies. This unification is possible because the electromagnetic and weak forces gauge groups can be described by a common gauge theory U(1) $\times$ SU(2). An important additional aspect of the electroweak symmetry group is the Higgs mechanism, a mechanism of spontaneous symmetry breaking [35, 36] that is responsible for generating the masses of the W and Z bosons while leaving the photon massless. It involves the introduction of a scalar field known as the Higgs field [26] and its associated particle, the Higgs boson. In the SM, the Higgs field is a complex scalar field that forms a doublet under the SU(2) gauge symmetry. It interacts with the weak bosons and fermions through Yukawa couplings, which determine the strength of their interactions with the Higgs field. The Higgs field has a non-zero Vacuum Expectation Value (VEV), which represents the average value of the Higgs field in its lowest energy state. The Higgs field acquires a VEV in its ground state due to its self-interactions. When the Higgs field acquires a non-zero VEV, the electroweak symmetry of the U(1) $\times$ SU(2) gauge group is spontaneously broken. This means that the ground state of the Higgs field does not possess the full symmetry of the underlying gauge group, resulting in the emergence of massive particles. Specifically, after electroweak symmetry breaking, the Higgs field can be written as a sum of its VEV and quantum fluctuations. The fluctuations correspond to excitations of the Higgs field and give rise to the Higgs boson, which was discovered at CERN in 2012 [2, 3].

The strong nuclear force, described by the QFT Quantum Chromodynamics (QCD), is responsible for the interactions between quarks and described by the gauge symmetry group SU(3). This symmetry is associated with the property called colour charge and the massless gluons [27], which are the carriers of the strong force, arise from the eight generators of the SU(3) group. QCD is a very challenging theory to experiment with because the interactions between quarks and gluons become stronger as the particles are pulled apart. This is seen in Figure 1.2, measurements confirm that for smaller momentum transfer Q, the coupling strength parameter α_s increases and the interaction between the quarks gets stronger. The more quarks are pulled apart, the stronger the force. This phenomenon leads to *colour confinement* [38]. Quarks have not been observed in isolation, as they are always confined within so-called hadrons, which are colourless. The exception here is the t that decays, with a mean lifetime of 5×10^{-25} s, too quickly to form hadrons because of its high mass of 172 GeV [37].

There are two main types[2] of hadrons: baryons and mesons. Baryons like protons p and neutrons n are non-elementary particles made up of three quarks, while mesons like pions $\pi^{0,\pm}$ or b-mesons B are non-elementary particles made up of a quark and an

[2]More exotic compositions like tetra- and penta-quarks are possible and have recently been observed [39].

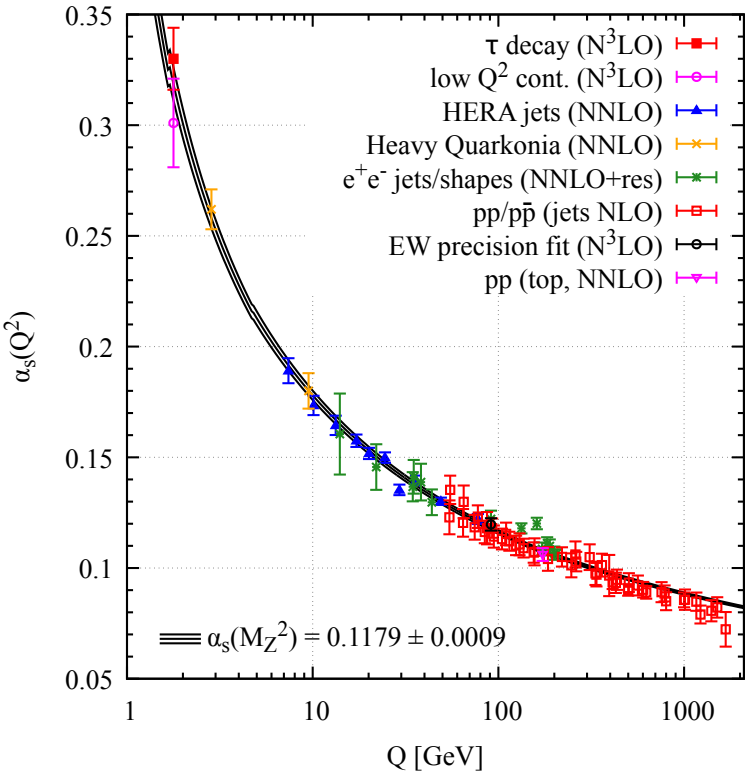

Figure 1.2: Summary of measurements of α_s a function of the energy scale Q. The respective degree of QCD perturbation theory used in the extraction of α_s is indicated in brackets (Next-to-leading Order (NLO), Next-to-next-to-leading Order (NNLO), NNLO matched to a resummed calculation (NNLO+res.), Next-to-NNLO (N^3LO)). Figure taken from [37].

anti-quark. A commonality is that all forms of hadrons are bound strongly by gluons as a result of colour confinement and the very nature of the strong force.

At high energy the SM can be combined to the symmetry group U(1) $\times$ SU(2) $\times$ SU(3), which allows for the successful description of a wide range of experimental observations, including the behaviour of particles at high-energy colliders and the predictions of various decay processes. However, the SM is limited in describing nature in several aspects. These limitations are discussed in Section 1.2.

1.2 Limitations of the Standard Model

While the SM has been tremendously successful in describing the behaviour of elementary particles, we fall short of encompassing a more comprehensive overarching model. Listed below are some of the main limitations of the SM:

Gravity is not included: The SM only describes the behaviour of three out of the four fundamental forces in nature. It does not include gravity, which is currently best described by general relativity [40, 41]. In theories of quantum gravity an elementary particle graviton, a spin-2 boson, is postulated to be the mediator of

the gravitational force. The limit on its mass is $\leq 1.76 \times 10^{-23}$ eV [42].

Dark matter and dark energy are not explained: According to cosmology, our visible, baryonic matter universe is only made up of about 5% of the universe's total mass-energy content. The SM cannot account for the observed amount of dark matter (27%) [7] and dark energy (68%) in the universe. This is confirmed through experimental evidence from measurements of rotation speeds of stars in galaxies showing that their velocities do not follow the radial dependency expected from the mass of ordinary matter (stars, gas, etc.) [4]. Another contribution to the mass distribution of galaxies must therefore exist that is non-luminous e.g. *dark*.

Neutrino masses are not predicted: The SM does not provide an explanation for why neutrinos have mass, the theory assumes that neutrinos are massless. But experiments have shown that they do have mass [5], therefore the SM is not complete.

Matter-antimatter asymmetry is unexplained: The SM predicts that matter and antimatter should have been produced in equal amounts in the early universe, but this is in contradiction with our observation of everyday life, consisting of protons, neutrons and electrons. The reason for this matter-antimatter asymmetry remains an open question.

Hierarchy problem: The Standard Model predicts that the Higgs boson should have a much larger mass than the observed $m_H = 125.25 \pm 0.17\,\text{GeV}$ [27]. This discrepancy is known as the "hierarchy problem". It arises because the contributions from high-energy virtual particles push the Higgs boson's calculated mass to extremely large values, close to the Planck scale, where quantum gravitational effects become important. Yet, the Higgs boson's observed mass is much smaller, leading to a fundamental mismatch of many orders of magnitude. Several proposed solutions have been put forward to address the hierarchy problem. One approach is Supersymmetry [6], which introduces new particles with properties that cancel out the large quantum corrections to the Higgs mass, maintaining its value at lower energies. However, at the time of writing this thesis, experiments have not confirmed the existence of supersymmetric particles [43].

Lepton universality and flavour violation: Lepton Universality (LU) is a principle within the SM that states that the interactions of different lepton flavours (e, μ and τ) are identical, assuming identical kinematic conditions. According to LU, the fundamental interactions mediated by the weak force, such as the decay processes of $W^{\pm}$ bosons, should treat all lepton flavours equally.

Lepton Flavour Violation (LFV) refers to processes where the flavours of charged leptons can change, violating the conservation of lepton flavour [44]. In recent results, 3.1 σ deviations from the SM hinting at LFV were observed in $b \to s\ell^+\ell^-$ decays [8]. LFV processes involve the conversion of one lepton flavour into

another, such as a μ decaying into an e without the mediation of neutrinos. LFV is a manifestation of physics beyond the SM and is not predicted within the framework of LU. Flavour changing in the SM is suppressed due to various reasons. One of the reasons is that the interactions between leptons and the gauge bosons W and Z, are mediated by coupling constants known as gauge couplings. These gauge couplings are unique for each lepton flavour and determine the strength of the interactions. Another reason is that the charged leptons are mass eigenstates. This means that the particles that propagate in interactions are the mass eigenstates themselves. As a result, the charged leptons that participate in particle interactions are well-defined and distinct from one another.

In certain extensions of the SM, labelled as "BSM theories", flavour violation can occur at higher energies. Several of these BSM theories predict particles, among others so-called leptoquarks, that can interact with both leptons and quarks. These particles are further explained in more detail in Section 1.3.

1.3 Leptoquarks Beyond the Standard Model

Leptoquarks (LQ) are hypothetical particles that are predicted as extension of the SM of particle physics. One of the main motivations for the existence of LQs is to explain the apparent similarity between the masses of the different generations of quarks and leptons. In the SM, the masses of these particles are generated by the Higgs mechanism, but this mechanism does not explain why the masses are so different between the generations. LQs could allow for the generation of the masses of the different generations in a more unified way because they mediate between leptons and quarks.

While there are many theories predicting different types of LQ this thesis concerns only SU(2) singlet vector-like LQ from the in this thesis analysed simplified U_1 model [9], meaning particles with spin one and not produced in pairs. A single LQ U_1 can be added to the SM lagrangian by employing the following (simplified, effective) interactions [45]:

$$\mathcal{L}_U \supset \frac{g_U}{\sqrt{2}} \left[\beta_L^{ij} \bar{Q}^{i,a} \gamma_\mu L^j + \beta_R^{ij} \bar{d}^{i,a} \gamma_\mu e^j \right] U^{\mu,a} + \text{h.c.} \tag{1.1}$$

The interaction Equation (1.1) to the SM contains the following:

- Q and L are the left-handed SM quark and lepton doublets. The corresponding right-handed fields are d and e.
- since quarks carry colour and leptons do not, and they interact with eachother, LQ need to carry colour charge to preserve colour conservation. $a \in \{1, 2, 3\}$ is the colour index.

- also three flavours of LQ can exist; $i, j \in \{1, 2, 3\}$ are the generation indices.

- The coupling g_U characterises the overall strength of the LQ interactions with the SM matter fields whereas β_L^{ij} and β_R^{ij} are (a priori) arbitrary complex 3×3 matrices in flavour space, describing the interaction strength between the different flavours:

$$\beta_L = \begin{pmatrix} 0 & 0 & \beta_L^{d\tau} \\ 0 & \beta_L^{s\mu} & \beta_L^{s\tau} \\ 0 & \beta_L^{b\mu} & \beta_L^{b\tau} \end{pmatrix} \qquad \beta_R = \begin{pmatrix} 0 & 0 & 0 \\ 0 & 0 & 0 \\ 0 & 0 & \beta_R^{b\tau} \end{pmatrix} \tag{1.2}$$

  where $|\beta_L^{d\tau,s\mu}| < |\beta_L^{s\tau,b\mu}| \ll 1$ and $\beta_{L,R}^{b\tau} = \mathcal{O}(1)$ [9]. For example, $\beta_L^{b\tau}$ (alternatively, β_L^{33}) is the pure third generation parameter of the full leptoquark coupling matrix to left-handed fermion fields; similarly, $\beta_R^{b\tau}$ and β_R^{23} are the pure right-handed third-generation coupling and pure left-handed coupling across 2nd and 3rd generations, respectively. The zeros in β_L and β_R matrices should be understood as being very small and having a negligible impact on the observables. Furthermore the normalisation of g_U is chosen such that $\beta_L^{b\tau} = 1$.

While there are many different LQ production and interference mechanisms, this thesis contains work on a search for LQs interfering with the SM through the process $b\bar{b} \to \tau^-\tau^+$. The search is described in Chapter 3.

The representative Feynman diagrams for the process is shown in Figure 1.3. From the diagram one can calculate the relation between the coupling parameter g_U and the mass of the vector LQ M_{U_1}. One distinguishes between two terms:

Interference: In the diagram of Figure 1.3c there is no LQ in the final state, e.g. no BSM particles, only two τ of the SM. The LQ therefore *interfere* with the SM. From the matrix element calculation the relation follows as:

$$g_U \sim \frac{1}{M_{U_1}^2} \tag{1.3}$$

BSM: On the contrary to the interference term, the BSM term considers final states with a U_1 LQ. This is the case for LQ pair production Figure 1.3a and single production Figure 1.3b. Again, using the matrix element calculation the relation for BSM term is:

$$g_U \sim \frac{1}{M_{U_1}^4} \tag{1.4}$$

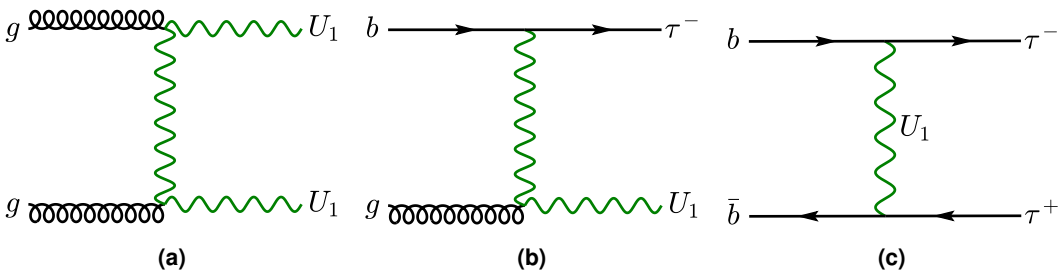

Figure 1.3: Feynman diagrams of the U_1 vector LQ pair-production (a), single (b) and t-channel Drell-Yan production (c). Figures taken from [9].

Chapter 2

The LHC and the ATLAS Experiment

The Large Hadron Collider (LHC) at the Conseil Européen pour la Recherche Nucléaire (CERN) is the world's latest and most powerful tool for high energy particle physics research. It is designed to collide protons or heavy ions at various Interaction Points (IPs) including its four main experiments:

ATLAS (A Toroidal LHC ApparatuS) [46]

CMS (Compact Muon Solenoid) [47]

ALICE (A Large Ion Collider Experiment) [48]

LHCb (Large Hadron Collider beauty) [49]

The following Section 2.1 will provide the details on how the LHC works and how particles are brought to collision at its IPs inside the experiments. The next upgrade stage for the LHC, the High-Luminosity LHC (HL-LHC), is explained in Section 2.2 This thesis presents work on the largest of these detectors – ATLAS. Its inner detectors are explained in great detail in Section 2.3. Section 2.4 is dedicated to the HL-LHC correlated ATLAS phase II upgrade: the ATLAS Inner Tracker (ITk).

2.1 The LHC

The LHC [50, 51] is a hadron accelerator and collider with a circumference of 26.7 km located between 45 m to 170 m below the Earth's surface. The design of the LHC relies on fundamental physics principles that are interconnected with (at the time) cutting-edge technology. Unlike particle-antiparticle colliders that can have both beams occupying the same phase space in a single ring, the LHC comprises two rings with counter-rotating beams that can fulfil various performance goals.

2.1.1 Performance Goals

The aim of the LHC is to precisely study the SM, Higgs boson, top and electroweak theories and reveal physics beyond the SM with centre of mass collision energies of up to 14 TeV at a design luminosity of $10^{34}\,\mathrm{cm}^{-2}\mathrm{s}^{-1}$. The rate of events produced per second from the LHC's collisions is determined by:

$$N_{\text{event}} = L\sigma_{\text{event}} \tag{2.1}$$

where L is the instantaneous luminosity and σ_{event} the cross section of the event under study. The unit of the cross section is the *barn* ($1\,\mathrm{b} = 10^{-28}\,\mathrm{m}^2$), therefore the unit of the luminosity L is $\mathrm{b}^{-1}/\mathrm{s}$, but can also be expressed in units of $\mathrm{cm}^{-2}\mathrm{s}^{-1}$. The discovery reach of the LHC ultimately depends on the total amount of events recorded and is referred to as *integrated* luminosity $L_{\text{int}} = \int L dt$. It is commonly given in units of $\mathrm{fb}^{-1} = 10^{-15}\,\mathrm{b}^{-1}$. For a Gaussian beam distribution, the machine luminosity depends only on the beam parameters:

$$L = \frac{N_b^2 n_\mathrm{b} f_{\text{rev}} \gamma_\mathrm{r}}{4\pi\epsilon_\mathrm{n}\beta^*} F \tag{2.2}$$

where N_b is the number of particles per bunch, n_b the number of bunches per beam, f_{rev} the revolution frequency, γ_r the relativistic gamma factor, ϵ_n the normalised transverse beam emittance, β^* the beta function at the collision point, and $F \sim \sigma^*/\theta_z\sigma_z$ the geometric luminosity reduction factor[1] .

The two general purpose experiments ATLAS and CMS in the LHC both strive for a peak (instantaneous) luminosity of $L = 10^{34}\,\mathrm{cm}^{-2}\mathrm{s}^{-1}$ during proton operation. Figure 2.1 shows that the designed luminosity has been surpassed in the recent years up to $2.07\times 10^{34}\,\mathrm{cm}^{-2}\mathrm{s}^{-1}$ [52]. The two experiments LHCb and TOTEM [53], which focus on b-physics and total cross section measurements respectively, aim for a peak luminosity of $L = 10^{32}\,\mathrm{cm}^{-2}\mathrm{s}^{-1}$ and $L = 2\times 10^{29}\,\mathrm{cm}^{-2}\mathrm{s}^{-1}$, respectively. Alongside proton beams, the LHC can also be operated with ion beams, and for nominal lead-lead ion operation, the LHC has ALICE as the one dedicated ion experiment which targets a peak luminosity of $L = 10^{27}\,\mathrm{cm}^{-2}\mathrm{s}^{-1}$. Therefore, the exploration of rare events in the LHC collisions requires both high beam energies and high beam intensities.

2.1.2 Acceleration of Protons

To generate a high energy beam of protons, a long chain of acceleration stages and beam guiding must be achieved. A detailed overview of these stages can be seen in the CERN accelerator complex graphic in Figure 2.2.

Initially, negative hydrogen ions are accelerated to 160 MeV with LINAC 4 [55] before

[1] θ_c is the full crossing angle at the IP, σ_z the Root Mean Square (RMS) bunch length, and σ^* the transverse RMS beam size at the IP.

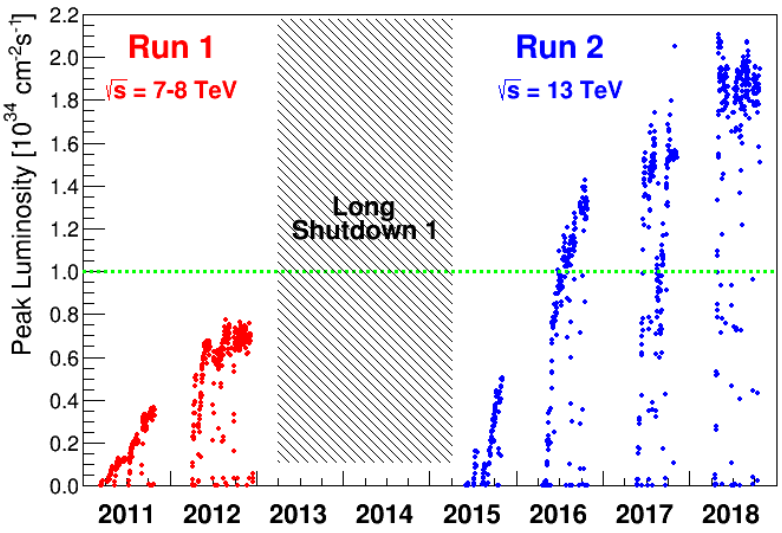

Figure 2.1: The peak luminosities of Run 1 and Run 2 delivered by the LHC up until 2018. The green horizontal line indicates the LHC's design luminosity. Note that this was before the installation of LINAC 4. Figure taken from [52].

being injected into the Proton Synchroton Booster (BOOSTER or PSB) where the electrons are then stripped off.

In this and the following stages, synchrotrons are used to gradually increase the energy of the remaining protons. In each revolution, the energy is increased slightly by Radio Frequency (RF) cavities until the extraction beam energy is reached and the beam is guided to the next acceleration stage. Due to the RF cavities the protons get separated in bunches, with around 10^{11} protons per bunch. For each stage the next accelerator has a longer circumference and the transition between accelerators happens in bunch-trains until the longer circumference is filled.

From the PSB the beam gets injected with an energy of 2 GeV into the Proton Synchroton (PS) [56]. The protons are accelerated to 26 GeV in the PS before going, train by train, into the Super Proton Synchroton (SPS), where the energy reaches 450 GeV. After the last stage, the protons are injected into the two beam pipes of the LHC, in which the bunches travel in opposite directions and are accelerated to their (current) final energy of 6.8 TeV. After the HL-LHC upgrade, the final energy is going to be 7 TeV.

Due to the reuse of the tunnels from the Large Electron Positron Collider (LEP) [57], reaching the designed collision energies was only possible through (at the time) technological improvements. For the LHC these improvements came principally through the superfluid helium system [58] – a system of superconductivity reaching temperatures of 1.9 K. For the available space in the tunnels a "two-in-one" superconducting magnet design [59] is used and the resulting magnetic field via the Lorentz force keeps the protons on their circular paths. "Two-in-one" refers to a configuration in which a single structure accommodates two adjacent beam-pipes,

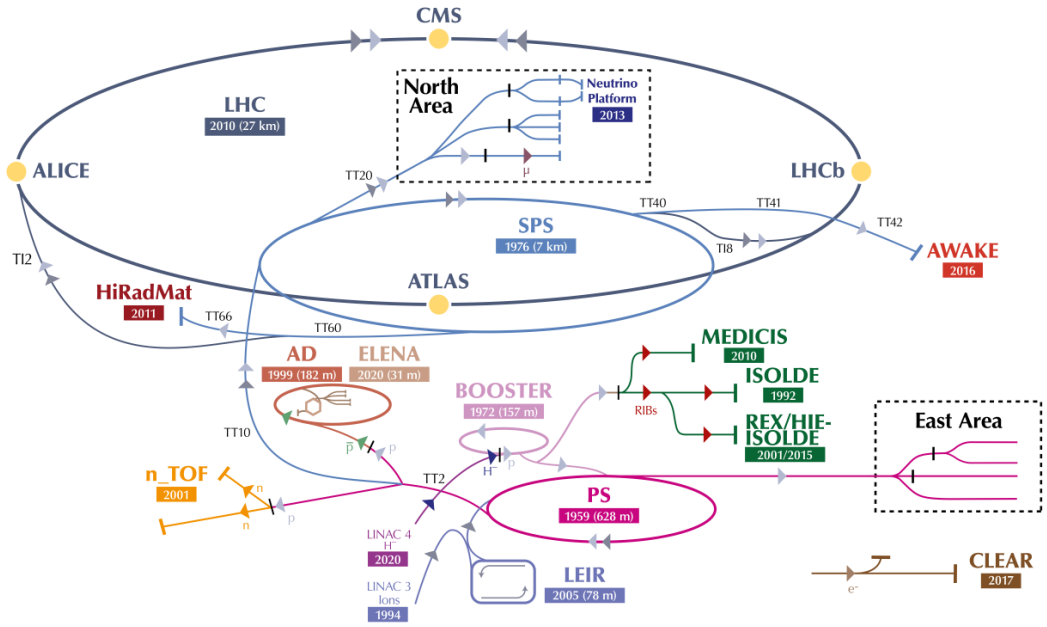

Figure 2.2: The CERN accelerator complex. Visible are the LHC and its main pre-accelerators plus many different, smaller experiments that profit from the several accelerators. Figure (adjusted) taken from [54].

each carrying protons travelling in opposite directions. In this system, dipole magnets are used to bend the beam around their circular path and quadrupole magnets are used to focus and steer the beams.

As mentioned above, the protons are separated in bunches by the RF cavities. These bunches are circulated in “bunch-trains” due to the injection and beam dumping strategy. In total, 2808 bunches are fit into the beam pipes and inside the bunch-trains, collisions happen every 25 ns (or at a crossing rate of 40 MHz) at the possible interaction points inside the detectors of the experiments. For the high luminosities mentioned above, there are multiple inelastic proton-proton interactions happening at the interaction points during each bunch crossing. This is referred to as pile-up, with $<\mu>$ expressing the mean number of simultaneous interactions per bunch crossing. Figure 2.3 shows the pile-up $<\mu> = 42.5$ for the ATLAS detector of the currently ongoing data taking period labelled as Run 3. As can be seen on the schedule in Figure 2.4, Run 3 will be the last data taking period before the LHC will be upgraded in the Long Shutdown 3 (LS3) for the High-Luminosity project.

2.2 HL-LHC – The LHC Upgrade

To significantly extend the physics program, such as the study of the Higgs boson or the substantial extension of the mass reach in searches for many signatures of BSM physics, in several cases well into the multi-TeV region, the LHC is being upgraded to the HL-LHC [62]. After the LS3 in 2029, the HL-LHC will provide a peak luminosity 5–7.5 times higher than the originally designed luminosity with levelling operation. The

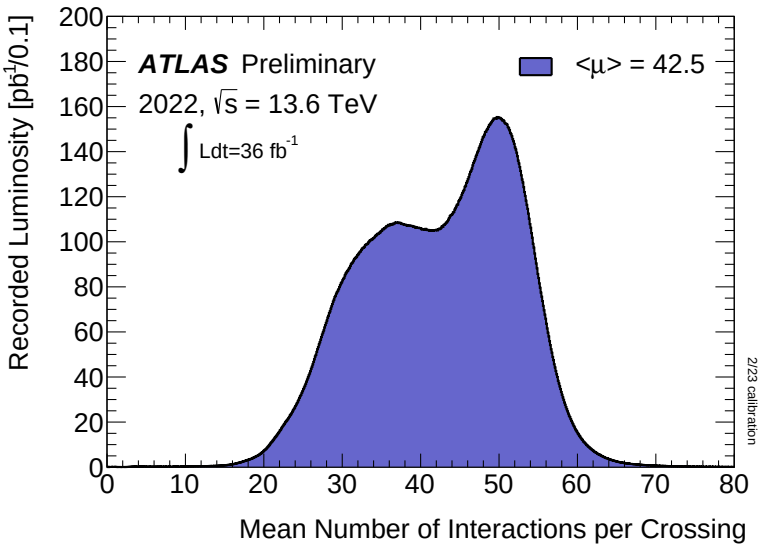

Figure 2.3: Mean number of interactions per bunch crossing of the ATLAS detector for Run 3. Figure taken from [60].

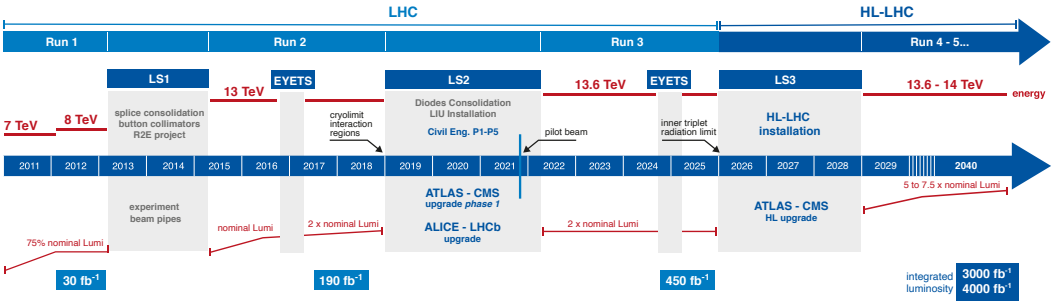

Figure 2.4: LHC schedule including the HL-LHC era. Figure taken from [61].

integrated luminosity is expected to reach 3000 fb^{-1} at the end of the HL-LHC program, about ten times the predicted luminosity reach of the LHC in its configuration after LS1 and 2 [62].

The following summarises [63] some of the main hardware features of the LHC upgrade:

Magnets: After approximately 300 fb^{-1}, parts of the Inner Triplet Magnets [64], responsible for the final focusing of the proton beams before collision, of the LHC will have received a dose of 30 MGy, which is in the range of radiation damage. While the quadrupoles may endure up to 400–700 fb^{-1}, the corrector magnets are likely to wear out, and some have already surpassed 300 fb^{-1}. As sudden electric breakdown is the most probable cause of failure, damage must be anticipated to avoid lengthy and serious repairs. The new Nb_3Sn focusing magnets feature a 11–12 T magnetic field (8.3 T currently [63]), which is used to reduce the β^* of Equation (2.2) at the interaction points.

RF Cavities: New *crab* cavities will help rotate and align the proton beams and increase the chances of collisions.

Cryogenics: To improve flexibility and availability, HL-LHC aims to add a new cryo-plant to cool the magnets more efficiently. Cooling of different parts gets more independent to avoid needing to warm up large magnet sections (a three-month operation with risks) during intervention in the focusing region.

Beam-pipe: Upgraded vacuum systems to reduce the impedance and improve beam stability.

While the LHC is the most powerful collider currently and produces exciting physics, the events are worthless without a detector to capture the events of the collision. The work presented in this thesis was performed within the upgrade activities for the ATLAS detector. This experiment is further explained in Section 2.3 and its upgrade for the HL-LHC phase in Section 2.4.

2.3 The ATLAS Detector

ATLAS is the largest, general-purpose particle detector experiment at the LHC. It features a cylindrical geometry[2] and consists of numerous sub-detectors as shown in the layout in Figure 2.5, each responsible for the detection of specific particles and their kinematics.

The four main sub-detectors extend radially starting from the IP $x = y = z = 0$ and have cylindrical shapes with barrel sections and endcaps. The sub-detector closest to the IP is the Inner Detector (ID) formed by the Pixel Detector, the SemiConductor Tracker (SCT) and by the Transition Radiation Tracker (TRT). The ID is immersed in a 2 T magnetic field generated by a solenoid magnet, which makes it possible to measure the curvature of a particle track (referred to as tracking) and, with the help of the Lorentz force equation, the particle's momentum and charge. The Pixel Detector and SCT consist of silicon sensors while the TRT consists of thin wall proportional drift tubes. The ID is further explained in Section 2.3.1.

The next sub-detector is the calorimetry system consisting of the Electromagnetic Calorimeter (ECAL), which can detect electromagnetic showers from mainly electrons or photons. To get energy measurements with high resolution, the ECAL is finely segmented and based on a lead-liquid argon radiator, designed to fully contain the electromagnetic showers. Just outside the ECAL, the Hadronic Calorimeter (HCAL) is able to detect hadrons like protons or neutrons and mesons like pions. It is segmented more coarsely than the ECAL since it is mainly aimed at reconstructing jets and at measuring missing transverse momenta or energy. Missing Transverse Energy (MET)

[2] ATLAS uses a right-handed coordinate system with its origin at the nominal IP in the centre of the detector and the z-axis along the beam pipe. The x-axis points from the IP to the centre of the LHC ring, and the y-axis points upward. Cylindrical coordinates (r, ϕ) are used in the transverse plane, ϕ being the azimuthal angle around the z-axis. The pseudorapidity is defined in terms of the polar angle θ as $\eta = -\ln(\tan(\theta/2))$.

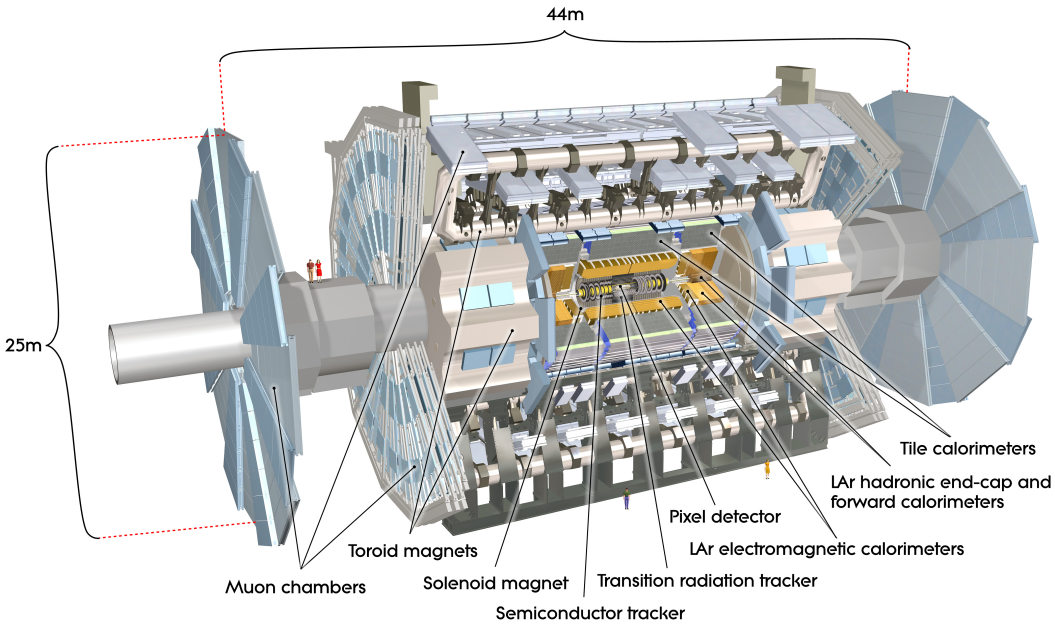

Figure 2.5: Rendering of the complete, current ATLAS detector and its main sub-detectors. Figure taken from [65].

is associated with particles not measurable by the detector. An example are neutrinos: as they are not charged and of very low mass, they are “invisible” to the detector. The missing transverse momentum E_T^{miss} can be reconstructed indirectly from the angular momenta distribution of the “visible” particle transverse momenta p_T:

$$E_T^{\text{miss}} = -\sum_i p_{T,i} \tag{2.3}$$

Both the ECAL and HCAL are more explained in Section 2.3.2.

Outside the calorimeters there is the muon system with its toroid magnet loops. They generate a magnetic field to bend the muons. Muons are among the most important signatures for interesting processes at the LHC. As an example, one channel of the Higgs boson discovery was the $H \to ZZ \to \mu^-\mu^+\mu^-\mu^+$ channel. Muons have a clear advantage that they are the only charged particles that are not stopped in the calorimeter (apart from rare cases of punch-through) and can then be detected in the muon system. The latter consists of two sub-detector types: one for precision measurements of the muon momenta, and the other for the trigger of muon events, which require very fast sub-detectors to uniquely associate the muons to a certain bunch crossing. The muon system is detailed in Section 2.3.3.

Besides the sub-detectors there is a sophisticated Trigger and Data Acquisition (TDAQ) that takes care of selecting interesting events and preparing them for storage. Section 2.3.4 explains this system in more detail.

2.3.1 The Inner Detector

The ATLAS ID [46,66] has been designed to provide robust pattern recognition and high momentum resolution with an average of 36 hits per track of charged particles for the pseudorapidity range $|\eta| < 2.0$ [46]. Both primary and secondary vertex measurements for charged tracks can be measured above a certain p_T threshold (nominally 0.5 GeV, but as low as 0.1 GeV in some cases) and within $|\eta| < 2.5$. It can also identify electrons over a range of energies (0.5 GeV to 150 GeV) within $|\eta| < 2.0$. This performance is at the limit of current technology and is required at the highest luminosities expected from LHC collisions.

The layout of the ID is illustrated in Figure 2.6. The ID has a cylindrical shape and is

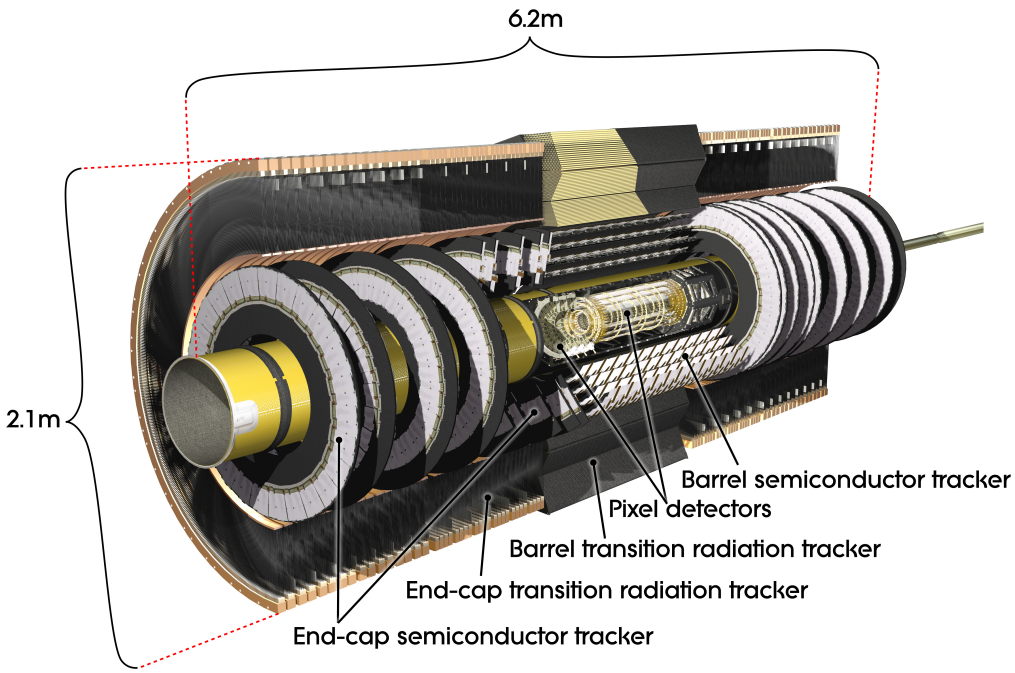

Figure 2.6: Rendering of the complete ATLAS ID with its dimensions. Figure taken from [67].

situated inside a solenoidal magnetic field of 2 T. It consists of three independent but complementary sub-detectors:

Pixels: The pixel detector system [68] is composed of modular units: read-out integrated circuits are mounted onto detector substrates to form 1744 barrel and disc modules [69]. These are all identical, simplifying construction and maintenance. The detector substrate is silicon, and the baseline design is an n^+-on-n^- bulk sensor material to allow for partially depleted operation, should this be needed following irradiation. The read-out integrated circuits are mounted on the 250 µm thick silicon sensor using the bump bonding technology. The nominal pixel size is $50 \times 400\,\mu m^2$ (about 90% of the pixels) and is dictated by the readout pitch of the front-end electronics. The sensors started operation with

a bias voltage of approximately 150 V. However, to ensure optimal charge collection efficiency over the ten-year operational span, higher operating voltages of up to 600 V might be necessary. The specific voltage requirement will vary based on factors such as sensor placement, integrated luminosity, and operational procedures.

The pixel modules were originally arranged in three barrel layers (ID B-layers 0-2) and two end-caps each with three disc layers. But, as shown in Figure 2.7, there is an additional layer of pixels called Insertable B-Layer (IBL) [70, 71] closest to the beam pipe. During LS1 IBL was installed for tracking robustness and precision (especially for *b*-tagging), to limit luminosity effects due to high occupancy in B-layers and to improve radiation robustness for Run 2 and 3. Furthermore it represented the opportunity to replace the original beam pipe with a smaller radius beam pipe. The FE-I3 (Pixel detector) and the FE-I4B (IBL)

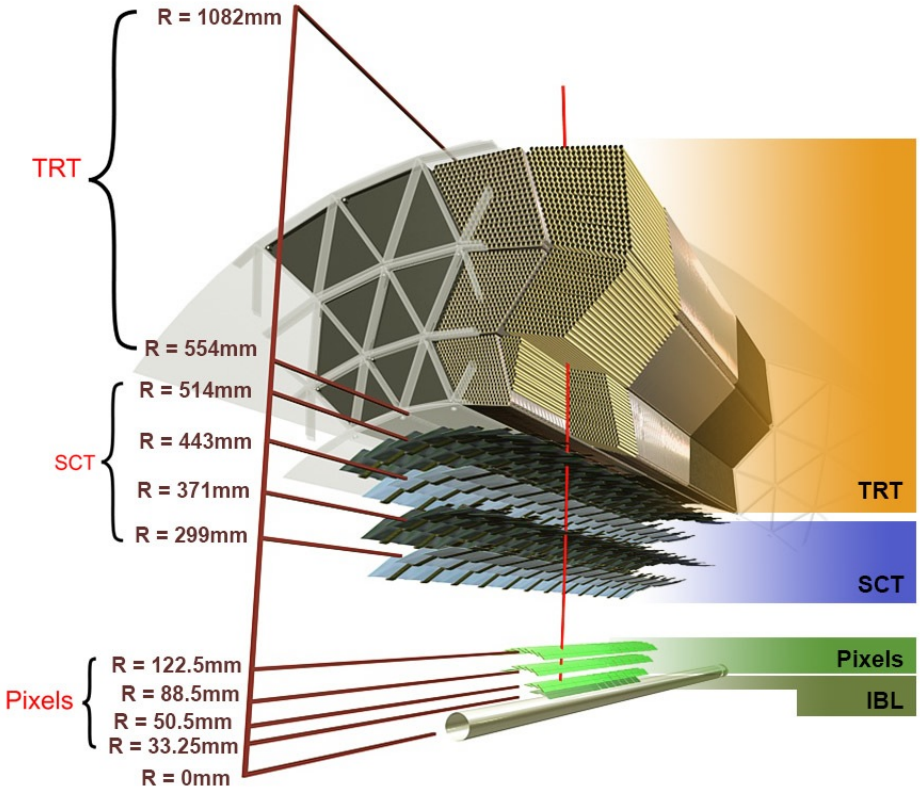

Figure 2.7: Schematic cut of the barrel section of the ATLAS ID and its three independent sub-detectors: Pixels (including IBL), SCT and TRT. At $R = 0$ the beam pipe is shown and just on top of it the Pixels including the IBL. The gap of space between Pixels and SCT is the space of the pixel support tube. After these services the strips of the SCT are pictured. The yellow horizontal tubes are the straws of the TRT. The red track is a simulated 10 GeV electron traversing the different layers. Figure taken from [72].

front-end chips configure the sensor and send its data out at speeds of up to 160 Mb/s. The FE-I4B ASIC is specified for ionising doses[3] of up to 250 Mrad.

SCT: The SemiConductor Tracker (SCT) [73] is composed of a total of 4088 modules

[3] 1 Mrad = 0.01 Gy; 1 Gy = 1 J/kg.

of silicon-strip detectors, which are organised into four concentric barrels (with 2112 modules) and two endcaps (with nine discs each, totalling 988 modules per endcap). To ensure cost-effectiveness and reliability, the SCT employs a classic single-sided p-in-n technology with AC-coupled readout strips for its 15912 sensors. At the start of operations of ATLAS, the sensors were operating at approximately 150 V bias voltage. However, to maintain good charge collection efficiency over a ten-year period, operating voltages ranging from 250 V to 350 V are possible, depending on factors such as sensor position, integrated luminosity and radiation damage.

The sensor thickness of 285 $\pm$ 15 µm strikes a balance between the required operating voltage, primary signal ionisation, and fabrication simplicity. The choice of strip pitch was determined by considerations such as required digitising precision, granularity, particle occupancy, and noise performance. For the rectangular barrel sensors, a strip pitch of 80 µm was selected, with two 6 cm-long sensors daisy-chained together. For the trapezoidal end-cap sensors, radial strips with a mean pitch of approximately 80 µm were chosen. This configuration results in a total of 768 active strips, each measuring 12 cm in length per sensor, along with two strips at bias potential to define the sensor edge.

In the SCT, every barrel or disc is equipped with two strip measurements, taken at a stereo angle, that are merged to form space-points. For particles originating from the IP, the SCT usually offers eight strip measurements (equivalent to four space-points). The strips are read out by radiation-hard front-end ABCD chips [74] mounted on flexible circuits named readout hybrids.

TRT: The Transition Radiation Tracker (TRT) [75] is divided into three sections: a central barrel [76] and two end-caps [77]. Its fundamental components are thin-walled proportional drift tubes, commonly referred to as *straw tubes* or simply *straws*. Straw tubes were selected as detection elements due to their modular nature, allowing for easy integration into a medium that generates transition radiation without interfering with the continuous tracking concept. Its working principle features a 30 µm diameter gold-plated tungsten wire in the centre of the tube that is put under high voltage with respect to the outer kapton film which is coated to the inner surface of the tube. The void between the gap of wire and wall is filled with a gas mixture of Xe-CO_2-O_2 70/27/3% which has been extensively validated in terms of high-rate performance and ageing behaviour. If a charged particle passes the gas electrons are induced in so-called ionisation clusters, they are drifted by the electric field and read-out once they are collected at the wire.

The barrel section consists of 52544 straws, each measuring 144 cm in length and aligned parallel to the beam. Each of the two end-caps contains 122880 straws, with a length of 37 cm and arranged radially along the beam axis. The

geometry of the detector ensures that particles pass through approximately 35–40 straws within a pseudorapidity range of $|\eta| < 2.0$. This configuration enables continuous tracking at larger radii within the ID while improving its pattern recognition capabilities.

Several requirements for optimal performance at the LHC often conflict with each other, necessitating compromises. For the straw tubes, a larger tube diameter would ensure a higher hit efficiency but would struggle to capture all the electrons within the short 25 ns bunch crossing time due to the lengthy drift time within the straw. To strike a balance, the TRT opted for tubes with an inner diameter of 4 mm. This choice represents a favourable compromise between response speed, the number of ionisation clusters, and mechanical and operational stability.

2.3.2 The Calorimeters

The ATLAS calorimeters [78, 79] are comprised of multiple sampling detectors designed with full ϕ symmetry to ensure coverage around the beam axis. The calorimeters are designed and split in two types according to their detection goal: the Electromagnetic Calorimeter (ECAL) can detect electromagnetic showers from particles such as electrons and photons and the Hadronic Calorimeter (HCAL) hadronic showers (jets) from protons, neutrons, pions, kaons and many more hadrons. Its primary, simplified goal is to stop all the above-mentioned particles inside its detector volumes to measure their energy and momenta.

As shown in Figure 2.8, the electromagnetic calorimeters are housed in three cryostats: one barrel and two end-caps. The electromagnetic barrel calorimeter is located within the barrel cryostat. Each of the two end-cap cryostats contains an Electromagnetic End-cap Calorimeter (EMEC), Hadronic End-cap Calorimeter (HEC) positioned behind the EMEC, and a Forward Calorimeter (FCal) that covers the region closest to the beam. All of these calorimeters utilise Liquid Argon (LAr) as the active detector medium, hence the three cryostats must be kept at temperatures below -184° C. Liquid argon was chosen for its desirable properties, including its linear response behaviour, stable response over time, and inherent resistance to radiation effects. The ATLAS precision electromagnetic calorimeters employ lead-liquid argon detectors with absorbers and electrodes arranged in an accordion-like shape. This specific geometry enables the calorimeters to have multiple active layers in the trajectory of particles. Within the precision-measurement region ($0 < |\eta| < 2.5$), there are three active layers, while in the higher-η region ($2.5 < |\eta| < 3.2$) and the overlap region between the barrel and EMEC, there are two active layers. In the precision-measurement region, precise position measurements are obtained by finely segmenting the first layer in η. The η-direction of photons is determined by the position of the photon cluster in both the first and second layers. Additionally, the calorimeter system provides electromagnetic coverage at higher η values ($3.1 < |\eta| < 4.9$) through

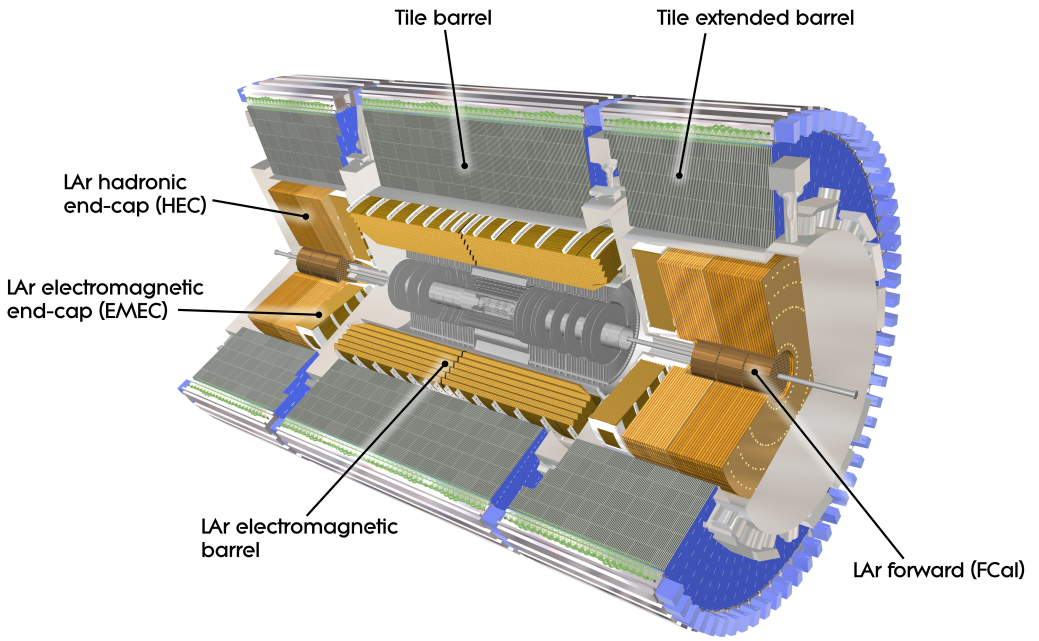

Figure 2.8: Rendering of the ATLAS calorimeters. One can see in orange the different LAr cryostats; electromagnetic barrel and the two end-caps EMEC, HEC, FCal on each side. In the outermost layer the hadronic calorimeters tile barrel and tile extended barrel are situated. Figure taken from [80].

the inclusion of the FCal.

The outer tile hadronic calorimeter in ATLAS utilises a combination of scintillator tiles as the sampling medium and steel as the absorber medium. The tile calorimeter is divided into three sections similar to the LAr calorimeter: one central barrel and two extended barrels. This technology choice allows for maximum radial depth while minimising costs.

The tile calorimeter covers the range $0 < |\eta| < 1.7$, which includes both the central and extended barrels. To extend the coverage of hadronic calorimetry to larger pseudorapidity, two additional detectors are employed. The first is the HEC, which is a copper/liquid-argon detector. The second is the FCal, which is a copper-tungsten/liquid-argon detector. These extensions enable the hadronic calorimetry to achieve one of its primary design goals: cover the pseudorapidity range $|\eta| < 4.9$.

2.3.3 The Muon System

The muon system or muon spectrometer [81] serves as the outermost component of the ATLAS detector and is specifically designed to detect charged particles as they exit the barrel and end-cap calorimeters, enabling the measurement of their momentum within the pseudorapidity range of $|\eta| < 2.7$. Furthermore, the muon spectrometer is designed to trigger on these particles in the region of $|\eta| < 2.4$.

The primary performance objective is to achieve a stand-alone transverse momentum resolution of approximately 10% for tracks with a momentum of 1 TeV. This resolution corresponds to a sagitta, a measure of the deviation or displacement of a charged particle's trajectory from its expected path due to the influence of magnetic fields along the z-axis of approximately 500 µm, which should be achieved with a resolution of $\leq$ 50 µm [46]. The muon spectrometer is capable of measuring muon momenta down to around 3 GeV due to energy loss in the calorimeters.

As seen in Figure 2.9, the precision-tracking chambers in the barrel region of the muon spectrometer are strategically positioned both between and on the eight coils of the superconducting barrel toroid magnet. Similarly, the end-cap chambers are located in front of and behind the two end-cap toroid magnets. This arrangement maintains the ϕ symmetry of the toroids and is reflected in the symmetric structure of the muon chamber system, which consists of eight octants. Each octant is further divided into two sectors

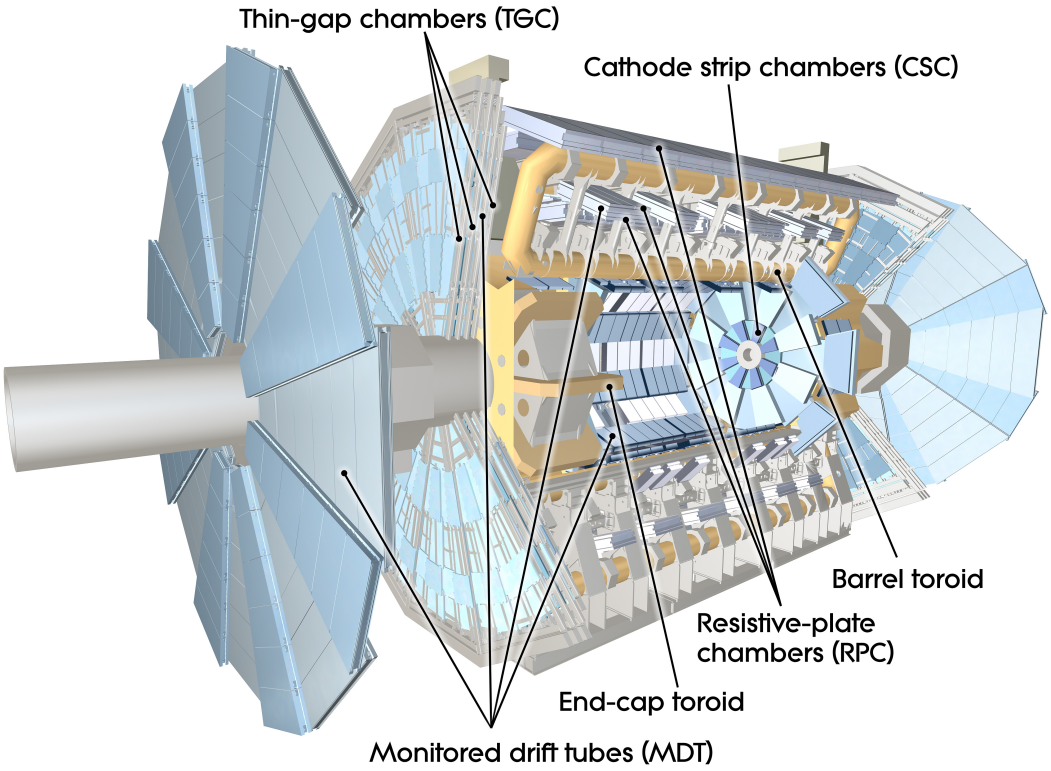

Figure 2.9: Rendering of the muon system with all other sub-detectors removed. Also visible is the large magnet system in orange-yellow; the barrel toroid and the end-cap toroid. Figure taken from [82].

in the azimuthal direction, with slightly different lateral extensions: a large sector and a small sector. This division results in an overlapping region in ϕ, which minimises any gaps in detector coverage. Additionally, the overlap allows for the relative alignment of adjacent sectors by utilising tracks recorded by both a large and a small chamber within the overlapping region.

To achieve precise momentum measurements, the Monitored Drift Tube (MDT) are utilised. These chambers offer a combination of high measurement accuracy,

predictable mechanical deformations, and a simple construction method. The MDT cover the pseudorapidity range of $|\eta| < 2.7$, with the exception of the innermost end-cap layer where their coverage is limited to $|\eta| < 2.0$. The MDT chambers consist of three to eight layers of drift tubes, which operate at an absolute pressure of 3 bar. They provide an average resolution of 80 µm per tube, or approximately 35 µm per chamber. This level of resolution allows for precise determination of particle momenta within the muon spectrometer.

Within the forward region of the muon spectrometer, specifically in the range of $2 < |\eta| < 2.7$, the innermost tracking layer utilises Cathode Strip Chambers (CSC) due to their superior rate capability and time resolution. The CSCs are multiwire proportional chambers where the cathode planes are segmented into strips that are oriented in orthogonal directions. This design enables the measurement of both coordinates by analysing the distribution of induced charge. The resolution of a CSC is approximately 40 µm in the bending plane, which is the direction perpendicular to the magnetic field, and approximately 5 mm in the transverse plane. The difference in resolution between the bending and non-bending planes arises from variations in the readout pitch and the fact that the azimuthal readout runs parallel to the anode wires. The CSCs provide valuable positional information for accurate tracking and momentum determination of particles in the forward region of the muon spectrometer.

To enable efficient triggering on muon tracks, the muon system was designed with the inclusion of fast trigger chambers. These chambers are capable of providing track information within a few tens of nanoseconds after a particle passes through them, allowing for rapid identification and triggering of muon events. In the barrel region of the muon system ($|\eta| < 1.05$), Resistive-Plate Chambers (RPC) were selected as the fast trigger chambers. For the end-cap region ($1.05 < |\eta| < 2.4$), Thin-Gap Chambers (TGC) were chosen for this purpose. Table 2.1 provides information on the intrinsic time resolution of these detectors, which must be supplemented with contributions from signal propagation and electronics. The design objective was to keep these additional contributions low enough to ensure reliable identification of beam crossings with a probability of $\geq$ 99%. Both the RPCs and TGCs deliver signals with a spread of 15–25 ns, allowing for accurate tagging of the beam crossing. These trigger chambers measure both coordinates of the track, one in the bending η plane and the other in the non-bending ϕ plane, providing comprehensive information for muon track identification and triggering purposes.

2.3.4 Trigger and Data Acquisition

As mentioned above in Section 2.1 the LHC beams consist of sequences of particle bunches, with a minimum time interval of 25 ns between successive bunches. This means that collisions can occur every 25 ns within a very short time interval, typically less than 1 ns, determined by the length (7 cm) of the bunches. With an instantaneous

		Chamber resolution (RMS) in			Measurements/track		Number of	
Type	**Function**	z/r	ϕ [mm]	time [ns]	barrel	end-cap	chambers	channels $\cdot 10^3$
MDT	tracking	35 µm (z)	-	-	20	20	1088 (1150)	339 (354)
CSC	tracking	40 µm (r)	5	7	-	4	32	30.7
RPC	triggering	10 mm (z)	10	1.5	6	-	544 (606)	359 (373)
TGC	triggering	2–6 mm (r)	3–7	4	-	9	3588	318

Table 2.1: Parameters of the four sub-systems of the muon detector. The quoted spatial resolution (columns z/r and ϕ) does not include chamber-alignment uncertainties. Column time lists the intrinsic time resolution of each chamber type, to which contributions from signal-propagation and electronics contributions need to be added. Numbers in brackets refer to the complete detector configuration as planned for 2009. Table taken from [46, Table 6.1].

luminosity of $10^{34}\,\mathrm{cm}^{-2}\mathrm{s}^{-1}$ and a bunch spacing of 25 ns, an average pile-up of approximately of 23 interactions occur per bunch-crossing, resulting in around 10^9 interactions per second. To handle this high interaction rate and due to the limited amount of storage, it is necessary to *trigger* only on interesting events. The ATLAS experiment employs a three-level Trigger and Data Acquisition (TDAQ) system [83–85] to store the interesting events: Level-1 trigger (L1), Level-2 trigger (L2), and the Event Filter (EF). The L2 and EF components combined form the High-Level Trigger (HLT). Figure 2.10 depicts a block diagram illustrating the trigger and data acquisition systems.

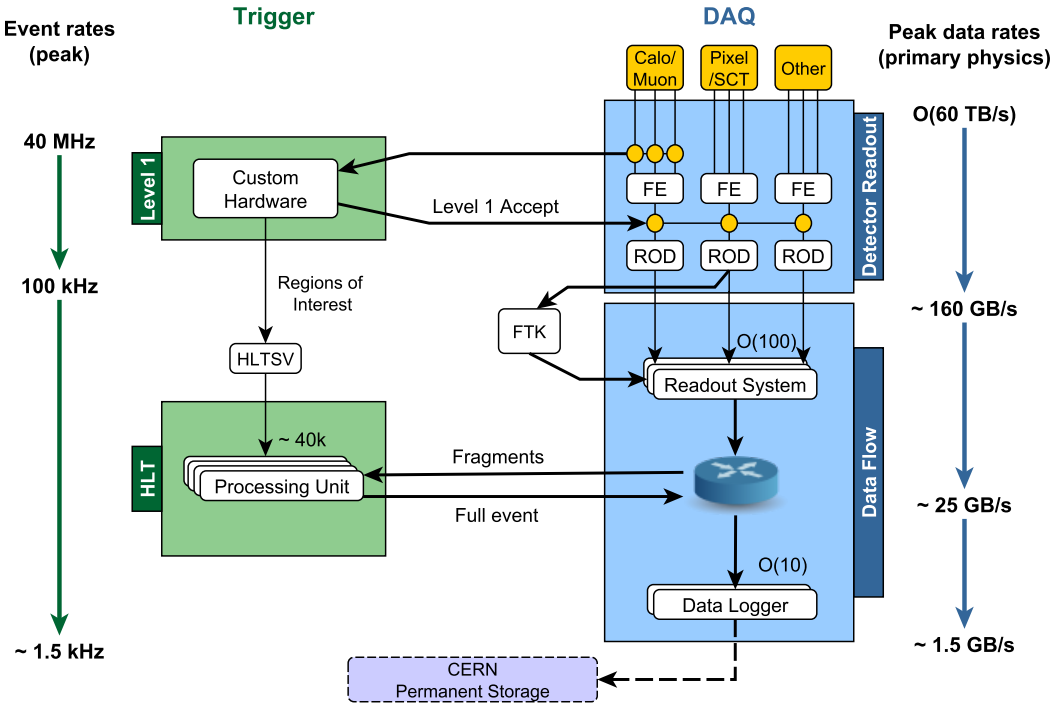

Figure 2.10: Functional diagram of the ATLAS TDAQ system for Run 2 showing expected peak rates and bandwidths through each component. Figure taken from [86].

The L1 trigger system performs searches for high-transverse-momentum particles such as muons, electrons, photons, jets, and τ-leptons that decay into hadrons, along with significant missing and total transverse energy signatures. This selection process relies on data from a subset of detectors: High-transverse-momentum muons are

distinguished through trigger chambers positioned in both the barrel and end-cap regions of the spectrometer. The calorimeter-based selections are guided by condensed data from all calorimeters. Central trigger processing takes the outputs from the L1 muon and calorimeter triggers, assembling a trigger "menu" composed of various trigger selections. This menu can be adjusted using pre-scaling to optimally allocate bandwidth based on varying luminosity and background conditions. Events that successfully pass through the L1 trigger selection proceed to subsequent stages of detector-specific electronics and eventually to data acquisition through point-to-point connections. Within each event, the L1 trigger also establishes one or more Region of Interest (ROI), denoting the specific geographical coordinates in η and ϕ where the selection process identified noteworthy features within the detector. ROI data encompass details about the type of detected feature and the fulfilled criteria, such as a threshold. This information subsequently informs the high-level trigger processing.

The L2 selection process is initiated by the ROI information furnished by the L1 trigger through a dedicated data pathway. Within L2 selections, all available detector data within the ROIs are utilised at their maximum granularity and precision, accounting for approximately 2% of the total event data. The design of L2 menus is geared towards diminishing the trigger rate to around 1.5 kHz, with an average event processing time of approximately 40 ms across all events [69].

Subsequently, the event filter undertakes the final phase of event selection, further lowering the event rate to roughly 200 Hz. These selections are executed using offline analysis techniques, with an average event processing time on the order of four seconds.

During LS1, the detector's readout system underwent an upgrade to accommodate a higher acceptance rate of 100 kHz. The L1, shown as a simplified scheme in Figure 2.11, is constructed using dedicated hardware and can process event data at the required rate of 40 MHz. This is achieved by utilising analog sums of calorimeter sub-system signals like electromagnetic clusters, jets, τ-leptons, E_T^{miss} and large total transverse energy $\sum E_T$ and signals from specific muon trigger chambers (RPCs and TGCs) with high-p_T muons. Consequently, event selection is based solely on energy depositions in the calorimeters and segments of muon tracks.

Data Acquisition (DAQ)

The transfer of events from the detector to mass storage begins with the selection of events by the L1 trigger. During the L1 trigger selection latency, which can be up to 2.5 µs, the event data is stored in memory buffers (maximum latency of about 3 µs) within the specific front-end electronics of the detector. This latency includes the time taken for signals to travel between the detectors and the trigger system, as well as the time required to transmit the trigger accept signals to the on-detector readout

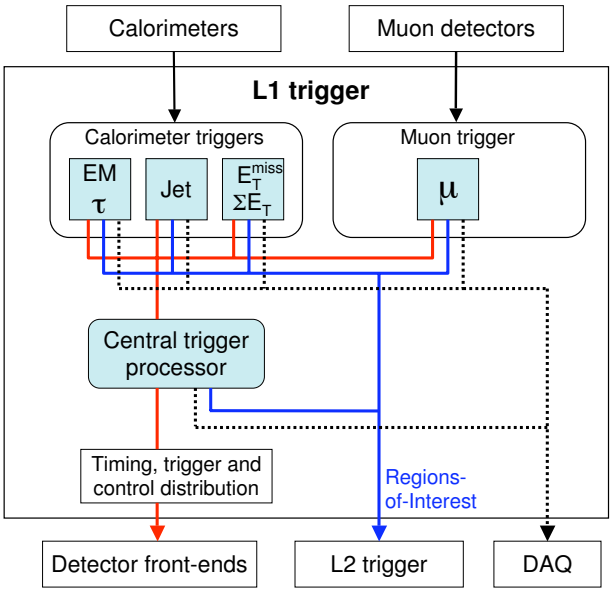

Figure 2.11: Block scheme of the L1 trigger. The overall L1 accept decision is made by the central trigger processor, taking input from calorimeter and muon trigger results. The paths to the detector front-ends, L2 trigger, and data acquisition system are shown from left to right in red, blue and black, respectively. Figure taken from [86].

electronics.

Once selected by the L1 trigger, the event data is transmitted to the DAQ/HLT system through Readout Links (ROLs), passing through the Readout Drivers (RODs). The ROD are detector-specific functional elements of the front-end systems, which achieve a higher level of data concentration and multiplexing by gathering information from several front-end data streams. Although each sub-detector uses specific front-end electronics and ROD, these components are built from standardised blocks and are subject to common requirements.

The L1 accept decisions are also transmitted through the Timing and Trigger Control (TTC) system [87] to both on-detector and off-detector readout electronics. At L1, the Central Trigger Processor (CTP) receives three clock signals from the accelerating radio cavities or more specifically, through the RF2TTC interface [88]. These clock signals have a frequency of 3564 times the revolution frequency of an 11.2 kHz bunch, resulting in a frequency of 40.078 MHz (one clock signal for each beam and one for the maximum collision rate). The CTP utilises the LHC clock signal to send information through the various sub-modules and systems.

Data corresponding to events that are accepted by the L1 trigger are further processed by software running on computer farms, providing the HLT: the events selected by the L2 trigger are subsequently transferred to the event-building system and then to the EF for final selection. Events that pass the selection criteria of the event filter are moved to permanent storage at the CERN computer centre. In addition to controlling movement of data down the trigger selection chain, the data acquisition system also provides for

the configuration, control and monitoring of the ATLAS detector during data-taking. Supervision of the detector hardware (gas systems, power-supply voltages etc.) is provided by the Detector Control System (DCS).

Detector Control System (DCS)

The DCS [89] plays a crucial role in ensuring the coordinated and safe operation of the ATLAS detector hardware. It acts as a unified interface for all sub-detectors and the technical infrastructure of the experiment. The DCS is responsible for controlling, continuously monitoring, and archiving the operational parameters of various systems. It promptly alerts operators of any abnormal behaviour and allows for manual or automatic corrective actions to be taken. These systems include high- and low-voltage systems for detectors and electronics, gas and cooling systems, magnetic field controls, temperature monitoring, and humidity levels.

Furthermore, the DCS facilitates bidirectional communication with the data acquisition system to ensure synchronisation between the detector's state and data-taking processes. It also facilitates communication between the sub-detectors and other independently controlled systems, such as the LHC accelerator, CERN technical services, ATLAS magnets, and the detector safety system. The DCS serves as a critical component in maintaining the operational integrity and functionality of the ATLAS detector.

2.4 ATLAS ITk – An LHC Phase II Upgrade

The higher instantaneous luminosity to be delivered by HL-LHC brings a significant increase in the average number of interactions per bunch crossing $<\mu>$. This number is expected to rise from approximately 55 at $2 \times 10^{34}\,\mathrm{cm^{-2}s^{-1}}$ to around 140 at $5 \times 10^{34}\,\mathrm{cm^{-2}s^{-1}}$. Consequently, the integrated luminosity also increases, necessitating a detector that can withstand exposure to high particle fluences. These elevated conditions have implications for the ATLAS experiment, including higher detector occupancy and increased radiation damage. To ensure a safety margin, the design studies for the proposed upgrades consider a maximum instantaneous luminosity of $7 \times 10^{34}\,\mathrm{cm^{-2}s^{-1}}$, up to 200 pile-up events, and an integrated luminosity of $3000\,\mathrm{fb^{-1}}$ over a ten-year period.

Towards the end of the currently ongoing Run 3, the components of the ATLAS detector will have been in operation for approximately 15–20 years. Following the Phase-I upgrade, the silicon tracking systems will have reached their maximum lifetimes, with the strip system lasting for $700\,\mathrm{fb^{-1}}$ and the pixel system, which experiences higher amount of radiation, for $400\,\mathrm{fb^{-1}}$. Additionally, the higher luminosity levels anticipated at the HL-LHC will lead to a significant increase in the occupancies

of both the silicon detectors and the straw tubes of the TRT, therefore greatly compromising the tracking performance. It is crucial to ensure excellent performance in vertex and track reconstruction, lepton identification, and heavy flavour tagging even in the high occupancy and radiation fluence conditions of the HL-LHC. Therefore, a complete replacement of the current ID is necessary. Drawing from the knowledge gained from the current tracker, a new design for an all-silicon tracker has been developed: the ATLAS Inner Tracker (ITk).

The new layout, see Figure 2.12 for a rendering and Figure 2.13 for a schematic view of one quadrant, incorporates a Pixel Detector [90] for precise position measurements and pattern recognition near the vertex, complemented by a Strip Detector [91] that enables accurate tracking at larger radii. The design of the system has been carefully

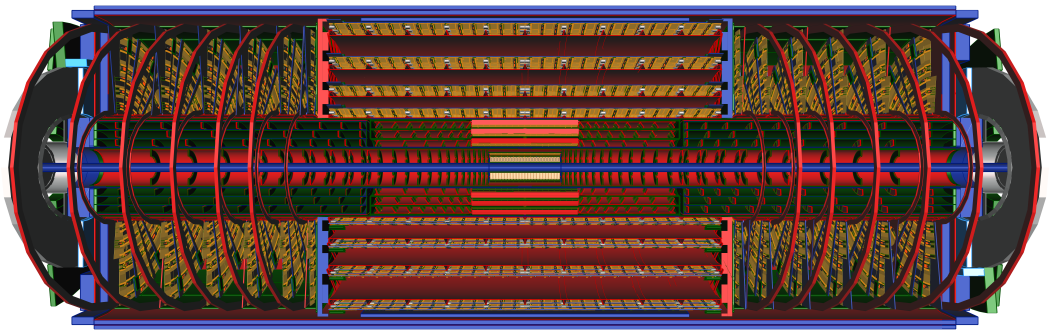

Figure 2.12: Computer generated image of the half-way opened ATLAS ITk with the Inclined Duals detector layout. The horizontal blue tube is the beam pipe. The Pixel detector, with the modules in green, wraps around the beam pipe and takes up about one third of the space of ITk. Wrapped around the Pixel Detector is the Strips Detector with its orange modules, shown here on top and on the bottom. The ITk's size is roughly 3 m in diameter and 7 m in length. Figure taken from [92].

optimised to reduce the amount of material. This is achieved by employing lightweight carbon fibre-based engineering materials for the support structures and by meticulously planning the arrangement of services and their pathways. Advancements in silicon sensor technologies have demonstrated their ability to withstand high levels of radiation, and modern ASIC technologies have been utilised to develop front-end electronics that possess the necessary radiation tolerance.

As this thesis contains work on the ITk Pixel Detector and its detector layout, which is from hereby on referred to as *Inclined Duals* layout, a detailed look is given in the following Section 2.4.1.

2.4.1 The ITk Pixel Detector

The ITk Pixel Detector incorporates a design with barrel staves and end-cap ring systems with inclined (tilted) modules for better coverage. The layout of the Pixel Detector modules, see Figure 2.14 for an overview, is composed of three complementary subsystems that have different implementation strategies and cover $|\eta| \leq 4.0$ – the full range of ITk. Not mapped are the monitoring devices Pixel

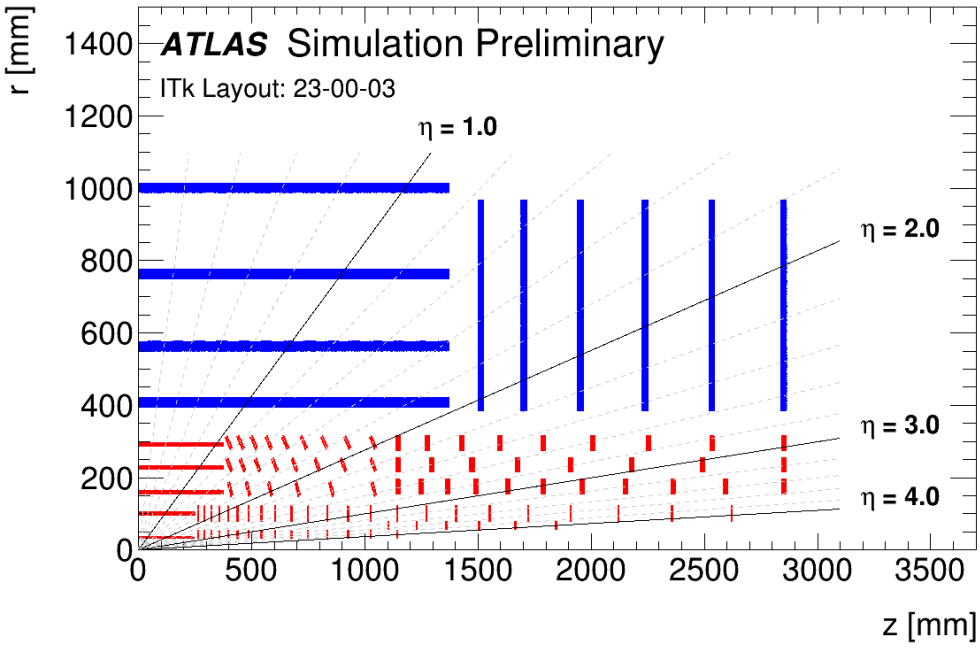

Figure 2.13: A schematic depiction of the ITk layout where only one quadrant and only active detector elements are shown. The active elements of the Strip Detector are shown in blue, and those of the Pixel Detector are shown in red. Figure taken from [92].

Luminosity Ring (PLR) and Beam Conditions Monitor Prime (BCM'), but they are later included in the itenary of the Optoboard system as they are expected to be in L1 between the rings of the innermost part of the Pixel Detector.

IS: The Inner System (IS) is divided into a barrel section and a ring section. The barrel section has modules on layer 0 and layer 1. The rings are further divided by their position in the detector and consequently their module mounting techniques: the Coupled Rings (CR) have modules of two layers mounted on the same support ring – therefore *coupled*. Intermediate Rings (IR) are between layer 0 and layer 1 on layer 0.5 and Quad Rings (QR) are the outermost rings on layer 1. The complete IS is designed to be replaced after LS4 or LS5 due to its limited radiation tolerance.

OB: The Outer Barrel (OB) system is split in Flat Layer (FL) or barrel and Inclined Layer (IL). Both regions extend from layer 2 to layer 4 and cover $|\eta| \leq 2.6$ with quads.

EC: The End Caps (EC) have rings with quad modules covering $2.0 \leq |\eta| \leq 4.0$. Initially they were proposed [90] with 4 MHz readout capability but this was ultimately abandoned due to bandwidth limitations and material budget reasons. Now the baseline capability is set at 1 MHz.

PLR: The PLR idea is to install additional ITkPix modules fully devoted to the luminosity measurement using the Pixel Cluster Counting (PCC) method [93]. It consists of eight L0 barrel triplet pixel modules (one module every 45°) with sensors tilted 30° towards the IP to use shape information.

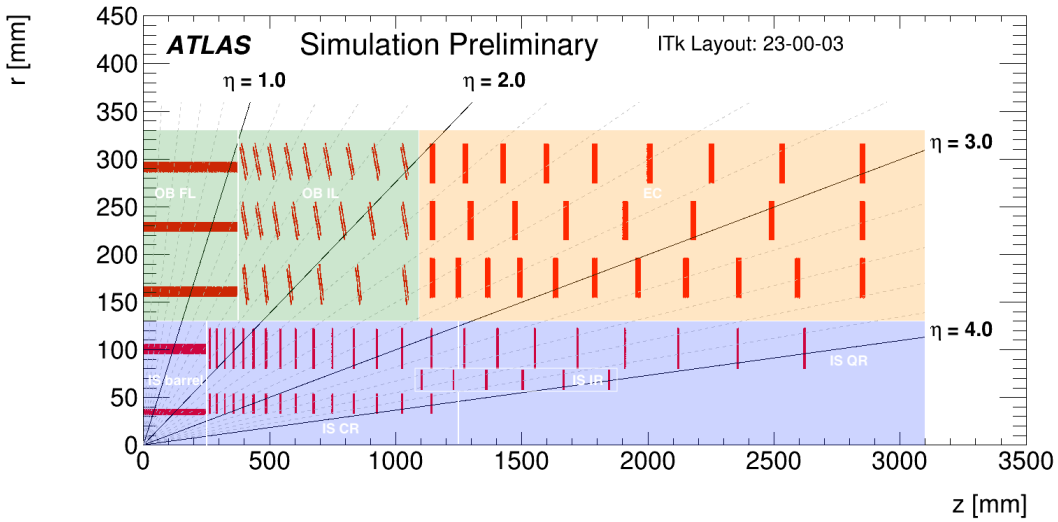

Figure 2.14: The Inclined Duals layout of the ITk Pixel Detector with its subsystems for one quadrant. Beginning from the IP the Inner System with two barrel layers (L0 and L1), the IS CR (L0), IR (L0.5) and QR (L1) extend fully along the beam pipe. The Outer Barrel system is subdivided in barrel and IL (both L2, L3 and L4). Between $|\eta|$ = 2.0 and $|\eta|$ = 4.0 lie the End Caps with also 3 layers (L2, L3 and L4). Figure (modified) taken from [92].

BCM': The BCM' [94] is a radiation hard beam monitoring system for protecting the inner part of the ITk from beam losses and for monitoring the delivered luminosity.

For the ITk Pixel Detector, the modules will consist of silicon sensors that are bump-bonded to RD53 FE chips [95], with planar sensor featuring a pitch of $50 \times 50\,\mu m^2$. The innermost layer of the barrel, as well as the L0 and L0.5 rings, utilise *triplets* with a $25 \times 100\,\mu m^2$ pitch. Triplets consist of three single bare modules, each with a readout chip bump bonded to a $2 \times 2\,cm^2$ sensor (based on 3D technology) [96]. These 3D sensors are preferred in these regions due to their excellent radiation tolerance and low power dissipation. The remaining sections of the ITk Pixel Detector employ quad modules, which consist of single bare modules, with four readout chips bump bonded to a single $4 \times 4\,cm^2$ planar sensor.

There are several prototype version of the RD53 FE chip: RD53a [97–99] with 400×192 pixel matrix is a prototype with different analog FE implementations for testing purposes: Synchronous, Linear and Differential FE. Its successor, the RD53b [100, 101] or ATLAS ITkPix, is the first FE that is tailored to the ITk's needs with 400×384 pixels per chip. For the assembly of the detector, ITkPixV2 will be used which is at the time of writing in the final design review.

The modules of the barrel region are mounted on *staves*, local support structures that play a crucial role in providing mechanical stability, facilitating cooling, and managing the routing of electrical services between the modules and the end of the support structures. A summary of the layers and the number of sensors per layer can be found in Table 2.2 and Table 2.3 for barrel and end-cap layers, respectively. For the exact position of the OB and EC modules, which is of relevance for the cable routing process and the

distribution of components in the Optoboard system, see also Appendix A.

Barrel Layer	r [mm]	Rows of Sensors	Flat Barrel $\|z\|$ [mm]	Flat Sensors per Row	Inclined Rings $\|z\|$ [mm]	Inclined Rings	Module Type
0	34	12	0–245	24	-	-	triplets
1	99	20	0–245	12	-	-	quads
2	160	32	0–372	18	380–1035	2×6	quads
3	228	44	0–372	18	380–1035	2×8	quads
4	291	56	0–372	18	380–1035	2×9	quads

Table 2.2: Positions in z and r coordinates, number of sensors and type of module for all ITk Pixel flat barrel layers and the inclined rings. The number of sensors per row refers to a complete stave in the central, flat part of the barrel where sensors are placed parallel to the beam line. The number of inclined rings refers to both sides of the detector. All values correspond to the ITk layout 23-00-03. Table taken from [102].

Ring Layer	r [mm]	$\|z\|$ [mm]	Rings	Sensors per Ring	Module Type
0	33.20	263–1142	2×15	18	triplets
0.5	58.70	1103–1846	2×6	30	triplets
1	80.00	263–2621	2×23	20	quads
2	154.50	1145.5–2850	2×11	32	quads
3	214.55	1145.5–2850	2×8	44	quads
4	274.60	1145.5–2850	2×9	52	quads

Table 2.3: Parameters for the ITk pixel end-caps in the ITk 23-00-03 layout. The radii refer to the innermost point of the sensors on a ring. The number of rings refers to both sides of the detector. Table taken from [102].

Serial Powering

The current power distribution scheme for the ATLAS ID Pixel Detector modules follows a parallel (direct) powering approach. In this scheme, each detector module has its own independent power supply and a corresponding set of cables. This parallel powering scheme offers the advantage of being able to operate modules individually, which is beneficial in various ways.

However, with the increased granularity of the ITk Pixel Detector, a greater number of cables is required for power distribution. Moreover, the higher current consumption of the FE components necessitates larger cable cross-sections. These factors contribute to increased power losses within the cables and an increased presence of passive material within the active detector volume. Consequently, these factors can lead to undesired interactions between particles and the inactive parts of the detector, potentially causing degradation in detector performance.

The solution is the usage of a Serial Powering (SP) scheme [103–105], different from the direct powering. In a serial powering configuration, the detector modules are arranged in series and powered by a constant current source. This allows for power transmission at low current and high voltage, minimising power losses. The reduction in transmitted

current is directly proportional to the number of modules in the SP chain, as highlighted in Figure 2.15. Figure 2.15a demonstrates the current parallel powering connection while Figure 2.15b shows the serial powering. To supply the FEs with the correct voltage the modules regulate the incoming voltage to the desired voltage through so-called shunt regulators [106].

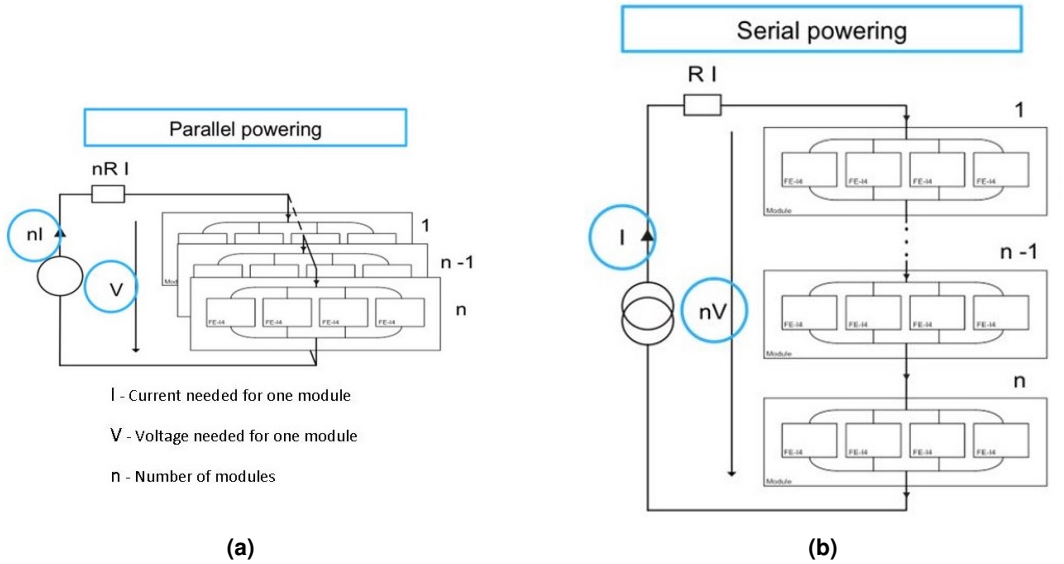

Figure 2.15: Block diagram (a) showing a general concept of a parallel powering scheme while the diagram (b) shows a general concept of a serial powering scheme. The highlighted variables show the difference in current *I* and voltage *V* for *n* modules at a constant power use. The resistor on top is visualising the loss of power in the cable, *nRI* for parallel and *RI* for serial powering. Figures taken from [104].

ITk TDAQ Upgrade

Besides the actual detector, the ATLAS TDAQ system also needs to incorporate several enhancements. One notable improvement will be the increased L0 trigger rate, which will be raised to 1 MHz from the previous 100 kHz. Similar to Run 2, a portion of the data from the MS and calorimeters is utilised for the initial trigger decision. The CTP disseminates the L0 trigger signal to the ITk, calorimeters, and MS through the FrontEnd LInk eXchange (FELIX) system. FELIX receives the event data from the detectors and forwards it for further processing. The EF then selects approximately 10 kHz of events (compared to the current $\sim$ 1 kHz) for storage onto disk. The higher L0 trigger rate, coupled with an increased number of readout channels and higher channel occupancies, necessitates a significant expansion in the bandwidth requirements for reading out the Pixel detector. In the ITk Pixel Detector, this bandwidth is increased by over a hundredfold compared to the ID pixel detector used in Run 2. Consequently, a complete replacement of the readout system and services is also necessary during the LS2 phase. The ITk Pixel data transmission chain is part of this readout system and the Optoboard system, discussed in Chapter 4, is the solution to handle the challenges and requirements mentioned above.

Chapter 3

The Search For Leptoquarks

There have been many searches for Leptoquarks (LQ) at the ATLAS and CMS detectors [107, 108] conducted. This thesis describes a LQ interpretation of a SM high-mass di-lepton production measurement. High-mass di-lepton production is defined as involving at least one hadronically decaying τ, τ_{had}, from LHC proton-proton (pp) collisions with $\sqrt{s} = 13\,\text{TeV}$.

The analysis is divided into two main parts:

1. A dedicated search for heavy leptoquarks exhibiting strong interactions with third-generation fermions. The investigation into heavy leptoquarks involves analysing the distributions of a detector-level parameter within different bins of b-jet multiplicity.
2. Measurements of fiducial differential di-lepton cross sections, where at least one of these leptons is a τ-lepton. Fiducial cross-sections are reported based on the visible mass, $m_{\ell\ell}^{\text{vis}}$, of the di-lepton pair.

I performed 1., therefore the cross section measurement (2.) is only briefly explained throughout this chapter.

To account for the impact of ATLAS event reconstruction, the data will be unfolded to obtain detector-invariant distributions. In order to prevent analyser bias based on observed data, the collision data is, at the time of writing, blinded in the high-mass di-lepton regions, where leptons have opposite electric charges and at least one reconstructed τ-lepton is present.

The analysis is scheduled, which is beyond the timeline of this thesis, for publication at the Moriond conference 2024.

Section 3.1 describes the datasets to be used and the simulated event samples to compare to the data. The reconstruction and identification of the relevant particles for this analysis are described in Section 3.2. Estimates of the background and the

uncertainties are explained in Section 3.3 and 3.4, respectively. The statistical model to analyse the simulated events is described in Section 3.5 with the expected results stated in Section 3.6.

3.1 Data and Simulated Samples

The analysis presented is performed on the full LHC Run 2 dataset, as collected by the ATLAS detector,corresponding to 139 fb^{-1} of pp collisions at 13 TeV that passed the ATLAS data quality checks.

In the ATLAS experiment, Monte Carlo (MC) simulation techniques [109] are employed to simulate and model both SM and BSM physics processes. This allows for the prediction of the expected quantity of SM background events, as well as the expected behaviour of the specific BSM model under investigation. By comparing these predictions with the actual number of events observed in the data, a statistical analysis (see Section 3.5) can be performed to validate or refute the SM, identify or rule out a particular BSM model, or establish cross section limits without relying on any specific theoretical framework.

Modelling events resulting from pp collisions poses challenges due to factors such as the complex substructure of protons, the presence of initial and final state radiation, and the non-perturbative nature of QCD at low energies. To address these complexities, the simulation of pp collisions is divided into several distinct steps, as depicted in Figure 3.1. Among these steps, some of the most crucial ones are:

- The computation of the production cross section for hard scatter events involves selecting two partons from the Parton Distribution Functions (PDFs) and determining the factorisation and renormalisation scales [111] before and after fixing them. The matrix element is then evaluated using perturbation theory.

- In a process known as parton showering, all partons have the ability to emit or split into additional partons. This results in the generation of initial and final state radiation as well as the formation of showers.

- During the parton showering process, as the energies of individual partons decrease, confinement takes place, leading to the formation of colour-neutral hadrons during the subsequent stage known as hadronisation.

- To simulate pile-up, low energetic (soft) QCD events are generated independently and then superimposed onto the hard scatter event.

- The simulated detector response to the final state particles generated is carried out using a GEANT4-based simulation of the ATLAS detector [112].

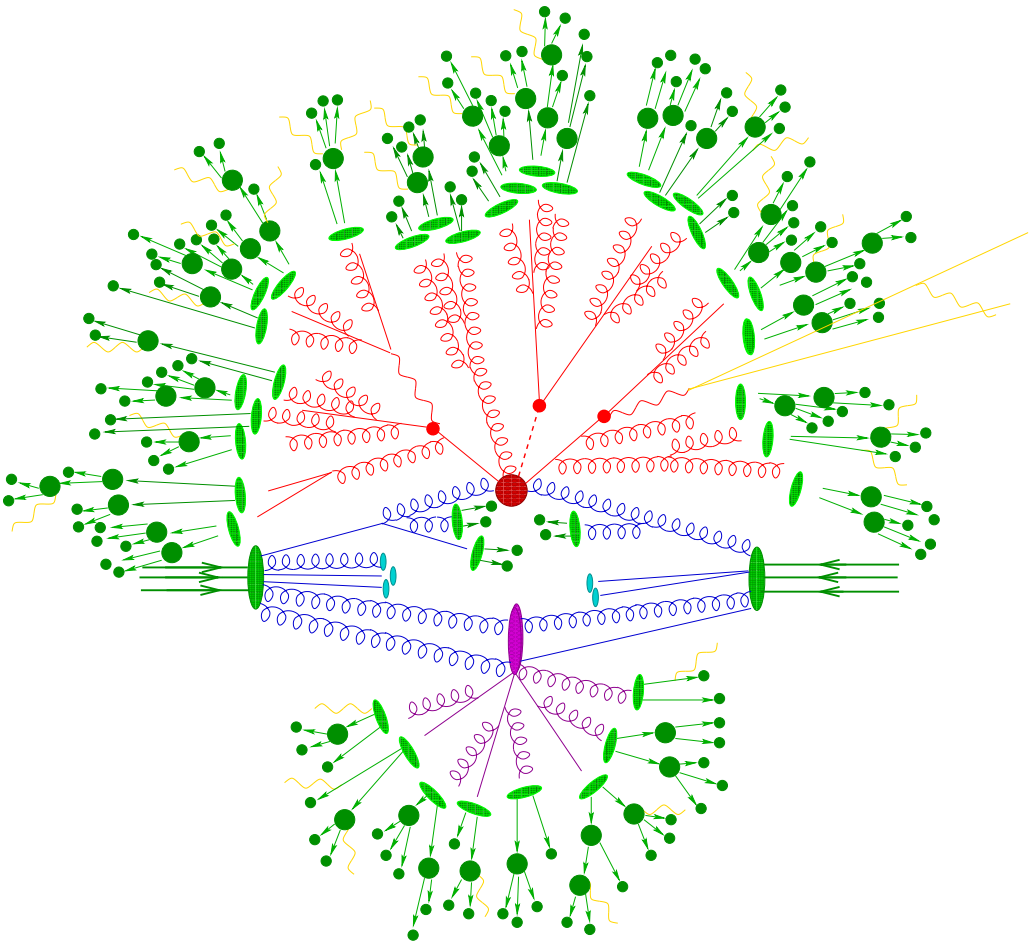

Figure 3.1: Pictorial representation of a $t\bar{t}H$ event as produced by an event generator simulating a pp collision. The hard interaction (big red blob) is followed by the decay of both top quarks and the Higgs boson (small red blobs). Additional hard QCD radiation is produced (red) and a secondary interaction takes place (purple blob) before the final-state partons hadronise (light green blobs) and hadrons decay (dark green blobs). Photon radiation occurs at any stage (yellow). Figure taken from [110].

The following Sections 3.1.1 to 3.1.2 state the software tools and libraries used for the generation of the different simulated samples. The simulated events are subjected to the same reconstruction process as the collision data, allowing for the design of analysis selections shown in Section 3.2.

3.1.1 Background Modelling

When searching for new particles or phenomena, it is crucial to identify and understand the background contributions that can mimic or overlap with the signal. These backgrounds can arise from various sources, such as known SM processes, instrumental effects, or environmental factors. An example for background of this analysis' $\tau\tau$ signal are two W decaying to two muons or electrons – possibly the same final state as the decayed $\tau\tau \rightarrow \ell\ell$. Background predictions aim to quantify the expected contributions from these sources in order to distinguish them from potential

signals. The major background for this analysis in the signal regions are jets misidentified as τ-jets. This is not part of the modelling but rather from a data-driven estimation "fake-factor", that is further explained in Section 3.3.

W+jets and Z+jets Modelling

The production of W+jets and Z+jets was simulated with the SHERPA 2.2.11 [113] generator using Next-to-leading Order (NLO) Matrix Elements (ME) for up to two partons, and Leading Order (LO) ME for up to five partons calculated with the COMIX [114] and OPENLOOPS [115–117] libraries. They were matched with the SHERPA parton shower [118] using the MEPS@NLO prescription [119–122] using the set of tuned parameters developed by the SHERPA authors. The NNPDF3.0NNLO set of PDFs [123] was used.

As an alternative to SHERPA, the POWHEG BOX V1 MC generator [124–127] was used for the simulation at NLO accuracy of the hard-scattering processes of W and Z boson production and decay in the e, μ, and τ-lepton channels. It was interfaced to PYTHIA 8.186 [128] for the modelling of the parton shower, hadronisation, and underlying event, with parameters set according to the AZNLO tune [129]. The CT10NLO PDF set [130] was used for the hard-scattering processes, whereas the CTEQ6L1 PDF set [131] was used for the parton shower. The effect of QED final-state radiation was simulated with PHOTOS++ 3.52 [132, 133]. The EVTGEN 1.2.0 program [134] was used to decay b and c hadrons.

In order to extend the statistical power of these predictions in the high $m_{\tau\tau}$ region, a dedicated high-statistics SHERPA sample was produced with $m_{\tau\tau} > 120\,\text{GeV}$, using otherwise identical settings to the inclusive sample described above. Similarly, a series of POWHEG BOX +PYTHIA samples are produced in exclusive bins of $m_{\tau\tau}$, starting from 120 GeV. The inclusive samples are therefore used exclusively for the $m_{\tau\tau} < 120\,\text{GeV}$ prediction, while the high-statistics samples are primarily used in the analysis signal region.

$t\bar{t}$ Modelling

The production of $t\bar{t}$ events was modelled using the POWHEG BOX V2 [124–126, 135] generator at NLO with the NNPDF3.0NLO [123] PDF set and the h_{damp} parameter[1] set to $1.5\,m_{\text{top}}$ [136]. The events were interfaced to PYTHIA 8.230 [137] to model the parton shower, hadronisation, and underlying event, with parameters set according to the A14 tune [138] and using the NNPDF2.3LO set of PDFs [139]. The decays of b and c hadrons were performed by EVTGEN 1.6.0 [134].

[1] The h_{damp} parameter is a resummation damping factor and one of the parameters that controls the matching of POWHEG ME to the parton shower and thus effectively regulates the high-p_{T} radiation against which the $t\bar{t}$ system recoils.

The impact of using a different parton shower and hadronisation model was evaluated by comparing the nominal $t\bar{t}$ sample with another event sample produced with the POWHEG BOX V2 [124–126, 135] generator using the NNPDF3.0NLO [123] PDF. Events in the latter sample were interfaced with HERWIG 7.04 [140, 141], using the H7UE set of tuned parameters [141] and the MMHT2014LO PDF set [142]. The decays of b and c hadrons were simulated using the EVTGEN 1.6.0 program [134].

To assess the uncertainty in the matching of NLO ME to the parton shower, the POWHEG sample was compared with a sample of events generated with MADGRAPH5_AMC@NLO 2.6.0 [143] interfaced with PYTHIA 8.230 [137]. The MADGRAPH5_AMC@NLO calculation used the NNPDF3.0NLO set of PDFs [123] and PYTHIA 8 used the A14 set of tuned parameters [138] and the NNPDF2.3LO set of PDFs [139]. The decays of b and c hadrons were simulated using the EVTGEN 1.6.0 program [134].

Single top-quark Modelling

The associated production of t quarks with W bosons (tW) was modelled by the POWHEG BOX V2 [124–126, 144] generator at NLO in QCD using the five-flavour scheme and the NNPDF3.0NLO set of PDFs [123]. The diagram removal scheme [145] was used to remove interference and overlap with $t\bar{t}$ production. The events were interfaced to PYTHIA 8.230 [137] using the A14 tune [138] and the NNPDF2.3LO set of PDFs [139].

Single-top t-channel production was modelled using the POWHEG BOX V2 [124–126, 146] generator at NLO in QCD using the four-flavour scheme and the corresponding NNPDF3.0NLO set of PDFs [123]. The events were interfaced with PYTHIA 8.230 [137] using the A14 tune [138] and the NNPDF2.3LO set of PDFs [139].

Single-top s-channel production was modelled using the POWHEG BOX V2 [124–126, 147] generator at NLO in QCD in the five-flavour scheme with the NNPDF3.0NLO [123] PDF set. The events were interfaced with PYTHIA 8.230 [137] using the A14 tune [138] and the NNPDF2.3LO PDF set.

The uncertainty due to the parton shower and hadronisation model was evaluated by comparing the nominal sample of events with a sample where the events generated with the POWHEG BOX V2 [124–126, 146] generator were interfaced to HERWIG 7.04 [140, 141], using the H7UE set of tuned parameters [141] and the MMHT2014LO PDF set [142].

To assess the uncertainty in the matching of NLO ME to the parton shower, the nominal sample was compared with a sample generated with the MADGRAPH5_AMC@NLO 2.6.2 [143] generator at NLO in QCD using the five-flavour scheme and the NNPDF2.3NLO [123] PDF set. The events were interfaced with

PYTHIA 8.230 [137], using the A14 set of tuned parameters [138] and the NNPDF2.3LO PDF set.

Multi-boson Modelling

Samples of diboson final states (VV) were simulated with the SHERPA 2.2.11 [113] generator. Fully leptonic final states and semileptonic final states, where one boson decays leptonically and the other hadronically, were generated using ME at NLO accuracy in QCD for up to one additional parton and at LO accuracy for up to three additional parton emissions. Samples for the loop-induced processes $gg \to VV$ were generated using LO-accurate ME for up to one additional parton emission for both the cases of fully leptonic and semileptonic final states. The matrix element calculations were matched and merged with the SHERPA parton shower based on Catani–Seymour dipole factorisation [114, 118] using the MEPS@NLO prescription [119–122]. The virtual QCD corrections were provided by the OPENLOOPS library [115–117]. The NNPDF3.0NNLO set of PDFs was used [123], along with the dedicated set of tuned parton-shower parameters developed by the SHERPA authors.

3.1.2 Leptoquark Signal Modelling

Potential off-shell LQ contributions to high-mass Drell-Yan production were simulated with MADGRAPH5_AMC@NLO 2.2.2 [143], using LO-accurate ME with up to two final-state partons in addition to the leptoquark-mediated interaction. The ME calculation employed the NNPDF3.0NLO set of PDFs [123] (H_T-sliced) / NNPDF2.3LO set of PDFs [139] (N_{parton}-sliced). Events were interfaced to PYTHIA 8.186 [128] for the modelling of the parton shower, hadronisation, and underlying event. The overlap between matrix element and parton shower emissions was removed using the CKKW-L merging procedure [148, 149]. The A14 tune [138] of PYTHIA 8 was used with the NNPDF2.3LO PDF set [139]. The decays of b and c hadrons were performed by EVTGEN 1.2.0 [134].

The simplified U_1 model for vector leptoquarks is used, this chapter follows the nomenclature introduced in Section 1.3.

The vector leptoquark signal samples use the `vector_LQ_UFO` model [150] and correspond separately to contributions from BSM interference with the SM amplitude and from pure BSM amplitudes. In the off-shell regime the kinematics of b-jets are similar between SM and BSM amplitudes, so the sample is initially generated with a pure SM amplitude at LO with up to two additional jets using CKKW-L merging. There can be more than two additional jets, but two covers most of the cases. The generation includes a minimum $\tau^+\tau^-$ mass of 120 GeV and is reweighted to the predictions for several LQ parameters.

As presented in Section 1.3, Figure 1.3 shows representative Feynman diagrams for leptoquark pair-production, single-leptoquark production, and Drell-Yan t-channel exchange available in the simplified U_1 leptoquark model. For very high-mass LQs, where single and pair production are suppressed due to proton PDFs, the negative interference term is expected to have the dominant impact on the $m_{\ell\ell}$ distribution. Figure 3.2 shows the impact on the predicted particle-level cross section of several scenarios involving heavy leptoquarks coupling preferentially to third generation fermions. Section 3.2 explains the selections and observables from the presented background and signal samples.

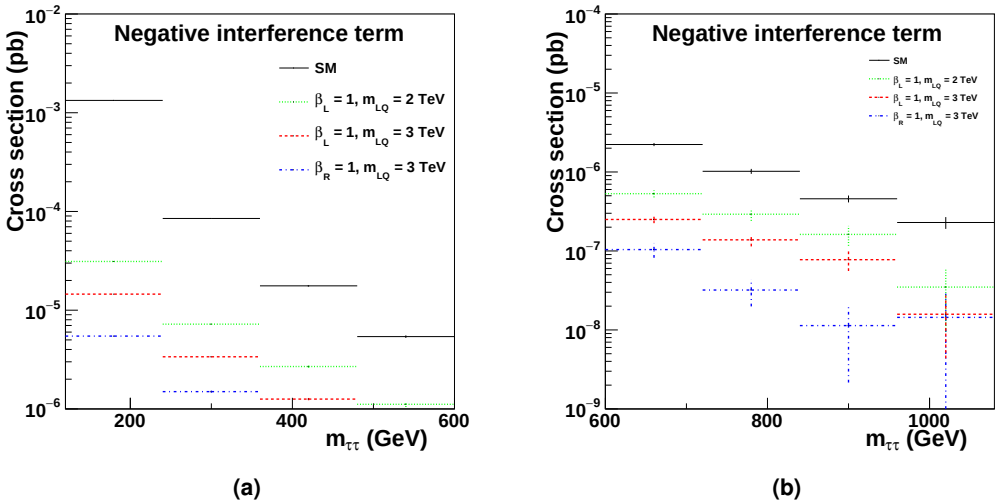

Figure 3.2: Predicted particle-level cross sections for Drell-Yan di-τ production for the SM as well the expected interference for several leptoquark scenarios. In all cases above, the predicted correction from interference reduces the total cross section, so its absolute value is reported. The differential $m_{\tau\tau}$ distribution is shown in the 1-b-jet region for: (a) $100 < m_{\tau\tau}/\text{GeV} < 600$, and (b) $600 < m_{\tau\tau}/\text{GeV} < 1000$. Note: these are *differential* cross sections ($\frac{d\sigma}{dm_{\tau\tau}}$ [pb / GeV]) despite the y-axis label.

3.2 Identification, Selection and Observables

From large datasets, such as the ones measured by ATLAS, with many processes it is crucial to identify and select the events necessary for this analysis based upon the values of the used observables.

Section 3.2.1 describes the detector object selection, while the key observables are explained in Section 3.2.2. In Section 3.2.3 the selection of events and the triggers used are listed. The particle-level object definition and event selection is further explained in 3.2.4.

3.2.1 Detector Object Selection

This analysis makes use of the reconstruction and identification of hadronically decaying τ leptons, muons, electrons and *b*-jets. In each case, standard ATLAS algorithms and calibrations are used for physics object reconstruction. The following subsections describe these in some detail.

Hadronically Decaying Tau Leptons

Hadronic τ-lepton candidates (τ_{had}) are seeded by jets built from locally calibrated topological clusters ("TopoClusters"); the FASTJET implementation [151] of the anti-k_t jet reconstruction algorithm [152] is used with a radius parameter $R = 0.4$. τ_{had} candidate jets must have $|\eta| < 2.47$ (excluding the "crack" region) and $p_{\text{T}} > 20\,\text{GeV}$ after applying the τ_{had} Energy Scale (TES) corrections. The τ_{had} candidate's momentum after applying TES corrections is known as the visible momentum, p^{vis}, and the visible transverse momentum is denoted $p_{\text{T}}^{\text{vis}}$.

Hadronic τ-lepton decays are identified using the Tight RNNIP identification working point. This is a Recurrent Neural Network (RNN) based identification algorithm trained on a wide range of simulated τ leptons on a relatively unpolarised sample of τ-leptons from pure γ^* Drell-Yan production.

In the semileptonic analysis regions, it is useful to enhance the rejection of electrons or muons with large energy deposits in the calorimeter. To attain additional electron rejection (especially with the $Z \to ee$ background), a specialised Boosted Decision Tree (BDT) is trained to discriminate between prompt electrons and hadronic τ-lepton decays ("eBDT"). Calorimeter-tagged muons have a particularly high mis-identification rate in the central η region due to poor coverage of the ATLAS muon system. For this region, τ_{had} candidates within $_{\Delta}R < 0.1$ of a calo-tagged muon are removed.

Differences between data and simulation are assessed for τ-leptons from Z decays for the TES, the RNN identification, and the eBDT selection. Correction factors are derived and applied to the simulation to achieve closure with the observed data.

Further information on the τ_{had} identification, background rejection, TES, and corrections to simulation can be found in Reference [153].

Electrons and Muons

Light leptons that originate directly from prompt τ-lepton decays as well as prompt leptons from other sources are targeted in the analysis. Since electrons and muons from τ-lepton decays tend to carry a rather small proportion of the original τ-lepton momentum, candidate light leptons are required to have $p_{\text{T}} > 7\,\text{GeV}$.

Electrons must fall in the fiducial region of the inner tracker and electromagnetic calorimeter ($|\eta| < 2.47$, excluding the "crack" region). The MEDIUM electron identification operating point is used, and electron candidates are also required to pass the FCHIGHPTCALOONLY isolation [154, 155].

Muons candidates must have $|\eta| < 2.5$ and pass the MEDIUM identification working point; the FCLOOSE isolation working point is used [155, 156].

Differences in reconstruction and identification efficiencies between data and simulation are accounted for by scale factors derived in the Z and J/ψ mass peaks, and the momentum scales are similarly calibrated using $Z \to \ell\ell$ decays [157, 158].

Jets

Jets are built from Particle Flow objects using the anti-k_t algorithm with radius parameter $R = 0.4$. The resulting jets' transverse momenta are further corrected to the corresponding particle-level jet p_{T} using simulation [159]. After these calibrations, jets with $p_{\mathrm{T}} < 25\,\mathrm{GeV}$ are removed. A multivariate discriminant method – Jet Vertex Tagger (JVT) – is used to remove jets with $p_{\mathrm{T}} < 60\,\mathrm{GeV}$ and $|\eta| < 2.4$ that have large estimated energy fractions from pileup collision vertices; above this p_{T} scale, the requirement becomes unnecessary [160]. Simulated jets are corrected for their JVT efficiencies and p_{T} scale and resolution using *in-situ* measurements of these quantities in multi-jet, γ+jets, and Z+jets data [159].

b-Tagging

To identify hadronic jets containing b-hadrons, the DL1r b-tagging algorithm [161] is used. The tagger operating point with a b-jet identification efficiency of 77% in an inclusive sample of b-jets from $t\bar{t}$ events is chosen. The b-jet and c-jet tagging probabilities are measured in a $t\bar{t}$-enriched sample in collision data [161, 162]. The light-jet mistag rate is measured in Z+jets events using the "flipped tagger" method [163]. Simulated tagging rates are corrected based on these measurements.

Overlap Removal

It may occur that the same set of tracks and calorimeter clusters is associated to more than one reconstructed object. An overlap removal algorithm is therefore applied in order to remove objects that correspond to the same detector signals. The criteria applied to perform the overlap removal are reported in Table 3.1 and are based on the angular separation $_{\Delta}R$ between the two reconstructed objects. In all cases the the angular separation is computed using the objects' rapidity y ($_{\Delta}R_y = \sqrt{(_{\Delta}y)^2 + (_{\Delta}\phi)^2}$),

Object to Remove	Object to Keep	Criteria
tau	electron	The tau is removed if $_{\Delta}R_y < 0.2$.
tau	muon	The tau is removed if $_{\Delta}R_\eta < 0.2$.
electron	muon	If they share a track, the electron is removed if the muon is associated with a signature in the muon spectrometer, otherwise the muon is removed.
jet	electron	Any jet within $_{\Delta}R_y = 0.2$ of an electron is removed.
jet	muon	Any jet within $_{\Delta}R_y = 0.2$ of a muon is removed.
electron	jet	Any electron within $_{\Delta}R_y = 0.4$ of a jet is removed.
muon	jet	Any muon within $_{\Delta}R_y = 0.4$ of a jet is removed.
jet	tau	Any jet within $_{\Delta}R_y = 0.2$ of a tau is removed.

Table 3.1: Criteria applied to perform the overlap removal between reconstructed objects. The criteria are listed following the order of application.

except for the tau-muon overlap, where the pseudorapidity η is used instead of rapidity ($_{\Delta}R_\eta = \sqrt{(_{\Delta}\eta)^2 + (_{\Delta}\phi)^2}$).

3.2.2 Key Observables

Of particular importance to the analysis are observables related to the di-lepton invariant mass $m_{\ell\ell}$. The visible mass of a dilepton system $m_{\ell\ell}^{\text{vis}}$ is the invariant mass of the visible components of the two leptons' momenta in the detector. In case LQ exist, their mass would be directly related to the tau jets (according to the Feynman diagram Figure 1.3c) and the high mass tail of the $m_{\ell\ell}$ would increase. For a light lepton, the visible momentum $\vec{p}^{\text{vis}}$ is merely the measured momentum; for a τ-lepton, this is the total momentum of its visible decay products (hadrons, photons, and light leptons).

Conventional Mass Observables

The transverse mass of two leptons is defined by:

$$m_{\text{T}}(\vec{p}_1^{\text{vis}}, \vec{p}_2^{\text{vis}}) = \sqrt{2|\vec{p}_1^{\text{vis}}||\vec{p}_2^{\text{vis}}|\left(1 - \cos\left(_{\Delta}\phi(\vec{p}_1^{\text{vis}}, \vec{p}_2^{\text{vis}})\right)\right)}$$

where $\vec{p}^{\text{vis}}$ is the visible momentum of the lepton. The total transverse mass of the di-lepton plus $\vec{p}_{\text{T}}^{\text{miss}}$ system is then:

$$m_{\text{T}}^{\text{total}} = \sqrt{m_{\text{T}}^2(\vec{p}_1^{\text{vis}}, \vec{p}_2^{\text{vis}}) + m_{\text{T}}^2(\vec{p}_1^{\text{vis}}, \vec{p}_{\text{T}}^{\text{miss}}) + m_{\text{T}}^2(\vec{p}_2^{\text{vis}}, \vec{p}_{\text{T}}^{\text{miss}})}$$

The $\sqrt{s}_{\text{min}}$ Method

The $\sqrt{s}_{\text{min}}$ method was proposed to approximate the true di-τ invariant mass, as well as other kinematic quantities, in the presence of invisible particles as part of the decay chain [164, 165]. To do so, the *minimal* centre of mass energy needed to reproduce

the measured momenta and $\vec{p}_{\mathrm{T}}^{\mathrm{miss}}$ of an event is derived as a function of the invisible particles' momenta. Unlike other, widely-utilised methods for reconstructing the di-τ invariant mass such as the MMC method [166], the $\sqrt{s}_{\mathrm{min}}$ method converges under all conditions, yielding a high efficiency even far from the Z and Higgs boson mass peaks.

The expression of the Mandelstam variable s for a system with n_{inv} invisible particles can be written as:

$$s = \left(E + \sum_{i=1}^{n_{\mathrm{inv}}} \sqrt{m_i^2 + \vec{p}_i^2}\right)^2 - \left(\vec{P} + \sum_{i=1}^{n_{\mathrm{inv}}} \vec{p}_i\right)^2$$

where E and $\vec{P}$ are the total visible energy and momenta, respectively.

When considered as a function of the unknown variables $\vec{p}_i$ subject to the constraint $\sum \vec{p}_i = -p_{\mathrm{T}}$, s has a global minimum:

$$\vec{p}_{i\mathrm{T}} = \frac{1}{2}\vec{P}_{\mathrm{T}}$$
$$p_{i,z} = \frac{1}{2}\frac{p_z}{\sqrt{E^2 - P_z^2}}P_{\mathrm{T}}^{\mathrm{miss}}$$

where i indexes invisible particles. Assuming two massless particles carry most of the missing momentum, which is the case for processes in which when the dominant source of invisible particles is a pair of hadronically-decaying τ leptons (for example in SM Drell-Yan production of two hadronically-decaying τ leptons), the minimum invariant mass of the di-τ system is given by:

$$\sqrt{s}_{\mathrm{min}} = \sqrt{E^2 - P_z^2} + \sqrt{p_{\mathrm{T}}^{\mathrm{miss}} + \hat{M}_{\mathrm{inv}}^2} \tag{3.1}$$

where $\hat{M}_{\mathrm{inv}}^2$ is the invariant mass of the system of invisible particles that minimises s.

Under these conditions the $\sqrt{s}_{\mathrm{min}}$ method approximates $m_{\tau\tau}$ with a very good resolution across a wide mass range, at the cost of a small negative bias.

3.2.3 Event Selection and Regions

Analysis regions are defined based on the flavour of reconstructed leptons, their charge, the number of b-tagged jets, and the visible di-lepton invariant mass. This yields data samples that are enriched in first-, second-, and third-generation leptons and differentiated between production processes. For example, the $e\mu$, $e\tau$, and $\tau_{\mathrm{had}}\tau_{\mathrm{had}}$ regions contain events with one electron and one muon, one electron and one τ_{had}, and two τ_{had} candidates, respectively. Similarly, the $\mu\tau + 2b$ region contains one muon, one τ_{had}, and two b-tagged jets. In all cases, at least two reconstructed and identified leptons must be present in an accepted event, where the lepton reconstruction and identification follows the definitions laid out in Section 3.2.

Triggers

The unprescaled triggers with the loosest selection criteria available in each data-taking period are used in this analysis. In analysis regions with at least one electron or muon present, the single-electron or single-muon triggers are used, as reported in Table 3.2. In the $\tau_{\text{had}}\tau_{\text{had}}$ analysis regions, a logical OR of single- and di-τ_{had} triggers is employed; see Table 3.3. For single-lepton triggers, at least one

Year	Period	Trigger name (EH channel)	Trigger name (MH channel)
2015	all	HLT_e24_lhmedium_L1EM20VH HLT_e60_lhmedium HLT_e120_lhloose	HLT_mu20_iloose_L1MU15 HLT_mu40
2016	A-D3	HLT_e26_lhtight_nod0_ivarloose HLT_e60_lhmedium_nod0 HLT_e140_lhloose_nod0	HLT_mu24_ivarmedium HLT_mu50
	D4-end	HLT_e26_lhtight_nod0_ivarloose HLT_e60_lhmedium_nod0 HLT_e140_lhloose_nod0	HLT_mu26_ivarmedium HLT_mu50
2017	All	HLT_e26_lhtight_nod0_ivarloose HLT_e60_lhmedium_nod0 HLT_e140_lhloose_nod0	HLT_mu26_ivarmedium HLT_mu50
2018	All	HLT_e26_lhtight_nod0_ivarloose HLT_e60_lhmedium_nod0 HLT_e140_lhloose_nod0	HLT_mu26_ivarmedium HLT_mu50

Table 3.2: Trigger list for the di-tau semi-leptonic decay channels. The triggers in the same period of each data taking year are applied in a logical OR.

Year	Period	Trigger name
2015	All	HLT_tau80_medium1_tracktwo_L1TAU60
		HLT_tau35_medium1_tracktwo_tau25_medium1_tracktwo_L1TAU20IM_2TAU12IM
2016	A	HLT_tau80_medium1_tracktwo_L1TAU60
		HLT_tau80_medium1_tracktwo_L1TAU60_tau50_medium1_tracktwo_L1TAU12
	B-D3	HLT_tau125_medium1_tracktwo
		HLT_tau80_medium1_tracktwo_L1TAU60_tau50_medium1_tracktwo_L1TAU12
	D4-end	HLT_tau160_medium1_tracktwo
		HLT_tau80_medium1_tracktwo_L1TAU60_tau50_medium1_tracktwo_L1TAU12
2017	B1-B7	HLT_tau160_medium1_tracktwo
		HLT_tau80_medium1_tracktwo_L1TAU60_tau50_medium1_tracktwo_L1TAU12
	B8-end	HLT_tau160_medium1_tracktwo_L1TAU100
		HLT_tau80_medium1_tracktwo_L1TAU60_tau60_medium1_tracktwo_L1TAU40
2018	B-J	HLT_tau160_medium1_tracktwoEF_L1TAU100
		HLT_tau80_medium1_tracktwoEF_L1TAU60_tau60_medium1_tracktwoEF_L1TAU40
	K-endxs	HLT_tau160_medium1_tracktwoEF_L1TAU100
		HLT_tau160_mediumRNN_tracktwoMVA_L1TAU100
		HLT_tau80_medium1_tracktwoEF_L1TAU60_tau60_medium1_tracktwoEF_L1TAU40
		HLT_tau80_mediumRNN_tracktwoMVA_L1TAU60_tau60_mediumRNN_tracktwoMVA_L1TAU40

Table 3.3: Trigger list for the di-tau fully-hadronic channel.

lepton of the corresponding flavour must closely overlap with the trigger object. For $\tau_{\text{had}}\tau_{\text{had}}$ triggers, two τ_{had} candidates must be reconstructed near to the triggering τ_{had} candidates.

In simulated events, a trigger efficiency scale factor is applied to account for differences between the predicted and observed trigger efficiencies [167–169].

High di-Lepton Mass Region

This analysis targets BSM scenarios that have an influence on experimental signatures at high di-lepton invariant mass. The high-mass signal region is defined by $m_{\ell\ell}^{\text{vis}} > 100\,\text{GeV}$, removing hadron resonances and the large $Z/\gamma^* \to \ell\ell$ production process at low invariant mass.

Same-charge and Opposite-charge Regions

One main physics target of this analysis is the LQ search and the main method for this is to measure opposite-charge or "Opposite-Sign" (OS) leptons at high $m_{\ell\ell}$; as such, the primary region of interest in which LQ signatures are probed requires a pair of opposite-sign reconstructed leptons. However, because the largest SM production processes produce pairs of opposite-sign leptons, selecting events with same-charge or "Same-Sign" (SS) lepton pairs provides a useful validation region enriched in mis-identified or non-prompt lepton candidates ("fakes").

Additional Detector-level Selection Criteria

A summary of analysis selections and regions is presented in Table 3.4.

Cut	Definition
di-lepton	at least two reconstructed leptons are required in all selected events.
lepton flavours	$\tau_{\text{had}}\tau_{\text{had}}$, $\mu\tau_{\text{had}}$, $e\tau_{\text{had}}$, and $e\mu$ regions are defined based on the flavours of the reconstructed leptons in an event
trigger	the trigger decisions laid out in Tables 3.2 and 3.3 must be satisfied for each lepton flavour combination.
high-mass	the visible di-lepton invariant mass must be $m_{\ell\ell}^{\text{vis}} > 100\,\text{GeV}$
lepton signs	two regions are used: the opposite-sign leptons signal region and the same-sign leptons validation region.
b-jet multiplicity	events are divided into 0-, 1-, and ≥ 2 b-jet regions based on the number of b-tagged jets.

Table 3.4: Summary of detector-level cuts defining analysis regions used throughout this analysis. All regions require at least two identified leptons with visible invariant mass $m_{\ell\ell}^{\text{vis}} > 100\,\text{GeV}$, and for each region both the opposite-sign lepton signal region and the same-sign background validation are used.

3.2.4 Particle-level Object and Event Selection

For the unfolded fiducial cross section measurement, particle-level objects (hadronically decaying taus, muons, electrons, and b-jets) are selected using criteria reflecting the detector-level requirements as closely as possible; this ensures minimal extrapolation from the observed detector-level data to the inferred particle-level cross sections, and maximal model independence in the final particle-level measurement.

Particle-level Object Definitions

Particle-level τ_{had} candidates are built from the visible decay products of prompt, hadronically-decaying τ-leptons; the momentum sum of these visible decay products must yield $p_{\text{T}} > 20\,\text{GeV}$ and $|\eta| < 2.47$ (excluding $1.37 < |\eta| < 1.52$). Similarly, particle-level electrons must be prompt and have dressed $p_{\text{T}} > 7\,\text{GeV}$ and $|eta| < 2.47$ (excluding $1.37 < |\eta| < 1.52$), while particle level muons must be prompt and have dressed $p_{\text{T}} > 7\,\text{GeV}$ and $|\eta| < 2.5$. "Prompt" here means that the lepton does not have a hadron ancestor beyond the initial-state protons. "Dressed" refers to the concept of taking into account the effects of surrounding particles and their interactions.

Jets at the particle-level are built from stable particles (those with $c\tau > 10\,\text{mm}$) using the anti-k_t algorithm with radius $R = 0.4$, including non-prompt neutrinos and light leptons from hadron decays. Prompt, dressed leptons and their associated photons are excluded from jet-finding, as are the decay products of prompt τ-leptons. Particle-level jets are required to have $p_{\text{T}} > 20\,\text{GeV}$ and $y < 4.4$. Jets are considered fiducial *b*-jets if they contain a weakly-decaying, ghost-associated *b*-hadron with $p_{\text{T}} > 5\,\text{GeV}$.

Fiducial Event Selection and Categories

Fiducial particle-level events must contain at least two fiducial leptons, as defined in the previous section. The $\tau_{\text{had}}\tau_{\text{had}}$, channel requires at least two fiducial τ_{had} in an event, and the leading pair is used to build the $m_{\ell\ell}^{\text{vis}}$ if more than two are accepted. The $e\tau_{\text{had}}$ ($\mu\tau_{\text{had}}$) channel requires exactly one fiducial τ_{had} and at least one electron (muon). Events with fewer than one accepted particle-level τ_{had} are treated as non-fiducial.

The $m_{\ell\ell}^{\text{vis}}$ is constructed from the visible lepton momenta: for τ_{had} candidates this is the visible momentum of its decay products; for light leptons this is the dressed lepton momentum. Fiducial events are further categorised by the number of *b*-jets into bins of 0, 1, of ≥ 2 *b*-jets.

Crucially, fiducially accepted events can originate from any particular production process, be that Drell-Yan, $t\bar{t}$, multi-boson, tW, or some other source. Any event that meets the particle-level fiducial requirements is treated as "signal" and will be included in the reported unfolded cross sections.

To summarise this section, an overview of the analysis signal, control and validation regions is given in Figure 3.3.

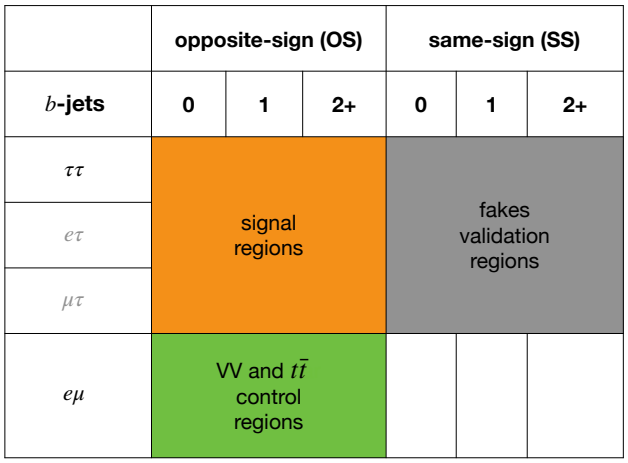

Figure 3.3: Signal, validation and control region for the high-mass di-lepton production analysis.

3.3 Background Estimate

The major background in both $\tau_{\text{lep}}\ \tau_{\text{had}}$ and $\tau_{\text{had}}\ \tau_{\text{had}}$ signal regions are from jets misidentified as τ-jets, due to large cross section of the QCD jet production at the LHC relative to that of τ production. This background is difficult to determine from simulation, in particular due to large uncertainties in multijet modelling. The method used to estimate the fake jet contribution in the signal region is therefore estimated via a data-driven estimate. Events in data which pass the signal region selection, but with the τ_{had} identification criteria inverted (anti-ID), are used in the signal region as the fake jet estimate. The correction factor by which the anti-ID taus should be weighted when extrapolated into the signal region is known as the *fake factor*. The fake factor method estimates the fake background by measuring the correction factors to be applied to data.

For the $\ell\tau_{\text{had}}$ channels, the analysis takes fake τ backgrounds from simulations. As seen on Figure 3.4, closure with the MC in the (high-mass) SS regions of interest is observed. The analysis plans additionally to perform a data-driven estimate to cross-check. Modelling uncertainties between fake τ-jets and real production can be correlated thanks to the simulated estimate.

3.4 Uncertainties

Several sources of uncertainty are considered. Here uncertainties are broadly partitioned into “modelling” uncertainties (see Section 3.4.1), which come from variations of the theoretical predictions for various production processes; “experimental” uncertainties (see Section 3.4.2), which arise from imperfect knowledge of the ATLAS detector, LHC beam conditions, or the reconstruction and identification of final-state objects; and “method” uncertainties (see Section 3.4.3), which result from

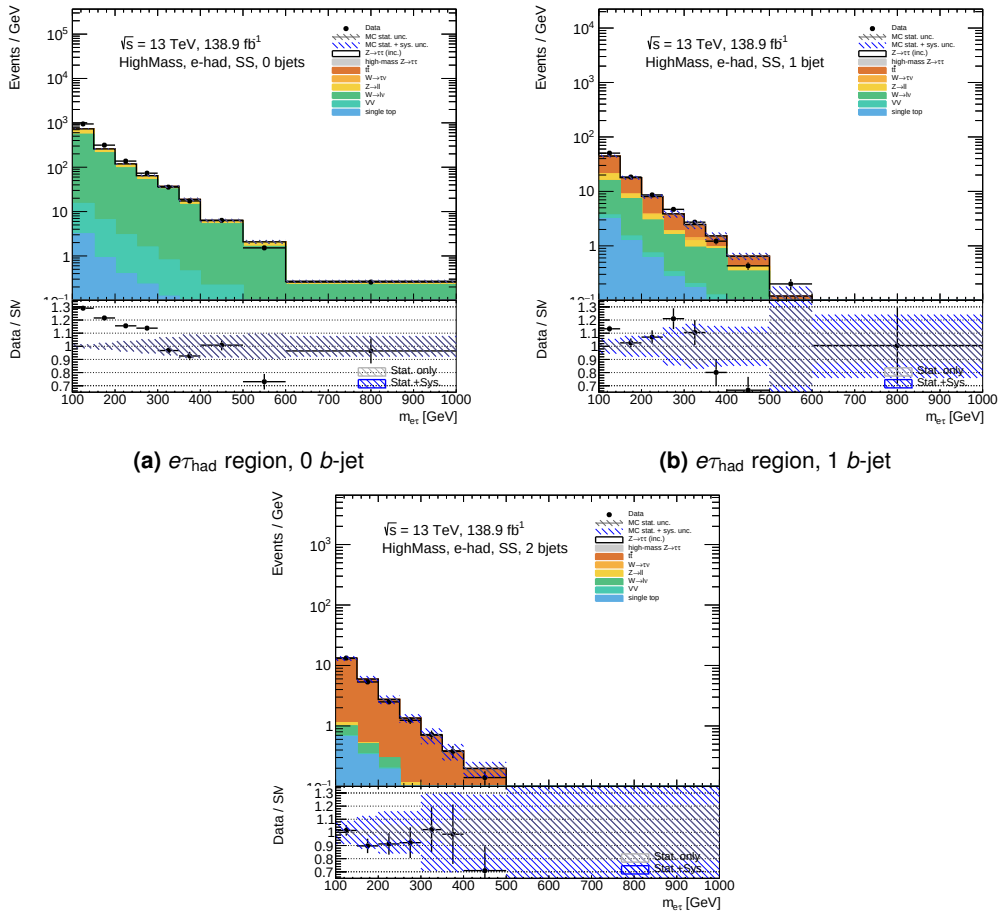

(a) $e\tau_{\text{had}}$ region, 0 b-jet

(b) $e\tau_{\text{had}}$ region, 1 b-jet

(c) $e\tau_{\text{had}}$ region, 2+ b-jet

Figure 3.4: Background processes for the $e\tau_{\text{had}}$ high mass regions. MC simulation follows the SS data when the light lepton ID removes the multijet background. In the worst case there is a $\sim$ 30% discrepancy at low $m_{\ell\ell}^{\text{vis}}$ but this has a negligible effect for the expected limits.

imperfect closure in the statistical fitting or unfolding procedure. Where applicable, the impact on fiducial and non-fiducial cross sections and event yields is treated coherently, altered for each variation. For example, variations on the τ_{had} energy scale will impact detector-level predictions for both signal and background events.

Only the expected dominant uncertainties considered for the final leptoquark search analysis are presented here. They are based on recent experience from ATLAS analyses involving the di-τ final state, both with- and without b-jets present [16, 170, 171], as well as sensitivity tests by the analysis team.

3.4.1 Modelling Uncertainties

Several uncertainties on the Drell-Yan, $t\bar{t}$ and single top production processes are considered through variations of the corresponding MC generator configurations. The following uncertainties are considered on the dominant production processes:

$t\bar{t}$ matching/merging scheme: the difference in $t\bar{t}$ MC matching and merging schemes (aMC@NLO+PYTHIA 8 vs. POWHEG BOX + PYTHIA 8)

$t\bar{t}$ parton-shower model: the difference in $t\bar{t}$ parton-shower MC models (POWHEG BOX + PYTHIA 8 vs POWHEG BOX + HERWIG 7)

$t\bar{t}$ scale variations: the difference in NLO $t\bar{t}$ MC scale choices (h_{damp} and α_s(ISR) variations)

$t\bar{t}$ / single top interference scheme: the difference between the diagram removal [145] and diagram removal schemes [136, 145]

Drell-Yan di-lepton production modelling: the difference in Z-jets matrix-element and parton-shower MC models (SHERPA 2.2.11 vs PYTHIA 8). Note that this uncertainty did not fully propagate to the results shown in Section 3.6.

Drell-Yan di-lepton production scale variations: the renormalisation and factorisation scale choices used in the $Z/\gamma^* \to \ell\ell$ MC predictions are varied by factors of 0.5 and 2.0, using the 7-point uncertainty envelope to estimate the total uncertainty

Proton parton distribution functions: PDFs are varied according to the PDF4LHC prescription [172] on the Z-jets, $t\bar{t}$, and single top production processes

Inclusive cross section uncertainties: these are still being established based on the latest theory predictions and/or measurements. For now, a conservative 10% uncertainty is assigned to each of the inclusive $Z \to \tau\tau$, $t\bar{t}$, single top-quark, and multi-boson production cross-sections.

3.4.2 Experimental Uncertainties

Uncertainties are considered on each of the "objects" used to define the event regions and observables used in this analysis: hadronically decaying τ-leptons, electrons, muons, hadronic jets, and b-jet identification. For hadronic τ-lepton candidates and b-jets, uncertainties on the rate of mis-identified objects are also considered; the electron and muon mis-identification rates are very subleading. The following experimental uncertainties are taken into account:

Luminosity: the uncertainty in the luminosity affecting the background predictions and total extracted cross sections

Hadronically decaying τ-leptons: uncertainties on the TES and τ_{had} identification simulation-to-data efficiency corrections

Mis-identified τ_{had} candidates: uncertainties on the τ_{had} identification mistag rates for quark-, gluon-, and pileup-initiated hadronic jets as well as the fractions of each jet origin in the analysis signal regions

Electron reconstruction and identification: uncertainties on the electron momentum and identification efficiency corrections

Muon reconstruction and identification: uncertainties on the muon momentum and identification efficiency corrections

Jet reconstruction: uncertainties on the jet energy scale, resolution, and JVT efficiency corrections

***b*-jet identification:** uncertainties on the *b*-, *c*-, and light[2]-jet tagging rate corrections.

A quantitative overview of the different impacts is shown in Figure 3.5 including pruning (see next subsection).

Experimental Uncertainty Pruning

To identify the systematic uncertainties that are not relevant to the total uncertainty and can, therefore, be neglected, a pruning procedure is carried out. The uncertainty pruning is performed before and after the unfolding, and the union of the uncertainties not discarded by the two pruning procedures is considered for the analysis results. The selection of the systematic uncertainties to be considered by the analysis is based on the di-lepton invariant mass ($m_{\ell\ell}$) in the $\tau_{\text{had}}\,\tau_{\text{had}}$ and $e\mu$ regions. The contribution of each uncertainty is evaluated varying the nominal MC distribution[3] of $m_{\ell\ell}$ at $\pm1\sigma$ using the combined performance software tools for each object.

The pruning criterium before the unfolding is the following: for each experimental systematic uncertainty (varied at $\pm1\sigma$), the relative variation[4] with respect to the nominal value is computed in each bin of the $m_{\ell\ell}$ distribution; to each bin the relative statistical uncertainty on the expected number of events (given by the Poissonian approximation $1/\sqrt{N}$, with N the number of MC events in the bin) is associated; the experimental uncertainty is neglected if its relative variation is smaller than 10% of the relative statistical uncertainty in every bin.

For the post-unfolding pruning, the relative systematic uncertainties are obtained using the unfolded distributions from each systematic uncertainty. The systematic and statistical uncertainties are obtained from slightly different methods. For the systematic uncertainty calculations, instead of using the difference between the varied and nominal bins, the systematic uncertainties are derived from the average difference between the $+1\sigma$ and the -1σ systematic variations divided by 2. The statistical uncertainty for each bin is instead derived using the RMS of 2000 Poisson-fluctuated MC toy experiments from the nominal bin, which should be giving the same result as using the Poissonian approximation method mentioned above. A 10% pruning threshold is used also in this case, so that the experimental uncertainty is discarded if it is lower than 10% of the statistical uncertainty for every bin.

[2] "light"-jet refers to *u*-, *d*- or *s*-jets.

[3] The MC distributions are obtained summing the V+jets, $t\bar{t}$, single-top and diboson MC predictions.

[4] The relative variation in a $m_{\ell\ell}$ bin is the difference between the varied and the nominal bin content divided by the nominal one.

To avoid large fluctuations between adjacent bins due to low statistics, a Gaussian filter with $\sigma = 2$ is applied twice, to the histograms of both the statistical uncertainty and the experimental uncertainties (both for the pre-unfolding and the post-unfolding studies).

A summary of the union of the experimental uncertainties surviving the pruning, before and after the unfolding for each reconstructed object, is as follows:

- Muon uncertainties from the resolution, energy scale, reconstruction, isolation and track to vertex (TTVA).
- Electron uncertainties from the energy scale, reconstruction and isolation.
- Tau uncertainties from the energy scale, reconstruction, identification, trigger and electron veto + overlap removal.
- Jet uncertainties from the energy scale and resolution, flavour, and flavour tagging.

Appendix D.1.1 lists the systematics used for the expected limit results shown in this work.

Figure 3.5 shows the effects of pruning on each group of experimental uncertainties and on the total uncertainty of the MC $m_{\ell\ell}$ distribution before the unfolding. The

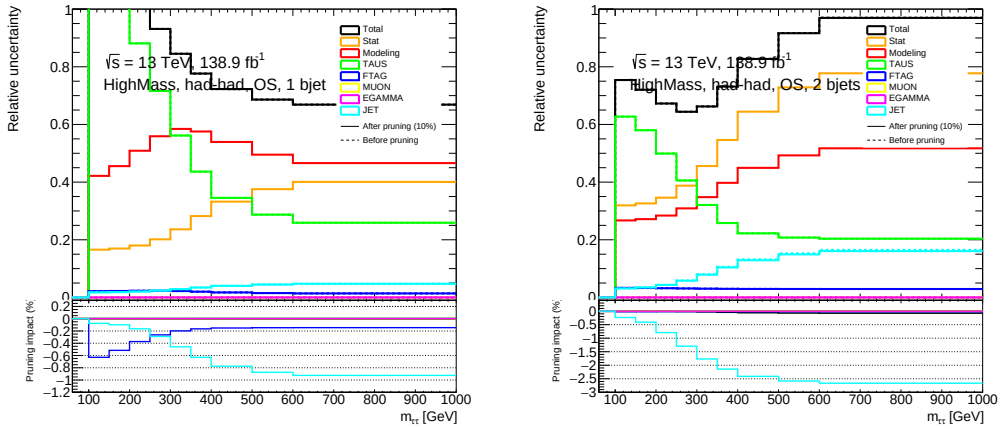

(a) $\tau_{\text{had}}\,\tau_{\text{had}}$ region, 1 *b*-jet

(b) $\tau_{\text{had}}\,\tau_{\text{had}}$ region, 2 *b*-jets

Figure 3.5: Impact of relative uncertainties before (solid lines) and after (dashed lines) pruning on the MC $m_{\ell\ell}$ distribution before the unfolding. The effects of pruning on the total and the experimental uncertainties is seen on the ratio pads. For the $\tau_{\text{had}}\,\tau_{\text{had}}$ 0 *b*-jet and $e\mu$ 0–2 *b*-jets regions see Figure D.1 in Appendix D.1.2.

difference of before and after pruning has no impact on the total uncertainty but reduces the histogram and fitting turnaround time by several hours. The individual relative experimental uncertainties are computed in this case as half the difference between the $+1\sigma$ and -1σ variations of the $m_{\ell\ell}$ distribution and then normalised to the nominal distribution. The impact of each experimental uncertainty group is shown in

Figure 3.5, as the sum in quadrature of all recommended systematic uncertainties and of all systematic uncertainties left after the pruning procedure relative to that group. Also shown are the statistical uncertainty, the modelling uncertainty (on Drell-Yan $\tau\tau$ and $t\bar{t}$ MC samples) and the total uncertainty (sum in quadrature of statistical, modelling and experimental uncertainties). For each experimental uncertainty group and for the total uncertainty, the impact of pruning (computed as the difference between the relative uncertainty after and before pruning, normalised by the uncertainty before pruning) is shown. Both in the $e\mu$ and in the τ_{had} τ_{had} regions the effects of pruning on the total uncertainty are negligible (smaller than 0.1% in all b-jet multiplicity bins).

Figure 3.6 is demonstrating the pruning effect as a ratio between the uncertainties before and after pruning on the MC $m_{\ell\ell}$ distribution after the unfolding. Also in this

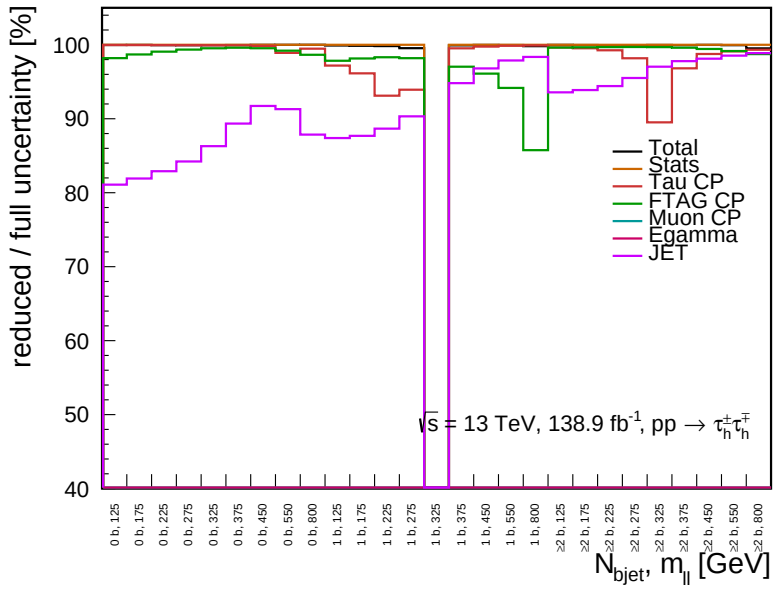

Figure 3.6: Ratio between the uncertainties before and after pruning on the MC $m_{\ell\ell}$ τ_{had} τ_{had} distribution after the unfolding. For the before and after pruning distributions, including the $e\mu$ region, see Figure D.2 in Appendix D.1. The gap at 1 b, 325 GeV is due to having empty bins.

case, the resulting post-unfolding uncertainty agrees very well with the pre-pruning results.

3.4.3 Method Uncertainties

Uncertainties on the statistical models used to extract parameters of interest from the observed data are considered. They are briefly introduced here:

Spurious Signal Uncertainties: The best-fit signal parameters are extracted for several sets of background-only pseudo-data, and any systematic non-zero signal extraction is taken as an uncertainty.

Signal Injection: Sets of pseudo-data are produced for several choices of signal parameters, and any systematic non-closure of the best-fit extracted parameters is considered an uncertainty.

Unfolding Stress Tests: Several variations are applied to the Drell-Yan and $t\bar{t}$ cross section predictions across many fiducial-region bins; any inability of the unfolding model to correctly reproduce fiducial cross sections is taken as an uncertainty.

3.5 Statistical Model and Fitting Framework

The search for leptoquarks with preferential couplings to third-generation fermions is performed through a profile-likelihood fit to the detector-level Asimov data. The variables $m_{\mathrm{T}}^{\mathrm{total}}$, $\hat{s}_{\mathrm{mim}}^{1/2}$ and $m_{\ell\ell}$, defined in Section 3.2.2, are the discriminating observables. In order to constrain the SM background predictions and to cover the full range of possible experimental signatures of leptoquark-like new physics, the fit is performed in several regions defined by the flavour of the reconstructed leptons, the charge of the leptons, and the multiplicity of *b*-tagged jets.

In this thesis, hypotheses with leptoquarks of masses $m_{\mathrm{LQ}} = 1.5\,\mathrm{TeV}$ and $m_{\mathrm{LQ}} = 2\,\mathrm{TeV}$ are tested. The leptoquark coupling parameter to third generation fermions β_L^{33} is one of the parameters of the fit model and set equal to one. The impact of new particles on the prediction are taken into account both through production processes involving only BSM interaction vertices (pure BSM terms s^{BSM}) and via interference with SM processes (interference terms s^{int}) (see also Section 1.3).

The likelihood function for the fit is defined as:

$$L(\mu,\theta) = \prod_{j=1}^{N} \frac{(\sqrt{\mu}s_j^{\mathrm{int}} + \mu s_j^{\mathrm{BSM}} + b_j)^{n_j}}{n_j!} e^{-(\sqrt{\mu}s_j^{\mathrm{int}} + \mu s_j^{\mathrm{BSM}} + b_j)} \prod_{k=1}^{M} \frac{u_k^{m_k}}{m_k!} e^{-u_k} \tag{3.2}$$

where μ is the strength of the signal process and θ denoted to all nuisance parameters. N is the amount of bins of the kinematic variable x with bin content n_j. s_j^{int}, s_j^{BSM} and b_j are the mean number of entries in the j-th bin of the signal and background, respectively. The mean number of entries are defined as:

$$s_j^{\mathrm{term}} = s_{\mathrm{tot}}^{\mathrm{term}} \int_{\mathrm{bin}\ j} f_s(x;\theta_s^{\mathrm{term}})dx \tag{3.3}$$

$$b_j^{\mathrm{term}} = b_{\mathrm{tot}}^{\mathrm{term}} \int_{\mathrm{bin}\ j} f_b(x;\theta_b^{\mathrm{term}})dx \tag{3.4}$$

with the functions $f_s(x;\theta_s^{\mathrm{term}})$ and $f_b(x;\theta_b^{\mathrm{term}})$ being the PDF of the variable x for signal and background events, and θ_s^{term} and θ_b^{term} represent parameters that characterise the shapes of PDFs. $s_{\mathrm{tot}}^{\mathrm{term}}$ and $b_{\mathrm{tot}}^{\mathrm{term}}$ are the total mean numbers of signal and background events, and the integrals in Equation (3.3) and (3.4) represent the probabilities for an event to be found in bin j.

The second product in Equation (3.2) can be further subsidiary measurements that help constrain the nuisance parameters. In this work these samples, with M amount of bins, are from the $e\mu$ control region where no τ_{had} is present in the final state. $u_k(\theta)$ is the expected value for the number of entries in the k-th bin m_k.

Systematic uncertainties are included in the fit as nuisance parameters θ with Gaussian constraint terms in the likelihood function. A linear approximation based on the nominal model and the available $\pm 1\sigma$ systematic variation points is used to smoothly interpolate over the parameter space.

In the absence of a significant deviation from the SM prediction, exclusion limits for leptoquark couplings are determined for each mass hypothesis using a modified CLs technique [173] with the maximum profile-likelihood ratio $\lambda(\mu)$ as the test statistic:

$$\lambda(\mu) = \frac{L(\mu, \hat{\hat{\theta}})}{L(\hat{\mu}, \hat{\theta})} \tag{3.5}$$

using the asymptotic approximation [174]. $L(\mu, \hat{\hat{\theta}})$ is the profile likelihood function. The quantity $\hat{\hat{\theta}}$ denotes the value of θ that maximises L for the specified μ, i.e., it is the conditional maximum-likelihood estimator of θ (and thus is a function of μ). $L(\hat{\mu}, \hat{\theta})$ is the maximised (unconditional) likelihood function, i.e., $\hat{\mu}$ and $\hat{\theta}$ are their maximum likelihood estimators. The above is summarised from Reference [174].

The `pyhf` framework [175], a `Python` based tool for `HistFactory` models [176] such as the one introduced above, is employed to find the maximum-likelihood point in parameter space and to approximate the likelihood function's shape around its optimum. The `cabinetry` toolkit [177] is used to steer the likelihood fit and to produce control plots such as the post-fit distributions shown below. Integrating `cabinetry` with the analysis framework outputs has been my main contribution to the high mass LQ search. Three key developments were necessary for the analysis:

- `cabinetry` should be usable with reproducible configuration files and with minimal run- and setup time.

- The different scaling of the LQ interference and BSM terms (see relation in Equation (1.3) and (1.4)) in the likelihood fit was achieved with a single parameter g^2 to handle not scaling square roots (see Equation (3.2)). The parameter g^2 will be the upper limit of the signal strength – the sensitivity. Above the signal strength was introduced with μ but to avoid confusion with the cross section it is replaced from here on as g^2. The following applies:

$$g_U \equiv g \qquad g \equiv \sqrt{\mu} \tag{3.6}$$

- Since the maximum-likelihood point is often found with the logarithm of the likelihood, negative terms like the interference terms can cause issues. In high

mass bins with few background events, the total events can go negative for certain values of g^2. The parameter bounds of the point of interest therefore had to be set carefully to restrict g^2 to not go negative.

All of the above were successfully achieved and the results are shown in Section 3.6.2. With the efforts above, I also became a contributor to the official `cabinetry` toolkit repository [178].

3.6 Expected Limits

As mentioned in the introduction of this chapter, the high-mass opposite-sign regions are, at the time of writing, blinded and therefore no published results are available. "Data / MC comparisons" in Section 3.6.1 show the expected predictions. Plots in Section 3.6.2 have data points, but they are "Asimov data". An Asimov dataset is constructed by setting the observed data to be equal to the expected values from a specific hypothesis or model.

Additionally, the estimated backgrounds from hadronically decaying τ-leptons, τ_{had}, have not yet been propagated into results of this section. At the time of producing the results, the $e\tau_{\text{had}}$ and $\mu\tau_{\text{had}}$ channels were not expected to adversely affect the expected results below since the MC achieved good closure with the high-mass same-sign lepton control regions.

3.6.1 Data vs. Simulation Comparisons

Figure 3.7 shows the SM prediction for various event kinematic distributions of interest in the τ_{had} τ_{had} signal region. Other regions are shown in Appendix D.2. They are split into regions defined by the flavour of the reconstructed leptons.

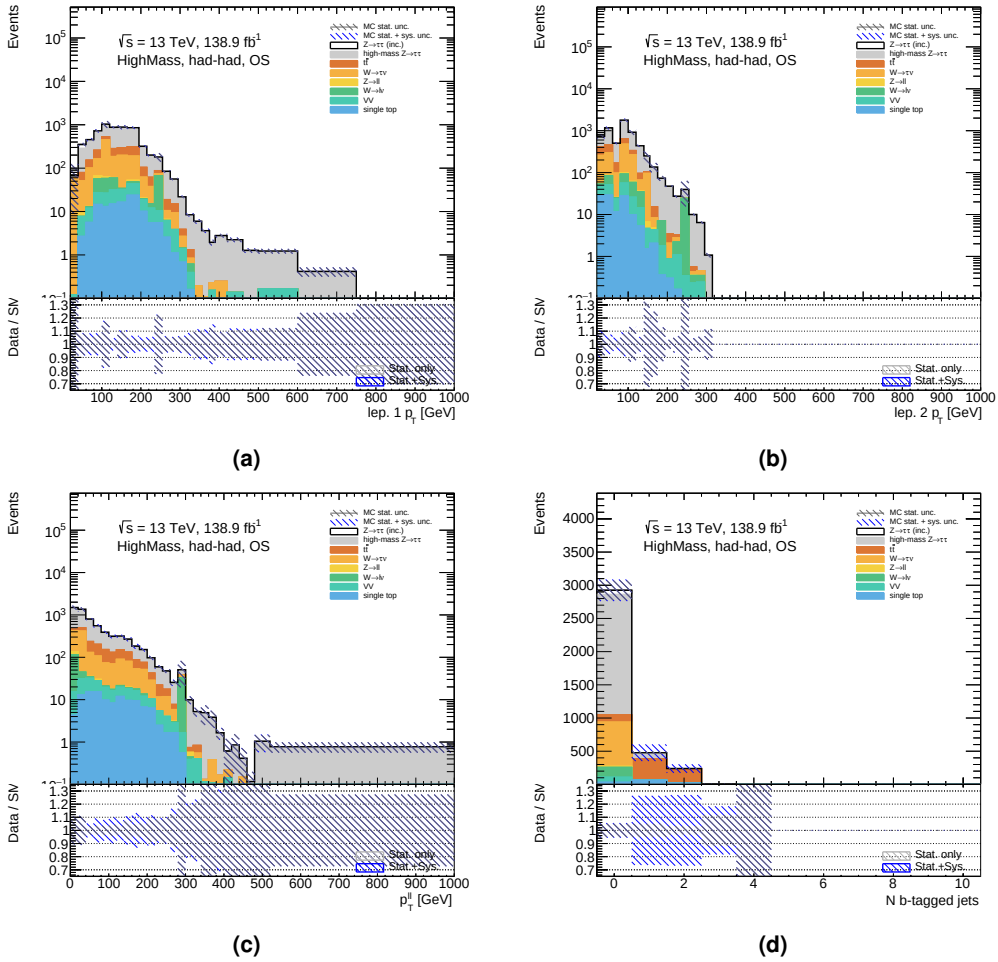

Figure 3.7: Distributions of MC simulation for a number of kinematic quantities in the high-mass, opposite-sign, $\tau_{\text{had}}\tau_{\text{had}}$ region: (a) the leading τ_{had} $p_{\text{T}}^{\text{vis}}$, (b) the subleading τ_{had} $p_{\text{T}}^{\text{vis}}$, (c) the $p_{\text{T}}^{\text{vis}}$ of the $\tau_{\text{had}}\tau_{\text{had}}$ system, and (d) the *b*-jet multiplicity.

3.6.2 Leptoquark Sensitivity Results

A profile-likelihood fit, as introduced in Section 3.5, has been applied over several vector leptoquark signal predictions.

Figure 3.8 shows the pure BSM and pure interference events of the LQ signals for the $m_{\text{T}}^{\text{total}}$ variable in the τ_{had} τ_{had} $e\mu$ regions and different masses. These are, together with the background processes, used as inputs for the fitting. Figures 3.9–3.14 show the post-fit predictions as given by `cabinetry` for $m_{\text{LQ}} = 1.5\,\text{TeV}$ (for $m_{\text{LQ}} = 2\,\text{TeV}$ see Appendix D.5), including the main SM background modelling and cross section uncertainties described in Section 3.4. As mentioned in Section 3.3, the τ_{had} τ_{had} is used as the signal region and the $e\mu$ as the control region. The fit is performed with Asimov data based on the SM prediction. Here the scenario corresponds to a vector leptoquark with $m_{\text{LQ}} = 1.5\,\text{TeV}$, $\beta_L^{b\tau} = 1$, $\beta_L^{ij} = 0$, where i, j involve at least one first- or second-generation index, and $\beta_R^{ij} = 0$ for all i, j.

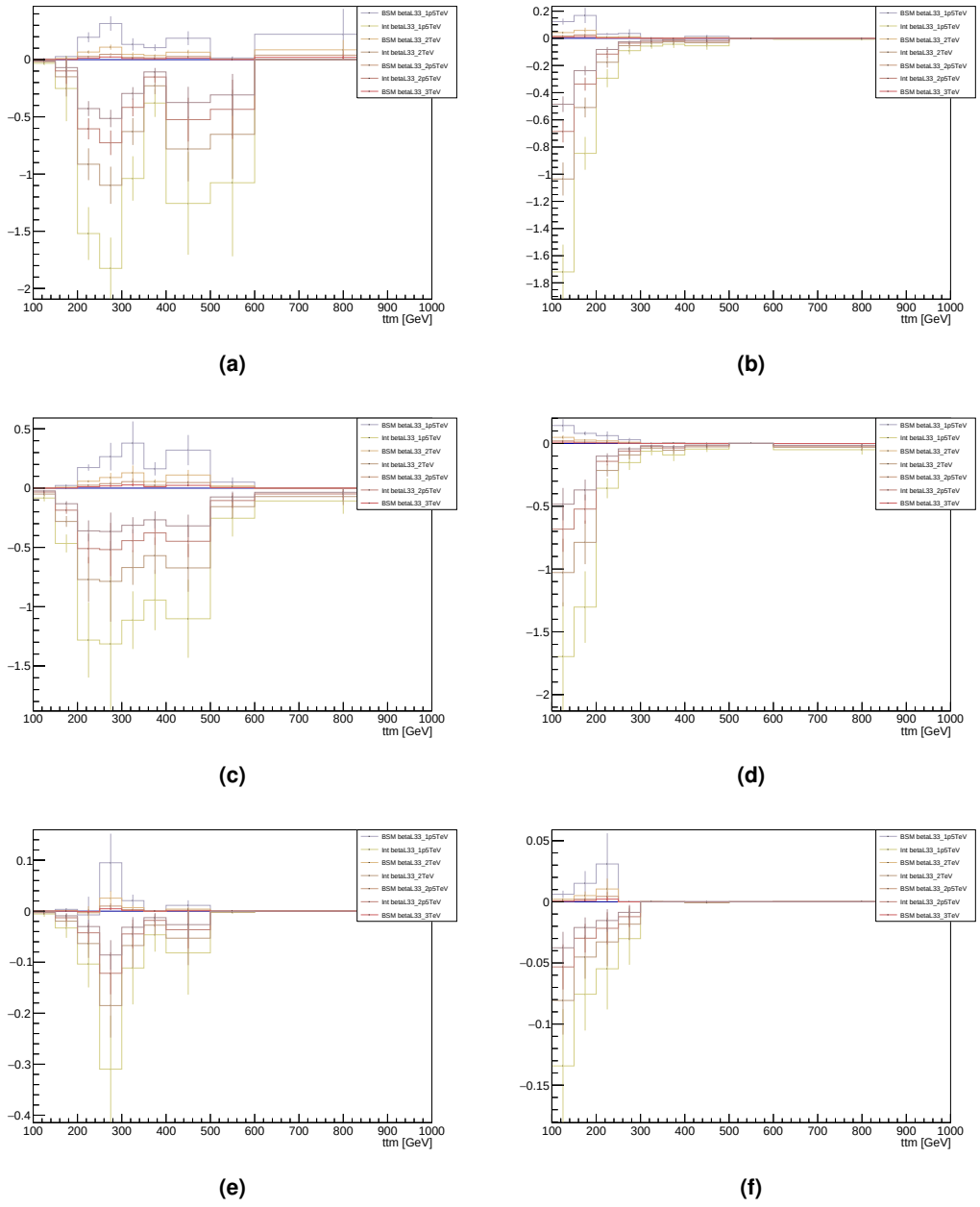

Figure 3.8: Signal events of the high mass opposite sign $\tau_{\text{had}}\,\tau_{\text{had}}$ (left side plots) and $e\mu$ (right side plots) regions for the $m_{\text{T}}^{\text{total}}$ variable for the different masses 1.5 TeV to 3 TeV. The $\hat{s}_{\text{mim}}^{1/2}$ and $m_{\ell\ell}$ variable can be found in the Appendix D.4. Visible are the above mentioned problematic negative bins for the maximum likelihood fit.

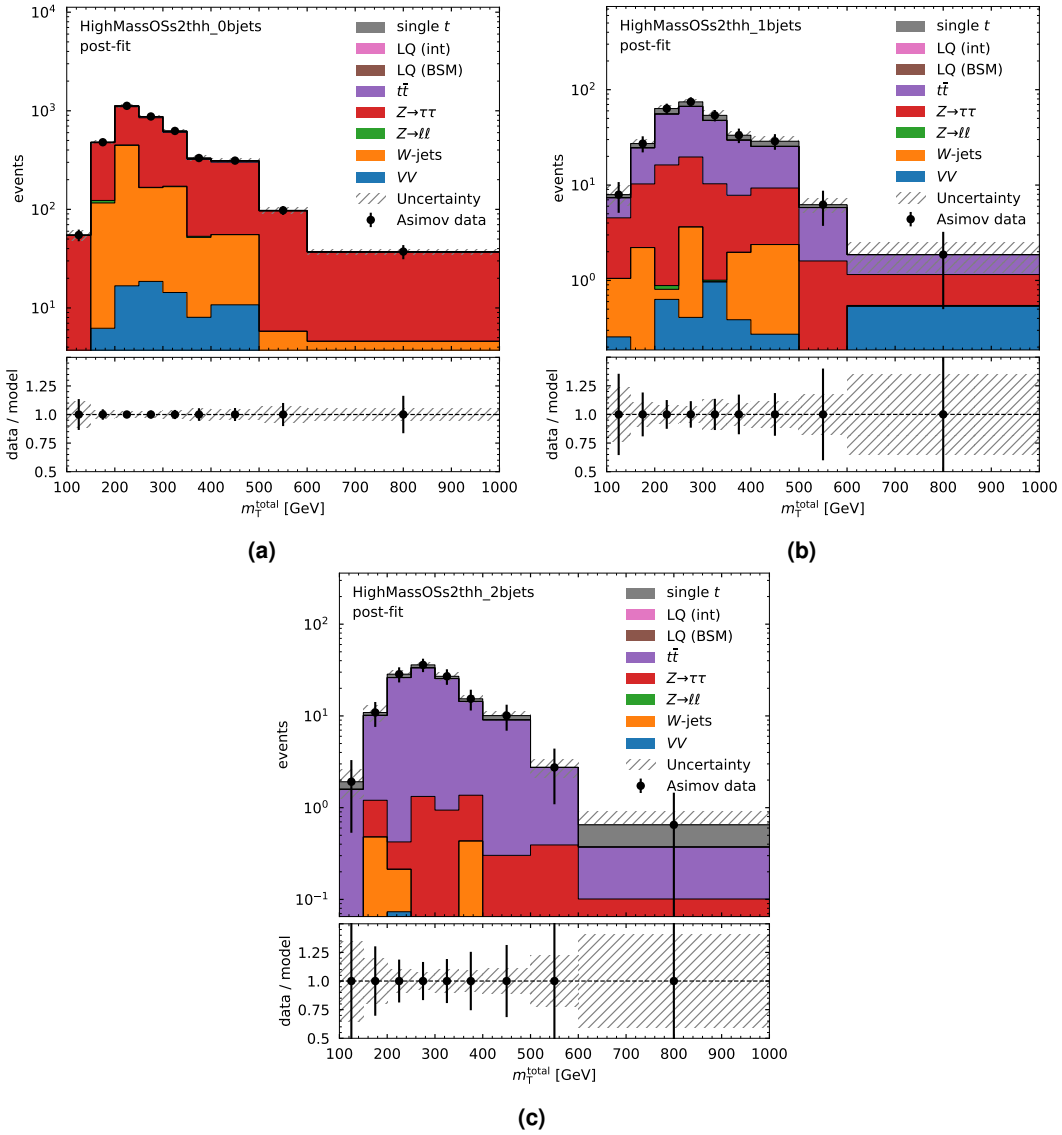

Figure 3.9: Post-fit distributions of the di-lepton $m_{\mathrm{T}}^{\mathrm{total}}$ in high-mass, opposite-sign $\tau_{\mathrm{had}}\tau_{\mathrm{had}}$ region for the $\beta_L^{b\tau} = 1$, $m_{\mathrm{LQ}} = 1.5\,\mathrm{TeV}$ fit. Distributions are shown (a) in the 0, (b) 1, and (c) 2+ b-jet multiplicity regions after the fit is performed. Uncertainties include the process modelling and cross section uncertainties described in Section 3.4.

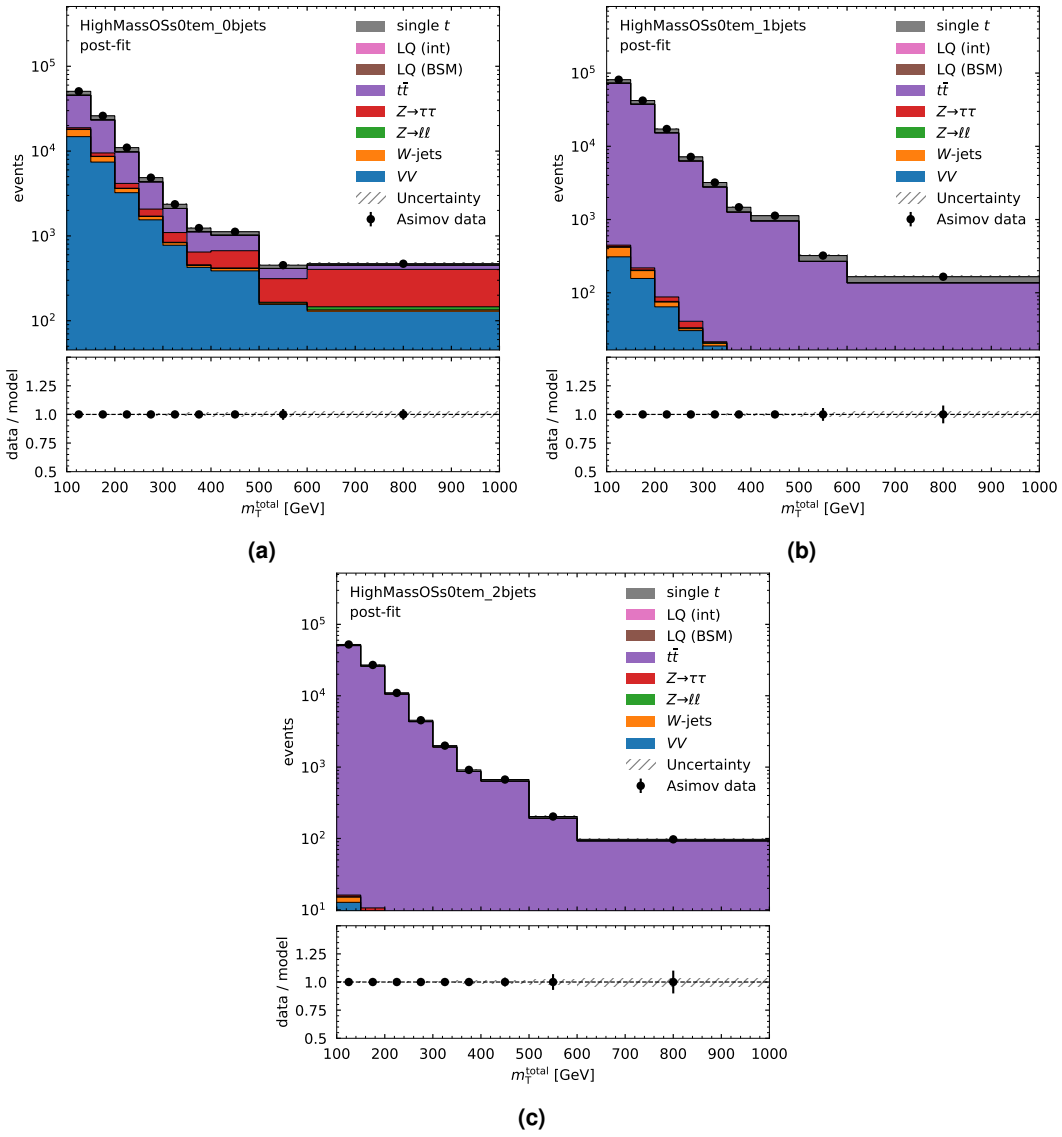

Figure 3.10: Post-fit distributions of the di-lepton $m_{\mathrm{T}}^{\mathrm{total}}$ in high-mass, opposite-sign $e\mu$ region for the $\beta_L^{b\tau} = 1$, $m_{\mathrm{LQ}} = 1.5$ TeV fit. Distributions are shown (a) in the 0, (b) 1, and (c) 2+ b-jet multiplicity regions after the fit is performed. Uncertainties include the process modelling and cross section uncertainties described in Section 3.4.

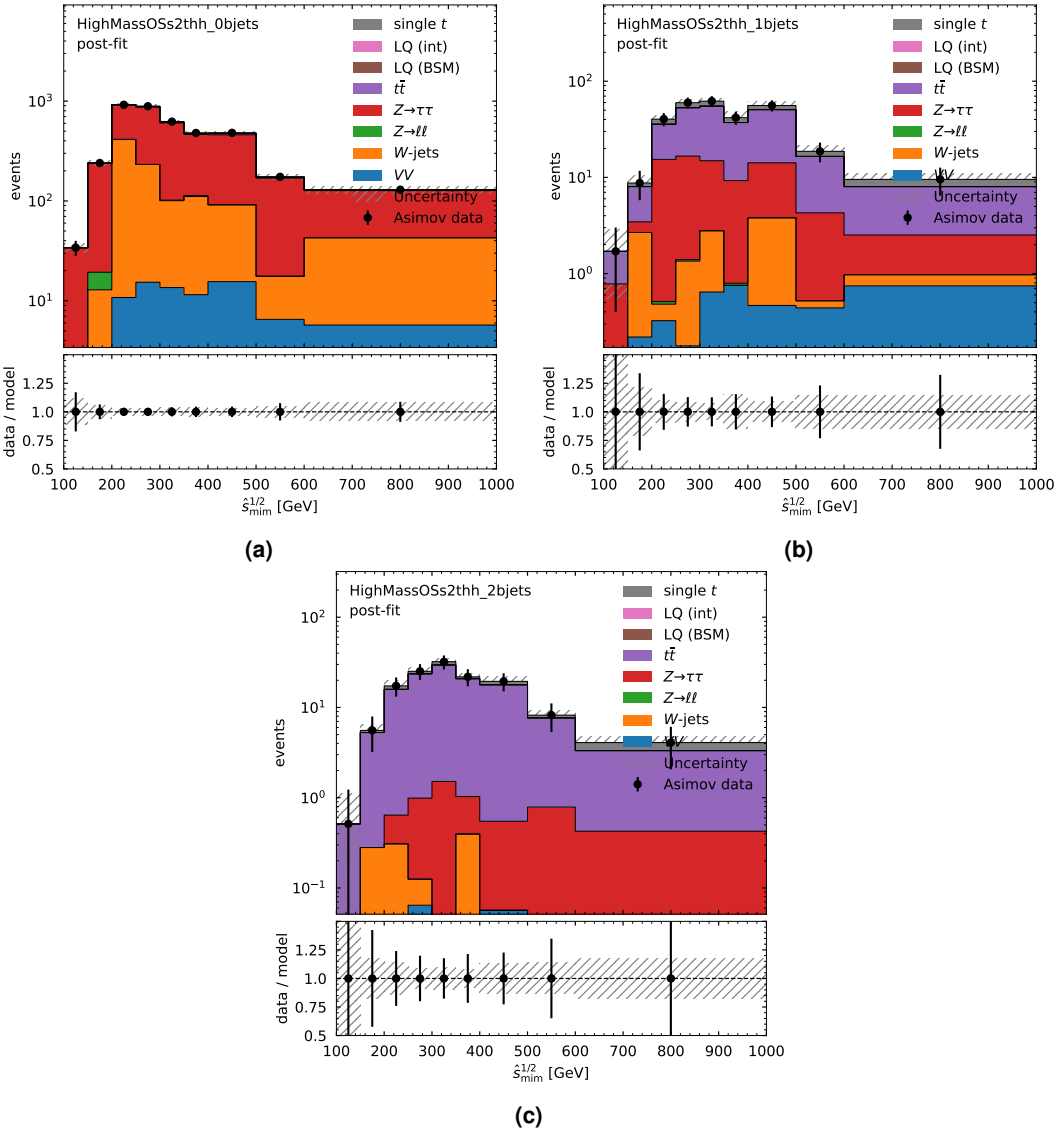

Figure 3.11: Post-fit distributions of the di-lepton $\hat{s}_{\text{mim}}^{1/2}$ in high-mass, opposite-sign $\tau_{\text{had}}\tau_{\text{had}}$ region for the $\beta_L^{b\tau} = 1$, $m_{\text{LQ}} = 1.5$ TeV fit. Distributions are shown (a) in the 0, (b) 1, and (c) 2 b-jet multiplicity regions after the fit is performed. Uncertainties include the process modelling and cross section uncertainties described in Section 3.4.

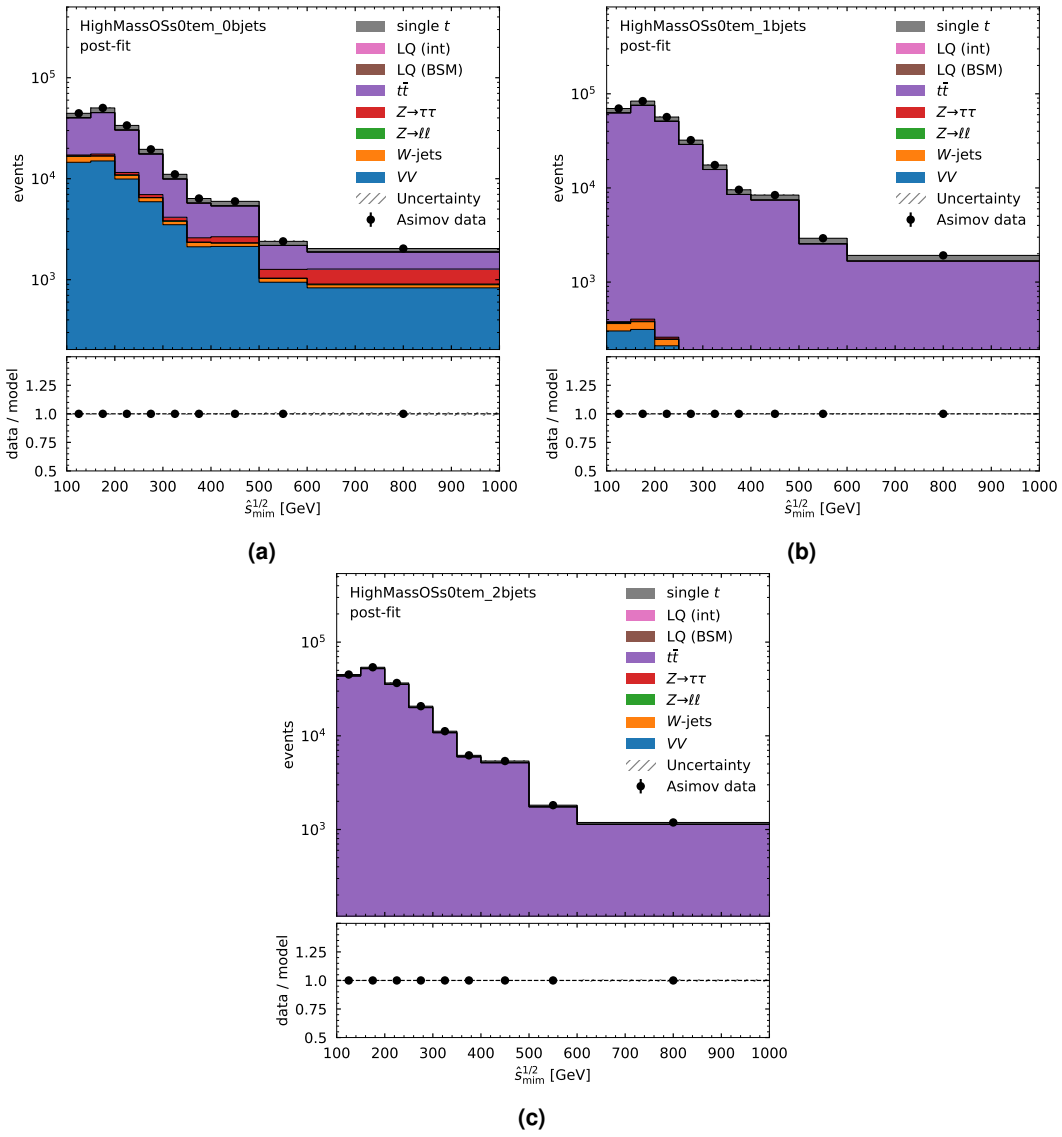

Figure 3.12: Post-fit distributions of the di-lepton $\hat{s}_{\text{mim}}^{1/2}$ in high-mass, opposite-sign $e\mu$ region for the $\beta_L^{b\tau}$ = 1, m_{LQ} = 1.5 TeV fit. Distributions are shown (a) in the 0, (b) 1, and (c) 2 b-jet multiplicity regions after the fit is performed. Uncertainties include the process modelling and cross section uncertainties described in Section 3.4.

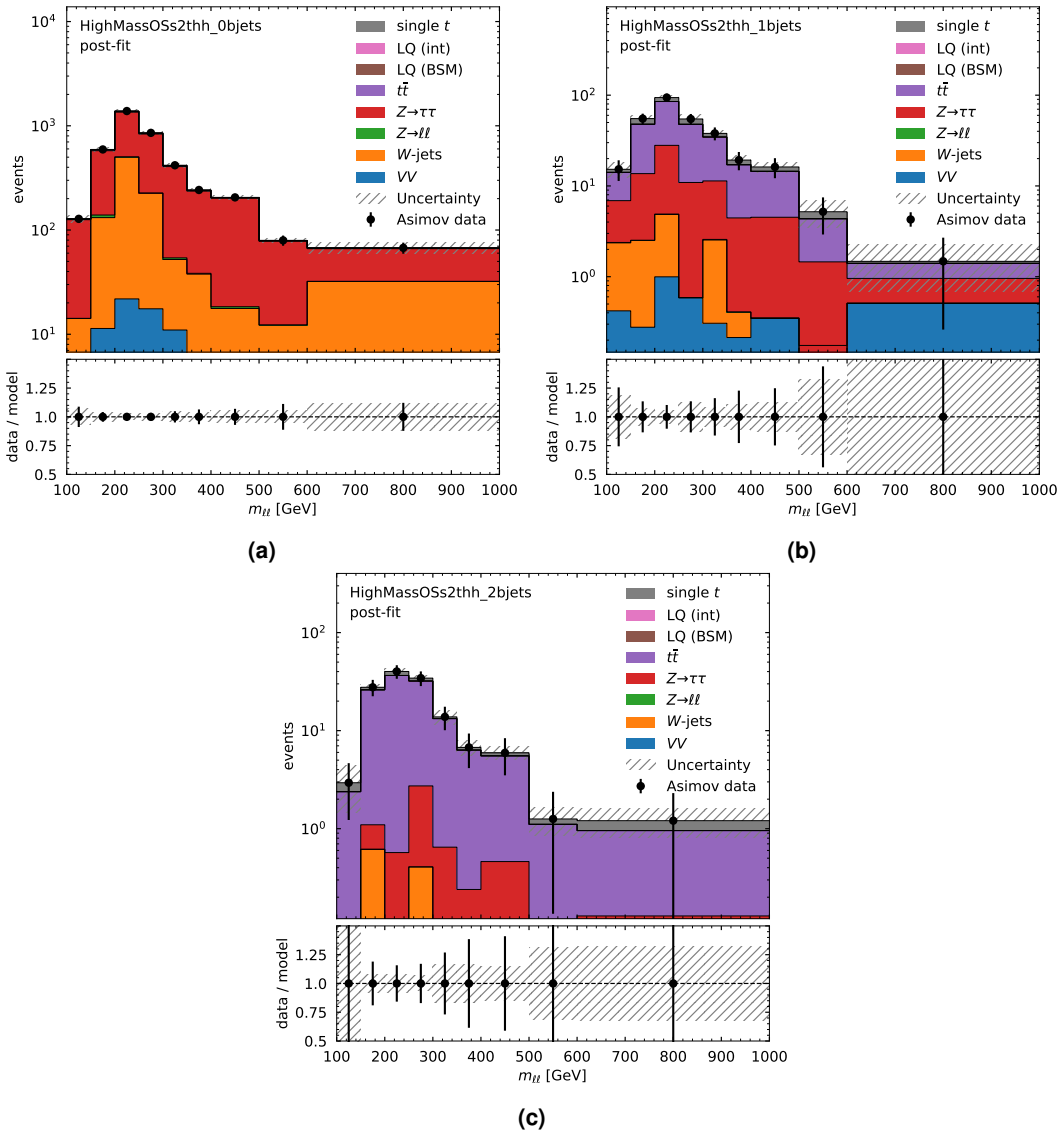

Figure 3.13: Post-fit distributions of the di-lepton $m_{\ell\ell}$ in high-mass, opposite-sign $\tau_{\text{had}}\tau_{\text{had}}$ region for the $\beta_L^{b\tau} = 1$, $m_{\text{LQ}} = 1.5$ TeV fit. Distributions are shown (a) in the 0, (b) 1, and (c) 2 b-jet multiplicity regions after the fit is performed. Uncertainties include the process modelling and cross section uncertainties described in Section 3.4.

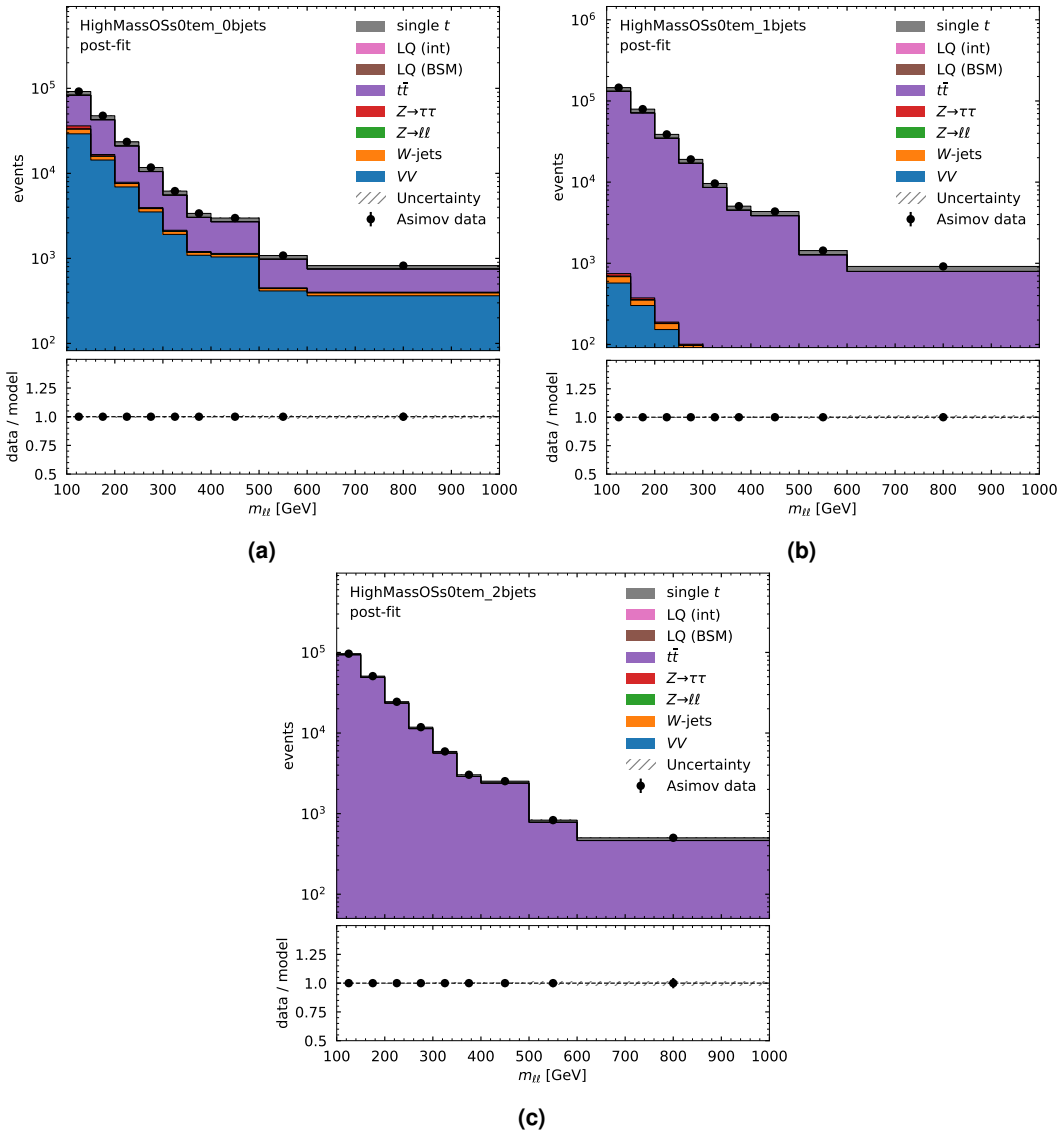

Figure 3.14: Post-fit distributions of the di-lepton $m_{\ell\ell}$ in high-mass, opposite-sign $e\mu$ region for the $\beta_L^{b\tau} = 1$, $m_{\text{LQ}} = 1.5\,\text{TeV}$ fit. Distributions are shown (a) in the 0, (b) 1, and (c) 2 b-jet multiplicity regions after the fit is performed. Uncertainties include the process modelling and cross section uncertainties described in Section 3.4.

Figure 3.15 shows the expected CLs from a set of Asimov data based on the the SM prediction for two choices of m_{LQ}. In these limits the signal regions are the $\tau_{had}\tau_{had}$ b-jet multiplicities and the control region $e\mu$ b-jet multiplicities for the m_T^{total} variable. The expected limit values are summarised in Table 3.5. To study the impact of the MC

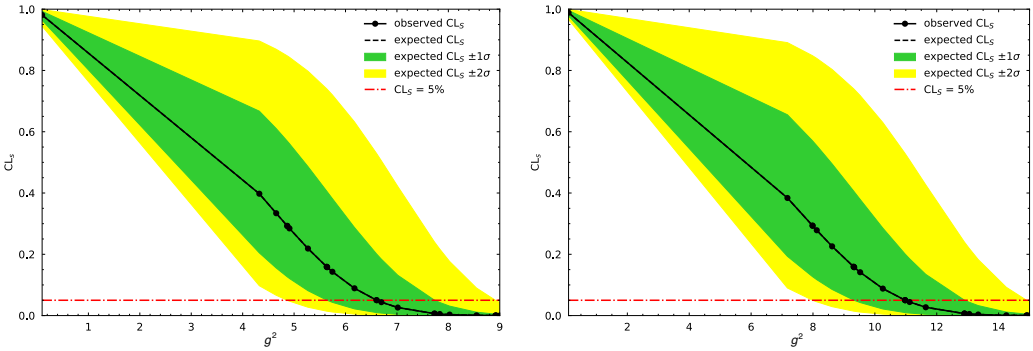

(a) **(b)**

Figure 3.15: Expected CLs as a function of signal-strength parameter g^2 for a vector leptoquark coupling purely to third-generation fermions for (a) m_{LQ} = 1.5 TeV and (b) m_{LQ} = 2 TeV based on a fit to the m_T^{total} in all opposite-sign charged lepton regions split by b-jet multiplicity. The "observed" CLs curves show the limit for a set of pseudo-data thrown from the SM prediction.

	g^2 (m_{LQ} = 1.5 TeV)	g^2 (m_{LQ} = 2 TeV)	Remark
m_T^{total}	$6.61^{+1.13}_{-0.95}$	$10.98^{+1.92}_{-1.65}$	with MC statistics & systematics
m_T^{total}	$5.98^{+0.99}_{-0.87}$	$10.01^{+1.70}_{-1.51}$	no MC statistics
$m_{\ell\ell}$	4.52	8.69	with MC statistics & systematics
$m_{\ell\ell}$	$4.40^{+0.89}_{-0.80}$	$8.44^{+1.77}_{-1.62}$	no systematics
$\hat{s}^{1/2}_{mim}$	6.29	$10.92^{+1.72}_{-1.40}$	with MC statistics & systematics

Table 3.5: Signal strength of g^2 of the observables with $\pm1\sigma$ confidence level for one variable at the time. Note: for the missing $\pm1\sigma$ values the underlying minimisation-algorithm `minuit` [179] of `cabinetry` did not converge to a minimum. The corresponding "pull-plots" of the systematics can be found in Appendix D.6.

statistics or the systematics, fits were made with them disabled. With a difference of less than 10% to the nominal fits the results prove the systematics and statistics are under control.

3.6.3 Comparison to CMS Analysis

The CMS collaboration has done a similar search for third generation LQ [21]. To compare the sensitivity of g^2 from this analysis with the coupling strength λ of CMS, a factor of $\frac{1}{\sqrt{2}}$ needs to be multiplied to the results of Table 3.5. The factor emerges from the differently used Lagrangians in the signal sample generation, Equation (1.1) has the factor and CMS does not. Table 3.6 shows the adjusted results for comparison with the results of CMS.

	λ (m_{LQ} = 1.5 TeV)	λ (m_{LQ} = 2 TeV)	Remark
$m_{\mathrm{T}}^{\mathrm{total}}$	$4.67^{+0.80}_{-0.67}$	$7.70^{+1.36}_{-1.17}$	with MC statistics & systematics
$m_{\mathrm{T}}^{\mathrm{total}}$	$4.23^{+0.70}_{-0.82}$	$7.08^{+1.20}_{-1.07}$	no MC statistics
$m_{\ell\ell}$	3.20	6.14	with MC statistics & systematics
$m_{\ell\ell}$	$3.11^{+0.63}_{-0.57}$	$5.97^{+1.25}_{-1.15}$	no systematics
$\hat{s}_{\mathrm{mim}}^{1/2}$	4.45	$7.72^{+1.22}_{-0.99}$	with MC statistics & systematics

Table 3.6: Signal strength of λ of the observables with $\pm 1\sigma$ confidence level for one variable at the time. The values here are the results from Table 3.5 multiplied by $\frac{1}{\sqrt{2}}$ to compare to the CMS results.

3.7 Expected Differential Fiducial Cross Sections Results

Figure 3.16 shows the closure of the unfolded differential cross sections with the nominal prediction as well as their expected statistical uncertainties; this closure test includes the subtraction of non-fiducial events from all MC-predicted processes. Good closure is observed between the true and unfolded differential cross sections. The expected uncertainty breakdown (for the available uncertainties) is shown in Figure 3.17 in the fiducial regions of interest.

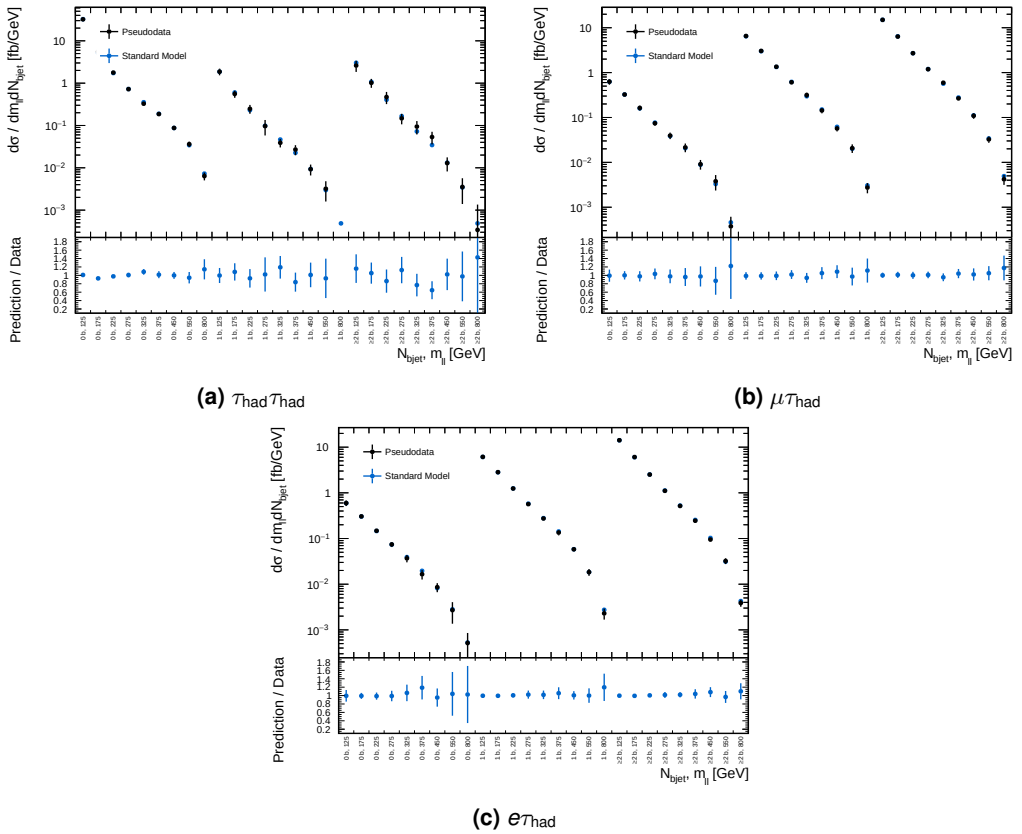

(a) $\tau_{\mathrm{had}}\tau_{\mathrm{had}}$ **(b)** $\mu\tau_{\mathrm{had}}$

(c) $e\tau_{\mathrm{had}}$

Figure 3.16: Unfolded fiducial differential cross sections of the di-lepton $m_{\ell\ell}^{\mathrm{vis}}$ in high-mass, opposite-sign regions. Poisson-fluctuated expected rates are used to throw a toy dataset input to the unfolding, and good closure between the true and unfolded fiducial cross sections is observed.

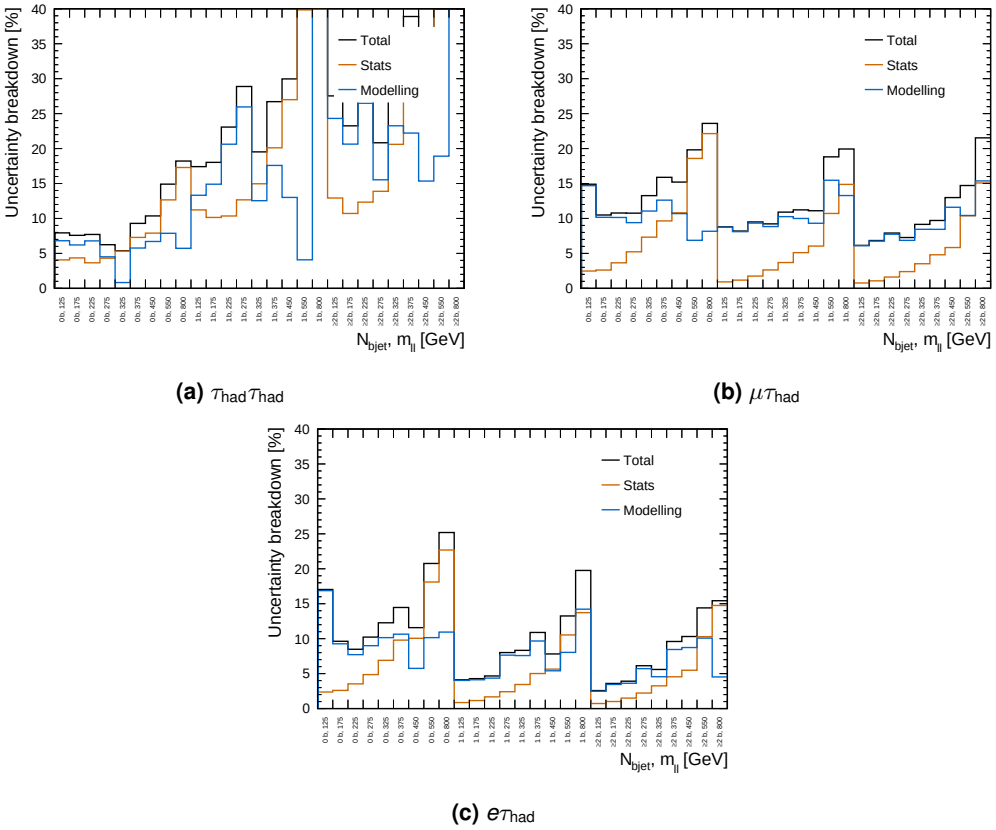

(a) $\tau_{\text{had}}\tau_{\text{had}}$ **(b)** $\mu\tau_{\text{had}}$

(c) $e\tau_{\text{had}}$

Figure 3.17: Uncertainty breakdowns for differential cross sections of the di-lepton $m_{\ell\ell}^{\text{vis}}$ in high-mass, opposite-sign regions.

Chapter 4

The Optoboard System for the ATLAS ITk Pixel Detector

The Optoboard system is a central part of the future ATLAS read-out system handling all data, command and trigger of the ATLAS ITk Pixel Detector. Figure 4.1 provides an overview of the readout and services with the Optoboard system in the centre, included are the connections of the various power supplies, Detector Control System (DCS) (including interlock system) and the four Patch Panels (PP). Section 4.1 gives a short introduction to the Optoboard system, while the Optoboard is explained in Section 4.2. The electrical and mechanical structures, called services, of the Optoboard system are introduced in Section 4.3, with the power distribution cables detailed in Section 4.4 and optical + electrical cables in Section 4.5, 4.6 respectively.

Due to limited lab access because of the COVID-19 pandemic, the initial work for this thesis has focused on activities that could be carried out while working from home: a detailed mapping of the connections between the Optoboards and the modules of the ITk Pixel Detector was defined and is presented in Section 4.7.

4.1 Optoboard System Overview

The Optoboard system is the modular optical-electrical conversion system dedicated to the readout of the entire ATLAS ITk Pixel detector. This pivotal component of the ITk Pixel data transmission chain contains at its heart a Printed Circuit Board (PCB), the Optoboard, that hosts a series of Application-Specific Integrated Circuits (ASICs) intended to aggregate electrical links and subsequently convert them to optical signals for transmission to the ATLAS counting room in USA15 via fibre optical cables. The second function operates in the reverse sense where optical signals are converted to electrical links and distributed to the modules providing clock and command signals.

The Optoboards are hosted in a mechanical structure known as an *Optobox*, up to

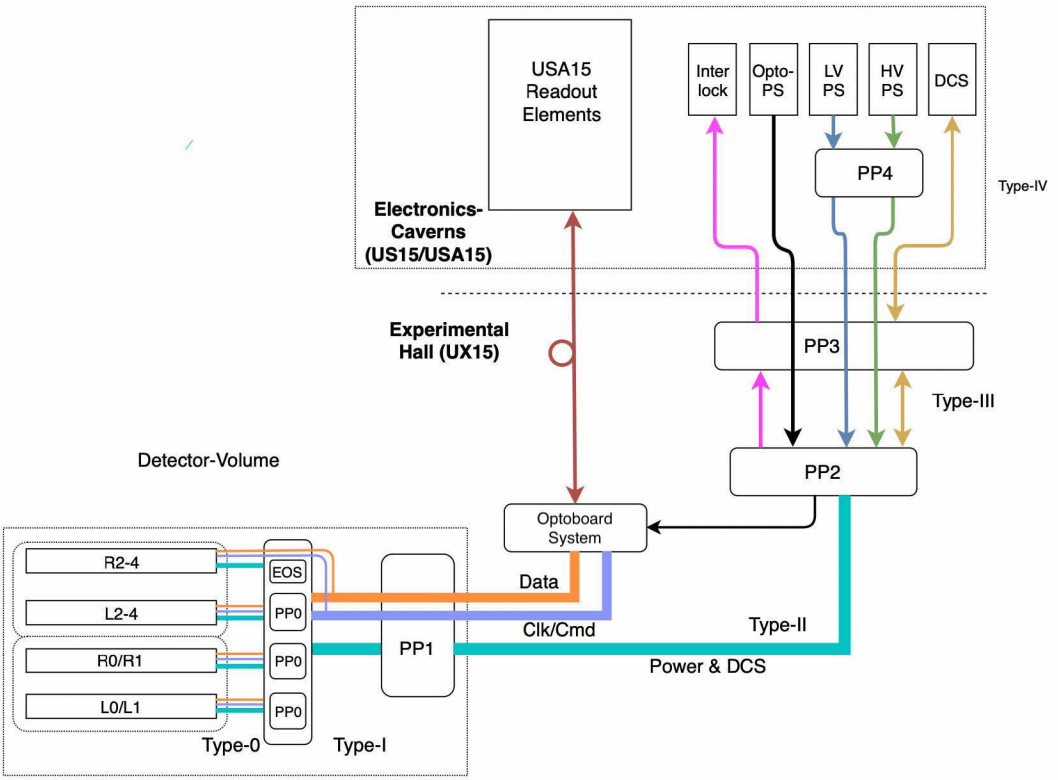

Figure 4.1: Schematic diagram of the ITk Pixel Detector. Following the readout from the detector volume (bottom left of the image), the power, data, clock (Clk) and command (Cmd) from the module Layer (L) and Rings (R) are patched at PP0 or End of Stave (EOS) cards. While the power lines are further patched at PP1, the data + clock/command are fed through and brought directly to the Optoboard System. The Optoboard system is powered from patched cables of PP2. Further up the readout there are PP3 and PP4 with different arrangements of feed-throughs (coloured line drawn) and breaking points (arrow stops/starts). US15 and USA15 are two different electronic caverns at opposite sides next to ATLAS, the Power Supplies (PS) are split between these two caverns.

eight Optoboards may reside inside an Optobox. The number of Optoboards per Optobox depends on the number of FEs, their bandwidth and location inside the ITk Pixel Detector (more on this in Section 4.7). The cables carrying electrical signals arrive at the Optoboxes and are connected to the Optoboards by means of termination boards (see Section 4.6). 28 Optoboxes are hosted in so-called *Optopanels*. There are four Optopanels at each side of the ATLAS detector, located at $|z| = 3.5\,\text{m}$ and $r = 1.4\,\text{m}$, totalling eight panels dedicated to the readout and control of the ATLAS ITk Pixel detector.

Figure 4.2 gives an overview of the different components of the Optoboard system. One Optoboard contains the following main components on its PCB that are further explained in Chapter 5: four lpGBTs (see Section 5.2), four GBCRs (see Section 5.3), one VTRx+ (see Section 5.4).

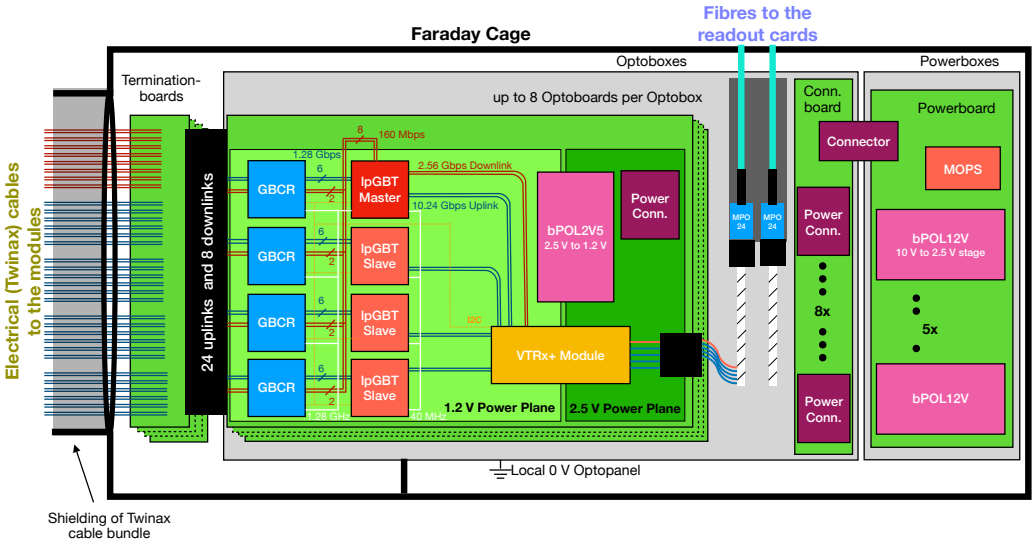

Figure 4.2: The ITk Pixel Detector data transmission scheme with focus on the Optoboard system. From left (uplink path): the FE modules connected to the type0 flex which are flexible PCBs also called pigtails. They have a type0 connector attached to the PP0 from where the electrical cables are connected to the Optoboard's Termination boards. The data passes the GBCR and lpGBT and gets converted to an optical signal with the VTRx+ which sends the data to the backend. Note that this shows the connections of the Optoboard version 2 which is of relevance for this thesis. The major difference with respect to the production version is that in the version 2 the downlinks are not bypassing the GBCR (see Section 4.2 for more details). The full data transmission chain (except the fibres) is encased in a faraday cage and has a single reference point at the Optopanels. Figure provided by Laura Franconi.

4.2 The Optoboard

The Optoboard is the main component of the Optoboard system: this PCB hosts the previously described ASICs that perform the (de-)multiplexing and the electrical-optical (optical-electrical) conversion. Optoboards will be reading out the entire ITk Pixel Detector and additionally the Pixel Luminosity Ring (PLR) detector and the new Beam Conditions Monitor Prime (BCM') detector. From the PP0, Type-1 cables (twinaxial cables called Twinax, see Section 4.6) leave the detector and transmit the data signal to the Optoboard system (and vice versa, Twinax cables transmit clock and commands to the detector).

An Optoboard of the final version is populated with:

- Either one (BCM'), two or four lpGBT chips depending on the connected subsystem and mapping. Every Optoboard has one lpGBT master (or lpGBT1) in transceiver mode and one or three lpGBT slaves (or lpGBT2–4) in transmitter mode.

- Two or four GBCR chips, which are used to recover the uplink signal after the transmission over the Twinax cables. Their identifiers correspond to the connected lpGBT e.g. GBCR1 to lpGBT1 and so on. Which of the four available pads is populated depends again on the mapping, it will be the same identifier number as the lpGBT.

- One VTRx+ module.
- One bPOL2V5 DCDC converter, mounted on a carrier board, that dispatches the power to the active components on the Optoboard.
- An ERM8 connector, where the Termination board is plugged.
- A TFM power connector, interfacing with the Connectorboard (see Section 4.4), which brings power to the board.
- Passive components.

To cool the individual chips the Optoboards are mounted on aluminium L-profiles.

There exist several versions of the Optoboard that evolved in several development stages with improvements or features:

Version 0.2: This is the very first version of the Optoboard combining one lpGBT (version 0 of the ASIC) and one VTRx+ on a PCB. Due to the bPOL2V5 ASIC not being available at the time of development, the 2.5 V to 1.2 V voltage transformation is done using the bPOL predecessor FEAST [180, 181]. Figure 4.3a shows the version 0.2 front side, which was used for testing the communication between the backend and the lpGBT, explained in more detail in Section 5.5. The communication is established through the I2C bus [182] lines, which are accessible from the ERM8 connector.

Version 1.1: The big leap in development happened with the Optoboard version 1.1 (Figure 4.3b). It is the first version featuring all four lpGBTs and also includes the four GBCRs. The VTRx+ has moved to the back side of the PCB and the FEAST has been replaced by the pads for the bPOL2V5 carrier board hosting the bPOL2V5 ASIC. The PCB also includes two holes (upper left of Figure 4.3b) for fixing the VTRx+ fibre pigtail and two holes for mounting the cooling L-profile. The ERM8 connector is now fully occupied by the data and command signals hence communication with the lpGBT is only possible through the fibre Internal Control (IC) protocol.

Version 2.0: The development of the Optoboard took another big step with the release of version 2.0. After gathering valuable insight and experience with version 1.1 in the first data transmission setup (see Section 5.5), version 2.0 features the following improvements:

1. Removing the I2C communication channel to the lpGBT1 master made interacting with the Optoboard V1.1 only possible through IC. Since the lpGBTv0 has no internal memory for the start-up procedure, the chip needs to be pre-configured through efusing (see also Section 5.2). The initial plan was to efuse the chip before mounting on the Optoboard but this was using

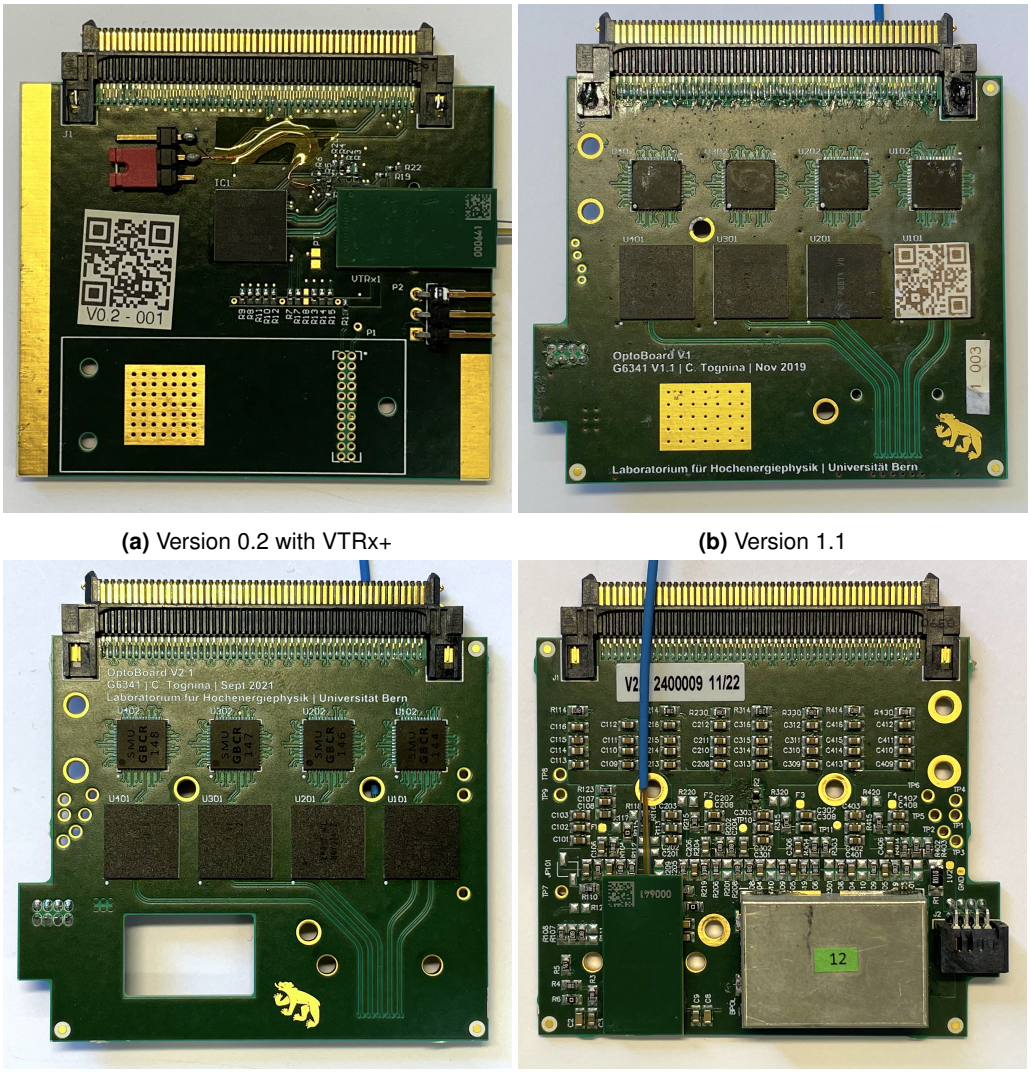

(a) Version 0.2 with VTRx+

(b) Version 1.1

(c) Version 2.1 (front) without bPOL

(d) Version 2.1 (back) with VTRx+ and bPOL

Figure 4.3: The different version of the Optoboard. (a) shows the Optoboard V0.2 with a single lpGBT and VTRx+ connected and a mounted jumper for selecting configuration modes. For versions $>$ 0.2 in (b), (c) the lpGBTs are the bottom four chips, while the upper four chips are the GBCRs. With the exception of the Optoboard V0.2, the VTRx+ is always connected in the back of the PCB. The numbering of the lpGBT1–4 and GBCR1–4 is from right to left.

too much time and external resources, therefore the I2C bus was made available again with through-hole pads.

2. The mounting of the cooling plate proved to be mechanically difficult with only two diagonal mounting holes, therefore a third hole next to lpGBT1 and lpGBT2 was implemented.

3. Since the data and clock lanes between GBCR and lpGBT cannot be probed from the PCB surface, testing points in form of through-hole pads were implemented. Each lpGBT slave has a single-ended test point, while the lpGBT master has differential test points. Through configuration it is possible to duplicate signals to the test points for debugging, however systematic tests are not possible as recommended by the designers [183].

4. Optoboard V2.0 also features lpGBT clock sharing to the GBCRs for the first time, enabling the use of the GBCR retiming mode, which has better signal recovery performance than just the equaliser mode [184].

After gathering experience from prototype testing of the previous Optoboard versions, points 1. and 3. were specifically requested by me. Access to I2C allowed the study of efusing and the test points enabled cross checking various internal signals of the lpGBTs and GBCRs.

Version 2.1: Shortly after the arrival of the Optoboard V2.0, the lpGBT team released the new lpGBT version 1 (lpGBTv1). With the now available internal Read-Only Memory (ROM) for the lpGBT start-up procedure and the observation of failures in the efuses after 150 Mrad irradiation [183], the efusing of Optoboards was discontinued (but with the I2C access still available). The lpGBT1 is hard configured with resistors. It can start up by reading the internal ROM, such that the backend can communicate with it. The rest of the internal configuration can then be done by software.

The Optoboard V2.1, as shown in Figure 4.3c, was necessary since the new lpGBT version also had some pin changes. The need of a new Optoboard design because of these small changes was also an opportunity for optimising the cooling of the bPOL2V5 carrier board. As visible on the lower part of Figure 4.3c, a part of the Optoboard PCB was cut out and enabled the latest version of the cooling L-profile to directly cool the carrier board. The bPOL carrier board (with its shield) is shown mounted on the back of the PCB in Figure 4.3d.

Version 3.0: The Optoboard version 3.0 is not used for any results in this thesis but is supported by test results presented in Section 5.5.1. This version is very similar to the v2.1 with the striking difference that the downlinks no longer pass through the GBCRs and instead are directly going from the lpGBT1's transmitter to the FE modules. The reason for this bypass is that the performance of the EPTX driver is similar to the downlink driver from the GBCR (see Section 5.5.1). Since all previous Optoboard versions all eight downlinks were utilised and each GBCR handled two downlinks, all GBCRs were necessary, even in the case of not equalising any uplinks. If the downlinks are bypassing the GBCR and no uplinks are equalised, the number of GBCRs can be reduced to the number of lpGBTs (see Section 4.7 for precise numbers).

4.3 Optoboard System Services and Interfaces

Around the Optoboard there are many services that handle powering, distribution of links, cooling, monitoring and more. This section summarises the most important ones.

Up to eight Optoboards are installed into a mechanical structure called *Optobox* (see

Figure 4.4), which also hosts the first part of the optical cable plant and the Connectorboard, a PCB that is part of the housing, distributing the power to the Optoboards. Another PCB, the Powerboard, is contained in a separate box, called

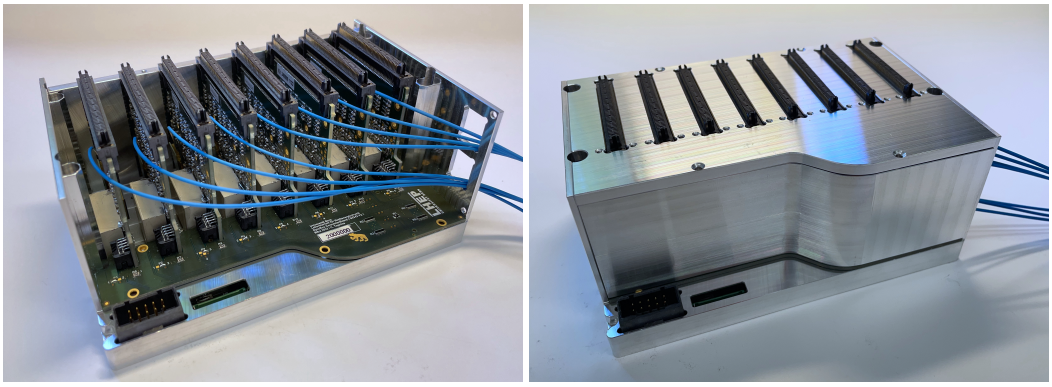

(a) (b)

Figure 4.4: Pictures of the Optobox fully populated with eight Optoboards and closed Powerbox below. (a) shows the Optobox with the top and side lid removed and (b) as it is mounted inside the Optopanel.

Powerbox. Both the Connectorboard and the Powerboard are detailed in Section 4.4. For servicing the ITk Pixel Detector, there are 220 Optoboxes (see Section 4.7 on how the numbers come together) and, correspondingly, 220 Powerboxes. The PLR and the BCM' detectors are serviced by one Optobox and one Powerbox each per ATLAS side.

In the ATLAS experiment, the Optoboxes will be installed inside mechanical structures called *Optopanels*, which also provide shielding against electromagnetic interference (EMI) and cooling of the system. The 4 mm thick walls and lid ensure the EMI shield, while the cooling is provided by the bottom cooling plate, in which cooling pipes guide coolant below the Optoboxes. The provided cooling is distributed to the Optoboards through the above mentioned cooling L-profiles. Each is screwed onto the floor of the Optobox.

The Optopanel structure is sketched in Figure 4.5. There are four Optopanels on each ATLAS side that host 28 Optoboxes each. They are located between $r = 1450$ mm and $r = 2400$ mm and at $z \approx 3500$ mm, .

Each Optopanel has an opening at low radius (left-hand side of Figure 4.5) that allows the cables to reach the Termination boards, and an *Opto Patch Panel* at high radius (right-hand side of the Figure 4.5), which hosts connectors for the power and the monitoring cables, and openings for the fibres. Fibres do not break at the Opto Patch Panel but go straight through its three openings. To keep the integrity of the Faraday cage, a U-shaped nose, with a thickness of 30 mm, is added around these openings.

Inside the Optopanels, the staggering of Optoboxes create channels dedicated either to the Twinax cables (represented in Figure 4.5 as yellow channels), or to the fibres and power & interlock and Controller Area Network (CAN) bus channels (represented as light-blue channels in Figure 4.5). This structure requires two versions of

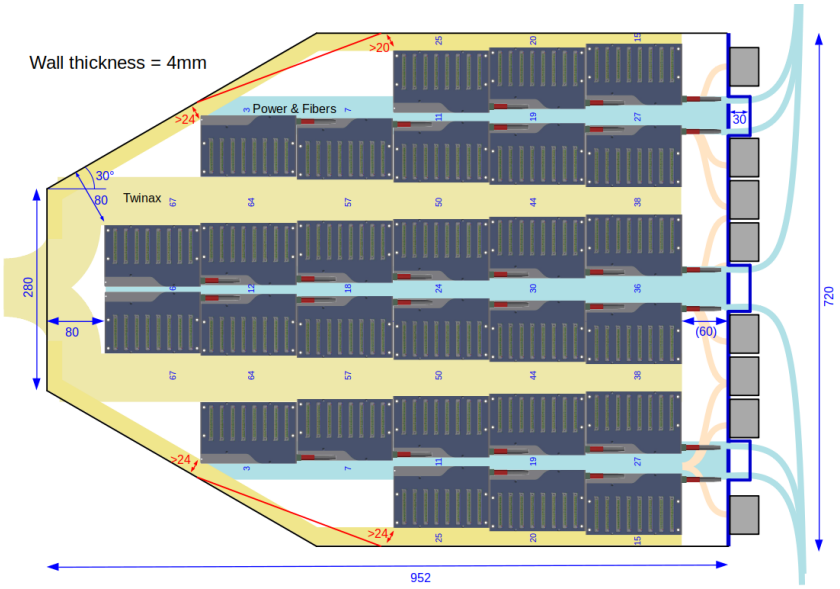

Figure 4.5: Computer generated drawing of an open Optopanel with its 28 Optoboxes. The yellow shaded area hosts the electrical link cables (Twinax) and the blue area the power, fibre and CAN bus cables.

Optoboxes, one “normal” type and one “mirrored”. As a consequence, there are mirrored versions of the Powerboard, of the Connectorboard and of the Termination board designs. Given the complexity of the Optoboard design, it was decided to have only one “normal” version of the Optoboard, with opposite orientations inside the Optoboxes with respect to the coordinate system.

4.4 Power Distribution and Monitoring

The power distribution system of the Optoboxes consists of a two-stage converter system with bPOL12V and bPOL2V5, described in Section 4.4.1. The main supply is provided at 9 V and 3 A. The bPOL12V converters are grouped in sets of five and mounted on the Powerboard (depicted in Figure 4.6). The power from these converters

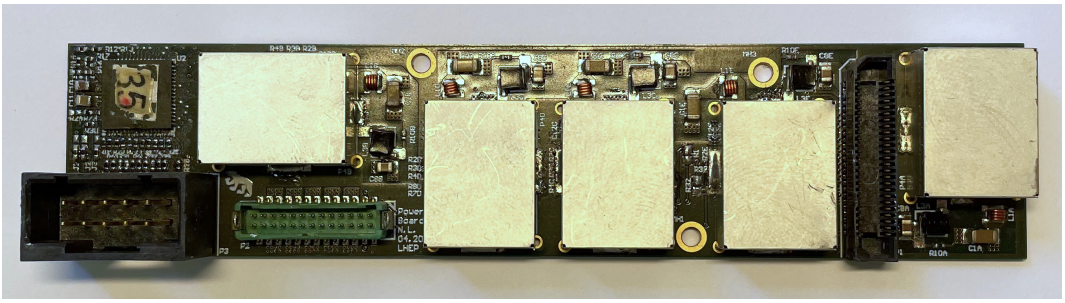

Figure 4.6: Photograph of the Powerboard. Visible are the five shields of the bPOL12V with their coils and ASICs underneath it. The green connector is for the power input coming from the detector services, while the black vertical connector mates with the Connectorboard of the Optobox. The MOPS can be seen in the upper left corner with its connector just below.

is distributed to up to eight Optoboards via the Connectorboard, shown in Figure 4.7,

which is part of the Optobox housing and connects through a slit in the Powerbox to the Powerboard from the top. The Connectorboard features a configurable

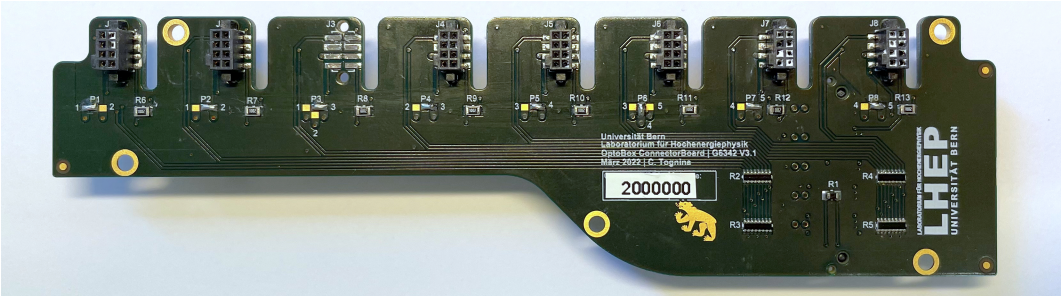

Figure 4.7: Photograph of the Connectorboard. On the upper end up to eight Optoboards can be plugged in vertically. The lower wide area of the PCB is used for monitoring circuits. The connector to the Powerboard is underneath the wider part.

arrangement of power channels, depending on the number of Optoboards that are plugged in. The configuration can be chosen by setting solder jumpers; each of the outermost bPOL12Vs can be connected to three of the outermost Optoboards, while the three middle bPOL12Vs can be connected to four different Optoboards. In summary the Powerboard hosts:

- Five bPOL12V converters.
- A Monitor of Pixel System (MOPS) chip (see Section 4.4.2), powered through a 2 V / 0.5 A supply line. Some of the monitoring voltage dividers are on the Connectorboard.
- An Controller Area Network (CAN) bus connector, connected to the Optoboard system-only CAN bus cable (1.2 V differential at 125 kbps).
- A connector to the Connectorboard.
- A power connector, connected to the power cable (which is routed only internally in the Optoboard system).

4.4.1 bPOL DCDC Converter

Buck Point of Load (bPOL) DCDC converters are used to transform voltages in the Optoboard system. The motivation for using DCDC converters comes from the power distribution scheme. A serious limitation to the detector would come from a distribution scheme where the on-detector low voltage electronics (1.2 V or 2.5 V in the case of the Optoboard) are directly powered from backend supplies, tens of metres away. Long cables would lead to a large cable resistivity R_c according to:

$$R_c = \frac{\rho l}{A} \tag{4.1}$$

where ρ is the density of the cable material, l is the length and A the cross section of the cable [185]. According to Ohm's law, a large R_c leads to a high voltage drop $U_{drop} = R_c I$ and a lower voltage U at the components:

$$U = U_{supply} - U_{drop} = U_{supply} - R_c I \tag{4.2}$$

This could be compensated by increasing the cross section of the cables and therefore reducing the resistivity. But a higher cross section leads to a larger mass of the cable, which is not desired: more mass absorbs more likely particles wanted at outer-radius detectors inside ATLAS – it adds to the material budget.

A way of solving this problem is the distribution of power at higher voltage, 10 V to 12 V, with local (on-detector) DCDC converters, regulating down to the voltage required by the front-end electronics. This also decreases the current flowing in the supply cables until the converters, since a higher voltage requires a lower current for the same amount of power. One drawback of this solution is that a DCDC converter, especially its inductor coil, generates electromagnetic noise during operation. This noise can then affect other electronic components inside the detector and lower their performance. Another drawback is that the conversion stage is 80% to 90% efficient, leading to power being dissipated as heat energy, which has to be carried away from the components through cooling. Both these problems are solved by using a metal shield over the bPOL and cooling plates attached to the Optoboards.

In the Optoboard system there are two flavours of the bPOL DCDC converter: five bPOL12Vs on the Powerboard, converting 12 V to 2.5 V, and one bPOL2V5 on each Optoboard itself, converting 2.5 V to 1.2 V. Tab. 4.1 summarises the characteristics.

Regulator	bPOL12V	bPOL2V5
U_{in} [V]	12	2–2.5
U_{out} [V]	2.5	1.2
P_{out}^{max} [W]	10	4
Efficiency	80–85%	85–90%

Table 4.1: Summary of all converters with their ratings taken from [186].

The bPOL is an ASIC fabricated in Complementary Metal-Oxide-Semiconductor (CMOS) technology, which has a high noise immunity and low static power consumption [187] – both vital for the environment at the detector. A buck step-down converter has, when compared to others, the simplest DCDC converter architecture [188]: it consists of an air coil inductor (which constitutes the largest part of the converter), a switching transistor, a diode and a few capacitors (mainly used for filtering). The basic operation of such a converter is briefly explained with the help of Figure 4.8. When the switch is closed, $V_{out} - V_{in}$ is applied across the inductor. This causes the inductor to store energy in its coil and the current linearly increases inside the inductor and flows to the load. Before reaching the maximum current, the switch

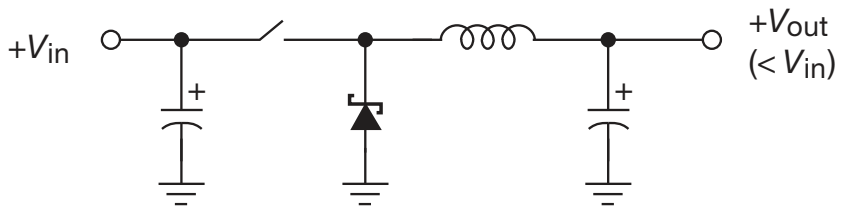

Figure 4.8: Simplified scheme [189] of a buck converter. Shown are the inductor (horizontal), two capacitors and a diode (all vertical), and a switch. The switch, in the case of the bPOL, is a transistor. Figure taken from [189].

gets opened. The current continues to flow in the same direction with the diode now conducting and closing the circuit. The inductor now has the fixed voltage $V_{out} - V_{diode}$ across it, causing its current to decrease linearly. This operation is now repeated many times, in the case of the bPOL with the frequency of 1 MHz to 3 MHz, leading to a sawtooth output current. The frequency of the switching also directly determines (together with the inductor impedance) the desired output voltage. The capacitors filter the current, making it a smooth output current [189]. This is called continuous mode operation.

Every bPOL also has a shield for its air coil, which protects sensible detector systems from the inductor's magnetic field. The air coil is also the bPOL's biggest component. The reason for this is that no iron coil, which would drastically reduce the footprint for the same amount of inductivity, could be used in the strong magnetic field of the ATLAS detector: the iron would be pulled out of the coil due to its ferromagnetic material.

While bPOL comes in different flavours for the output voltages, it also has two configurations for its mounting. The bPOL2V5 is mounted on the bPOL2V5 carrier board which itself is soldered onto the Optoboard, while the bPOL12V is directly mounted onto the Powerboard.

4.4.2 Monitoring – MOPS

The Monitor of Pixel System (MOPS) chip [190, 191], which is mounted on the Powerboard (see Figure 4.6, upper left corner), serves as the monitoring system for the Optoboard system. It actively monitors various parameters, including all bPOL output voltages (5×2.5 V and 8×1.2 V), the output currents of the bPOL2V5 chips (8 signals), the temperature of the Optoboards and Powerboard ($8 + 1$ signals), as well as the temperatures from two bPOL12V chips. The MOPS chip is read out through a CAN bus [192], and up to four MOPS chips can be connected to a single CAN bus. A cable, which integrates two CAN buses, is used to connect multiple Powerboards. Figure 4.9 shows the connection of the CAN bus to the MOPS IDs of the Powerboards. Furthermore, the MOPS chip is supplied with an independent voltage of 1.6 V through a dedicated line, integrated into the same cable.

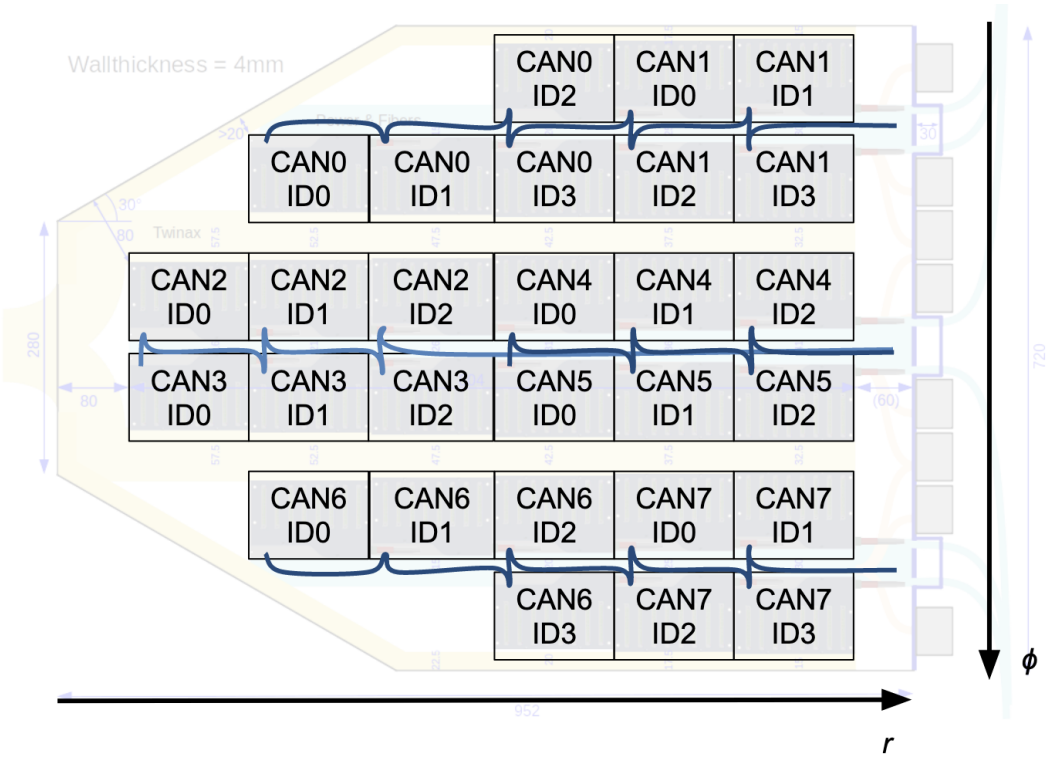

Figure 4.9: One Optopanel with the routing of the CAN bus and the MOPS's ids.

4.5 Optical Fibre Plant

The optical section of the ITk Pixel data transmission chain has been designed to minimise the number of needed readout FELIX cards and reduce the number of unused (*dark*) uplink fibres. Figure 4.10 illustrates the conceptual layout of the optical section, which includes the following components:

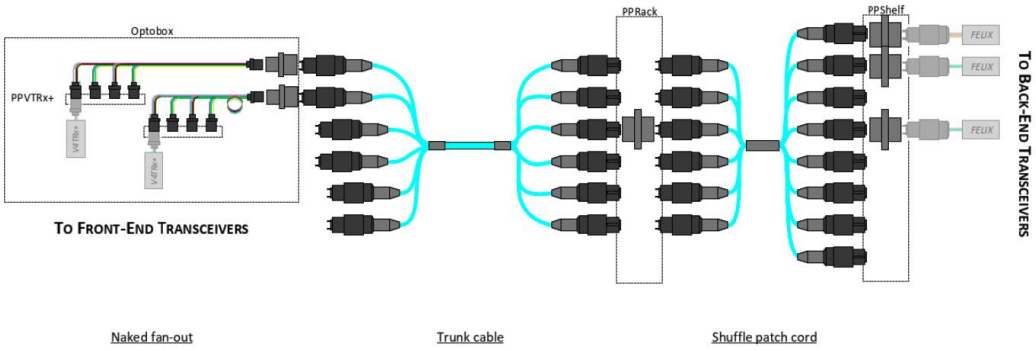

Figure 4.10: Scheme of the ITk Pixel Detector fibre cable plant. The trunk cable is approximately 90 m long while the naked fan-out is inside the Optobox and the Shuffle patch cord for rearranging up- and downlinks inside the shelf at USA15. Figure taken from [193].

- The VTRx+ module pigtail is composed of five fibres (four uplinks and one downlink), terminated with an MT12 connector. Although the MT12 connector has 12 fibres, only up to five will be utilised depending on the Optoboard.

- An optical fan-out collects the signals from several VTRx+ modules. There are three variants of the optical fan-out, each connecting to a different number of Optoboards (either four or eight) and accommodating a different number of uplink and downlink fibres. On the Optoboard side, the fan-out connectors consist of MT12 ferrules, and the multiple branches (ranging from four to eight) are arranged with a 1.5 cm stagger, matching the pitch between Optoboards within the Optobox. At the other end, the fan-out is terminated with an MT24 connector, which can support up to 24 active fibres (16 uplinks and 8 downlinks). Each Optobox typically contains one or two optical fan-outs.

- One or two MT-Multi-fiber Termination Push-on (MTP) adapters[1], one per optical fan-out, on the wall of each Optobox.

- Optical trunk cables, connecting the Optoboard system to the USA15 electronics cavern. These cables feature six MPO24 connectors at each end, allowing them to connect with up to six Optoboxes. The length of the branches on both sides is approximately 2.5 m. This length ensures proper connections to the Optoboxes, accommodating some take-up length, as well as connections to the shuffle boxes.

- Shuffle patch cords, required because of the different number and arrangement of uplinks and downlinks in the MPO24 connectors of the trunk cables and of the FELIX readout cards. The trunk cables have up to 16 uplinks and 8 downlinks per MPO24 connector, while the MPO24 connectors at the FELIX side can accommodate 12 uplinks and 12 downlinks. As a result, shuffle patch cords enable the re-routing of the uplink and downlink fibres. There are four different types of shuffle patch cords available.

4.6 Twinax Cables and Termination Board

The electrical signals of the ITk Pixel Detector are transmitted through twinaxial (Twinax) cables that share similarities with a coaxial cable. However, Twinax cables consist of two insulated copper wire conductors at the centre instead of a single conductor. The two wires are needed because the transmitted signal is *differential*. This means that there is a positive (P) and a negative (N) signal of which the difference is taken at the receiver for better signal quality and higher signal to noise ratio. These two central conductors, of size AWG34[2] , are surrounded by a shielding jacket, which is further enclosed by an outer conductor, typically made of another wire, foil, or a combination of both. To provide additional protection against environmental factors, the entire assembly is then covered with an insulating and protective outer layer. This construction offers several

[1] The MT12 connector refers to a specific type of MTP configuration. While MTP connectors such as MT24 have 2×12 fibres in a row, MT12 has 2×6 fibres.

[2] For a copper wire this is roughly a diameter of 0.16 mm.

advantages such as reduced cable losses, defence against ground loops and capacitive fields and protection against low-frequency magnetic noise that may pass through the shield. Figure 4.11 shows the frequency dependent attenuation of the twinax cables. For the example of a 640 MHz clock signal, the loss is about 11 dB.

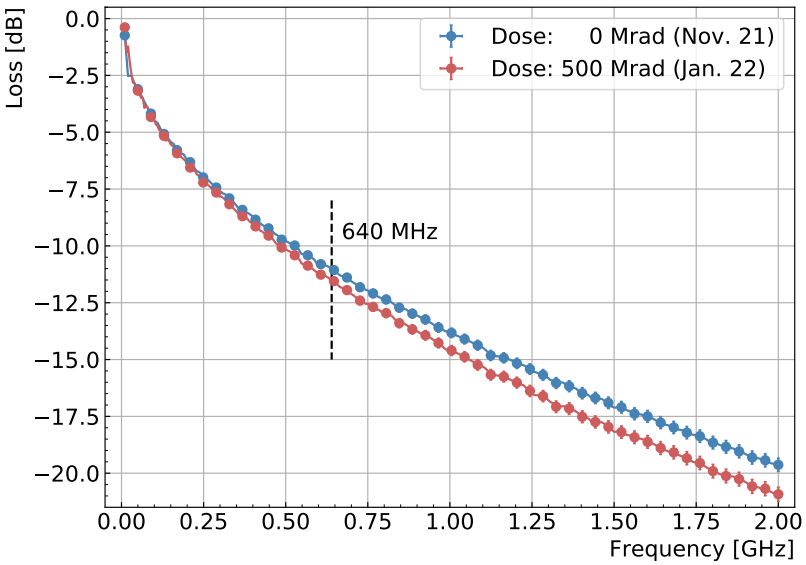

Figure 4.11: Signal attenuation in a 6 m Twinax cable before and after irradiation of 500 Mrad. See Section 5.1.1 for more on the effect of radiation. Figure and results provided by Lea Halser.

Each Optoboard establishes communication with the modules through a Termination Board (TB), where the incoming and outcoming differential cables are soldered. There are seven different variants of TBs. The existence of multiple TB variants is driven by the number of uplinks and downlinks at the detector level, while also aiming to minimise the number of optical uplinks and FELIX cards.

At the time of writing, two vendors have been identified to produce the Twinax cables. One notable difference between the two designs is the grounding implementation. In one design the ground is transmitted through a separate ground wire that runs parallel to the P and N wires inside the cable. In the other design, grounding relies on the shielding around the differential wires. Consequently, two sets of Termination boards are being developed, one at SLAC and another one at CERN.

The seven TB variants, spanning both design styles, can be categorised into three main groups: L-shaped, Slim, and Super-slim TBs. The L-shaped TB can accommodate up to 24 uplink signals and eight downlink signals. The Slim TB has 20 soldering pads and can connect up to 12 uplinks and 8 downlinks, while the Super-slim TB has 12 soldering pads and can connect up to 6 uplinks and 6 downlinks.

As mentioned in Section 4.3, there will also be mirrored types of TB. For the L-shaped TB, a sketch of the mirrored versions of Optoboxes and TBs is presented in Figure 4.12.

For each type, short and long L-shaped TBs will be alternated, to allow for optimised

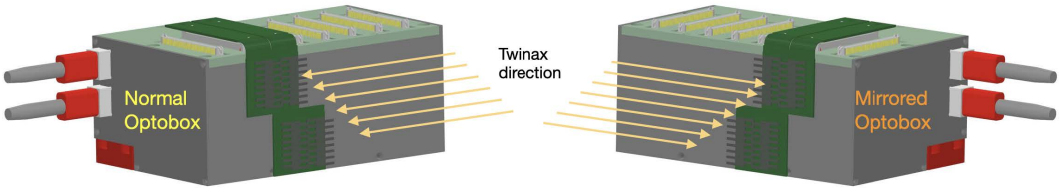

Figure 4.12: CAD drawing of the arrangement of the L-shaped TBs on the side walls of the Optoboxes for the “normal” Optobox (left) and the “mirrored” Optobox (right). The Twinax cables, represented as yellow arrows, come from the common Twinax channel inside the Optopanel. For each type, short and long L-shaped TBs will be alternated, to allow for optimised Twinax cable space management.

Twinax cable space management. In the case of the Slim TB, the addition of buried ground vias (making the solder pads available from both sides of the PCB) allows the same TB to be used for both normal and mirrored Optoboxes.

4.7 Assignment and Layout of Optoboards

This section presents the final mapping between all FEs and the Optoboards which has major implications on space handling, signal quality, power and material usage. The mapping sets the distribution of the number of lpGBTs on Optoboards, the number of Optoboards in Optoboxes, the distribution of Optoboxes in the Optopanels, the length and number of cables in the different channels of the Optopanels.

Before distributing the Optoboards and Optoboxes, one needs to understand how many Optoboards are needed for reading out the ITk Pixel Detector. The following constraints are given from the proposed detector and FE design (see Section 2.4.1) and the design of the Optoboard system (see Section 4.2):

- SP-chain types. These are the identifiers for the different subsystems:

  Inner System (IS): Triplets (T) and Quads (Q) are separately powered, L0-T or L1-Q for the barrel layers and EC0-T and EC1-Q for the rings.

  Outer Barrel (OB): for the FL there are short and long chains, for the IL there are half-rings powered from the different caverns US15 and USA15.

  End Caps (EC): each half ring has a SP-chain.

- Amount of modules per SP chain. These numbers can be extracted from Table 2.2 and 2.3.

- Amount of links per module. These values determine the number of up- and downlinks and ultimately the number of cables.

- Amount of uplinks (downlinks) an Optoboard can maximally handle due to its PCB

design e.g. mounted chips: 6 (6) per lpGBT, 6 (2) per GBCR, therefore 24 (8) per Optoboard.

- Furthermore a single downlink can provide control and trigger for up to four FEs.

The mapping has a set of defined constraints or rules for all subsystems:

1. One SP chain is only connected to one single Optoboard, meaning all arriving and departing eLinks from an SP chain are not split over multiple Optoboards. This is the most limiting factor for reducing the number of Optoboards but is motivated by the interlock system and operation, as the handling is facilitated in case one Optoboard fails.
2. One Optobox is connected to a single type of subsystem, no mix of IS, OB and EC. The Optoboxes are also attributed to a subsystem-layer, with the following exceptions: IS 1L0+L1 and IS L0+2L1 are collected as IS barrel and OB IL2 and IL3 are grouped together as ID OB IL2&3. For the EC L2 (L4) the Optoboxes are further attributed to rings 1–5 and the other rings 6–11 (1–7 and 8–9).
3. All up- and downlinks from an FE are connected to the same Optoboard.
4. Optoboard, Powerboard, CAN bus, FE module, PP0–4 are all powered from power supplies situated in the same cavern US15 or USA15.
5. Optoboards only share a bPOL12V if connected to the same SP chain.
6. IS and OB staves on both ATLAS A/C sides are powered by the same US15/USA15 cavern.
7. Distribute Optoboxes in Optopanels for shortest cable length: low-z modules connected to low-r Optoboxes as a best effort.
8. Keep SP chains coming from the same PP1 feedthrough designator together.
9. EC modules distributed symmetrically to ease EC PP0 development.
10. Reduce the number of Optoboard types. To save chips and power, some Optoboard PCBs do not have all ASICs populated. There are two types, Optoboard-a (Ob-a) and Optoboard-b (Ob-b), and depending on the subsystem layer the PCBs either have four or two lpGBTs + GBCRs populated.

The following Tables 4.2, 4.3 and 4.4 present a summary of the numbers for the preparation of the distribution of Optoboards. In the tables the ITk Pixel Detector subsystems are marked with a background colour in different saturations, these will be of relevance later. The given design values are labelled in a rose background. Yellow background is used for hard coded numbers emerging from specific design choices of the subsystems. The columns of Tables 4.2, 4.3 and 4.4 are calculated[3] as

[3]The symbol $\lceil x \rceil$ ($\lfloor x \rfloor$) means that x is rounded up (down) to the next integer.

following:

$$\text{FEs/SP} = \text{Modules/SP chain} \times \begin{cases} 1, & \text{if triplet} \\ 4, & \text{otherwise} \end{cases}$$

$$\text{Upl./FE} = \text{Upl./SP chain} \times \begin{cases} 1, & \text{if triplet} \\ \frac{1}{4}, & \text{otherwise} \end{cases}$$

$$\text{Upl./SP} = \text{Modules/SP chain} \times \text{Upl./Module}$$

$$\text{Downl./SP} = \text{Modules/SP chain} \times \text{Downl./Module}$$

$$\text{Cables/SP} = \text{Upl./SP} + \text{Downl./SP}$$

$$\text{lpGBTs/SP} = \left\lceil \frac{\text{Upl./SP}}{\text{Upl./lpGBT}} \right\rceil$$

$$\text{Optoboards/SP} = \max\left(\left\lceil \frac{\text{Modules/SP}}{\lceil \text{Upl./lpGBT} \times \frac{\text{lpGBT/Optoboard}}{\text{Upl./Module}} \rceil} \right\rceil, \left\lceil \frac{\text{Modules/SP}}{\lceil \frac{\text{Downl./Optoboard}}{\text{Downl./Module}} \rceil} \right\rceil \right)$$

$$\text{bPOL12V/Optoboard} = (\text{Optoboards/SP})^{-1}$$

	SP Chain types	Modules/ SP chain	Links/Module Upl.	Links/Module Downl.	FEs/ SP	Upl./ FE	Upl./ SP	Downl./ SP	Cables/ SP	lpGBTs/ SP	Optoboards/ SP	bPOL12V/ Optoboard
IS 1L0+L1 (IS Barrel)	L0-T	12	4	1/3	12	4	48	4	52	8	2	0.5
	L1-Q	6	2	1	24	0.5	12	6	18	2	1	1
IS L0+2L1 (IS Barrel)	L0-T	12	4	1/3	12	4	48	4	52	8	2	0.5
	L1-Q	6	2	1	24	0.5	12	6	18	2	1	1
	L1-Q	6	2	1	24	0.5	12	6	18	2	1	1
IS Coupled Ring	EC0-T	9	3	1/3	9	3	27	3	30	5	2	0.5
	EC1-Q	10	4	1	40	1	40	10	50	8	2	0.5
IS Intermediate Ring	EC0-T	15	2	1/3	15	2	30	5	35	5	2	0.5
IS Quad Ring	EC1-Q	10	4	1	40	1	40	10	50	8	2	0.5

Table 4.2: Assignment numbers for IS. Yellow background numbers are hardcoded and not calculated.

	SP Chain types	Modules/ SP chain	Links/Module Upl.	Links/Module Downl.	FEs/ SP	Upl./ FE	Upl./ SP	Downl./ SP	Cables/ SP	lpGBTs/ SP	Optoboards/ SP	bPOL12V/ Optoboard
OB Flat Layer 2	short chain	6	2	1	24	0.5	12	6	18	2	1	1
	long chain	12	2	1	48	0.5	24	12	36	4	2	0.5
OB Flat Layer 3	short chain	6	1	1	24	0.25	6	6	12	1	1	1
	long chain	12	1	1	48	0.25	12	12	24	2	2	0.5
OB Flat Layer 4	short chain	6	1	1	24	0.25	6	6	12	1	1	1
	long chain	12	1	1	48	0.25	12	12	24	2	2	0.5
OB Inclined Layer 2	half ring US	8	2	1	32	0.5	16	8	24	3	1	1
	half ring USA	8	2	1	32	0.5	16	8	24	3	1	1
OB Inclined Layer 3	half ring US	11	1	1	44	0.25	11	11	22	2	2	0.5
	half ring USA	11	1	1	44	0.25	11	11	22	2	2	0.5
OB Inclined Layer 4	half ring US	14	1	1	56	0.25	14	14	28	3	2	0.5
	half ring USA	14	1	1	56	0.25	14	14	28	3	2	0.5

Table 4.3: Assignment numbers for OB.

	SP Chain types	Modules/ SP chain	Links/Module Upl.	Links/Module Downl.	FEs/ SP	Upl./ FE	Upl./ SP	Downl./ SP	Cables/ SP	lpGBTs/ SP	Optoboards/ SP	bPOL12V/ Optoboard
EC Layer 2 (rings 6-11)	half ring	8	4	1	32	1	32	8	40	6	2	0.5
EC Layer 2 (rings 1-5)	half ring	8	2	1	32	0.5	16	8	24	3	1	1
EC Layer 3	half ring	11	2	1	44	0.5	22	11	33	4	2	0.5
EC Layer 4 (rings 1-7)	half ring	13	1	1	52	0.25	13	13	26	3	2	0.5
EC Layer 4 (rings 8-9)	half ring	13	2	1	52	0.5	26	13	39	5	2	0.5

Table 4.4: Assignment numbers for EC.

From the number of Optoboards/SP chain two different types of Optoboard flavours, Ob-

a and Ob-b, are defined. Both types can either have four or two lpGBTs + GBCRs but flavour type Ob-b only gets used in the case of two Optoboards/SP chain. The reason for this is to limit the number of differently populated Optoboards and the number of chips used. As an example, it would not make sense to use an Optoboard with four lpGBTs and GBCRs for an OB IL3 half ring. Only 11 uplinks are needed and two lpGBTs cover 12 uplinks, two additional lpGBTs would just add more material, more power and more cost to the overall detector budget. Similarly, the OB IL2 only has Ob-a flavour Optoboards with four lpGBTs + GBCRs to handle the 16 up- and 8 downlinks of the SP chain. There is only one Optoboard needed per SP chain and consequently also only one flavour.

Tables 4.5, 4.6 and 4.7 summarise the two types – Ob-a and Ob-b – needed for the mapping. The columns up to the distribution per quadrant are calculated as following:

$$\text{Ob-a Downl.} = \begin{cases} \left\lceil \frac{\text{Downl./SP}}{2} \right\rceil, & \text{if Optoboards/SP = 2} \\ \text{Downl./SP}, & \text{if Optoboards/SP = 1} \end{cases}$$

$$\text{Ob-a Upl.} = \frac{\text{Ob-a Downl.} \times \text{Upl./SP}}{\text{Downl./SP}}$$

$$\text{Ob-b Downl.} = \begin{cases} \min\left(\left\lceil \frac{\text{Downl./SP}}{2} \right\rceil, \text{Downl./SP} - \text{Ob-a Downl.}\right), & \text{if Optoboards/SP = 2} \\ 0, & \text{if Optoboards/SP = 1} \end{cases}$$

$$\text{Ob-b Upl.} = \frac{\text{Ob-b Downl.} \times \text{Upl./SP}}{\text{Downl./SP}}$$

$$\text{lpGBTs/Optoboard} = \left\lceil \max\left(\frac{\text{Ob-a Upl.}}{\text{Upl./lpGBT}}, \frac{\text{Ob-a Downl.}}{\text{Downl./Optoboard}} \right) \right\rceil$$

$$\text{Ob/side} = \text{Optoboards/SP} \times \text{SPs/side}$$

To understand the numbers in the quadrant separation, columns SP chains and Optoboards per quadrant, one needs to understand how the cables from the FEs are exiting the sealed ITk. Figure 4.13 shows a rendering of the ITk, vertically cut in half, with the Data Feedthroughs (DFT) at the PP1 location of the A-side and the location of the Optopanels. There are four DFTs per side (s=A/C) of ATLAS: DFT s1-8, DFT s2-3, DFT s4-5 and DFT s6-7. In principle they are further split-up by subsystems but for the needs here they are referred to as one feedthrough. The background colours are again important for the detailed arrangement of the Optoboxes inside the Optopanels (see Section 4.7.2).

To distribute the Optoboards across the quadrants, the following formulae are used:

$$\text{SP chains/quadrant} = \begin{cases} \left\lceil \frac{\text{SPs/side}}{4} \right\rceil, & \text{for DFT s1-8, s4-5, s6-7} \\ \text{SPs/side} - \sum_{\text{quadrants}}^{\text{not s2-3}} \text{SP chains/quadrant}, & \text{for DFT s2-3} \end{cases}$$

$$\text{Optoboards/quadrant} = \text{SP chains/quadrant} \times \text{Optoboards/SP}$$

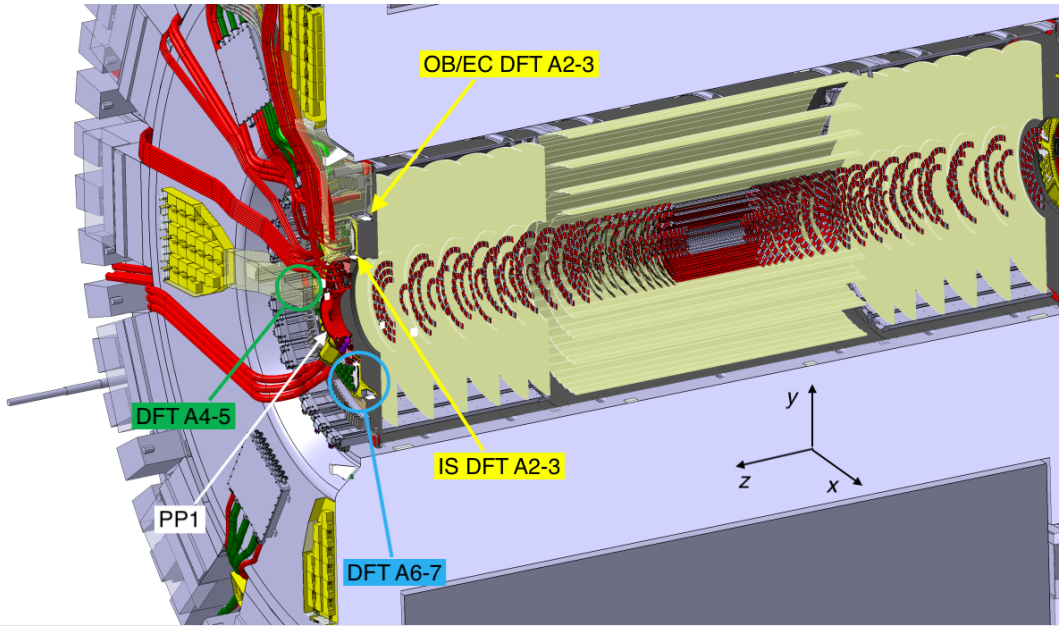

Figure 4.13: Computer generated drawing of a cut-in-half ITk. Visible are the ITk Pixel Detector's individual modules and the ITk Strips (light yellow) surrounding them. Three out of four Optopanels (in yellow) are shown with power lines (in red) for the ITk Pixel Detector coming from high r to PP1. Three DFTs are visible with the DFT A2-3 with more detail on the exact IS and OB/EC feedthrough, the fourth DFT A1-8 is cut away in this rendering. Drawing provided by Martin Janda.

$$\text{Optoboards/side} = \sum_{\text{quadrants}} \text{Optoboards/quadrant}$$

	SP Chain types	Optoboard flavours Ob-a Upl.	Ob-a Dl.	Ob-b Upl.	Ob-b Dl.	lpGBTs/ Optoboard Ob-a	lpGBTs/ Optoboard Ob-b	SPs/ side	Ob/ side	SP chains/ quadrant DFT s2-3	DFT s6-7	DFT s1-8	DFT s4-5	Optoboards/ quadrant DFT s2-3	DFT s6-7	DFT s1-8	DFT s4-5	Opto-boards/ side
IS 1L0+L1 (IS Barrel)	L0-T	24	2	24	2	4	4	4	8	1	1	1	1	2	2	2	2	
	L1-Q	12	6			2		4	4	1	1	1	1	1	1	1	1	
IS L0+2L1 (IS Barrel)	L0-T	24	2	24	2	4	4	8	16	2	2	2	2	4	4	4	4	44
	L1-Q	12	6			2		8	8	2	2	2	2	2	2	2	2	
	L1-Q	12	6			2		8	8	2	2	2	2	2	2	2	2	
IS Coupled Ring	EC0-T	18	2	9	1	4	4	30	60	8	6	8	8	16	12	16	16	120
	EC1-Q	20	5	20	5	4	4	30	60	8	6	8	8	16	12	16	16	
IS Intermediate Ring	EC0-T	18	3	12	2	4	4	12	24	4	0	4	4	8	0	8	8	24
IS Quad Ring	EC1-Q	20	5	20	5	4	4	16	32	4	4	4	4	8	8	8	8	32

Table 4.5: IS numbers for the distribution of the Optoboard flavours and quadrant distribution. Yellow background numbers are hardcoded due to detector design and not calculated.

The distribution of the calculated number of Optoboards inside the Optoboxes and Optopanels is listed Tables 4.8, 4.9 and 4.10. The Optoboards per Optobox distribution is completely hardcoded for the IS and OB, while for the EC the Optoboards are only in DFT s1-8 and DFT s4-5 due to the design of the EC, their values are calculated as following:

$$\text{Optoboards/1.Optobox} = \begin{cases} \min\left(\text{Optoboards/quadrant}, 5\right), & \text{Optoboards/SP} = 1 \\ \min\left(\text{Optoboards/quadrant}, 8\right), & \text{Optoboards/SP} = 2 \end{cases}$$

	SP Chain types	Optoboard flavours Ob-a Upl.	Ob-a Dl.	Ob-b Upl.	Ob-b Dl.	lpGBTs/ Optoboard Ob-a	Ob-b	SPs/ side	Ob/ side	SP chains/ quadrant DFT s2-3	DFT s6-7	DFT s1-8	DFT s4-5	Optoboards/ quadrant DFT s2-3	DFT s6-7	DFT s1-8	DFT s4-5	Opto-boards/ side
OB Flat Layer 2	short chain	12	6			2		16	16	8	8	0	0	8	8	0	0	48
	long chain	12	6	12	6	2	2	16	32	8	8	0	0	16	16	0	0	
OB Flat Layer 3	short chain	6	6			2		22	22	5	5	6	6	5	5	6	6	66
	long chain	6	6	6	6	2	2	22	44	5	5	6	6	10	10	12	12	
OB Flat Layer 4	short chain	6	6			2		28	28	7	7	7	7	7	7	7	7	84
	long chain	6	6	6	6	2	2	28	56	7	7	7	7	14	14	14	14	
OB Inclined Layer 2	half ring US	16	8			4		12	12	6	6	0	0	6	6	0	0	24
	half ring USA	16	8			4		12	12	6	6	0	0	6	6	0	0	
OB Inclined Layer 3	half ring US	6	6	5	5	2	2	16	32	8	8	0	0	16	16	0	0	64
	half ring USA	6	6	5	5	2	2	16	32	8	8	0	0	16	16	0	0	
OB Inclined Layer 4	half ring US	8	8	6	6	2	2	18	36	18	0	0	0	36	0	0	0	72
	half ring USA	8	8	6	6	2	2	18	36	0	18	0	0	0	36	0	0	

Table 4.6: OB numbers for the distribution of the Optoboard flavours and quadrant distribution. Yellow background numbers are hardcoded due to detector design and not calculated.

	SP Chain types	Optoboard flavours Ob-a Upl.	Ob-a Dl.	Ob-b Upl.	Ob-b Dl.	lpGBTs/ Optoboard Ob-a	Ob-b	SPs/ side	Ob/ side	SP chains/ quadrant DFT s2-3	DFT s6-7	DFT s1-8	DFT s4-5	Optoboards/ quadrant DFT s2-3	DFT s6-7	DFT s1-8	DFT s4-5	Opto-boards/ side
EC Layer 2 (rings 6-11)	half ring	16	4	16	4	4	4	24	48	0	0	12	12	0	0	24	24	48
EC Layer 2 (rings 1-5)	half ring	16	8			4		20	20	0	0	10	10	0	0	10	10	20
EC Layer 3	half ring	12	6	10	5	4	4	32	64	0	0	16	16	0	0	32	32	64
EC Layer 4 (rings 1-7)	half ring	8	8	5	5	2	2	28	56	0	0	14	14	0	0	28	28	56
EC Layer 4 (rings 8-9)	half ring	16	8	10	5	4	4	8	16	0	0	4	4	0	0	8	8	16

Table 4.7: EC numbers for the distribution of the Optoboard flavours and quadrant distribution. Yellow background numbers are hardcoded due to detector design and not calculated.

$$\text{Optoboards/2.Optobox} = \begin{cases} \min(\text{Optoboards/quadrant}, \text{Optoboards/1.Optobox}, 5), & \text{Optoboards/SP} = 1 \\ \min(\text{Optoboards/quadrant}, \text{Optoboards/1.Optobox}, 8), & \text{Optoboards/SP} = 2 \end{cases}$$

$$\text{Optoboards/n.Optobox} = \begin{cases} \min(\text{Optoboards/quadrant}, \text{Optoboards/(n-1).Optobox}, 5), & \text{Optoboards/SP} = 1 \\ \min(\text{Optoboards/quadrant}, \text{Optoboards/(n-1).Optobox}, 8), & \text{Optoboards/SP} = 2 \end{cases}$$

The second Optoboards/Optobox columns (b) give the sums of Optoboards per Optobox and subsystem layer.

	SP Chain types	Optoboards/Optobox (a) DFT s2-3 1.	2.	3.	4.	5.	6.	DFT s6-7 1.	2.	3.	4.	5.	6.	DFT s1-8 1.	2.	3.	4.	5.	DFT s4-5 1.	2.	3.	4.	5.	Optoboards/Optobox (b) DFT s2-3 1.	2.	3.	4.	5.	6.	DFT s6-7 1.	2.	3.	4.	5.	6.	DFT s1-8 1.	2.	3.	4.	5.	DFT s4-5 1.	2.	3.	4.	5.
IS 1L0+L1 (IS Barrel)	L0-T	2	0	0	0	0	0	2	0	0	0	0	0	2	0	0	0	0	2	0	0	0	0																						
	L1-Q	1	0	0	0	0	0	1	0	0	0	0	0	1	0	0	0	0	1	0	0	0	0																						
IS L0+2L1 (IS Barrel)	L0-T	2	2	0	0	0	0	2	2	0	0	0	0	2	2	0	0	0	2	2	0	0	0	7	4	0	0	0	0	7	4	0	0	0	0	7	4	0	0	0	7	4	0	0	0
	L1-Q	1	1	0	0	0	0	1	1	0	0	0	0	1	1	0	0	0	1	1	0	0	0																						
	L1-Q	1	1	0	0	0	0	1	1	0	0	0	0	1	1	0	0	0	1	1	0	0	0																						
IS Coupled Ring	EC0-T	4	4	4	4	0	0	4	4	4	4	0	0	4	4	4	4	0	4	4	4	4	0	8	8	8	8	0	0	8	8	8	0	0	0	8	8	8	8	0	8	8	8	8	0
	EC1-Q	4	4	4	4	0	0	4	4	4	4	0	0	4	4	4	4	0	4	4	4	4	0																						
IS Intermediate Ring	EC0-T	8	0	0	0	0	0	0	0	0	0	0	0	8	0	0	0	0	8	0	0	0	0	8	0	0	0	0	0	0	0	0	0	0	0	8	0	0	0	0	8	0	0	0	0
IS Quad Ring	EC1-Q	8	0	0	0	0	0	8	0	0	0	0	0	8	0	0	0	0	8	0	0	0	0	8	0	0	0	0	0	8	0	0	0	0	0	8	0	0	0	0	8	0	0	0	0

Table 4.8: Optoboard distribution per Optobox and DFT for IS. These values are completely hardcoded due to the detector design. The numbers 1.–6. in the 3rd header row refer to the Optobox number.

Up to here it was defined how many uplinks and downlinks each Optoboard must have to read the specific detector part, how many Optoboards will be installed in each Optobox and how many Optoboxes will be needed for each subdetector in each Optopanel. The next step is to define where each of these Optoboxes will be positioned inside the Optopanel.

To distribute the Optoboxes inside the Optopanels one needs to know how many cables

	SP Chain types	Optoboards/Optobox (a)																						Optoboards/Optobox (b)																	
		DFT s2-3						DFT s6-7						DFT s1-8					DFT s4-5					DFT s2-3						DFT s6-7						DFT s1-8					DFT s4-5				
		1.	2.	3.	4.	5.	6.	1.	2.	3.	4.	5.	6.	1.	2.	3.	4.	5.	1.	2.	3.	4.	5.	1.	2.	3.	4.	5.	6.	1.	2.	3.	4.	5.	6.	1.	2.	3.	4.	5.	1.	2.	3.	4.	5.
OB Flat Layer 2	short chain	2	2	2	2	0	0	2	2	2	2	2	0	0	0	0	0	0	0	0	0	0	0	0	6	6	6	0	0	6	6	6	6	0	0	0	0	0	0	0	0	0	0	0	0
	long chain	4	4	4	4	0	0	4	4	4	4	4	0	0	0	0	0	0	0	0	0	0	0	0																					
OB Flat Layer 3	short chain	2	3	0	0	0	0	2	3	0	0	0	0	2	2	2	0	0	2	2	2	2	0	0	8	7	0	0	0	0	8	7	0	0	0	0	6	6	6	0	0	6	6	6	0	0
	long chain	6	4	0	0	0	0	6	4	0	0	0	0	4	4	4	0	0	4	4	4	4	0	0																					
OB Flat Layer 4	short chain	2	3	2	0	0	0	2	3	2	0	0	0	2	3	2	0	0	2	3	2	2	0	0	8	7	6	0	0	0	8	7	6	0	0	0	8	7	6	0	0	8	7	6	0	0
	long chain	6	4	4	0	0	0	6	4	4	0	0	0	6	4	4	0	0	6	4	4	4	0	0																					
OB Inclined Layer 2	half ring US	2	2	2	2	0	0	2	2	0	0	0	0	0	0	0	0	0	0	0	0	0	0	0	8	8	8	8	6	6	6	6	8	8	8	8	0	0	0	0	0	0	0	0	0	0
	half ring USA	0	0	0	0	2	2	0	0	2	2	2	2	0	0	0	0	0	0	0	0	0	0	0																					
OB Inclined Layer 3	half ring US	6	6	6	6	0	0	4	4	0	0	0	0	0	0	0	0	0	0	0	0	0	0	0																					
	half ring USA	0	0	0	0	4	4	0	0	6	6	6	6	0	0	0	0	0	0	0	0	0	0	0																					
OB Inclined Layer 4	half ring US	8	8	4	8	8	0	0	0	0	0	0	0	0	0	0	0	0	0	0	0	0	0	0	8	8	4	8	8	0	8	8	4	8	8	0	0	0	0	0	0	0	0	0	0	0
	half ring USA	0	0	0	0	0	0	8	8	4	8	8	0	0	0	0	0	0	0	0	0	0	0	0																					

Table 4.9: Optoboard distribution per Optobox and DFT for OB. These values are completely hardcoded due to the detector design. The numbers 1.–6. in the 3rd header row refer to the Optobox number.

	SP Chain types	Optoboards/Optobox (a)																						Optoboards/Optobox (b)																	
		DFT s2-3						DFT s6-7						DFT s1-8					DFT s4-5					DFT s2-3						DFT s6-7						DFT s1-8					DFT s4-5				
		1.	2.	3.	4.	5.	6.	1.	2.	3.	4.	5.	6.	1.	2.	3.	4.	5.	1.	2.	3.	4.	5.	1.	2.	3.	4.	5.	6.	1.	2.	3.	4.	5.	6.	1.	2.	3.	4.	5.	1.	2.	3.	4.	5.
EC Layer 2 (rings 6-11)	half ring	0	0	0	0	0	0	0	0	0	0	0	0	8	8	8	0	0	8	8	8	0	0	0	0	0	0	0	0	0	0	0	0	0	0	8	8	8	0	0	8	8	8	0	0
EC Layer 2 (rings 1-5)	half ring	0	0	0	0	0	0	0	0	0	0	0	0	5	5	0	0	0	5	5	0	0	0	0	0	0	0	0	0	0	0	0	0	0	0	5	5	0	0	0	5	5	0	0	0
EC Layer 3	half ring	0	0	0	0	0	0	0	0	0	0	0	0	8	8	8	8	0	8	8	8	8	0	0	0	0	0	0	0	0	0	0	0	0	0	8	8	8	8	0	8	8	8	8	0
EC Layer 4 (rings 1-7)	half ring	0	0	0	0	0	0	0	0	0	0	0	0	8	8	8	4	0	8	8	8	4	0	0	0	0	0	0	0	0	0	0	0	0	0	8	8	8	4	0	8	8	8	4	0
EC Layer 4 (rings 8-9)	half ring	0	0	0	0	0	0	0	0	0	0	0	0	8	0	0	0	0	8	0	0	0	0	0	0	0	0	0	0	0	0	0	0	0	0	8	0	0	0	0	8	0	0	0	0

Table 4.10: Optoboard distribution per Optobox and DFT for EC. The numbers 1.–6. in the 3rd header row refer to the Optobox number.

are arriving per layer and Optobox. Once the number is known, placing bundles with many cables at minimal radii r reduces overall cable material and cable length. To calculate the number of cables, the following equations were used:

$$\frac{\text{Cables}}{\text{Optobox}} = \frac{\text{Optoboards}}{\text{n.Optobox}} \times \begin{cases} (\text{Ob-a Upl.} + \text{Ob-a Downl.}), & \text{if Optoboards/SP} = 1 \\ (\text{Ob-a Upl.} + \text{Ob-a Downl.} \\ \quad + \text{Ob-b Upl.} + \text{Ob-b Downl.})/2, & \text{if Optoboards/SP} = 2 \end{cases}$$

Tables 4.11, 4.12 and 4.13 show the number of cables per Optobox, per quadrant and the total number per layer.

	SP Chain types	Cables/Optobox																						Cables/ quadrant				Cables total
		DFT s2-3						DFT s6-7						DFT s1-8					DFT s4-5									
		1.	2.	3.	4.	5.	6.	1.	2.	3.	4.	5.	6.	1.	2.	3.	4.	5.	1.	2.	3.	4.	5.	DFT s2-3	DFT s6-7	DFT s1-8	DFT s4-5	
IS 1L0+L1 (IS Barrel)	L0-T																											
	L1-Q																											
IS L0+2L1 (IS Barrel)	L0-T	158	88	0	0	0	0	158	88	0	0	0	0	158	88	0	0	0	158	88	0	0	0	246	246	246	246	984
	L1-Q																											
	L1-Q																											
IS Coupled Ring	EC0-T	160	160	160	160	0	0	160	160	160	0	0	0	160	160	160	160	0	160	160	160	160	0	640	480	640	640	2400
	EC1-Q																											
IS Intermediate Ring	EC0-T	140	0	0	0	0	0	0	0	0	0	0	0	140	0	0	0	0	140	0	0	0	0	140	0	140	140	420
IS Quad Ring	EC1-Q	200	0	0	0	0	0	200	0	0	0	0	0	200	0	0	0	0	200	0	0	0	0	200	200	200	200	800

Table 4.11: Cable distribution per Optobox and DFT for IS. The numbers 1.–6. in the 3rd header column refer to the Optobox number.

	SP Chain types	Cables/Optobox DFT s2-3 1.	2.	3.	4.	5.	6.	DFT s6-7 1.	2.	3.	4.	5.	6.	DFT s1-8 1.	2.	3.	4.	5.	DFT s4-5 1.	2.	3.	4.	5.	Cables/ quadrant DFT s2-3	DFT s6-7	DFT s1-8	DFT s4-5	Cables total
OB Flat Layer 2	short chain	108	108	108	108	0	0	108	108	108	108	0	0	0	0	0	0	0	0	0	0	0	0	432	432	0	0	864
	long chain																											
OB Flat Layer 3	short chain	96	84	0	0	0	0	96	84	0	0	0	0	72	72	72	0	0	72	72	72	0	0	180	180	216	216	792
	long chain																											
OB Flat Layer 4	short chain	96	84	72	0	0	0	96	84	72	0	0	0	96	84	72	0	0	96	84	72	0	0	252	252	252	252	1008
	long chain																											
OB Inclined Layer 2	half ring US	114	114	114	114	92	92	92	92	114	114	114	114	0	0	0	0	0	0	0	0	0	0	640	640	0	0	1280
	half ring USA																											
OB Inclined Layer 3	half ring US																											
	half ring USA																											
OB Inclined Layer 4	half ring US	112	112	56	112	112	0	112	112	56	112	112	0	0	0	0	0	0	0	0	0	0	0	504	504	0	0	1008
	half ring USA																											

Table 4.12: Cable distribution per Optobox and DFT for OB. The numbers 1.–6. in the 3rd header column refer to the Optobox number.

	SP Chain types	Cables/Optobox DFT s2-3 1.	2.	3.	4.	5.	6.	DFT s6-7 1.	2.	3.	4.	5.	6.	DFT s1-8 1.	2.	3.	4.	5.	DFT s4-5 1.	2.	3.	4.	5.	Cables/ quadrant DFT s2-3	DFT s6-7	DFT s1-8	DFT s4-5	Cables total
EC Layer 2 (rings 6-11)	half ring	0	0	0	0	0	0	0	0	0	0	0	0	160	160	160	0	0	160	160	160	0	0	0	0	480	480	960
EC Layer 2 (rings 1-5)	half ring	0	0	0	0	0	0	0	0	0	0	0	0	120	120	0	0	0	120	120	0	0	0	0	0	240	240	480
EC Layer 3	half ring	0	0	0	0	0	0	0	0	0	0	0	0	132	132	132	132	0	132	132	132	132	0	0	0	528	528	1056
EC Layer 4 (rings 1-7)	half ring	0	0	0	0	0	0	0	0	0	0	0	0	104	104	104	52	0	104	104	104	52	0	0	0	364	364	728
EC Layer 4 (rings 8-9)	half ring	0	0	0	0	0	0	0	0	0	0	0	0	156	0	0	0	0	156	0	0	0	0	0	0	156	156	312

Table 4.13: Cable distribution per Optobox and DFT for EC. The numbers 1.–6. in the 3rd header column refer to the Optobox number.

4.7.1 Influence of the Support Structure

To distribute the Optoboards optimally inside the Optopanels, a closer look to the support structure of the barrels and rings is necessary. An example of how to go from the numbers in the tables above to the assignment is given in this section. For a detailed view of all subsystem layers see Appendix B.

As already discussed in Section 2.4.1, all modules are mounted either on barrel staves or rings. Each stave or ring can have multiple SP chains and can be powered from different caverns, US15 and USA15. Figure 4.14 explains the barrel and ring sketch: Each small box represents one mechanical structure that can have multiple SP chains (2 in the OB, 1 in the IS). The quadrants' DFT are assigned with the background colours introduced above. Furthermore, the border colour marks the location US15 or USA15 for the power supplies of the specific structure e.g. from where the SP chains are powered.

The total numbers for one (top) and both (bottom) ATLAS sides can be found in Table 4.14.

	Modules	FEs	Upl.	Downl.	lpGBTs	SPs	Optoboards/ Quadrant DFT s2-3	DFT s6-7	DFT s1-8	DFT s4-5	Optoboards	Optoboxes/ Quadrants DFT s2-3	DFT s6-7	DFT s1-8	DFT s4-5	Optoboxes	Cables/ Quadrant DFT s2-3	DFT s6-7	DFT s1-8	DFT s4-5	Cables
Inner System	1174	2914	3826	778	840	120	59	43	59	59	220	8	6	8	8	30	1226	926	1226	1226	4604
Outer Barrel	2236	8944	2716	2236	764	224	140	140	39	39	358	20	20	6	6	52	2008	2008	468	468	4952
Endcap	1172	4688	2364	1172	704	112	0	0	102	102	204	0	0	14	14	28	0	0	1768	1768	3536
PLR	24	24	96	8	16	2	0	4	0	0	4	0	1	0	0	1	0	104	0	0	104
Total (one side)	4606	16570	9002	4194	2324	458	199	187	200	200	786	28	27	28	28	111	3234	3038	3462	3462	13196
Inner System	2348	5828	7652	1556	1680	240	118	86	118	118	440	16	12	16	16	60	2452	1852	2452	2452	9208
Outer Barrel	4472	17888	5432	4472	1528	448	280	280	78	78	716	40	40	12	12	104	4016	4016	936	936	9904
Outer Endcap	2344	9376	4728	2344	1408	224	0	0	204	204	408	0	0	28	28	56	0	0	3536	3536	7072
Total (both sides)	9164	33092	17812	8372	4616	912	398	366	400	400	1564	56	52	56	56	220	6468	5868	6924	6924	26184
PLR	48	48	192	16	32	4	0	8	0	0	8	0	2	0	0	2	0	208	0	0	208
BCM'					32																
Grand Total	9212	33140	18004	8388	4680	916	398	374	400	400	1572	56	54	56	56	222	6468	6076	6924	6924	26392

Table 4.14: Overview of the total numbers for some of the components in the Optoboard System. Included here as well are the PLR and BCM' (see Section 2.4.1), which each have a reserved Optobox but are still under development.

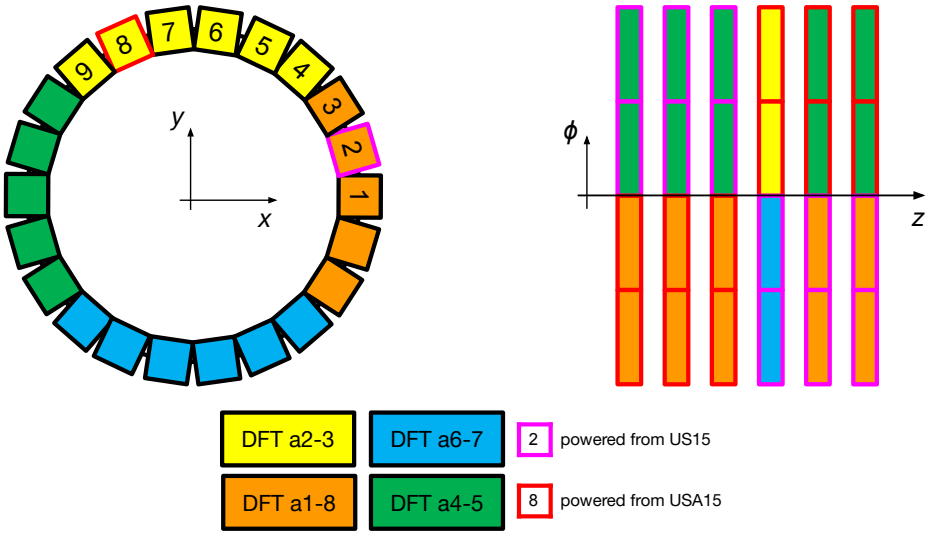

Figure 4.14: An A-side barrel (left) and 6 rings (right, divided in quarters) as sketch explanation. Each square or rectangle represents one mechanical structure (stave or ring), background colour represents through which DFT the cables are routed and the border colour highlights the cavern from where the power is coming from. The number inside the rectangle is going in the ϕ direction and labels the barrel staves.

4.7.2 Arranging Optoboards and Optoboxes inside Optopanels

Based on the numbers in Section 4.7, the mapping of the different Optoboards and Optoboxes inside the Optopanels was done.

To identify Optoboxes via an ID, the following naming scheme, which is similar to the one for the OB, has been created:

CSYS-SubSystemIdentifier-LocalSupportIdentifier-DetectorSide-ItemIdentifier

where:

- CSYS: G for ATLAS global coordinate system
- SubSystemIdentifier: OS for Optoboard system
- LocalSupportIdentifier: L for large[4] Optopanel and ATLAS sector number (DFT 1-8: sector 1 / DFT 2-3: sector 5 / DFT 4-5: sector 9 / DFT 6-7: sector 13)
- DetectorSide: A or C
- ItemIdentifier: CANxy, based on CAN bus numbering. x = CAN bus number, y = Node ID. See Figure 4.9 for an example of these numbers.

[4] At the beginning of the Optoboard system design there were small Optopanels foreseen at high r regions. Due to the 4 MHz to 1 MHz read-out speed decision, all Optoboards fit now into the large Optopanels and the small ones were discarded but the ID local support identifier L has been kept.

An example of an Optobox identifier is G-OS-L1-A-CAN61, which means: large Optopanel sector 1 (DFT A1-8), side A, CAN bus 6, node ID 1.

Since there are 1572 Optoboards with 26392 cables to be assigned to 224 Optoboxes in 8 Optopanels, only one example with two rings (8 and 9) of the EC L4 A-side is presented, for the full mapping per Optopanel see Appendix B.

According to Table 4.7, the EC L4 rings 8 and 9 have four SP chains per quadrant for both sides, so two SP chains per half ring per side. Due the simplicity of the design, we look at each one half ring with the following identifiers:

G-EC-L4_R08_N-A-SP1	G-EC-L4_R08_N-A-SP2
G-EC-L4_R09_N-A-SP1	G-EC-L4_R09_N-A-SP2

The “N” stands for the negative of the y-axis of the ring, meaning the SP chain is powered by USA15 and the data bundles will arrive through the DFT a4-5. Figure 4.15 shows the explanatory sketch for the EC L4 rings.

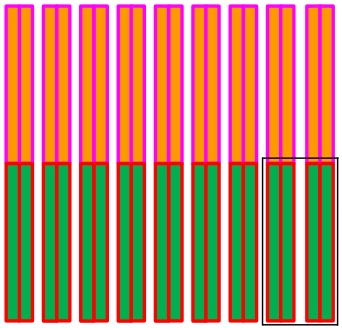

Figure 4.15: Sketch of the EC L4 rings. The black border marks the four SP chains of ring 8 and 9 used in the example.

From Table 4.4 one can observe that there are two Optoboards/SP chain so 8 Optoboards in total for the above four SP chains. Table 4.7 and 4.10 confirm that there are 8 Optoboards in one Optobox for the DFT s4-5. From Table 4.13 one can get that there are 156 cables ending at the Optobox’s Termination boards.

Before these Optoboards can be assigned to an Optobox inside an Optopanel one needs to understand the length of cables inside the Optopanel. An estimation of cable length within the Optopanel is done for all Optoboxes (referenced at the last Termination board of the Optobox) and is given in Table 4.15. For the estimation an initial bend of 150 mm is added to the length of the number of Optoboxes (134 mm per Optobox). The outer cable channels take the diagonal shape of the Optopanel into account and add 600 mm cable length before the start of the first outermost Optobox.

To estimate the total length of the cables, including the feedthrough of the cables at PP1, more parameters, which are summarised in Table 4.16, are needed. By knowing the (r, z) coordinates of fixed points where the cables need to pass through, the total length

1002	868	734			
954	820	686	552	418	
954	820	686	552	418	284
954	820	686	552	418	284
954	820	686	552	418	
1002	868	734			

Table 4.15: Cable lengths inside an Optopanel in millimetre, starting from the entry at low *r*. Every value represents the length of the Twinax cables from the entry point of the Optopanel to the high *r* of each Optobox position inside the Optopanel. They are calculated by taking an estimate of the initial bend of 150 mm inside the Optopanel into account and going through the various cable channels. The rows of Optoboxes then add 134 mm per Optobox to the length estimation.

Type	Position or Length [mm]
PP1 *z* (IS feedthrough)	3218
PP1 *r* (IS feedthrough)	430
PP1 *z* (OB/EC feedthrough)	3150
PP1 *r* (OB/EC feedthrough)	710
OB service support shell *r*	343.7
PP1 ϕ routing	100
Optopanel *r*	1500
Optopanel *z*	3405
Take up (outside Optopanel)	300
length of one Optobox (row length)	134
Optopanel initial bend	150
length to outermost Twinax channel incl. initial bend	600

Table 4.16: Parameters for the calculation of the cable lengths.

can be calculated. Between modules and PP1 and between PP1 and the Optopanels the difference in *r* and *z* is added up to the length estimate.

Since the modules on ring 8 and 9 are at the outermost point of the ITk Pixel Detector (from Table 2.3: $z = 2533$ mm and $z = 2850$ mm) and the feedthrough is less than a metre away ($r = 710$ mm, $z = 3150$ mm), the data bundles are routed to an Optobox at a high *r* value. This will keep the slots for Optoboxes at lower *r* values free for type-1 cables that originate from the very centre of the ITk Pixel Detector (e.g. IS barrel). The proper arrangement will save up to 720 mm of cable.

This optimisation is done for all the Optoboards from the different subsystems, according to the rules stated at the beginning of the section. One of the layout results is shown in Figure 4.16, which shows the whole A side sector 9 Optopanel. All other Optopanels from all other sectors can be found in Appendix C. The above example of the EC L4 rings 8 and 9 Optobox can be found in the third row and first column (highest *r* value) with identifier G-OS-L9-A-CAN42. The layout provides the following information for the reader.

- Each box represents an Optobox

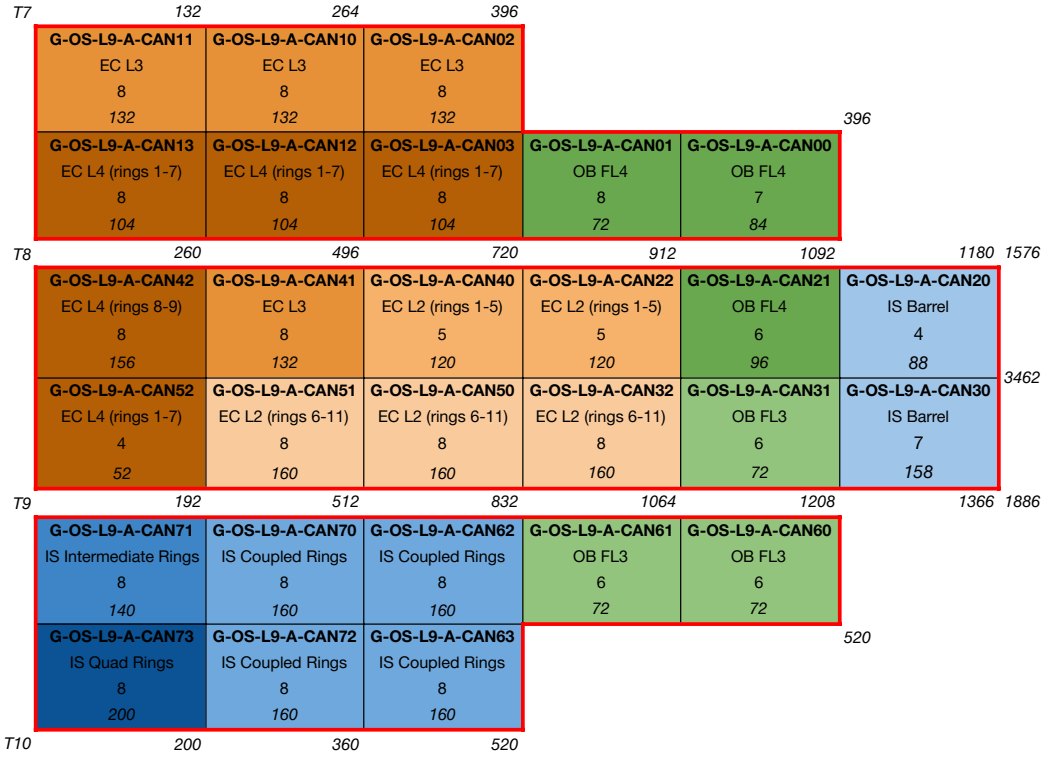

Figure 4.16: Optobox distribution in the A side sector 9 Optopanel (DFT a4-5). Each box represents an Optobox, its background colour is to distinguish the different layers. The Optobox ID is bold and the layer name is given below. The first number in each box is the amount of Optoboards and the italic number the amount of Twinax cables ending at that Optobox. The thicker, coloured border indicates the source of powering cavern – in this sector all the same from USA15.

- The background colour is to distinguish the different layers and follows the same colouring as Tables 4.2–4.13.
- The first row of each box in bold is the identifier.
- The second and third row state the subsystem layer and the number of Optoboards inside the Optobox, respectively.
- The italic numbers represent the number of cables ending at the Optobox. The number of cables is also given outside the boxes and provides information on how many cables are in the respective cable channel (*T7–T10* in the example provided in Figure 4.16) at the beginning of the Optobox.
- The border around the boxes indicates the source of the powering cavern, US15 or USA15.

From the Optopanel arrangement one can calculate the maximum cable length, which is important for cable and data quality tests. Table 4.17 shows the longest cables per Optobox for the ATLAS A side (see Table C.1 in Appendix C.2 for C side) and Table 4.18 a summary of the minimum and maximum cable lengths for all sectors and overall.

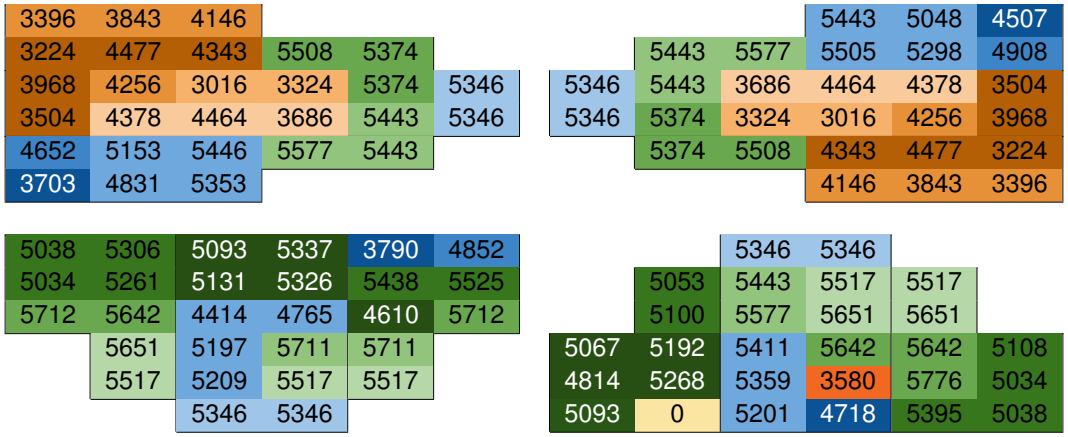

Table 4.17: The lengths of the longest cables in millimetre that are terminated at each Optobox in the Optopanels of the ATLAS A side. The top two Optopanels from the left are sectors 9 (DFT a4-5) and 1 (DFT a1-8). The lower two Optopanels are sectors 5 (DFT a2-3) and 13 (DFT a6-7). The background colours represent the different layers of the corresponding subsystem.

	Minimum length [mm]		Maximum length [mm]	
	A-side	C-side	A-side	C-side
Sector 1	3016	3224	5577	5609
Sector 5	3790	4339	5712	5712
Sector 9	3016	3016	5577	5577
Sector 13	3580	3580	5776	5651
All sectors	3016	3016	5776	5712
Total	3016		5776	

Table 4.18: Minimum and maximum Twinax cable lengths per sector and per side.

Based on the information in Table 4.18, the data transmission has been validated with type-1 cables of 3 m and 6 m.

Chapter 5

Validation of the Optoboard System

While the Optoboard was developed independently with constraints and design rules on paper, the integration into the ITk Pixel Detector data transmission chain needed to be validated with the actual (prototype) detector components. Section 5.1 introduces data transmissions in High Energy Physics (HEP) environments, including how to qualify them. Sections 5.2 to 5.4 introduces the components Low Power Giga Bit Transceiver (lpGBT), Giga-Bit Cable Receiver (GBCR) and Versatile Link Transceiver Plus (VTRx+) of the Optoboard, which are relevant for the data transmission. The validation of the data transmission chain including the production backend cards and prototype modules is described in Section 5.5.

This thesis uses occasionally decimal numbers in binary or hexadecimal notation: the first number always denotes the number of bits, while the letter after the apostrophe `'` defines the format (decimal `d`, binary `b` or hexadecimal `h`) of the value following. As an example, the decimal number `7'd82` is `7'b1010010` and `7'h52`, binary and hexadecimal notation, respectively. Furthermore, chips have a dedicated memory logic to store configuration or measurement values. These are called registers and are of one byte size, which is eight bits. Each register can have multiple sub-divisions labelled by the number of bits. As an example, the `Example[8:0] = 8'b01010010` register consists of two sub-divisions. They are labelled as `Sub1[7:4] = 4'b0101` and `Sub2[3:0] = 4'b0010`. This style of notation follows the Most Significant Bit (MSB) first convention, which is used in this work for all the relevant data transmission components in the ITk.

5.1 Basics of Data Transmissions in HEP

A data transmission involves encoding digital data into discrete binary digits (zeros and ones) and converting them into analogue waveforms through modulation. The signals, like the example in Figure 5.1a, are transmitted over media such as wires and fibres as

an analogue signal with correction techniques implemented for reliability. Transmission protocols define rules for data encapsulation and error control. At the receiving end, demodulation and decoding processes recover the original digital data. Signal processing techniques like filtering and error correction are applied to enhance received signals. Digital signal transmission forms the backbone of the experiment read-out and control.

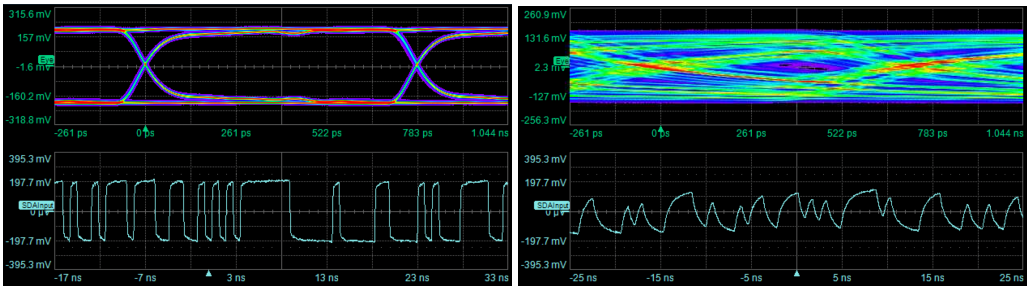

(a) **(b)**

Figure 5.1: Example of a signal with 1.28 Gb/s data rate captured by an oscilloscope by taking the difference of the positive and negative amplitudes of the differential signals. The lower waveforms show a 50 ns time range of the signal voltage while the upper graphs show the eye-diagram of many signal transitions. For reference, the logical signal transmitted between −7 ns and 3 ns is `13'b1001100101010`. (a) shows the output close after the generation of the signal while (b) shows the signal after about 6 m of Twinax. Note that the time of acquisition for (a) and (b) was taken at different positions and the bit sequence does not match.

While transmitters can output a nearly perfect signal, the medium of transportation, in this work copper cables and fibres, always affect this signal through attenuation, electromagnetic interference (EMI) and noise, as the example in Figure 5.1b shows. In High Energy Physics (HEP) environments radiation can further affect the transmission of signals, less in the cables itselves, but primarily in integrated circuits with transistors in use. The following Section 5.1.1 summarises some of the main effects.

5.1.1 Radiation

The effect of radiation leads to degradation of PCB materials and components and/or can induce Single Event Upset (SEU) (see Figure 5.2). Figure 5.3 shows a simulation of the Total Ionisation Dose (TID) of the ITk Pixel Detector. To prevent failure in data transmissions due to radiation, several measures are implemented: all parts inside the ITk Pixel Detector and therefore also the ASICs on the Optoboard are radiation hard, meaning they are specifically designed to withstand the radiation environment. One of the common methods is implementing triplification of internal chip logic to cast a 2-out-of-3 vote on the proper line in case one of them is affected (as for example with the SEU in Figure 5.2). Furthermore, the materials are chosen such that they cannot become radioactive and self-induce radiation inside the chips or materials, causing unwanted signal generation or degradation of performance.

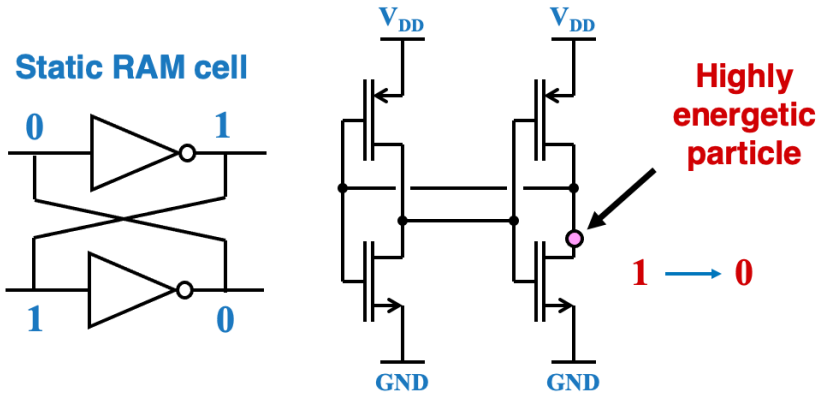

Figure 5.2: An SEU in a static Random Access Memory (RAM) cell that stores a 1 or 0 as long as there is supply power. While the state of the cell can be changed by V_{DD} on the transistors, radiation in the form of a high energetic particle can induce a voltage and an unwanted change or "bit flip" in the memory. Figure taken from [194].

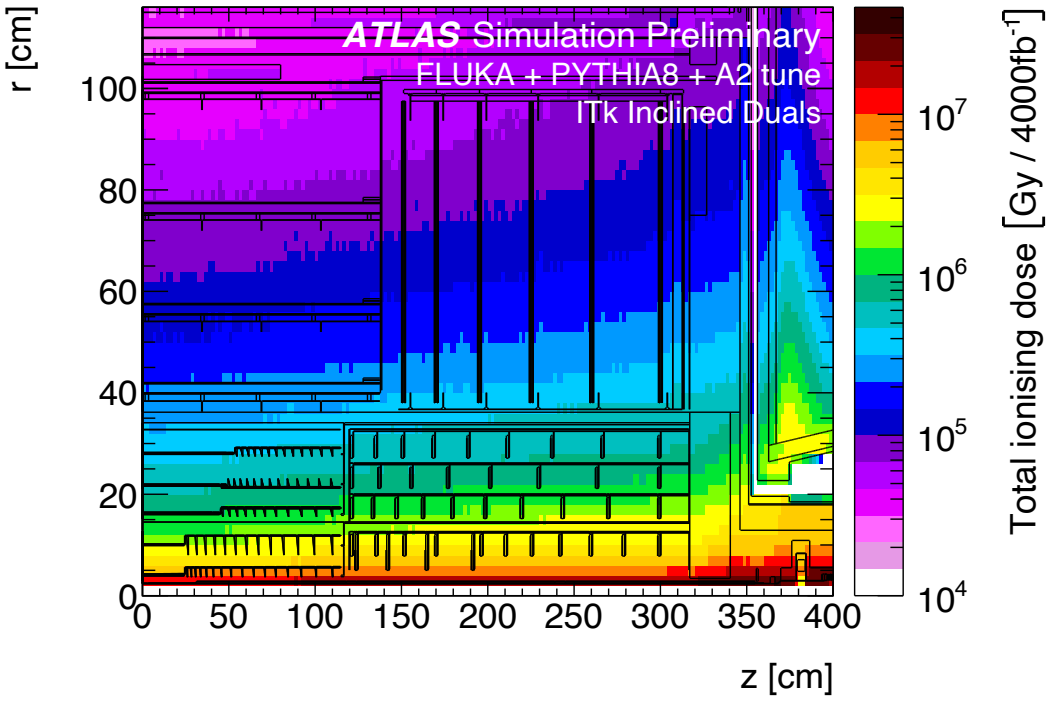

Figure 5.3: FLUKA [195] simulation of the expected total ionisation dose on the ATLAS ITk Pixel Detector Inclined Duals layout. Figure taken from [196].

5.1.2 Qualifying Data Transmissions

The data transmission of the ITk Pixel Detector has been qualified using the following methods: impedance and attenuation measurements, eye diagram analysis, jitter measurements and Bit Error Rate Tests (BERTs). This thesis introduces and presents results of the last two methods.

Jitter

Jitter are short-term non-cumulative variations of the significant instants of a digital signal from their ideal positions in time. This so-called significant instant of a digital signal can be defined as a rising or falling edge from a bit transition crossing a voltage threshold level [197].

The most common way to analyse the jitter is the jitter histogram. Generating the histogram is heavily dependent on the measurement device and is mostly done in real time with an oscilloscope. Closely related to the jitter is the eye diagram, where many amplitudes of the signal are recorded and overlaid in the same canvas and horizontally scaled to roughly three bits. The top diagrams of Figure 5.1 show two eye diagrams: (a) an *open* eye with an amplitude of roughly 320 mA and (b) a *closed* eye, where for the receiver it will be difficult to differentiate between the logical 0 or 1 states. In an eye diagram, the jitter can be seen at the 0-to-1 and 1-to-0 crossing. The larger the spread around the centre of the crossing, the larger the jitter. Jitter is divided into several subcategories as shown in Figure 5.4a, each providing clues to the origin of the jitter, allowing the designer or user to more easily find errors in the design.

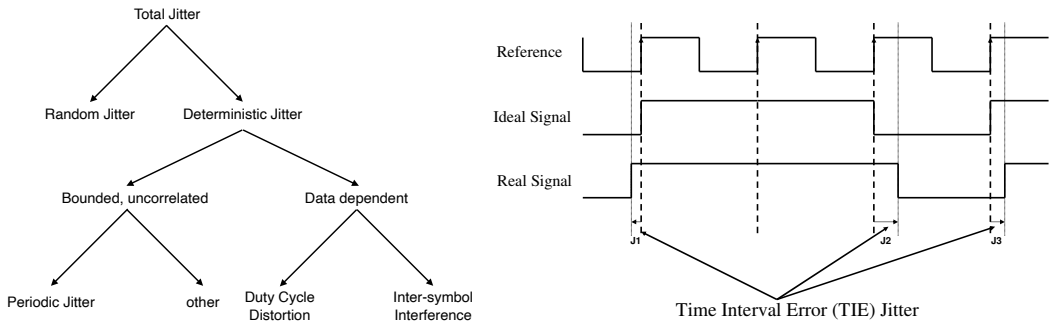

(a) **(b)**

Figure 5.4: (a) shows the hierarchy of the different jitter categories and (b) the standard definition of jitter on a digital signal, also referred to as TIE or total jitter. A reference signal is provided or generated (usually a clock) and the real signal is compared to the 0-to-1 or 1-to-0 transitions of the reference signal. Figures taken from [197, 198].

The following gives a description of the different types of jitter:

Total Jitter (TJ) or Time Interval Error (TIE): The above definition of jitter will be easier to understand with the help of Figure 5.4b, which describes TIE, the most common jitter definition. In this case a perfect reference clock is defined as timing. An ideal data signal should have the rising and falling edges timing aligned with this clock for each bit but a real signal will in turn have an imperfect timing, and this timing difference is the TIE. One needs to keep in mind that there can only be a jitter value if there is a transition from 0-to-1 or vice versa. In the case of clock signals, the maximum deviation of each single period of the jittered clock from the previous period of the same clock is defined as the cycle-to-cycle jitter [199].

Random Jitter (RJ): Random jitter is defined as being unbounded in the sense that there is always a probability, although it can be very small, of the jitter value reaching any value. In any semiconductor device there are multiple noise sources, like shot noise or thermal noise, that contribute to the generated random jitter. It is therefore common to use a Gaussian distribution to model the random jitter behaviour [197].

Deterministic Jitter (DJ): In contrast to the RJ, the deterministic jitter is bounded by maximum or minimum jitter values. In this category fall the periodic jitter or bounded uncorrelated jitter.

Bounded Uncorrelated Jitter (BUJ): Bounded uncorrelated jitter is defined as deterministic jitter that is bounded but uncorrelated with the data pattern. One example of a mechanism that causes this type of jitter is the crosstalk from an adjacent data line belonging to a different bus with a different frequency.

Periodic Jitter (PJ): Periodic jitter corresponds to jitter that has a periodic nature but is not correlated to the signal data pattern. One example is the crosstalk from an adjacent non-correlated clock signal into the data signal being measured.

Data Dependent Jitter (DDJ): Data dependent jitter is threshold-crossing time deviation correlated to the previous bits on the current data bit – it is also known as pattern jitter. DDJ is often caused by bandwidth limitations of the system or electromagnetic reflections of the signal [200]. The Duty-Cycle Distortion (DCD) and Inter-Symbol Interference (ISI) are subcategories of the DDJ, but are not of relevance for this thesis.

For this thesis a LeCroy Teledyne SDA 816Zi-B 16 GHz oscilloscope [201] was used for measuring the jitter. It has a specific sub program called Serial Data Analysis (SDA) package III [198] implemented to make the measurements easier for the user[1]. Determining jitter at a very small bit error ratio *BER* on a real-time oscilloscope

[1]These models and programs might be different for other oscilloscopes and depend heavily on the implementation by the maker. In this case, the SDA III package is also based on the SDA II package [202].

requires algorithms that extrapolate the measured data. It is not sufficient simply calculating peak-to-peak or RMS values directly from the acquired measurements. The reason for requiring extrapolation is simple: to measure TJ directly rather than via extrapolation requires a data set that could easily take a whole day to acquire. The SDA III package uses a dual-Dirac jitter model for its algorithm. The dual-Dirac jitter model describes TJ as having a dual-Dirac shape, with two Gaussian functions (see Figure 5.5) that grow with the *BER*. Measuring jitter for small *BER*, such as the

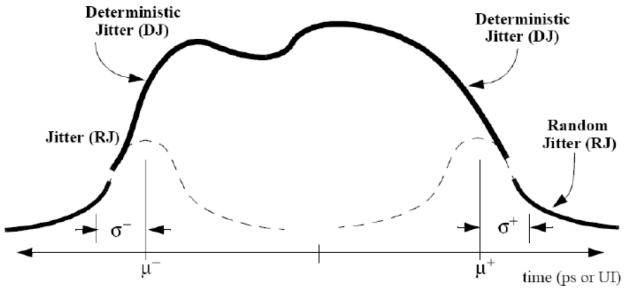

Figure 5.5: The TIE histogram showing the dual-Dirac model's two Gaussian distributions. Figure taken from [202].

commonly used value of $BER < 10^{-12}$, can take several hours to acquire for *slow* bit rates like 160 Mb/s (see next subsection). To get preliminary results within seconds, a model must be employed to extrapolate beyond the measurements actually taken. In the dual-Dirac model, TJ is the sum of DJ and RJ, with RJ weighted by a multiplier corresponding to the *BER*. The SDA III package uses the TIE measurement as the source of the jitter measurements for the analysis. The measurements are aligned in time to create a "jitter track" and are histogrammed as well. The first step in the analysis flow is to calculate data-dependent jitter. The result is removed from the jitter track to form the RJBUJ track trace, and from the TIE histogram to form the RJBUJ Histogram.

The Fast Fourier Transform (FFT) of the signal histogram, the RJBUJ spectrum trace, is first analysed for peaks that can be associated with periodic jitter. These peaks are removed, and the remaining spectrum is associated with random jitter. This corresponds to the σ value for the dual-Dirac Gaussian. The measured value of σ is used to fit the tails of the RJBUJ histogram, and the optimal mean positions of the Gaussians are determined. The next step is to add back the DDJ by convolving it with the RJBUJ Histogram to form the Parton Distribution Function (PDF). The PDF is integrated from both sides toward the centre to form the Cumulative Density Function (CDF). The space between the sides of the CDF is the TJ value for that *BER*. To determine RJ and DJ, four points are taken from the CDF and fitted to the Dual Dirac model to get the TJ:

$$\mathrm{TJ} = \alpha(BER) \cdot \mathrm{RJ} + \mathrm{DJ} \tag{5.1}$$

where $\alpha(BER)$ is the confidence interval at a confidence level of $1 - BER$ for a single "normal" Gaussian. In this work, the confidence interval is $\alpha = 14.07$ [198] for the

$BER = 10^{-12}$.

It is important to understand that the jitter measurements taken with the SDA III package are estimates based on the dual-Dirac jitter model, as opposed to directly measured results like a straight-forward RMS or peak-to-peak value [198, 202]. To observe the behaviour of the estimate with increased amount of measurement time, the TJ is plotted in a trend line over time for the results in this chapter.

Bit Error Rate Test (BERT)

While jitter gives valuable insight into the design, the BERT checks for errors in the logical path of the data transmission. The basic principle is that a known sequence of bits (a pattern) gets transmitted and checked at the receiver – if a 1 is supposed to be a 0 (or vice versa a 0 should be a 1) then the counted number of errors gets incremented otherwise not. By following reference [203], the bit error ratio[2] *BER* is then defined as:

$$BER = \frac{N_{\text{err}}}{N_{\text{bits}}} \tag{5.2}$$

with N_{err} the counted errors and N_{bits} the transmitted bits. Equation (5.2) is used both for measured and actual *BER* values; the measured value approaches the actual *BER* in the limit as $N_{\text{bits}} \to \infty$. To not measure indefinitely and reach a certain upper limit of the bit error rate to 95% confidence level, one has to measure a certain number of bits that can be calculated with statistics. Since there are exactly two possible outcomes: either a bit was measured as error, or not, the measurement is a binomial process. With the assumption that the observed errors are independent from each other, and the conditions do not change over time, we can model a *BER* measurement using the Binomial distribution. But since the *BER* is supposed to be very small (usually $< 10^{-12}$) and $N_{\text{bits}} \gg 10^5$, a Poisson distribution approximates the Binomial distribution (within per mille precision). The bit error rate to 95% confidence level $BER_{95\%}$ is defined with the average number of expected errors μ for a certain number of measured bits N_{bits}:

$$BER_{95\%} = \frac{\mu}{N_{\text{bits}}} \tag{5.3}$$

and the PDF of the Poisson distribution is as follows:

$$P_{\text{Poisson}}(N_{\text{err}}, \mu) = \frac{e^{-\mu}\mu^{N_{\text{err}}}}{N_{\text{err}}!} = \frac{e^{-BER_{95\%}\cdot N_{\text{bits}}}(BER_{95\%} \cdot N_{\text{bits}})^{N_{\text{err}}}}{N_{\text{err}}!} \tag{5.4}$$

Defining the upper confidence level limit $BER_{95\%}$ so that *the chance of having more errors than the measured N_{err} is less than 95%*, yields with Equation (5.3) and (5.4) the

[2] In a technical sense the bit error ratio and bit error rate are two different numbers. The bit error rate is the bit error ratio multiplied by the bit rate or the bit error divided by a time window. This thesis uses the bit error rate at a specified bit rate of 1.28 Gb/s.

condition:

$$\sum_{0}^{N_{\text{err}}} P_{\text{Poisson}}(N_{\text{err}}, \mu) \stackrel{!}{=} 1 - 0.95 \tag{5.5}$$

It follows that the number of bits that one needs to transmit/measure with the assumption $N_{\text{err}} = 0$ is:

$$\sum_{0}^{N_{\text{err}}} P_{\text{Poisson}}(0, \mu) = 0.05$$

$$\Rightarrow \qquad N_{\text{bits}} = -\frac{\log(0.05)}{BER_{95\%}}$$

With the industry standard being $BER \stackrel{!}{<} 10^{-12}$, one needs to send at least:

$$N_{\text{bits}} \approx 2.996 \times 10^{12} \text{ bits}$$

error free to get to 95% confidence level. Note that in the case of $N_{\text{err}} > 0$, Equation (5.5) cannot be solved analytically. For $0 < N_{\text{err}} < 10$, the Poisson upper limits of the average number of errors μ from Table 5.1 are implemented in the `optoboard_felix` test software for BERTs (see Section 5.5.1).

N_{err}	1	2	3	4	5	6	7	8	9	10
μ	4.74	6.30	7.75	9.15	10.51	11.84	13.15	14.43	15.71	16.96

Table 5.1: Average number of errors μ for the non-analytical solution of Equation (5.5). Table taken from [204].

Figure 5.6 graphically represents the case for a range of N_{err} and N_{bits} for the 95% confidence level.

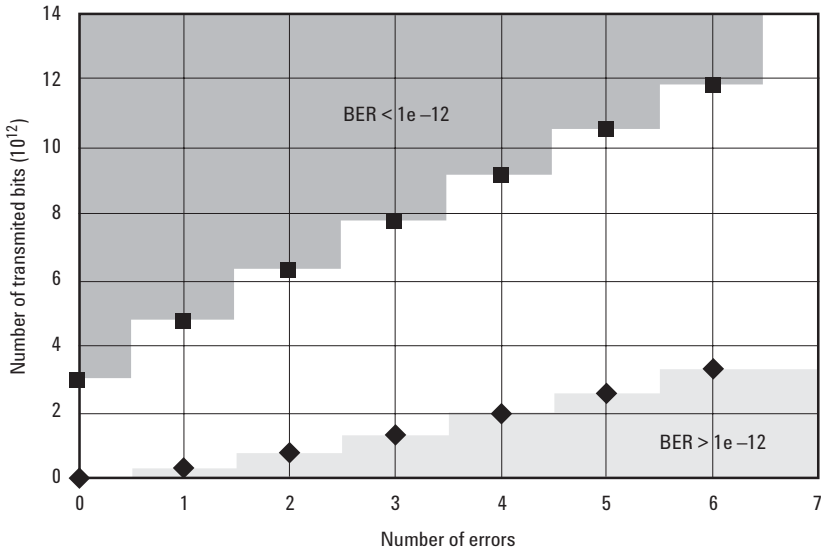

Figure 5.6: The 95% confidence level boundaries for upper (dark grey) and lower (light grey) limits on a *BER* of 10^{-12}. For the $BER > 10^{-12}$ area, Equation (5.5) needs to be set to 0.95. Note that there is a gap (white area) where the *BER* is close to 10^{-12} but without 95% confidence level. Figure taken from [203].

For $\mu > 16.96$, the Poisson distribution can be approximated by a Normal distribution, a Gaussian 97.5 percentile approximation is implemented in this case to calculate the $BER_{95\%}$:

$$BER_{95\%} = \frac{\mu + 1.96\sqrt{\mu}}{N_{\text{bits}}} \approx \frac{N_{\text{err}} + 1.96\sqrt{N_{\text{err}}}}{N_{\text{bits}}} \tag{5.6}$$

Note that in Equation (5.6) $\mu \approx N_{\text{err}}$, it was implemented to `optoboard_felix` for completeness sake. As seen in Figure 5.6 the number of transmitted bits N_{bits} to still meet the $BER < 10^{-12}$ requirement increases drastically. The time for a single measurement would take more than 2 h for the data rate 1.28 Gb/s.

5.2 Low Power Giga Bit Transceiver (lpGBT)

At the heart of the Optoboard system lies the Low Power Giga Bit Transceiver (lpGBT) [205, 206]. The lpGBT is a radiation-tolerant ASIC that is used for multipurpose high speed bidirectional optical links for the ATLAS and CMS phase-II upgrades. Logically, the link provides three “distinct” data paths for Timing and Trigger Control (TTC), Data Acquisition (DAQ) and Slow Control (SC) information. In practice, the three logical paths do not need to be physically separated and are merged into a single optical link in so-called *frames*. The aim of such an architecture is to allow a single bidirectional link to be used simultaneously for data readout, trigger data, timing, experiment control and monitoring using as little material budget as possible with high read-out rates. The goal is to establish a point-to-point bidirectional optical link (two fibres) that can function with very high reliability in the harsh radiation environment of detectors.

The general architecture of the lpGBT ASIC and its main external connections are displayed in Figure 5.7. As the lpGBT is a highly flexible link interface chip, a few relevant features for this work are described.

The lpGBT in transceiver mode receives the optical to electrical converted signal from the backend through the Link Receiver (LR). The Clock Data Recovery (CDR) and Phase-Locked Loop (PLL) circuit [207] receives in parallel the high-speed serial data (in the case of ATLAS ITk Pixel Detector 2.56 Gb/s). From the signal, the CDR/PLL block recovers and generates an appropriate high speed clock, needed by internal blocks of the lpGBT. For lpGBTs that do not receive a downlink signal and are in transmitting mode, the CDR must use an externally generated clock which will serve as a reference for the serialiser. The quality of the optical downlink signal is of great importance, as the internal clock is also used to sample the incoming data stream which correlates to the data quality. Results of a measurement of the optical signal quality in a setup with the Optoboard can be found in [208]. After the LR, the serial data is then de-serialised with the De-Serialiser (DeSER), namely it is transformed from serial to parallel form according to the data frame (see Section 5.2.1) and

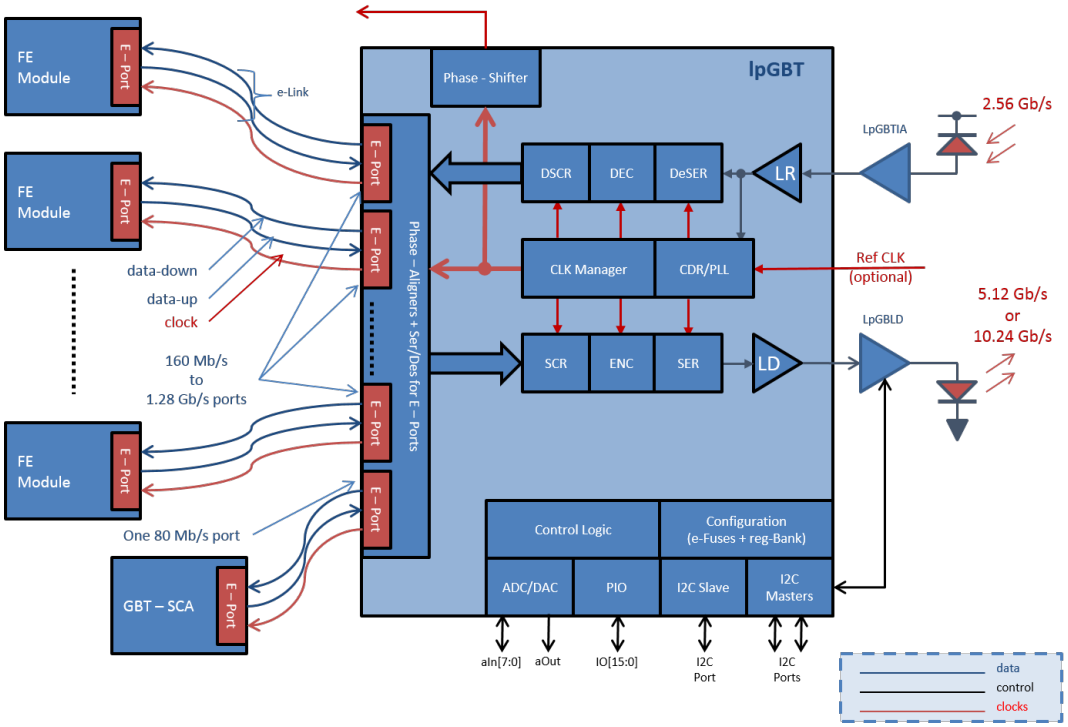

Figure 5.7: Overview of the lpGBT architecture. The downlink is defined as going from right to left, whereas the uplink goes from the FE modules on the left to the right. Note that in the case of the ITk Pixel data transmission chain, no specific clock lines are used between the FE modules and the ePorts. The clock is embedded in the electrical downlink (here "data-down"). Figure taken from [183].

decoded with the Decoder (DEC). After the decoding with appropriate error corrections, the data gets de-scrambled with the De-Scrambler (DSCR) (see Section 5.2.2). Scrambling or de-scrambling is useful to enable accurate timing recovery and reduce interference [209].

After the descrambler, the on-chip input/output Electrical Links (eLinks) facilitate connections to the FE modules. The eLinks are designed using the CERN Low Power Signaling (CLPS)[3] and offer programmable signal amplitudes to meet the transmission distance and power consumption requirements at a bit rate of 1.28 Gb/s. The lpGBT drives the eLinks via a series of ePorts, which are associated to FE modules ePorts. The data rate and number of active eLinks are programmable.

General control and monitoring logic takes care of controlling the different parts of the chip according to the selected operation mode and the ASIC configuration information. The lpGBT incorporates multiple *e-fuses*: each bit of the first 240 writeable configuration registers has a corresponding fuse to store a permanent configuration. By programming the fuse array, the desired configuration parameters for the lpGBT can be stored. During the chip's automatic power-up sequence, the transfer of information from the fuses to the configuration registers takes place. This enables the lpGBT to autonomously configure itself into an operational state upon power-up. While

[3]A signal generation protocol that should avoid confusion with Low Voltage Differential Signaling (LVDS) [210] or Scalable Low Voltage Signaling (SLVS) [211]. See also [212].

for version 0 of the lpGBT (lpGBTv0) efusing is the only option to automatically power-up the chip, for lpGBTv1 initial configuration information can also be taken from the on chip Read-Only Memory (ROM), requiring no efusing. While control and configuration of the lpGBT is always available over I2C protocol, IC communication only works after the lpGBT passes through a successful power-up sequence regardless of the version of the ASIC.

In the transmitter part (uplink), the data to be transmitted is scrambled with the Scrambler (SCR) to obtain a DC balanced signal, and then encoded with a Forward Error Correction (FEC) before being serialised and sent to the laser driver of the VTRx+ (see Section 5.4). The configuration of the laser driver can be performed via an I2C connection from the lpGBT.

5.2.1 High Speed Links – Data Protocol and Data Frame

When sending or receiving signals, the transmitted data is always formatted in a data protocol and has a data frame. Generally speaking, the protocol defines the rules, syntax, semantics and synchronisation of communication and possible error recovery methods. By knowing the protocol, it enables the receiver to correctly interpret the received data frame, like one language between two humans. A data frame is a container in a specific protocol, including the relevant data to be used. Any other frame in the protocol has the same structure but different user data. In the case of the Optoboard system, the user data contains the hit data of the FE modules. In detail, those pixel sensors that have received enough charge (depending on the respective threshold tuning) to claim a charged particle has passed through the sensor, their FE module send the time and time-over-threshold data. The downlink and the uplink frame of the lpGBT are explained in the following subsections.

Downlink Frame

The downlink frame is composed of 64 bits that are transmitted every 25 ns (the LHC bunch crossing period) resulting in a data rate of 2.56 Gb/s. As shown in Figure 5.8 the 64 bits consist of a header + control frame (8 bits), the user data (32 bits) and 24 Forward Error Correction (FEC) bits. The frame is transmitted using the convention of MSB first, where `H[3]` is the first bit to be transmitted, while the last is `FEC[0]`. The different parts are:

Header + Control: A total of four bits are the header `H[3:0]` = `4'b1001`, which identify the start of the frame. Two bits `IC[1:0]` are Internal Control (IC) and two bits `EC[1:0]` are External Control (EC) fields. In the case of the Optoboard only the IC field is changed in the case of sending a command to the lpGBT control circuit.

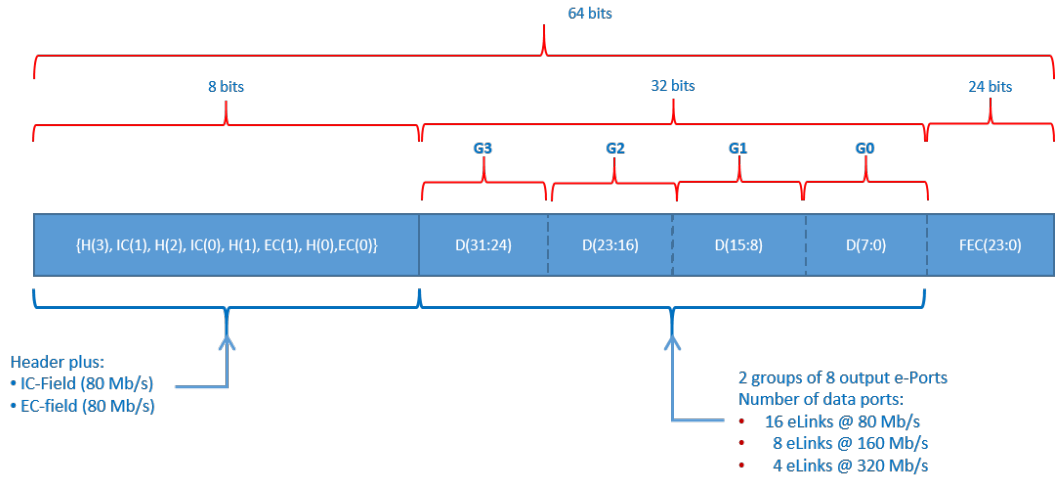

Figure 5.8: The lpGBT downlink frame before interleaving, i.e. rearranging the code for error corrections at the transmitter or after it has been de-interleaved at the receiver. The uplink frame is very similar to this one, differing only in bit lengths. Figure taken from [183].

User data: The central part carries four groups of user data `D[31:0]` to be transmitted to the FE by the links (or eLinks). For the Optoboard system, 8 eLinks are used at 160 Mb/s and the data content is commands and triggers for the FE-modules.

Forward Error Correction (FEC): In the case of the Optoboard, the `FEC[23:0]` bits of the downlink frame are reserved for the FEC12 code. Due to noise, intersymbol interference or Single Event Upset (SEU) errors could happen during the transmission, leading to corrupted data. FEC is code that enables correction of corrupted data without the need to re-transmit the data. The FEC code used for the lpGBT receiver is a Reed-Salomon (RS) code [213] RS(n,k) = RS(7,5). Figure 5.9 gives an overview of this code. RS(7,5) operates on symbols formed of $m = 3$ bits. A message composed of $k = 5$ symbols is encoded into a n symbol word, in this case with $n = 2^m - 1 = 7$ symbols. This enables the FEC to correct $t = 1$ symbol.

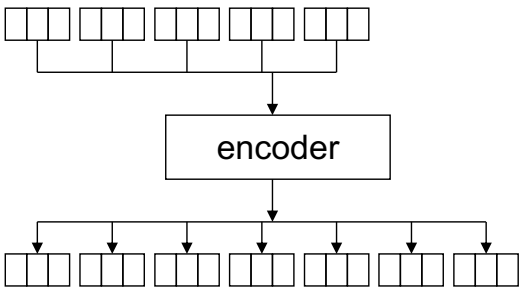

Figure 5.9: The simplified encoding of the Reed-Salomon code RS(7,5). In the top row the $k = 5$ symbols to be sent, each of 3 bits size. They are fed to the encoder and the $n = 7$ symbols effectively transmitted are shown in the bottom row. With this code 1 symbol (3 bits) can be corrected with the drawback that 2 additional symbols need to be transmitted. Figure taken from [214].

For the lpGBT four code groups are implemented through interleaving (see Section 5.2.3) allowing correction of up to $t = 4$ symbols or equivalently

$4 \times 3 = 12$ consecutive bits. Potentially the RS code can handle up to 60 user bits but only 40 are effectively used and transmitted due to the limited size of the frame: `H[3:0]` + `IC[1:0]` + `EC[1:0]` + `D[31:0]`. The remaining 20 bits are *padding bits* that are added ("padded") for encoding reasons. They are not transmitted as they are assumed to have no errors during transmission, the decoder of the receiver knows the padding and removes these again from the data content to then correct for errors (if needed).

Uplink Frame

The uplink frame is very similar to the downlink frame, it has the same header + control length. The differences, when operating the lpGBT in transceiver mode for the Optoboard, are the user data, which are now 192 bits shared over six groups and an additional Latency Measurement (LM) field, which allows estimating the round-trip latency of the transceiver link (excluding eLinks). The user data in this case is the Aurora encoded [215] hit data of the FE. For the FEC12 code, which contains 48 bits, a RS(15,13) enables correction of up to 24 consecutive bits. A data rate of 1.28 Gb/s per eLink is used. Adding up the six possible eLinks and including the FEC, the total uplink data rate is 10.24 Gb/s.

5.2.2 Scrambling

In the lpGBT, CDR circuits are employed to produce a clock signal that precisely matches the frequency and phase of the incoming serial bit stream. To enable the CDR to extract the required frequency and phase information, it is necessary for the bit stream to contain "0-to-1" and "1-to-0" transitions, which define the boundaries between bits. A high number of these transitions directly affects the CDR circuit's ability to accurately track the phase and frequency information, resulting in lower jitter (phase noise) for the recovered clock. However, there is no initial guarantee that the data transmitted via the lpGBT high-speed links will exhibit a high density of transitions e.g. it is possible that many zeros or ones are behind each other without any transition. To prevent this, scrambling techniques are implemented to ensure that the transmitted data exhibits the characteristics of random data, thereby promoting a high density of transitions in the serial bit stream. The lpGBT systems utilise a scrambler circuit in the transmitter and a descrambler circuit in the receiver to effectively scramble and recover the original data, respectively.

5.2.3 Interleaving

Interleaving is a technique used to improve the reliability of data transfer in noisy or error prone transmission setups. It involves reordering or rearranging the transmitted

data in a specific manner before transmission and restoring it to its original order at the receiving end. Interleaving provides two main benefits:

- First, it helps mitigate the effects of burst errors, where multiple consecutive bits or symbols are corrupted or lost due to channel conditions. By distributing the data, burst errors are broken into smaller error segments that can be corrected or detected more effectively.
- Second, it helps counteract the effects of fading or interference in noisy channels, as interleaved data provides diversity in time or frequency, improving the chances of error recovery.

As an example in Table 5.2, the interleaved downlink frame structure `IFRMDWN[63:0]` as received by the lpGBT. The encoder on the uplink path interleaves the different bits in a similar way.

Interleaved Frame	Assignment	Code Group
`IFRMDWN[2:0]`	`FEC[2:0]`	0
`IFRMDWN[5:3]`	`FEC[8:6]`	1
`IFRMDWN[8:6]`	`FEC[14:12]`	2
`IFRMDWN[11:9]`	`FEC[20:18]`	3
`IFRMDWN[14:12]`	`FEC[5:3]`	0
`IFRMDWN[17:15]`	`FEC[11:9]`	1
`IFRMDWN[20:18]`	`FEC[17:15]`	2
`IFRMDWN[23:21]`	`FEC[23:21]`	3
`IFRMDWN[26:24]`	`Data[2:0]`	0
`IFRMDWN[29:27]`	`Data[14:12]`	1
`IFRMDWN[32:30]`	`Data[26:24]`	2
`IFRMDWN[35:33]`	`Data[11:9]`	3
`IFRMDWN[38:36]`	`Data[5:3]`	0
`IFRMDWN[41:39]`	`Data[17:15]`	1
`IFRMDWN[44:42]`	`Data[29:27]`	2
`IFRMDWN[47:45]`	`Data[23:21]`	3
`IFRMDWN[50:48]`	`Data[8:6]`	0
`IFRMDWN[53:51]`	`Data[20:18]`	1
`IFRMDWN[56:54]`	`EC[0], Data[31:30]`	2
`IFRMDWN[59:57]`	`H[1], EC[1], H[0]`	HEADER, 3
`IFRMDWN[63:60]`	`H[3], IC[1], H[2], IC[0]`	HEADER, 3

Table 5.2: The interleaved downlink frame structure of the lpGBT. “Column Interleaved Frame” is what the lpGBT DEC receives and decodes to the second column “Assignment”. Table taken from [183].

5.2.4 Electrical Links (eLinks)

eLinks interconnect the lpGBT with the FE electronics through electrical cables to so-called ePorts. Each eLink consists physically of three differential pairs: two to transmit

data from the FE to the lpGBT receiver, from here on referred to as ePortRx (EPRX), or from the lpGBT transmitter, from here on referred to as ePortTx (EPTX), to the FE and a differential pair to transmit a clock, from here on referred to as ePortClk (ECLK). Four of the ePorts are grouped in one eGroup, depending on the selected mode different number of ePorts per eGroup are activated (see next paragraph). The lpGBT and this thesis use the terms group (G) and channel (C) for eGroup and ePort respectively. The naming convention for the registers of the electrical signal links is such that [G] represents the group number and [C] the channel number

While the lpGBT technically can support many different combination of number of eLinks and bandwidth, for the Optoboard the 10.24 Gb/s transceiver or transmitter mode in combination with FEC12 and the FE data rate of 1.28 Gb/s limits the number of EPRX to maximum six per lpGBT. This means up to six quad modules can be connected to a single lpGBT and therefore 24 per Optoboard. For this configuration only channel 0 of each eGroup is available. With the command and trigger bandwidth to the FE set to 160 Mb/s, the downlink is limited to two EPTX per eGroup totalling eight per lpGBT and therefore also per Optoboard (since only the lpGBT master utilises downlinks). The number of ECLK is not attached to any mode of the lpGBT (up to 29 independent ECLK are possible per lpGBT), the Optoboard uses four ECLK on the lpGBT1 and each one ECLK on the lpGBT2–4.

eLink Driver and Receiver

The interconnections between the lpGBT and the frontend devices are made through differential cables or transmission lines and the signalling adopted is defined by the ad-hoc “standard” CLPS. Its main feature used for the Optoboard’s lpGBTs is the programmable signalling level with differential amplitude between 200 mV to 800 mV for a load impedance of 100 Ω [216]. Since the programmable amplitude has profound implications on the signal transmission and the results presented in this thesis, the architecture and basic settings of the eLink driver (EPTX, Figure 5.10) and receiver (EPRX, Figure 5.11) are explained:

EPTX: The driver is responsible for sending the deserialised command and trigger signals to the FE-modules. It has been designed to drive 100 Ω loads with programmable strengths and controlled amounts of pre-emphasis. Pre-emphasis is a technique used in communication systems to enhance the signal quality and improve the signal-to-noise ratio (SNR) during transmission. It involves boosting the higher frequency components of the signal before it is transmitted over the cable that introduces attenuation. The pre-emphasis of the EPTX is programmable to a self-timed mode or clock-timed mode, where the later is used as default in the Optoboards channel control `EPTX[G][C]ChnCntr[4:3] = 3`. Clock-timed mode means that 1/2 of the 1.28 Gpbs data bit-rate period is used

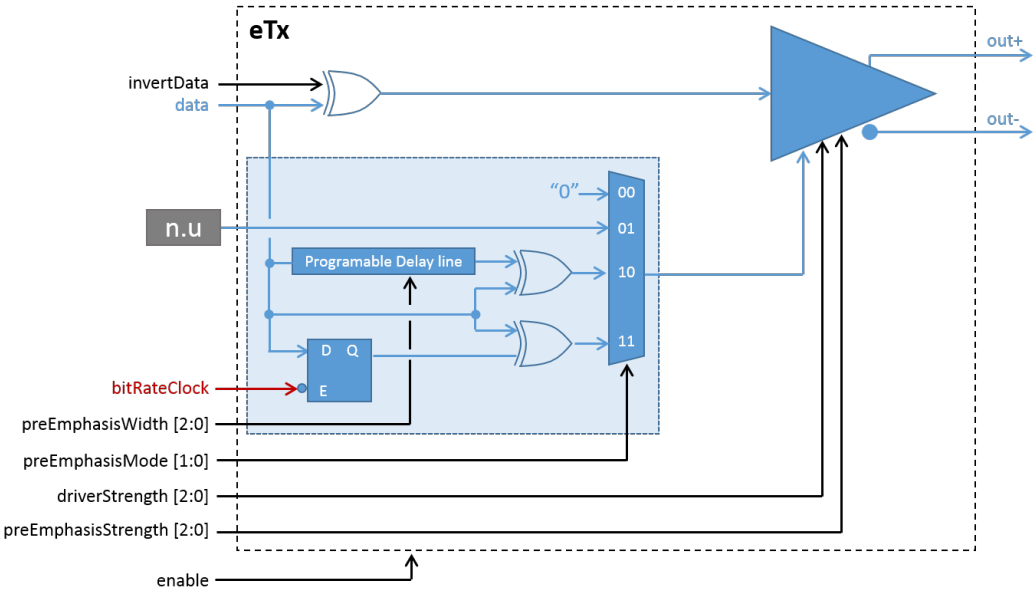

Figure 5.10: The eLink driver architecture with the pre-emphasis block (light blue background) and driver amplifier (top right) as the main components. The labelled arrows detail the corresponding setting in the lpGBT register and what it affects. "n.u" stands for not used. Figure taken from [183].

as the pulse duration.

The pre-emphasis is added to the signal amplifier which is programmable from 1 mA to 4 mA in steps of 0.5 mA (`EPTX[G][C]DriveStrength[2:0]`) and creates the actual differential signal. The signal also needs to be enabled (`EPTX10Enable` or `EPTX32Enable`) as the individual channels are disabled by default in order to save power.

Since the signals are transmitted using differential lines, one usually wants to connect the positive (P) signal with the P port and the negative (N) signal with the N port at the ASIC terminals. This is not always possible due to the routing design of a PCB or one of the many components (breakout board, adapters etc.) of a data transmission setup leading to an inversion of the polarity, meaning P is connected to N and all sent bits can change from 1 to 0 and vice versa. The lpGBT has a built in inverter logic for the driver (as well as the receiver) that can be triggered by setting bit 7 or 3 of register `EPTX[G]_0[C]ChnCntr` to ensure that a sent 1 bit is arriving as 1 bit without the need of hardware modifications.

EPRX: The receiver is responsible for merging the differential data signal from the FE into a single signal to be sent to the counting room through the high speed links. The input differential signal, in the case for the Optoboard lpGBTs, is coming from the output of a dedicated equalisation ASIC, the Giga-Bit Cable Receiver (GBCR) (see Section 5.3). The receiver has a dedicated logic block for terminating the attached line to 100 Ω, which can be enabled by setting `EPRX[G]0ChnCntr[1]` (the default for the Optoboard).

Additionally the receiver has a built-in Equaliser (Eq) for signal enhancement and an AC bias block. Both are not used as the GBCR is used for equalisation.

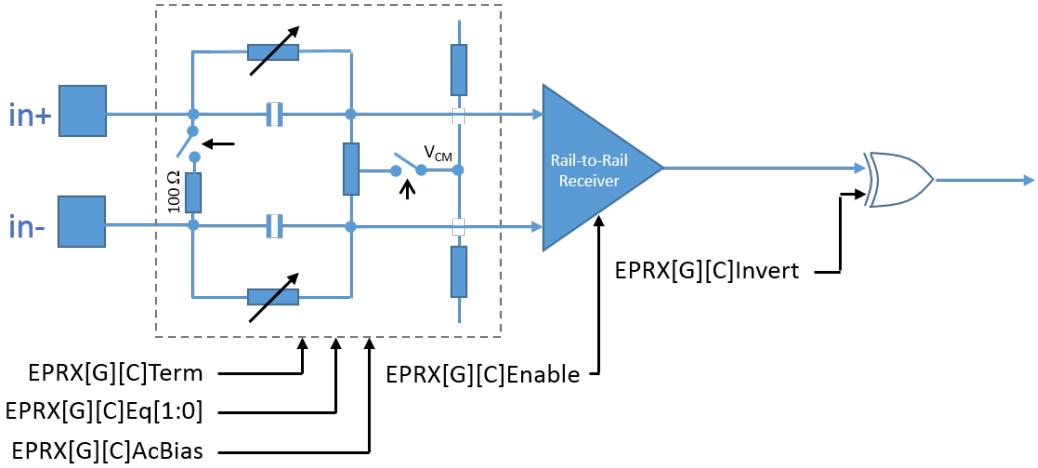

Figure 5.11: The eLink receiver architecture. The labelled arrows detail the corresponding setting in the lpGBT register and what it affects. Figure taken from [183].

Similar to the driver the receiver also has an enable (setting `EPRX[G]Control[4]`) and inversion of polarity (setting `EPRX[G]0ChnCntr[3]`) block.

As in all data transmission systems, phase delays between the lpGBT and the FE due to cable lengths and delays in the circuits are present. It is thus necessary for the eLink receiving ports to provide a way to adjust the phases of the incoming data signals so that data is sampled reliably in the middle of the eye-opening. Figure 5.12 gives an overview of the implemented logic of the lpGBT Phase Aligner (PA) or Adjuster. For

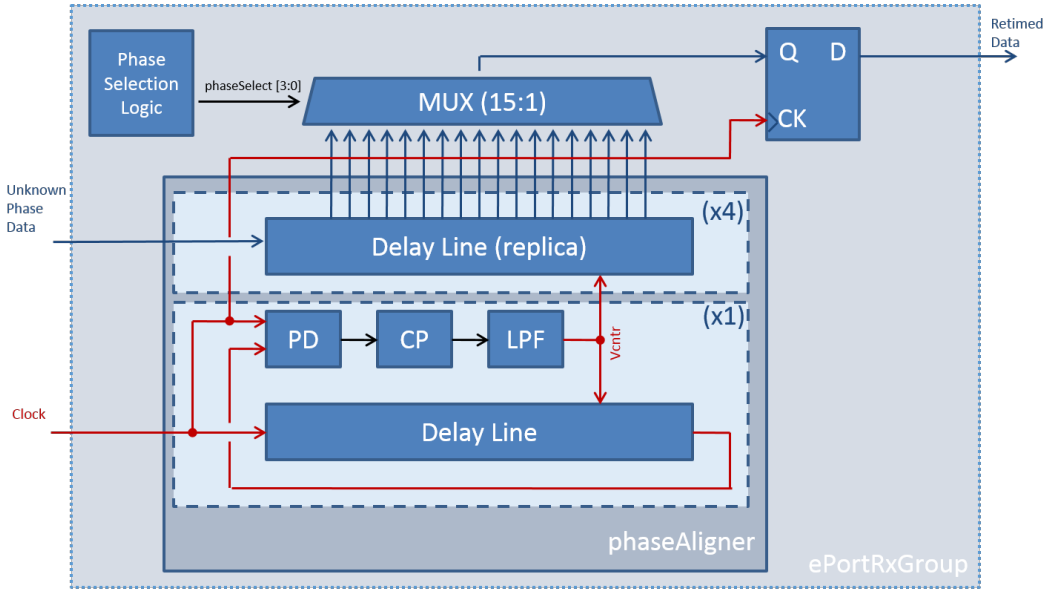

Figure 5.12: The eLink phase aligner. It consists mainly of the DLL (lower light blue background rectangle) and four delay lines (upper light blue background). The Phase Selection Logic sets the phase `EPRX[G]0ChnCntr[7:4]` with the Multiplexer (MUX) and together with the lpGBT outputs the retimed data. Figure taken from [183].

the EPRX the phase of the incoming data to the lpGBT is unknown. However, the

data rate is known from the lpGBT and FE module's design. The lpGBT clocks are synchronous with the FE module clocks with a fixed and stable phase relationship. It is thus unnecessary to recover the clock from the data but it is necessary to phase align the incoming data with the internal clocks in the lpGBT for each eLink. The lpGBT phase aligner channels can operate in four different modes: fixed phase, initial training, Continuous Phase Tracking (CPT) and CPT with initial phase. For the Optoboard CPT is used during the prototyping stage while in the final detector setup fixed-phase mode is going to be used after an initial training.

CPT is useful during testing of FE data streams with many interventions to the setup as it allows setting the optimum phase and dynamically adjusting it free of the user recalibrating/training. The algorithm used to step the phase up or down is based on an average of 8 samples and phase-changes are done incrementally in steps of $\pm T/8$, where T is the bit period. The phase-changes are done in such a way that no data transmission errors are introduced when that phase is being changed on the fly. For all modes the locking state machine counts the number of transitions that fall in the expected region. If 64 transitions are detected, then the channel is declared as locked (status bits asserted in `EPRX[G]Locked`). Conversely, the channel is considered unlocked if 64 transitions fall outside the expected range.

For the commissioning of the Optoboards the fixed phase is used because the delays along the transmission are not expected to change anymore and to save the power from the lock detection machine. A static phase can handle relatively larger amounts of jitter and accept data without any DC balance restrictions [183].

5.2.5 Bit Error Rate Test Capabilities of the lpGBT

The lpGBT is equipped with a pattern checker for bit error rate tests (see Section 5.1.2 for more details) of the eLinks from the FE. The basic principle is that the user sets the FE module's serialiser into Pseudo Random Bit Sequence (PRBS) mode with a known pattern (PRBS7 in this case) and checks the arriving bits with the lpGBT PRBS7 pattern checker.

The lpGBT pattern checker can be set up with `BERTMeasTime[7:4]` for the measurement time in 40 MHz clock cycles and therefore the N_{bits}. Since the Optoboard uses 1.28 Gb/s on its elinks, 32 bits get transmitted per 40 MHz clock cycle. For an overview of the possible limits one can achieve with the lpGBT pattern checker if no error is detected, see Table 5.3.

`BERTMeasTime[7:4]`	N_{bits} (clock cycles)	measurement time [s]	$BER_{95\%}$
`4'd0` (min)	2^5 (32)	0.8×10^{-6}	2.9×10^{-3}
`4'd11`	2^{27} (128M)	3.4	7.0×10^{-10}
`4'd15` (max)	2^{35} (32G)	859	2.7×10^{-12}

Table 5.3: Selected measurement times of the lpGBT pattern checker and the corresponding *BER* limit with 95% confidence level if no error is detected. For all measurements shown in this thesis the longest measurement time with `4'd15` was chosen. See Section 5.1.2 for the calculation of *BER*.

5.3 Giga-Bit Cable Receiver (GBCR)

To meet the demand of electrical data transmission through thin cables, the ASIC GBCR [184, 217–219] has been designed and is used on the Optoboard.

Figure 5.13 illustrates the block diagram of GBCR. Each uplink channel consists of several components: a passive attenuator, an equaliser, a Limiting Amplifier (LA), a DC-offset-cancellation circuit, retiming logic, and a Current-Mode Logic (CML) driver. The programmable passive attenuator is used to prevent saturation in the subsequent equaliser. The long cable used before the uplink channels attenuates high-frequency components more than low-frequency ones, leading to significant ISI jitter on the receiver side. The equaliser, which is a Continous Time Linear Equaliser (CTLE) [220], acts as a high-pass filter, reducing the impact of low-frequency components and compensating for the high-frequency components. Optionally, the equalised signal can be retimed using a 1.28 GHz phase-adjustable clock, that is shared by the corresponding lpGBT, provided by a phase shifter. This phase shifter is shared among seven uplink channels, although only six are in use in the Optoboard system. The equalised or retimed data is then sent to the electrical receiver EPRX of the lpGBT.

On the other hand, each downlink channel on the GBCR can add pre-emphasis to the signal from the lpGBT's electrical transmitter EPTX port and transmits it to the ITkPix's receiver using similar cables as the uplink channels. All settings, a total of 32 register bytes, can be adjusted through an I2C bus connection (I2C target).

5.4 Versatile Link Transceiver Plus (VTRx+)

The Versatile Link Transceiver Plus (VTRx+) is the component on the Optoboard that takes the multiplexed electrical signals from up to four lpGBTs and turns them into optical signals for the uplink at 4×10.24 Gb/s. In the downlink path, it receives the 2.56 Gb/s downlink and converts them to electrical signals for the lpGBT. The layout of the VTRx+ is shown in Figure 5.14. It contains the following main parts:

- Low-power radiation-hard laser driver array (LDQ10) [222]: it delivers the current to the laser diode. It also contains the I2C slave of the VTRx+, through which the VTRx+ is controlled by the lpGBT I2C master. Parameters, such as the pre-

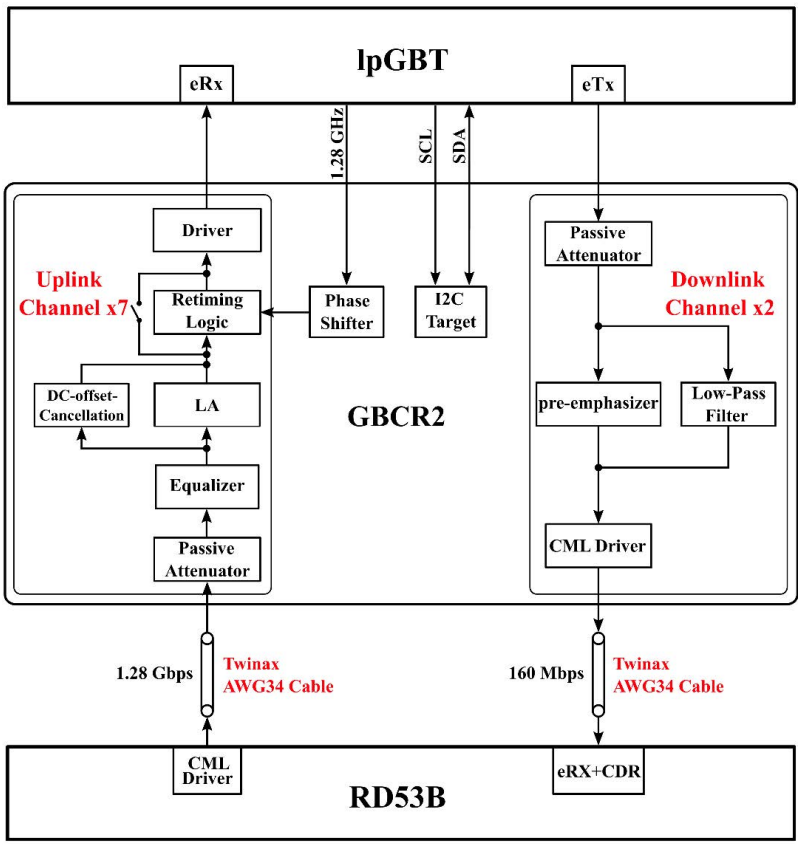

Figure 5.13: Block diagram of the second version of the GBCR, GBCR2, the version used for the Optoboard versions from V0 to V2.1 in this thesis. The uplink data path is on the left while the downlink is shown on the right. Figure taken from [184].

emphasis and the modulation of the optical signal, can be set ad-hoc. For this work two different versions of the VTRx+ were used with different versions of the laser driver. Version 1.2 is mounted on the prototype VTRx+ (mint pigtail, shown in Figure 5.15) and version 1.3 on the production VTRx+ (blue pigtail).

- Vertical-Cavity Surface-Emitting laser (VCSEL) diode array: This is the laser that generates the light for the fibres.

- Positive Intrinsic Negative (PIN) diode: this is the receiver of the optical signal from the downlink.

- Transimpedance Amplifier (TIA) [222] in single-channel format: it converts the current from the PIN diode into a usable format for the lpGBT1.

The VTRx+ is an individual component with a connector and, in the case of the Optoboard, it is plugged and fixed by screws as a permanent connection.

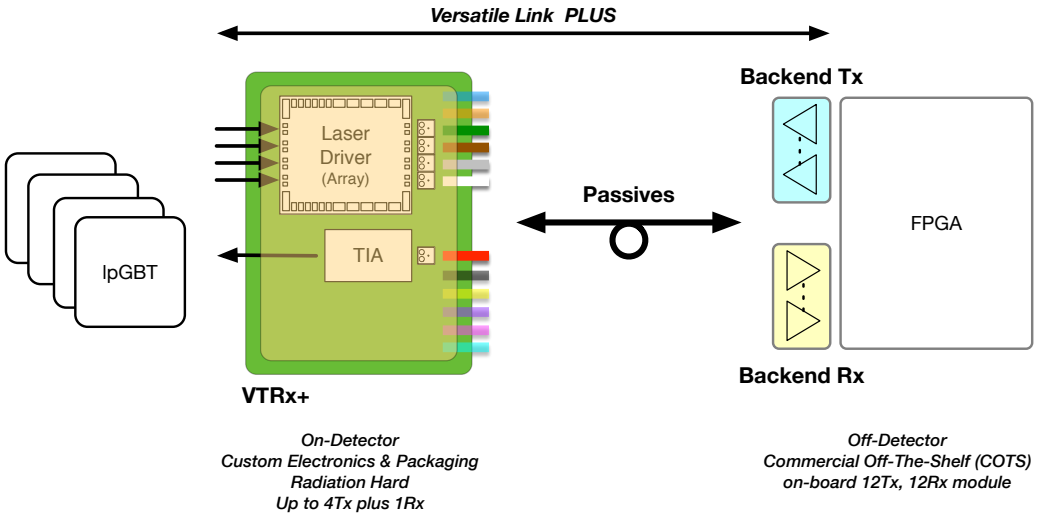

Figure 5.14: Layout of the VTRx+. One can see the four uplinks coming from the lpGBTs going through the laser driver array and the VCSEL (four small squares). On the receiving end the downlink goes to the PIN diode (small square next to red fibre) and from there to the TIA. Note that the colours on the diagram match the colour code of fibres and the colours on Figure 5.15. Figure taken from [221].

5.5 Validating the ITk Pixel Detector Data Transmission Chain

Due to non-availability of FELIX cards and FE modules in the beginning of the work, I performed the validation of Optoboards within the ITk Pixel Detector data transmission chain in several stages:

- First, a setup for communicating with the Optoboard's lpGBTs and GBCRs was designed by me, including a software/Guided User Interface (GUI) to configure and test Optoboards. In this work, this setup is labelled as *KC705 – Optoboard – CDR53b* after the scheme "backend – Optoboard – frontend".

- As a next step, I carried out first BERTs of the electrical signal with test components. The setup was used to do first tests before irradiation campaigns.

- When the FELIX backend FLX-712 (BNL-711 V2) card became available, fibre connections were included and I adjusted the testing setup with a small fibre plant.

- After RD53a and ITkPix modules became available, the Optoboard was integrated by me into the data transmission chain with the prototype components. This setup is labelled as *FELIX – Optoboard – RD53a*. I also extended the initial software for better usability and compatibility. The culmination were the ITk Pixel system tests at the loading and integration site SR1 at CERN.

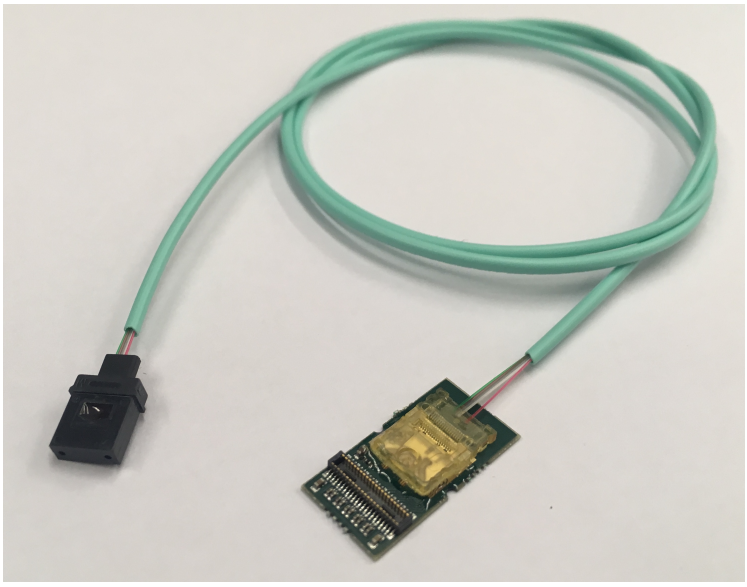

Figure 5.15: Photograph of the VTRx+ with the attached pigtail and the black MT connector [223]. The pigtail goes from the Optoboard's VTRx+ to the fibre fan-out, which is connected to the MPO-24 connector on the Optobox. Visible are also the four uplink fibres (green, brown, grey and white) and after a small gap the downlink fibre (red).

5.5.1 KC705 – Optoboard – CDR53b Setup

For the first setup without FELIX, a communication channel with the Optoboard's lpGBT was made through a KC705 Field Programmable Gate Array (FPGA) with a custom developed firmware [208]. With an adapter board successful configuration was achieved with the lpGBT master through I2C and conventionally over fibre via IC. While a single write to one of the lpGBTs control register was a few lines of code or commands through the terminal, it was evident that configuring a full Optoboard with multiple lpGBTs and GBCRs would mean configuring up to 500 registers at least just for initial start-up through the command line. Since this is time-consuming and impractical, regardless of the backend card, I developed a software called `optoboard_felix`, including a GUI, for fast configuration and a few basic tests for the Optoboard. Figure 5.16 shows a screenshot of the first version of the GUI, coded in `Python` with the `tkinter` library [224], used in the lab.

I defined a test to measure the jitter for the command and control lpGBT EPTX and GBCR driver settings. In particular, the necessity of the GBCR pre-emphasis should be investigated. In case the GBCR pre-emphasis is not needed, the GBCR is not needed in the downlink direction, reducing the number of GBCR chips in the Optoboard system in case there are less than the maximum number of uplinks used. To investigate this aspect, two Optoboard V1.1s were used: one with all lpGBTs and GBCRs and one with only the four lpGBTs whereas the GBCR data lanes are replaced by wire bonds bridging the signal pads as seen in Figure 5.17. The two setups are shown in Figure 5.18, both downlink paths include the 6 m Twinax cable and end at the oscilloscope. The SMA cables used to connect the different components together have

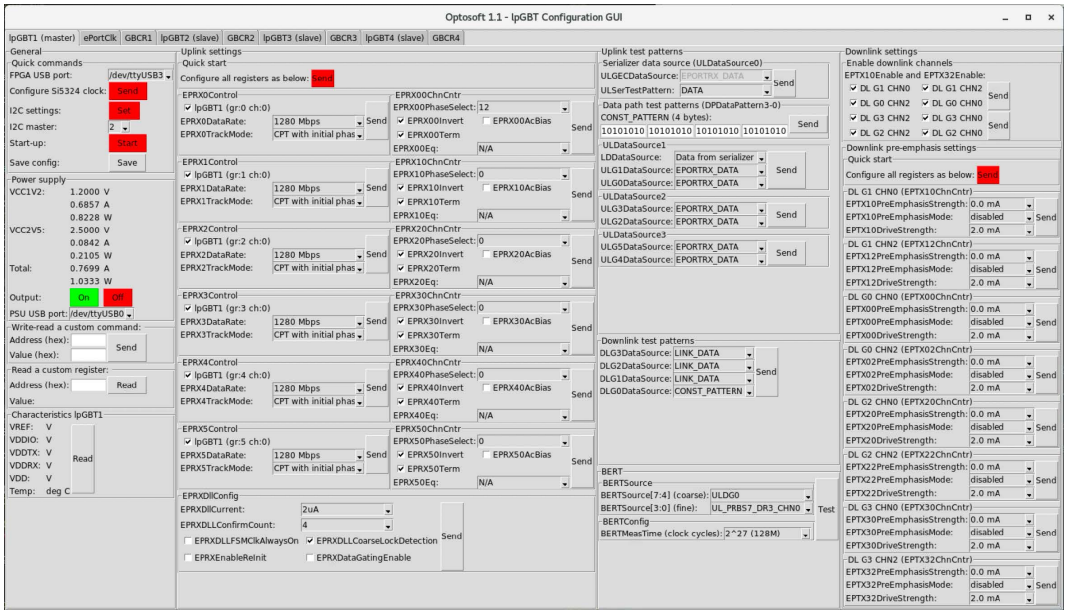

Figure 5.16: Overview tab for the lpGBT1 (master). On the very left a few quick commands to control the FPGA can be executed and the power supply can be remotely controlled. The uplink settings tab has the most important configurable eLink registers such as driver strength, track mode, polarity and phase settings. A testing column has been implemented to select various test data stream patterns and execute BERT. The last tab is for the most relevant downlink settings, similar to the uplink settings.

a combined length of 2.75 m with an estimated 2 dB attenuation of the signal. The configuration of the lpGBT EPTX driver are in register `EPTX00ChnCntr`, with `EPTX00PreEmphasisStrength = 3'd0,1,3,5,7` setting the different strengths, while `EPTX00PreEmphasisMode = 2'd3` and `EPTX00DriveStrength = 3'd7` are fixed. The GBCR registers `CH1DOWNLINK0` and `CH1DOWNLINK1` are responsible for the downlink settings, the strength of the pre-emphasis is configured through `TX1DLSR = 3'd0,1,3,5,6` while the attenuator is set to `TX1DLATT = 2'd3`. For all measurements a total of 2.5 million samples for the eye diagram or 350 total jitter samples are taken. Figure 5.19 shows the results for all possible settings. For comparison, two oscilloscope screenshots with both 4.0 mA lpGBT pre-emphasis strength (`EPTX00PreEmphasisStrength = 3'd7`) are presented: one in Figure 5.20 with the GBCR mounted and setting `TX1DLSR = 5` and one in Figure 5.21 with the GBCR removed. In the figures there are four quadrants: top left the eye diagram, bottom left the shape of the signal, top right the RJBUJ spectrum and bottom right the total (orange) and deterministic (pink) jitter trend line overlayed with the RJBUJ histogram. Both RJBUJ spectrum show a peak at ∼40 MHz. This is interference of the lpGBTs clock with the signal. Below the four quadrants are two horizontal sections: the top one is giving all possible outputs of the SDA III package, most notably the TJ, RJ DJ and the estimation of the *BER*. The lower section gives all measured parameters from the eye diagram, notably the eye height and eye crossing.

One can see that the lowest jitter values can be achieved with `TX1DLSR = 3'd5` settings but also without the GBCR the results are comparable with maximum pre-emphasis strength on the lpGBT EPTX. Later after the results it was ultimately

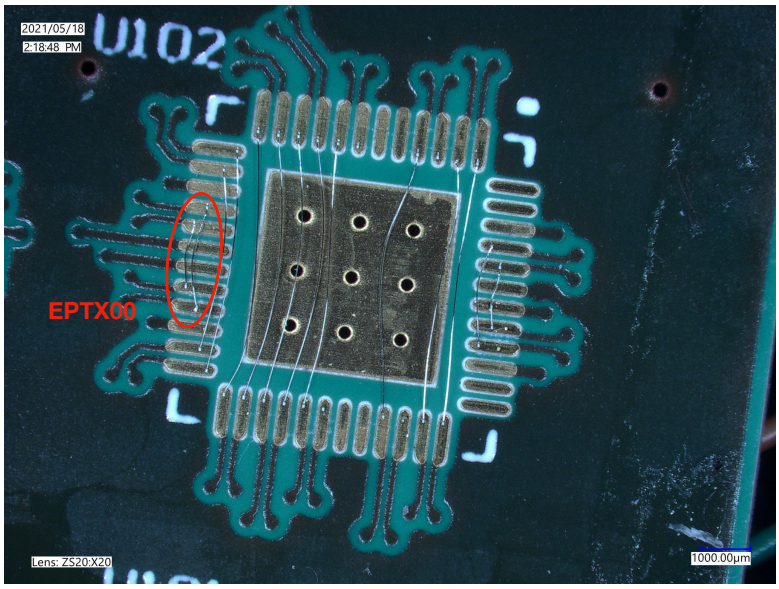

Figure 5.17: Photograph of the GBCR pad on the Optoboard V1.1. Marked are the downlink wire bonds for the lpGBT1 EPTX00.

decided to drop the GBCR downlink as it saves 1640 GBCRs[4] since a GBCR is only needed if there is the corresponding lpGBT on the Optoboard.

[4] From the numbers of Table 4.14 by calculating the number of Optoboards times four minus the number of lpGBTs.

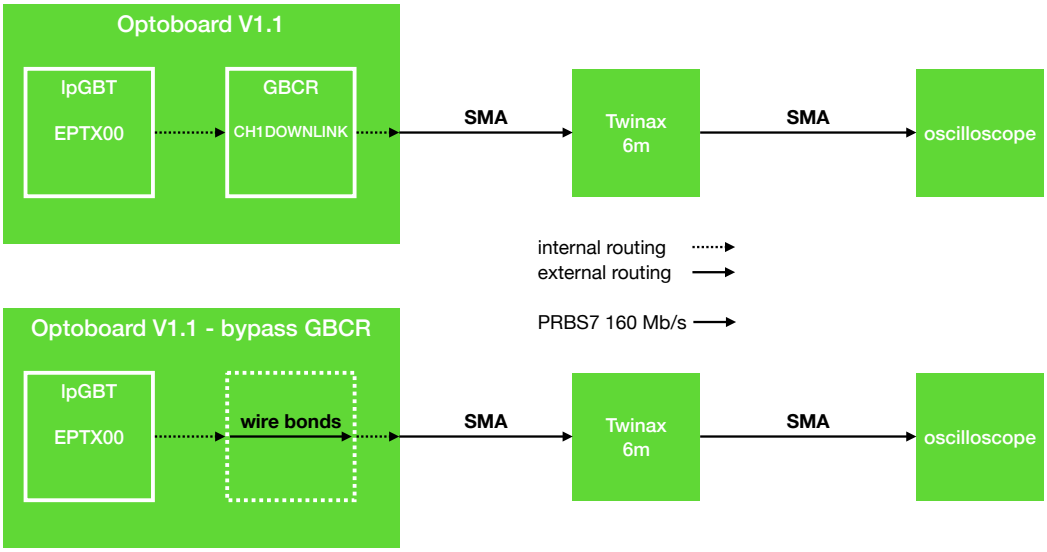

Figure 5.18: The two setups used to measure the jitter at the oscilloscope. Top: with the GBCR mounted. Bottom: setup in which the GBCR is replaced by wire bonds.

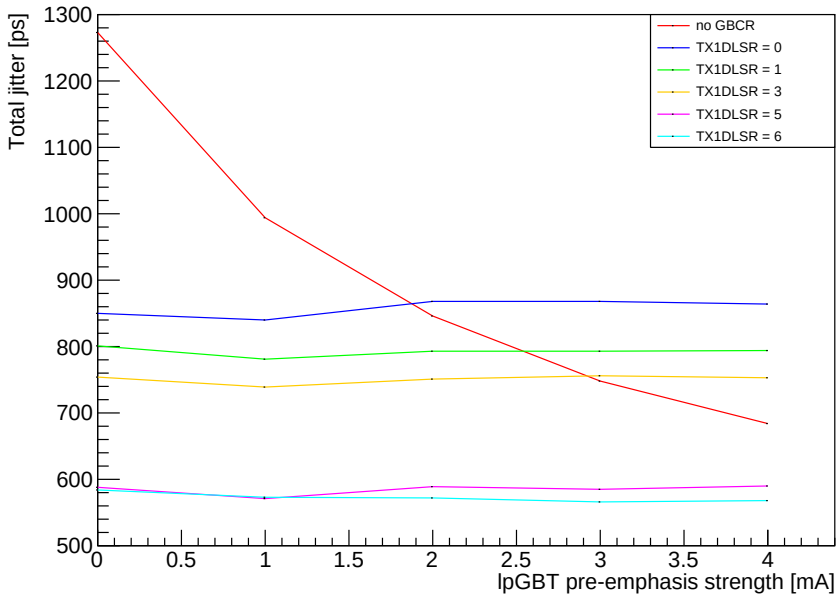

Figure 5.19: Total jitter measurements comparing the downlink EPTX00 with GBCR pre-emphasis and without GBCR.

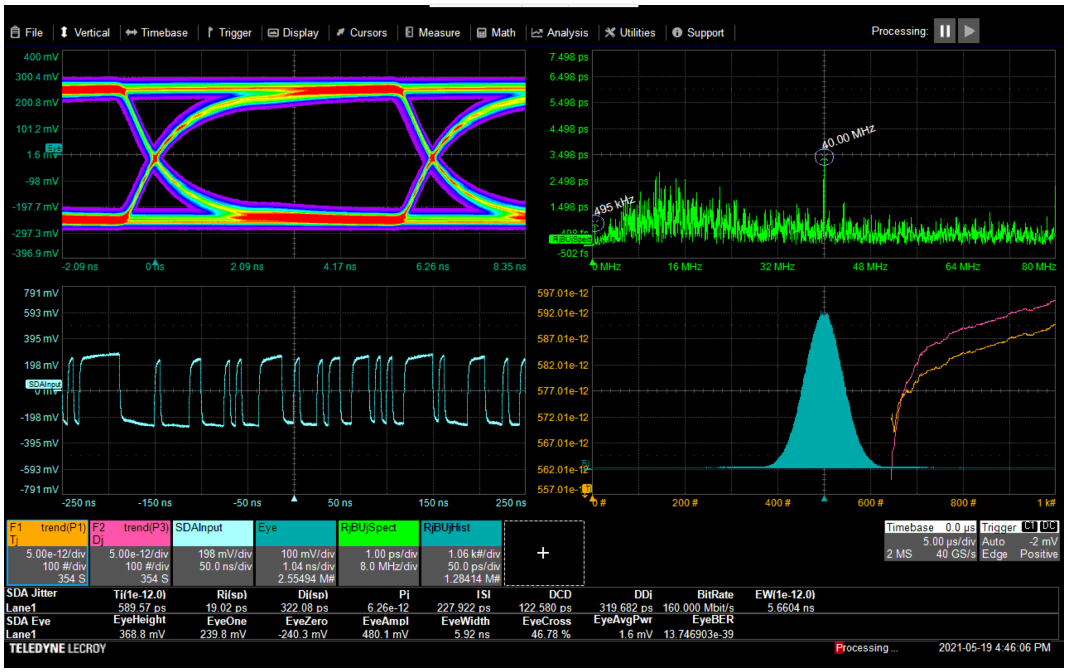

Figure 5.20: Oscilloscope measurements with GBCR mounted and `TX1DLSR = 3'd5`, lpGBT pre-emphasis strength of 4.0 mA.

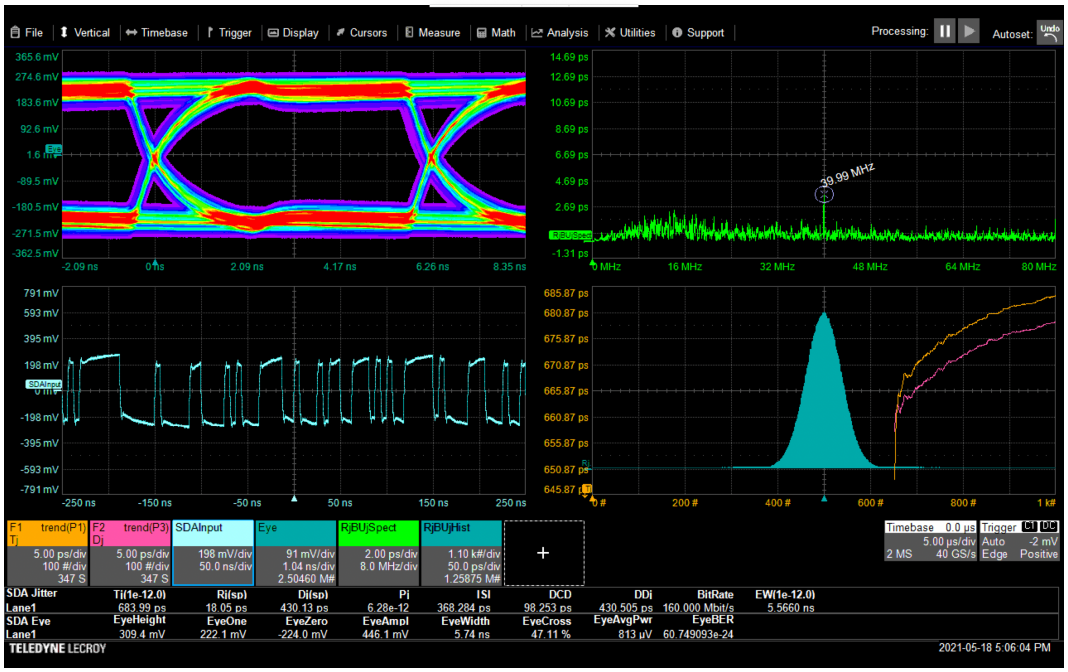

Figure 5.21: Oscilloscope measurements without GBCR, lpGBT pre-emphasis strength of 4.0 mA.

5.5.2 Cyclotron Setup

With the initial communication established, a preliminary data transmission chain setup used for irradiation tests on the Twinax cables at the Bern Medical Cyclotron [225], was designed and assembled by me. Figure 5.22 shows all the components of the chain, the setup is called *cyclotron setup*. The KC705 FPGA, as mentioned above, controls

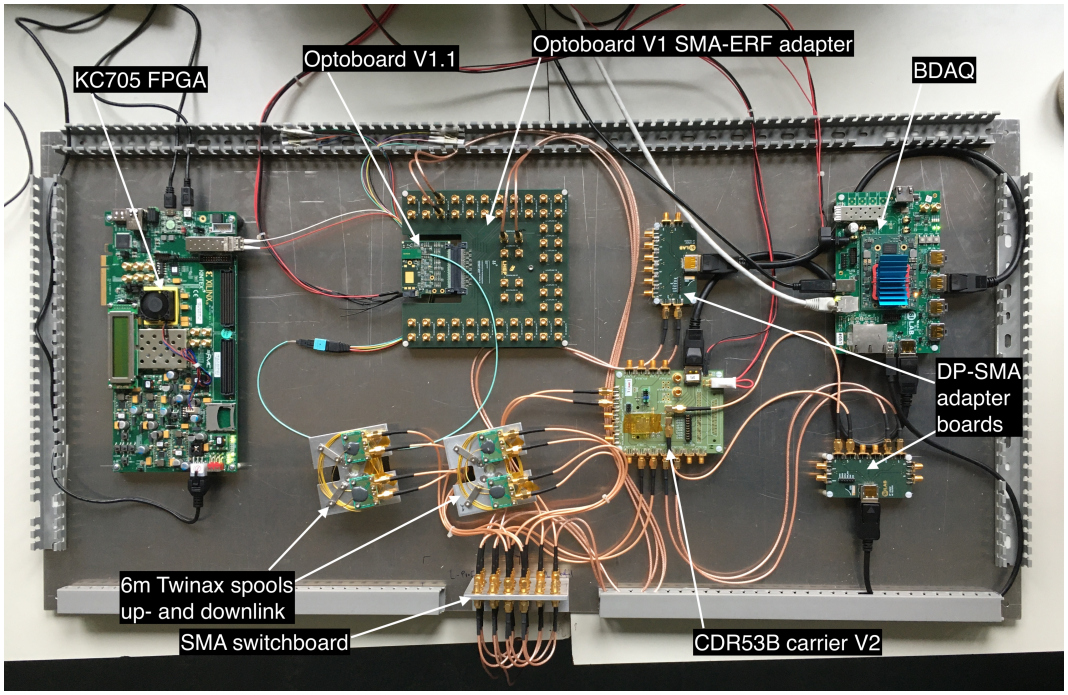

Figure 5.22: The preliminary ITk Pixel data transmission setup. Not visible are the power supplies and the host computer. Everything is mounted on a transportable plate, the only outside connections are the USB connections to the host computer and the power supply cables. This made transporting the setup between the laboratory and the cyclotron a lot simpler. Note that the downlink roughly goes from left to right and the uplink from right to left.

the Optoboard via fibre and is able to configure the individual chips. The Optoboard is connected through its ERM connector with the SMA-ERF breakout board from where SMA cables are routed to the 6 m Twinax cable spools that are removable for insertion into the irradiation setup. For testing flexibility a small SMA switchboard was also added to enable the user to bypass cables in the up- and downlink direction. After the Twinax, the signal arrives at the CDR53b carrier board V2, a test board that hosts the CDR53b [226] of the RD53b FE. The CDR53b is controlled through the BDAQ53 [227], a versatile pixel detector readout and test system for the ATLAS and CMS HL-LHC upgrades, and display port to SMA (DP-SMA) adapters. Through the BDAQ53 the CDR35b can be configured in a test pattern output mode, in this case PRBS7, to be able to measure the uplink signal pattern after the Twinax cables at the lpGBTs pattern checker (see Section 5.2.5).

Figure 5.23 shows the combined results of 256 BERT. Each square represents one *BER* measurement with `BERTMeasTime[7:4] = 4'd15` or approximately 3.4×10^{10} bits with the z axis being the *BER* with 95% CL. The x and y axis represent the register

settings `CH1CTLEMFSR` and `CH1CTLEHFSR` of the GBCR, respectively, and correspond to the strength of the CTLE.

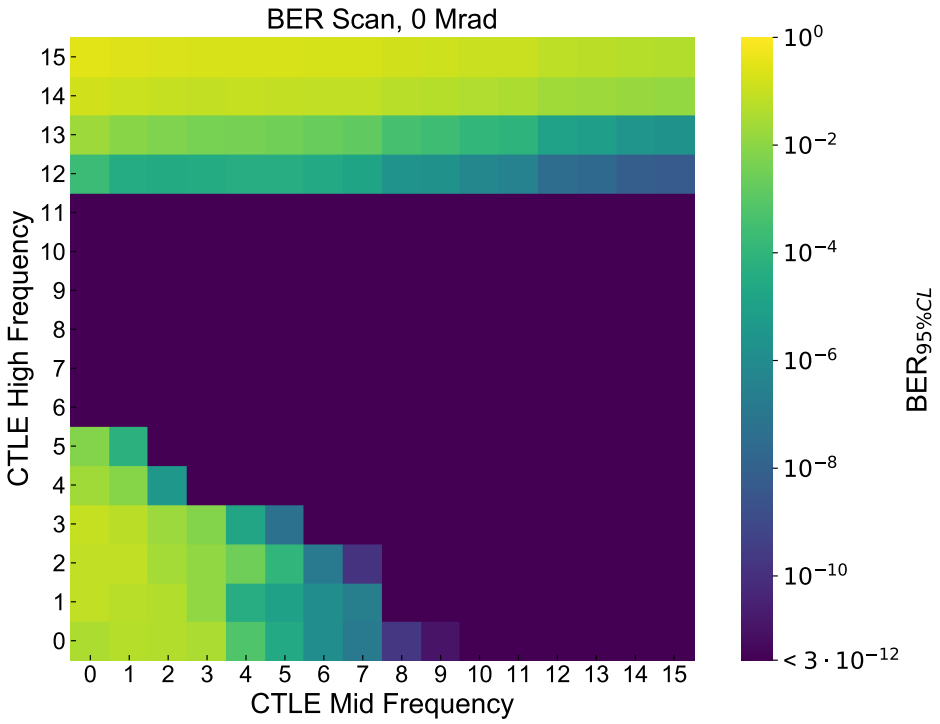

Figure 5.23: PRBS7 BERTs of the EPRX00 channel of the lpGBT1. The values of the CTLE mid and high frequency correspond to the register setting, higher means more equalisation. Figure provided by Lea Halser.

5.5.3 FELIX – Optoboard – RD53a Setup

The availability of the FELIX FLX-712 card and RD53a FE (mounted on the Single Chip Card (SCC)) enabled the swap of the custom FPGA and the CDR53b + BDAQ53 setup, effectively simplifying the test setup to the one shown in Figure 5.24. Additionally the Optoboard V2 was designed by us and became available. The FELIX card is now directly installed in the host computer's PCIe slot and the cables are connected through SMA-Twinax adapters to the DP-SMA adapter of the RD53a. To control and configure the Optoboard with the FELIX card, the backend of the GUI needed to be updated with an `ic-over-netio` library [228], that later got incorporated into the `itk-felix-sw`, and a fall-back option to access the FELIX low level tool `fice` through `Python` subprocesses. The `ic-over-netio` backend also cut the time of configuring a full Optoboard from about 15 min to less than 20 s. The GUI evolved into a class based backend `optoboard_felix` [229] in preparation for the ITk Pixel system test demonstrator software. Many features were developed with fast testing capabilities and easy use for the Optoboard system users in mind. To control and steer the RD53a the `YARR` [230, 231] readout software was used.

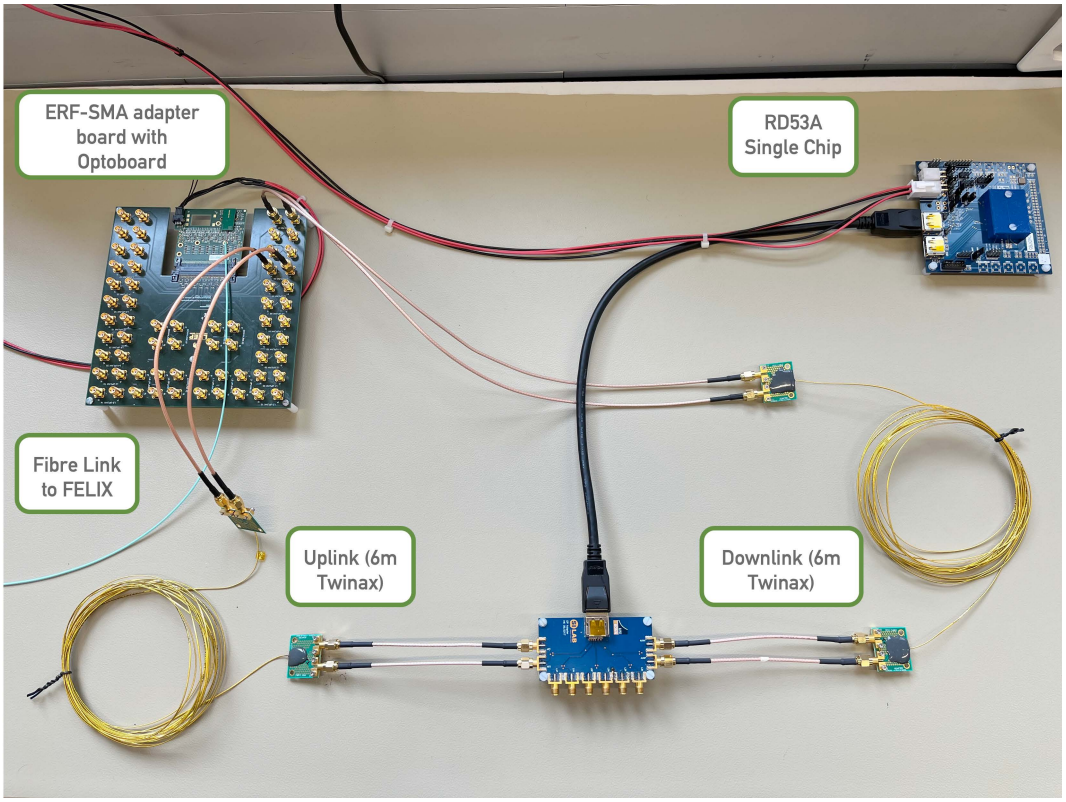

Figure 5.24: The FELIX - Optoboard - RD53a setup at the University of Bern laboratory. This prototype RD53a SCC does not have a sensor mounted and the spools for the cables have been removed.

The setup in Figure 5.24 was successfully commissioned by performing a digital scan on the RD53a FE. The digital scan consists of injecting 100 charge pulses (hits) at the output of the discriminator of the FE circuit of each pixel. In this way the digital part of the readout electronics is tested without being affected by the analogue and sensor part of the pixel, which could have damages or is non-existent. If there are pixels that do not pass the digital circuit, the hit is not count. Figure 5.25 shows the result of one digital scan.

5.5.4 ITk Pixel Detector System Tests

After successfully establishing the data transmission chain on a table-top setup without any services, an Optobox Prototype Panel (see Figure 5.26) was built for the ITk Pixel system tests [232], an intermediate step between individual prototypes and the Loaded Local Supports (LLS). The LLS will have all components coming from pre-production and are before the full ITk Pixel Detector integration, during which the production components are tested. Each sub-region of the detector has its own system test site with so-called demonstrators. These are prototype parts of the ITk Pixel Detector with a fully realistic read-out chain from the modules to the backend. Furthermore, the system tests aid in the development of the necessary infrastructure e.g. cooling, humidity, control, interlocking, DCS and powering. The tests also focus on the DAQ of

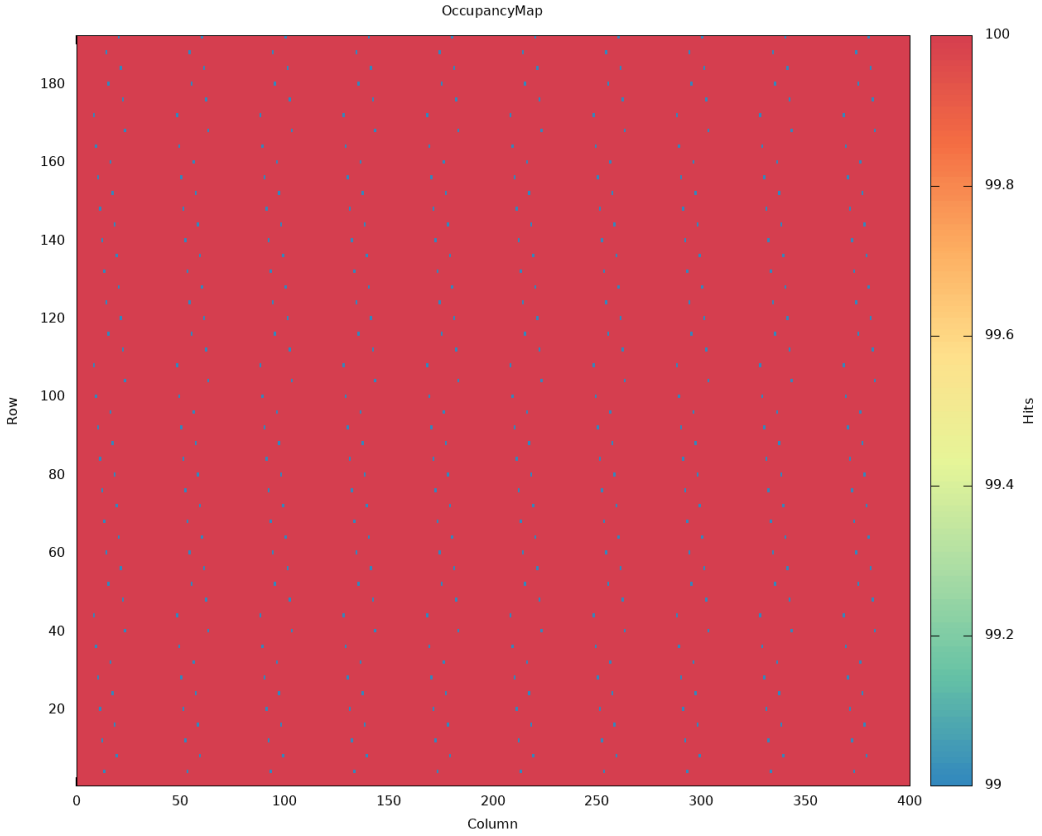

Figure 5.25: Digital scan with 100 injections per pixel with `YARR` on the RD53a, configured and readout through the Optoboard. The pixels with 99 hits are FELIX software problems due to missing triggers inside the FPGA. The x and y axis correspond to the 400 $\times$ 192 pixel matrix of the RD53a.

the serially powered modules with a full data transmission chain for comparison before and after loading the demonstrators.

The tests are carried out at three different sites and are summarised below. Due to availability at the time of measurement for this thesis, the modules used at all test sites are RD53a and ITkPix modules.

IS system test at SLAC: The Inner System system test is commissioning one fully loaded coupled ring prototype:

- one L1 outer ring with 10 planar modules
- one L0 inner ring with three 3D modules (triplets)

Each ring is powered by one SP chain. Additionally there are two half-loaded L1 staves, each with six modules and powered by one SP chain. The demonstrator was under construction but a Optobox Prototype Panel with four Optoboards was delivered to SLAC and successfully commissioned within the scope of this thesis, by establishing communication between the Optoboards and FELIX, by me.

EC system test at Liverpool: The End Caps system test is carried out with one fully loaded ring prototype with one SP chain (11 modules) per side. While working

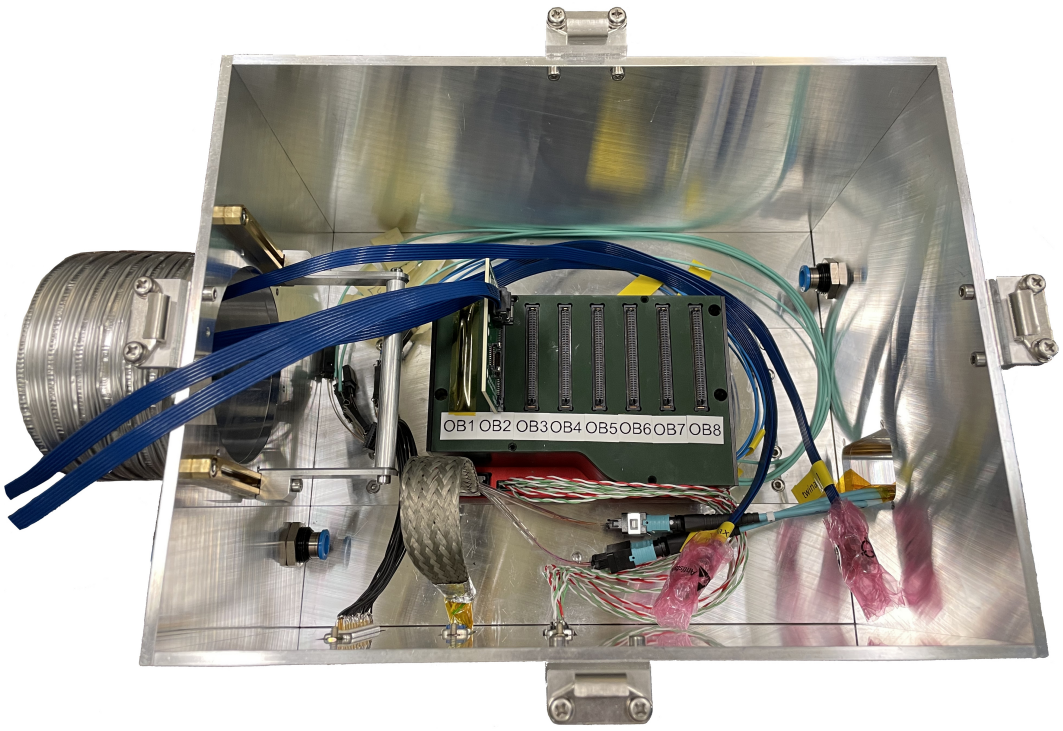

Figure 5.26: The Optobox Prototype Panel at the OB system test at CERN SR1. It houses an Optobox with seven Optoboards V2.1 including bPOL2V5s and Powerbox with bPOL12Vs. The fibres are connected to the FELIX cards about 90 m away and cooling is provided through the bottom cooling plate.

for this thesis, the demonstrator was still in construction, hence no Optobaords or Optobox Prototype Panel were delivered.

OB system test at CERN: The Outer Barrel system test consists of one longeron powered by two SP chains (6 and 12 modules). The six module chain has already been installed and is shown on Figure 5.27. At the time of commissioning the Optobox Prototype Panel the inclined half-ring, powered by one SP chain (11 modules), was not installed yet but first data taking with Sr-90 sources on six planar modules has been performed with the results shown below.

To commission all the components in the OB system test setup, a dedicated source test was carried out at six different positions. A highly collimated Sr-90 source was positioned approximately in the middle of the silicon sensor and data was taken for several hours. One can see the combined results in the form of an occupancy map, representing hits per pixel, in Figure 5.28. These results have also been published and made public in J. Instrum. 18 (2023) C03014, *System tests of the ATLAS ITk planar and 3D pixel modules* [232].

While the data taking period was limited, one can spot the red zone of the source beam spot and Surface Mounted Device (SMD) components becoming visible on the M-T-1 module (top left). For the other modules data was received but with little statistics at the available measurement time. These first occupancy results prove, with the detection of the electrons from the Sr-90 source, that all prototype

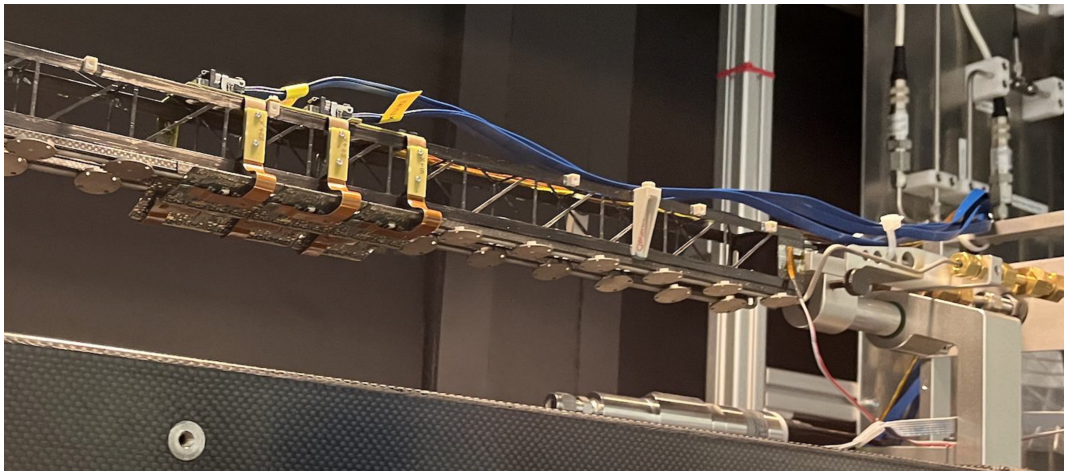

Figure 5.27: Picture of the six modules (centre left) on the carbon support structure inside the Outer Barrel system test chamber at CERN. The view shows them from below, the three modules that are slightly behind or overlapped are the bottom modules (M-B), the other three are the top modules (M-T). The modules are connected with the brownish flexible PCB pigtail that deliver power and transmit data. On top of the mechanical support (longeron) is the PP0 prototype, where the blue data cables (Twinax) are connected through firefly connectors. On the right side of the picture (and the background) there is the piping of the CO_2 cooling. Photograph taken by Brian Moser.

components work together.

In summary, the Optoboard System proves to be a reliable component of the ITk Pixel Detector data transmission chain: the Optoboard can recover an electrical PRBS7 signal with $BER_{95\%} < 2.7 \times 10^{-12}$, performing digital (and other) scans and full readout with prototype pixel sensors is successful both on table top setups and at the IS and OB system test sites. Additionally control and command of the Optoboard and its chips is simple for users and takes less than 20 s. Many Optobox Prototype Panels are, at the time of writing, in use for the LLS.

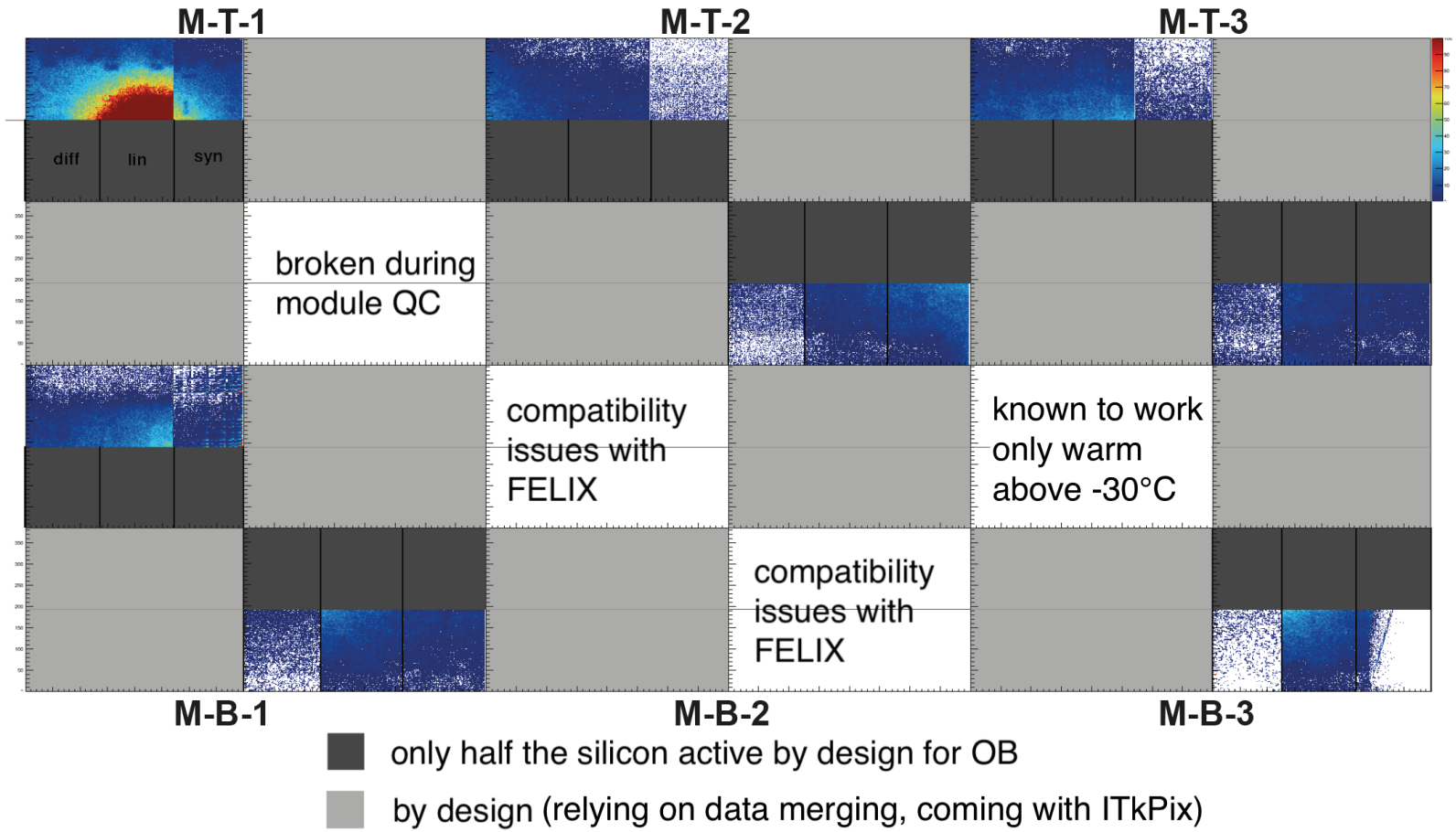

Figure 5.28: Occupancy map of six planar RD53a modules. While all FE are shown for completeness, the light grey areas are, due to design differences of the RD53a and ITkPix data handling, disabled and the dark grey areas are not active silicon sensors by design. Diff, lin, syn refer to the different implementations of the RD53a analogue FE design: differential, linear and synchronous. The areas with white background describe the problems of these front-ends at the time of measurement. Figure taken from [232].

Conclusions

Throughout my doctoral studies, I was an integral part of the ATLAS Collaboration, an experience that allowed me to co-author almost 150 ATLAS publications [233]. My engagement was notably prominent in advancing detector technology for the forthcoming HL-LHC phase and in the pursuit of testing new theories of physics beyond the SM.

The data analysis work presented in this thesis contains an interpretation in a SM precision measurement of the fiducial differential cross section for processes $pp \to \tau\tau$. Since $b \to c\tau\nu$ rates in other precision measurements of b-hadron decay fractions are in disagreement with the SM, this interpretation focused on new high-energy physics with flavour-dependent coupling to quarks and leptons, namely third generation leptoquarks. The analysis is an effort of several institutes, I carried out a sensitivity study for several LQ mass points and detector observables with Asimov data. For determining the limits on the sensitivities a framework was developed by me to use the `cabinetry` toolkit, extracting the following expected limits for the variables $m_{\mathrm{T}}^{\mathrm{total}}$, $m_{\ell\ell}$ and $\hat{s}_{\mathrm{mim}}^{1/2}$ as results: The analysis is complete but ATLAS publication rules involve

	g^2 (m_{LQ} = 1.5 TeV)	g^2 (m_{LQ} = 2 TeV)	Remark
$m_{\mathrm{T}}^{\mathrm{total}}$	$6.61^{+1.13}_{-0.95}$	$10.98^{+1.92}_{-1.65}$	with statistics & systematics
$m_{\mathrm{T}}^{\mathrm{total}}$	$5.98^{+0.99}_{-0.87}$	$10.01^{+1.70}_{-1.51}$	no MC statistics
$m_{\ell\ell}$	4.52	8.69	with statistics & systematics
$m_{\ell\ell}$	$4.40^{+0.89}_{-0.80}$	$8.44^{+1.77}_{-1.62}$	no systematics
$\hat{s}_{\mathrm{mim}}^{1/2}$	6.29	$10.92^{+1.72}_{-1.40}$	with statistics & systematics

internal acceptance processes before actual detector data is being unblinded, which did not complete yet. The limits themselves are a success as the implementation of the framework, with additional contributions to the `cabinetry` toolkit by me, that lead to the consistent treatment of negative interference terms. Having a signal parameter of interest scaling linearly and quadratically is a first for `cabinetry` thanks to this analysis. Even with the working framework the successful calculation of the likelihood minima was heavily dependent on the MC inputs provided. In some background samples and mass ranges the SM event count was very low leading to a small positive yield including the interference terms but with large statistical uncertainties reaching into the negative. Therefore careful tuning of the parameter bounds was necessary so

the fit did not terminate by reaching any infinities. That the values are comparable to the signal strength parameter λ of CMS is a success. Additionally the $m_{\mathrm{T}}^{\mathrm{total}}$ and $m_{\ell\ell}$ sensitivities with and without MC statistics or systematics, respectively, provided valuable input to the people working on the fine-tuning of the pruning. Additionally the statistical framework is in use with stronger kinematic variable cuts on the large $t\bar{t}$ background. The expected limits presented in this work are therefore an intermediate step, with better cuts the analysis will be more sensitive to leptoquarks.

The plan was to show first limits on the unblinded detector data in this thesis but the τ-fakes estimation, an external effort by other institutes, has more complexity for the τ_{had} τ_{had} region than initially thought. The data will be unblinded soon after the completion of the thesis and the publication of the full analysis is scheduled for the Moriond conference in March 2024.

Reaching higher sensitivities for leptoquarks in the future can be reached with the ATLAS ITk upgrade for the HL-LHC era. Since an analysis like to one presented in this thesis is dependent on *b*-jets detection/tagging, the ATLAS ITk upgrade will extend the reach for detecting *b*-jets up to $|\eta| = 4.0$ and increase the number of events for processes with high energetic (boosted) *b*-hadrons.

The ATLAS ITk upgrade is a necessity for dealing with the increase in instantaneous luminosity to a maximum of $7 \times 10^{34}\,\mathrm{cm}^{-2}\mathrm{s}^{-1}$ and up to 200 pile-up events. The ITk features an all-silicon design with more than 10000 pixel modules and the number of readout channels will be two orders of magnitude larger compared to the current Inner Detector. To cope with the increased data rates, a new readout system is currently in the pre-production phase. Part of the ITk Pixel Detector readout is the data transmission chain, including the Optoboard System – the main focus of this thesis.

The Optoboard System is the on-detector data aggregation and electrical-to-optical conversion stage. All hit data of the FE modules of the ITk Pixel Detector are arriving as electrical signals and get sent optically to the backend FELIX network cards. To distribute the links with minimal cable length and adjust to the complex SP scheme I assigned each module to a specific Optoboard inside the Optopanels. This is now one of the foundations for the robust pin-to-pin mapping of the ITk Pixel Detector and resulted in the first estimated electrical cable lengths between 3016 mm and 5776 mm. The actual cable lengths will be known as soon as the complete model of the ITk between modules and PP1 and Optopanels is completed, which will be the case in spring 2024.

Initially the mapping assignment was an alternative to laboratory activities due to limited access to both the university and CERN in 2020 due to COVID-19. In the end this proved to be an opportunity to develop a software `optoboard_felix` for fast and easy control of the Optoboards (also via remote during that time). The later integration of `optoboard_felix` into the ATLAS ITk Pixel System Test Microservices [234], the high-level online software for ITk pixel + strips system tests at CERN, proves the

usefulness and necessity for developing such a control tool. Since the software is in use at different LLS sites, I created a documentation website (ATLAS internal) for the Optoboard System and established a central support channel (with almost 50 members and growing) for the users of Optoboards.

With reliable control established, the transmission of electrical signals to the Optoboard is validated with BERTs and $BER_{95\%} < 2.7 \times 10^{-12}$. For a truly $BER_{95\%} < 10^{-12}$ the single measurement time would need to increase three times the amount of the maximum pattern checker capability of the lpGBT, but from the many consecutive measurements of the CTLE parameters scan the limit of 10^{-12} has been surpassed. Assuming the electrical transmission path to be the weakest link in the data transmission chain, it is safe to say that this part is under control with the right parameter settings. The near future development is to establish a “soft-error counter”, where in the FELIX backend an error counter can be enabled to analyse the data stream coming from the FE module. This enables the error checking through the full chain, including the optical signal, and uses the realistic uplink data frame instead the generic PRBS7 pattern. Furthermore the full data transmission chain with prototype FE modules was successfully tested and is heavily in use at the OB system test site at CERN. For the first time electrons from a Sr-90 were detected with the full ITk Pixel Detector data transmission chain readout. Currently efforts at all system test sites are progressing, with the OB site having installed the IL half-demonstrator, the IS site testing the L0 stave with triplets and the EC are preparing cables for the connection to the Optoboards delivered to their site.

The Optoboard System is on schedule for production and to be integrated in 2027 with the new ATLAS ITk.

Bibliography

[1] F. Dürrenmatt, *Der Mitmacher*. Diogenes Verlag, 1976. https://www.diogenes.ch/leser/titel/friedrich-duerrenmatt/der-mitmacher-9783257230543.html. Cited on page V.

[2] ATLAS Collaboration, *Observation of a new particle in the search for the Standard Model Higgs boson with the ATLAS detector at the LHC*, Phys. Lett. B **716** (2012) 1–29, arXiv:1207.7214. Cited on pages 1 and 8.

[3] CMS Collaboration, *Observation of a new boson at a mass of 125 GeV with the CMS experiment at the LHC*, Phys. Lett. B **716** (2012) 30–61, arXiv:1207.7235. Cited on pages 1 and 8.

[4] E. Corbelli and P. Salucci, *The extended rotation curve and the dark matter halo of M33*, Mon. Not. R. Astron. Soc. **311** (2000) 441–447, arXiv:9909252 [astro-ph], https://academic.oup.com/mnras/article/311/2/441/965167. Cited on pages 1 and 10.

[5] The Super-Kamiokande Collaboration, *Evidence for oscillation of atmospheric neutrinos*, Phys. Rev. Lett. **81** (1998) 1562–1567, arXiv:9807003 [hep-ex], https://journals.aps.org/prl/abstract/10.1103/PhysRevLett.81.1562. Cited on pages 1 and 10.

[6] S. P. Martin, *A supersymmetry primer*, Perspect. Supersymmetry Ii **1-153** (2010), arXiv:9709356 [hep-ph], http://www.worldscientific.com/doi/abs/10.1142/9789812839657_0001. Cited on pages 1 and 10.

[7] G. Duda and K. Garrett, *Dark matter: A primer*, Adv. Astron. **2011** (2011), arXiv:1006.2483. Cited on pages 1 and 10.

[8] LHCb Collaboration, *Test of lepton universality in beauty-quark decays*, Nat. Phys. 2022 183 **18** (2022) 277–282, arXiv:2103.11769, https://www.nature.com/articles/s41567-021-01478-8. Cited on pages 1 and 10.

[9] C. Cornella, et al., *Reading the footprints of the B-meson flavor anomalies*, J. High Energy Phys. **2021** (2021) 1–53, arXiv:2103.16558, https://link.springer.com/article/10.1007/JHEP08(2021)050. Cited on pages 1, 11, 12, and 13.

[10] ATLAS Collaboration, *Measurement of the $Z \to \tau\tau$ cross section with the ATLAS detector*, Phys. Rev. D **84** (2011) 112006, arXiv:1108.2016 [hep-ex]. Cited on page 1.

[11] ATLAS Collaboration, *Simultaneous measurements of the $t\bar{t}$, W^+W^-, and $Z/\gamma^* \to \tau\tau$ production cross-sections in pp collisions at $\sqrt{s}$ = 7 TeV with the ATLAS detector*, Phys. Rev. D **91** (2015) 52005, arXiv:1407.0573 [hep-ex]. Cited on page 1.

[12] ATLAS Collaboration, *Measurement of τ polarisation in $Z/\gamma^* \to \tau\tau$ decays in proton–proton collisions at $\sqrt{s}$ = 8 TeV with the ATLAS detector*, Eur. Phys. J. C **78** (2018) 163, arXiv:1709.03490 [hep-ex]. Cited on page 1.

[13] ATLAS Collaboration, *Evidence for the Higgs-boson Yukawa coupling to tau leptons with the ATLAS detector*, JHEP **04** (2015) 117, arXiv:1501.04943 [hep-ex]. Cited on page 1.

[14] ATLAS Collaboration, *Test of CP invariance in vector-boson fusion production of the Higgs boson in the $H \to \tau\tau$ channel in proton–proton collisions at $\sqrt{s}$ = 13 TeV with the ATLAS detector*, Phys. Lett. B **805** (2020) 135426, arXiv:2002.05315 [hep-ex]. Cited on page 1.

[15] ATLAS Collaboration, *Measurements of Higgs boson production cross-sections in the $H \to \tau^+\tau^-$ decay channel in pp collisions at $\sqrt{s}$ = 13 TeV with the ATLAS detector*, arXiv:2201.08269 [hep-ex]. Cited on page 1.

[16] ATLAS Collaboration, *Search for Heavy Higgs Bosons Decaying into Two Tau Leptons with the ATLAS Detector Using pp Collisions at $\sqrt{s}$ = 13 TeV*, Phys. Rev. Lett. **125** (2020) 51801, arXiv:2002.12223 [hep-ex]. Cited on pages 1 and 54.

[17] BABAR Collaboration, *Evidence for an excess of $\bar{B} \to D^{(*)}\tau^-\bar{\nu}_\tau$ decays*, Phys. Rev. Lett. **109** (2012) 101802, arXiv:1205.5442 [hep-ex]. Cited on page 1.

[18] LHCb Collaboration, *Measurement of the ratio of branching fractions $\mathcal{B}(\bar{B}^0 \to D^{*+}\tau^-\bar{\nu}_\tau)/\mathcal{B}(\bar{B}^0 \to D^{*+}\mu^-\bar{\nu}_\mu)$*, Phys. Rev. Lett. **115** (2015) 111803, arXiv:1506.08614 [hep-ex]. Cited on page 1.

[19] C. Cornella, et al., *Reading the footprints of the B-meson flavor anomalies*, JHEP **08** (2021) 50, arXiv:2103.16558 [hep-ph]. Cited on page 1.

[20] ATLAS Exotics Working Group, *Exotics Physics Searches*, 2023. https://twiki.cern.ch/twiki/bin/view/AtlasPublic/ExoticsPublicResults, last accessed: 2023-09-04. Cited on page 2.

[21] CMS Collaboration, *The search for a third-generation leptoquark coupling to a τ lepton and a b quark through single, pair and nonresonant production at $\sqrt{s}$ = 13 TeV*, https://cds.cern.ch/record/2815309. Cited on pages 2 and 70.

[22] OpenAI, *GPT3.5, a language model developed by OpenAI*, 2023. https://openai.com. Cited on page 3.

[23] J. Woithe, G. J. Wiener, and F. F. Van Der Veken, *Let's have a coffee with the Standard Model of particle physics!*, Phys. Educ. **52** (2017) 034001,

https://iopscience.iop.org/article/10.1088/1361-6552/aa5b25. Cited on page 5.

[24] A. Bettini, *Introduction to elementary particle physics*. Cambridge University Press, Jan, 2008. Cited on page 5.

[25] A. Purcell, *Go on a particle quest at the first CERN webfest. Le premier webfest du CERN se lance à la conquête des particules*, https://cds.cern.ch/record/1473657. Cited on page 6.

[26] S. Weinberg, *A model of leptons*, Phys. Rev. Lett. **19** (1967) 1264–1266, https://journals.aps.org/prl/abstract/10.1103/PhysRevLett.19.1264. Cited on pages 6 and 8.

[27] Particle Data Group, et al., *Review of Particle Physics*, Prog. Theor. Exp. Phys. **2022** (2022) 1–878, https://academic.oup.com/ptep/article/2022/8/083C01/6651666. Cited on pages 7, 8, and 10.

[28] R. P. Feynman, *Quantum Electrodynamics*. CRC Press, 1 ed., 1998. Cited on page 7.

[29] L. Di Lella and C. Rubbia, *60 Years of CERN Experiments and Discoveries: The Discovery of the W and Z Particles*. Sep, 2015. http://www.worldscientific.com/doi/abs/10.1142/9789814644150_0006. Cited on page 7.

[30] C. S. Wu, et al., *Experimental Test of Parity Conservation in Beta Decay*, Phys. Rev. **105** (1957) 1413–1415, https://journals.aps.org/pr/abstract/10.1103/PhysRev.105.1413. Cited on page 7.

[31] R. L. Garwin, L. M. Lederman, and M. Weinrich, *Observations of the failure of conservation of parity and charge conjugation in meson decays: The magnetic moment of the free muon*, Phys. Rev. **105** (1957) 1415–1417, https://journals.aps.org/pr/abstract/10.1103/PhysRev.105.1415. Cited on page 7.

[32] C. S. Wu, *The discovery of the parity violation in weak interactions and its recent developments*, Lect. Notes Phys. **746** (2008) 43–70, https://link.springer.com/chapter/10.1007/978-4-431-77056-5_4. Cited on page 7.

[33] W. Greiner and B. Müller, *Gauge theory of Weak Interactions*. Springer Berlin, Heidelberg, 4 ed., 2009. Cited on page 8.

[34] A. Salam and J. C. Ward, *Electromagnetic and weak interactions*, Phys. Lett. **13** (1964) 168–171. Cited on page 8.

[35] L. Süsskind, *Dynamics of spontaneous symmetry breaking in the Weinberg-Salam theory*, Phys. Rev. D **20** (1979) 2619, https://journals.aps.org/prd/abstract/10.1103/PhysRevD.20.2619. Cited on page 8.

[36] T. W. Kibble, *Spontaneous symmetry breaking in gauge theories*, Philos. Trans. R. Soc. A Math. Phys. Eng. Sci. **373** (2015), https://royalsocietypublishing.org/doi/10.1098/rsta.2014.0033. Cited on page 8.

[37] Particle Data Group, *Review of Particle Physics*, PTEP **2022** (2022) 083C01. Cited on pages 8 and 9.

[38] J. Greensite, *An Introduction to the Confinement Problem*. Lecture Notes in Physics. Springer Berlin Heidelberg, Berlin, Heidelberg, 1 ed., 2011. https://link.springer.com/10.1007/978-3-642-14382-3. Cited on page 8.

[39] The LHCb Collaboration, *Observation of $J/\psi p$ Resonances Consistent with Pentaquark States in $\Lambda_b^0 \to J/\psi K^- p$ Decays*, Phys. Rev. Lett. **115** (2015) 072001, https://journals.aps.org/prl/abstract/10.1103/PhysRevLett.115.072001. Cited on page 8.

[40] A. Einstein, *Die Grundlage der allgemeinen Relativitätstheorie*, Ann. Phys. **354** (1916) 769–822. Cited on page 9.

[41] C. W. Misner, K. S. Thorne, and J. A. Wheeler, *Gravitation*. Princeton University Press, Oct, 2017. https://press.princeton.edu/books/hardcover/9780691177793/gravitation. Cited on page 9.

[42] R. Abbott, et al., *Tests of general relativity with binary black holes from the second LIGO-Virgo gravitational-wave transient catalog*, Phys. Rev. D **103** (2021) 122002, arXiv:2010.14529, https://journals.aps.org/prd/abstract/10.1103/PhysRevD.103.122002. Cited on page 10.

[43] ATLAS Collaboration, *SUSY March 2023 Summary Plot Update*, Mar, 2023. https://cds.cern.ch/record/2852738. Cited on page 10.

[44] E. Graverini, ATLAS Collaboration, CMS Collaboration, and LHCb Collaboration, *Flavour anomalies: a review*, J. Phys. Conf. Ser. **1137** (2019) 012025, arXiv:1807.11373, https://iopscience.iop.org/article/10.1088/1742-6596/1137/1/012025. Cited on page 10.

[45] U. Haisch, L. Schnell, and S. Schulte, *Drell-Yan production in third-generation gauge vector leptoquark models at NLO+PS in QCD*, J. High Energy Phys. **2023** (2023) 1–27, arXiv:2209.12780, https://link.springer.com/article/10.1007/JHEP02(2023)070. Cited on page 11.

[46] ATLAS Collaboration, *The ATLAS experiment at the CERN large hadron collider*, JINST **3** (2008) S08003. Cited on pages 15, 22, 27, and 29.

[47] CMS Collaboration, *The CMS experiment at the CERN LHC*, J. Instrum. **3** (2008) S08004, https://iopscience.iop.org/article/10.1088/1748-0221/3/08/S08004. Cited on page 15.

[48] ALICE Collaboration, *The ALICE experiment at the CERN LHC*, J. Instrum. **3** (2008) S08002, https://iopscience.iop.org/article/10.1088/1748-0221/3/08/S08002. Cited on page 15.

[49] LHCb Collaboration, *The LHCb Detector at the LHC*, J. Instrum. **3** (2008) S08005, https://iopscience.iop.org/article/10.1088/1748-0221/3/08/S08005. Cited on page 15.

[50] L. Evans and P. Bryant, *LHC Machine*, J. Instrum. **3** (2008) S08001, https://iopscience.iop.org/article/10.1088/1748-0221/3/08/S08001. Cited on page 15.

[51] O. S. Brüning, et al., *LHC Design Report*, Cern. Geneva **1** (2004) 548, https://cds.cern.ch/record/782076. Cited on page 15.

[52] R. Steerenberg, et al., *Operation and performance of the CERN Large Hadron Collider during proton Run 2*, 10th Int. Part. Accel. Conf. (2019) 504–507, http://cds.cern.ch/record/2696126. Cited on pages 16 and 17.

[53] TOTEM Collaboration, *The TOTEM experiment at the CERN Large Hadron Collider*, J. Instrum. **3** (2008) S08007, https://iopscience.iop.org/article/10.1088/1748-0221/3/08/S08007. Cited on page 16.

[54] E. Lopienska, *The CERN accelerator complex, layout in 2022*, Feb, 2022. https://cds.cern.ch/record/2800984. Cited on page 18.

[55] L. Arnaudon, et al., *Linac4 Technical Design Report*, tech. rep., CERN, Dec, 2006. https://cds.cern.ch/record/1004186. Cited on page 16.

[56] R. Steerenberg, et al., *Fifty years of the CERN Proton Synchrotron : Volume 1*, tech. rep., 2011. https://cds.cern.ch/record/1359959. Cited on page 17.

[57] S. Myers and E. Picasso, *The design, construction and commissioning of the CERN large Electron–Positron collider*, Contemp. Phys. **31** (1990) 387–403, https://www.tandfonline.com/doi/abs/10.1080/00107519008213789. Cited on page 17.

[58] J. Casas, et al., *Design concept and first experimental validation of the superfluid helium system for the Large Hadron Collider (LHC) project at CERN*, Cryogenics (Guildf). **32** (1992) 118–121. Cited on page 17.

[59] J. P. Blewett, *200-GeV Intersecting Storage Accelerators*, eConf **C710920** (1971) 501, https://lss.fnal.gov/conf/C710920/p501.pdf. Cited on page 17.

[60] ATLAS Collaboration, *Public ATLAS Luminosity Results for Run-3 of the LHC*, Mar, 2023. https://twiki.cern.ch/twiki/bin/view/AtlasPublic/LuminosityPublicResultsRun3, last accessed: 2023-04-24. Cited on page 19.

[61] The HighLumi Collaboration, *LS3 schedule change | High Luminosity LHC Project*, Mar, 2022. https://hilumilhc.web.cern.ch/article/ls3-schedule-change, last accessed: 2023-04-24. Cited on page 19.

[62] I. Béjar Alonso, et al., *High-Luminosity Large Hadron Collider (HL-LHC): Technical design report*, tech. rep., CERN, Dec, 2020. https://e-publishing.cern.ch/index.php/CYRM/issue/view/127. Cited on pages 18 and 19.

[63] O. Brüning and L. Rossi, *The High Luminosity Large Hadron Collider*. World Scientific, 2015. https://www.worldscientific.com/doi/abs/10.1142/9581. Cited on page 19.

[64] R. Ostojic, T. M. Taylor, and S. Weisz, *Systems layout of the low beta insertions for the LHC experiments*, in *17th IEEE Part. Accel. Conf. (PAC 97) Accel. Sci. Technol. Appl.* 1997. Cited on page 19.

[65] J. Pequenao, *Computer generated image of the ATLAS Liquid Argon*, 2008. https://cds.cern.ch/record/1095928. Cited on page 21.

[66] ATLAS Collaboration, *ATLAS inner detector : Technical Design Report, 1*, tech. rep., 1997. https://cds.cern.ch/record/331063. Cited on page 22.

[67] J. Pequenao, *Computer generated image of the ATLAS inner detector*, Mar, 2008. https://cds.cern.ch/record/1095926. Cited on page 22.

[68] ATLAS Collaboration, *ATLAS pixel detector: Technical Design Report*, tech. rep., 1998. https://cds.cern.ch/record/381263. Cited on page 22.

[69] ATLAS Collaboration, *ATLAS pixel detector electronics and sensors*, J. Instrum. **3** (2008) P07007, https://iopscience.iop.org/article/10.1088/1748-0221/3/07/P07007. Cited on pages 22 and 30.

[70] ATLAS Collaboration, *ATLAS Insertable B-Layer Technical Design Report*, tech. rep., Sep, 2010. https://cds.cern.ch/record/1291633. Cited on page 23.

[71] ATLAS Collaboration, *ATLAS Insertable B-Layer Technical Design Report Addendum*, Tech. Rep. May, May, 2012. https://cds.cern.ch/record/1451888. Cited on page 23.

[72] ATLAS Collaboration, *Track Reconstruction Performance of the ATLAS Inner Detector at $\sqrt{s}$=13 TeV*, tech. rep., CERN, Jul, 2015. https://cds.cern.ch/record/2037683. Cited on page 23.

[73] ATLAS Collaboration, *Operation and performance of the ATLAS semiconductor tracker*, J. Instrum. **9** (2014) P08009, arXiv:1404.7473, https://iopscience.iop.org/article/10.1088/1748-0221/9/08/P08009. Cited on page 23.

[74] F. Campabadal, et al., *Design and performance of the ABCD3TA ASIC for readout of silicon strip detectors in the ATLAS semiconductor tracker*, Nucl. Instruments Methods Phys. Res. Sect. A Accel. Spectrometers, Detect. Assoc. Equip. **552** (2005) 292–328. Cited on page 24.

[75] ATLAS TRT Collaboration, *The ATLAS Transition Radiation Tracker (TRT) proportional drift tube: design and performance*, J. Instrum. **3** (2008) P02013, https://iopscience.iop.org/article/10.1088/1748-0221/3/02/P02013. Cited on page 24.

[76] ATLAS TRT Collaboration, *The ATLAS TRT Barrel Detector*, J. Instrum. **3** (2008) P02014, https://iopscience.iop.org/article/10.1088/1748-0221/3/02/P02014. Cited on page 24.

[77] ATLAS TRT Collaboration, *The ATLAS TRT end-cap detectors*, J. Instrum. **3** (2008) P10003, https://iopscience.iop.org/article/10.1088/1748-0221/3/10/P10003. Cited on page 24.

[78] ATLAS Collaboration, *ATLAS liquid-argon calorimeter: Technical Design Report*. Technical design report. ATLAS. CERN, Geneva, 1996. https://cds.cern.ch/record/331061. Cited on page 25.

[79] ATLAS Collaboration, *ATLAS tile calorimeter: Technical Design Report*. Technical design report. ATLAS. CERN, Geneva, 1996. https://cds.cern.ch/record/331062. Cited on page 25.

[80] J. Pequenao, *Computer Generated image of the ATLAS calorimeter*, Mar, 2008. https://cds.cern.ch/record/1095927. Cited on page 26.

[81] ATLAS Collaboration, *ATLAS muon spectrometer: Technical Design Report*. Technical design report. ATLAS. CERN, Geneva, 1997. https://cds.cern.ch/record/331068. Cited on page 26.

[82] J. Pequenao, *Computer generated image of the ATLAS Muons subsystem*, Mar, 2008. https://cds.cern.ch/record/1095929. Cited on page 27.

[83] ATLAS TDAQ Collaboration, *The ATLAS Data Acquisition and High Level Trigger system*, J. Instrum. **11** (2016) P06008, https://iopscience.iop.org/article/10.1088/1748-0221/11/06/P06008. Cited on page 29.

[84] ATLAS Collaboration, *Technical Design Report for the Phase-I Upgrade of the ATLAS TDAQ System*, tech. rep., 2013. https://cds.cern.ch/record/1602235. Cited on page 29.

[85] ATLAS Collaboration, *Performance of the ATLAS trigger system in 2015*, Eur. Phys. J. C 2017 775 **77** (2017) 1–53, arXiv:1611.09661, https://link.springer.com/article/10.1140/epjc/s10052-017-4852-3. Cited on page 29.

[86] ATLAS Collaboration, *Approved Plots DAQ*, 2017. https://twiki.cern.ch/twiki/bin/view/AtlasPublic/ApprovedPlotsDAQ, last accessed: 2023-05-31. Cited on pages 29 and 31.

[87] E. G. Taylor, *TTC Distribution for LHC Detectors*, IEEE Trans. Nucl. Sci. **45** (1998) 821–828. Cited on page 31.

[88] S. Ask, et al., *The ATLAS central level-1 trigger logic and TTC system*, J. Instrum. **3** (2008) P08002, https://iopscience.iop.org/article/10.1088/1748-0221/3/08/P08002. Cited on page 31.

[89] A. Barriuso Poy, et al., *The detector control system of the ATLAS experiment*, J. Instrum. **3** (2008) P05006, https://iopscience.iop.org/article/10.1088/1748-0221/3/05/P05006. Cited on page 32.

[90] ATLAS Collaboration, *Technical Design Report for the ATLAS Inner Tracker Pixel Detector*, tech. rep., CERN, Geneva, 2017. https://cds.cern.ch/record/2285585. Cited on pages 33 and 34.

[91] ATLAS Collaboration, *Technical Design Report for the ATLAS Inner Tracker Strip Detector*, tech. rep., CERN, Geneva, 2017. https://cds.cern.ch/record/2257755. Cited on page 33.

[92] ATLAS Collaboration, *Expected tracking and related performance with the updated ATLAS Inner Tracker layout at the High-Luminosity LHC*, Jul, 2021. https://cds.cern.ch/record/2776651https://atlas.web.cern.ch/Atlas/GROUPS/PHYSICS/PUBNOTES/ATL-PHYS-PUB-2021-024/. Cited on pages 33, 34, and 35.

[93] W. Mccormack and ATLAS Collaboration, *Pixel-cluster counting luminosity measurement in ATLAS*, Proc. Sci. **282** (2017) 1064, http://pos.sissa.it/. Cited on page 34.

[94] B. MačEk, et al., *Development of a System for Beam Abort and Luminosity Determination at the HL-LHC based on polycrystalline CVD diamond*, J. Phys. Conf. Ser. **2374** (2022) 012056, https://iopscience.iop.org/article/10.1088/1742-6596/2374/1/012056. Cited on page 35.

[95] J. Chistiansen and M. Garcia-Sciveres, *RD Collaboration Proposal: Development of pixel readout integrated circuits for extreme rate and radiation*, Tech. Rep. CERN-LHCC-2013-008. LHCC-P-006, CERN, Geneva, Jun, 2013. https://cds.cern.ch/record/1553467. Cited on page 35.

[96] M. Samy, et al., *Cold temperature characterization of ring triplets based on RD53A readout chip*, J. Instrum. **17** (2022) C11005, https://iopscience.iop.org/article/10.1088/1748-0221/17/11/C11005. Cited on page 35.

[97] M. Garcia-Sciveres and RD53 Collaboration, *RD53A Integrated Circuit Specifications*, tech. rep., CERN, Geneva, 2015. https://cds.cern.ch/record/2113263. Cited on page 35.

[98] S. Marconi, et al., *Design implementation and test results of the RD53A, a 65 nm large scale chip for next generation pixel detectors at the HL-LHC*, 2018 IEEE Nucl. Sci. Symp. Med. Imaging Conf. Proc. (2018) 1–4. Cited on page 35.

[99] L. Gaioni, *Test results and prospects for RD53A, a large scale 65 nm CMOS chip for pixel readout at the HL-LHC*, Nucl. Instruments Methods Phys. Res. Sect. A Accel. Spectrometers, Detect. Assoc. Equip. **936** (2019) 282–285. Cited on page 35.

[100] M. Garcia-Sciveres and RD53 Collaboration, *RD53B Design Requirements*, tech. rep., CERN, Geneva, 2019. https://cds.cern.ch/record/2663161. Cited on page 35.

[101] M. Garcia-Sciveres, F. Loddo, J. Christiansen, and RD53 Collaboration, *RD53B Manual*, tech. rep., CERN, Geneva, 2019. https://cds.cern.ch/record/2665301. Cited on page 35.

[102] ATLAS Collaboration, *ITk Pixel Layout Updates*, Apr, 2020. https://atlas.web.cern.ch/Atlas/GROUPS/PHYSICS/PLOTS/ITK-2020-002/, last accessed: 2023-06-05. Cited on pages 36 and 161.

[103] D. Ta, et al., *Serial powering: Proof of principle demonstration of a scheme for the operation of a large pixel detector at the LHC*, Nucl. Instruments Methods Phys. Res. Sect. A Accel. Spectrometers, Detect. Assoc. Equip. **557** (2006) 445–459, https://linkinghub.elsevier.com/retrieve/pii/S016890020502214X. Cited on page 36.

[104] V. Filimonov, et al., *A serial powering pixel stave prototype for the ATLAS ITk upgrade*, J. Instrum. **12** (2017) C03045, https://iopscience.iop.org/article/10.1088/1748-0221/12/03/C03045. Cited on pages 36 and 37.

[105] F. Hinterkeuser and ATLAS ITk Collaboration, *Prototyping Serial Powering with RD53A and ITkPixV1*, Proc. Sci. **414** (2022) 689, https://pos.sissa.it/. Cited on page 36.

[106] J. Kampkötter, et al., *Characterization and verification of the Shunt-LDO regulator and its protection circuits for serial powering of the ATLAS and CMS pixel detectors*, J. Phys. Conf. Ser. **2374** (2022) 012071, https://iopscience.iop.org/article/10.1088/1742-6596/2374/1/012071. Cited on page 37.

[107] A. Sopczak, *Searches for Leptoquarks with the ATLAS Detector*, arXiv:2107.10094, https://cds.cern.ch/record/2775380/. Cited on page 39.

[108] F. Romeo, ATLAS Collaboration, and CMS Collaboration, *Search for leptoquark-like signatures with the ATLAS and CMS detectors*, Nucl. Part. Phys. Proc. **273-275** (2016) 638–643. Cited on page 39.

[109] A. Buckley, et al., *General-purpose event generators for LHC physics*, Phys. Rep. **504** (2011) 145–233, arXiv:1101.2599. Cited on page 40.

[110] T. Gleisberg, et al., *Event generation with SHERPA 1.1*, J. High Energy Phys. **2009** (2009) 007, arXiv:0811.4622, https://iopscience.iop.org/article/10.1088/1126-6708/2009/02/007. Cited on page 41.

[111] J. C. Collins, D. E. Soper, and G. Sterman, *Factorization for short distance hadron-hadron scattering*, Nucl. Phys. B **261** (1985) 104–142. Cited on page 40.

[112] S. Agostinelli, et al., *Geant4—a simulation toolkit*, Nucl. Instruments Methods Phys. Res. Sect. A Accel. Spectrometers, Detect. Assoc. Equip. **506** (2003) 250–303. Cited on page 40.

[113] E. Bothmann and Others, *Event generation with Sherpa 2.2*, SciPost Phys. **7** (2019) 34, arXiv:1905.09127 [hep-ph]. Cited on pages 42 and 44.

[114] T. Gleisberg and S. Höche, *Comix, a new matrix element generator*, JHEP **12** (2008) 39, arXiv:0808.3674 [hep-ph]. Cited on pages 42 and 44.

[115] F. Buccioni, et al., *OpenLoops 2*, Eur. Phys. J. C **79** (2019) 866, arXiv:1907.13071 [hep-ph]. Cited on pages 42 and 44.

[116] F. Cascioli, P. Maierhöfer, and S. Pozzorini, *Scattering Amplitudes with Open Loops*, Phys. Rev. Lett. **108** (2012) 111601, arXiv:1111.5206 [hep-ph]. Cited on pages 42 and 44.

[117] A. Denner, S. Dittmaier, and L. Hofer, COLLIER*: A fortran-based complex one-loop library in extended regularizations*, Comput. Phys. Commun. **212** (2017) 220–238, arXiv:1604.06792 [hep-ph]. Cited on pages 42 and 44.

[118] S. Schumann and F. Krauss, *A parton shower algorithm based on Catani–Seymour dipole factorisation*, JHEP **03** (2008) 38, arXiv:0709.1027 [hep-ph]. Cited on pages 42 and 44.

[119] S. Höche, F. Krauss, M. Schönherr, and F. Siegert, *A critical appraisal of NLO+PS matching methods*, JHEP **09** (2012) 49, arXiv:1111.1220 [hep-ph]. Cited on pages 42 and 44.

[120] S. Höche, F. Krauss, M. Schönherr, and F. Siegert, *QCD matrix elements + parton showers. The NLO case*, JHEP **04** (2013) 27, arXiv:1207.5030 [hep-ph]. Cited on pages 42 and 44.

[121] S. Catani, F. Krauss, B. R. Webber, and R. Kuhn, *QCD Matrix Elements + Parton Showers*, JHEP **11** (2001) 63, arXiv:0109231 [hep-ph]. Cited on pages 42 and 44.

[122] S. Höche, F. Krauss, S. Schumann, and F. Siegert, *QCD matrix elements and truncated showers*, JHEP **05** (2009) 53, arXiv:0903.1219 [hep-ph]. Cited on pages 42 and 44.

[123] R. D. Ball and Others, *Parton distributions for the LHC run II*, JHEP **04** (2015) 40, arXiv:1410.8849 [hep-ph]. Cited on pages 42, 43, and 44.

[124] P. Nason, *A new method for combining NLO QCD with shower Monte Carlo algorithms*, JHEP **11** (2004) 40, arXiv:0409146 [hep-ph]. Cited on pages 42 and 43.

[125] S. Frixione, P. Nason, and C. Oleari, *Matching NLO QCD computations with parton shower simulations: the POWHEG method*, JHEP **11** (2007) 70, arXiv:0709.2092 [hep-ph]. Cited on pages 42 and 43.

[126] S. Alioli, P. Nason, C. Oleari, and E. Re, *A general framework for implementing NLO calculations in shower Monte Carlo programs: the POWHEG BOX*, JHEP **06** (2010) 43, arXiv:1002.2581 [hep-ph]. Cited on pages 42 and 43.

[127] S. Alioli, P. Nason, C. Oleari, and E. Re, *NLO vector-boson production matched with shower in POWHEG*, JHEP **07** (2008) 60, arXiv:0805.4802 [hep-ph]. Cited on page 42.

[128] T. Sjöstrand, S. Mrenna, and P. Skands, *A brief introduction to PYTHIA 8.1*, Comput. Phys. Commun. **178** (2008) 852–867, arXiv:0710.3820 [hep-ph]. Cited on pages 42 and 44.

[129] ATLAS Collaboration, *Measurement of the Z/γ^* boson transverse momentum distribution in pp collisions at $\sqrt{s}$ = 7 TeV with the ATLAS detector*, JHEP **09** (2014) 145, arXiv:1406.3660 [hep-ex]. Cited on page 42.

[130] H.-L. Lai and Others, *New parton distributions for collider physics*, Phys. Rev. D **82** (2010) 74024, arXiv:1007.2241 [hep-ph]. Cited on page 42.

[131] J. Pumplin and Others, *New Generation of Parton Distributions with Uncertainties from Global QCD Analysis*, JHEP **07** (2002) 12, arXiv:0201195 [hep-ph]. Cited on page 42.

[132] P. Golonka and Z. Was, *PHOTOS Monte Carlo: a precision tool for QED corrections in Z and W decays*, Eur. Phys. J. C **45** (2006) 97–107, arXiv:0506026 [hep-ph]. Cited on page 42.

[133] N. Davidson, T. Przedzinski, and Z. Was, *PHOTOS Interface in C++: Technical and physics documentation*, Comput. Phys. Commun. **199** (2016) 86–101, arXiv:1011.0937 [hep-ph]. Cited on page 42.

[134] D. J. Lange, *The EvtGen particle decay simulation package*, Nucl. Instrum. Meth. A **462** (2001) 152. Cited on pages 42, 43, and 44.

[135] S. Frixione, G. Ridolfi, and P. Nason, *A positive-weight next-to-leading-order Monte Carlo for heavy flavour hadroproduction*, JHEP **09** (2007) 126, arXiv:0707.3088 [hep-ph]. Cited on pages 42 and 43.

[136] ATLAS Collaboration, *Studies on top-quark Monte Carlo modelling for Top2016*, Atl-phys-pub-2016-020, 2016, https://cds.cern.ch/record/2216168. Cited on pages 42 and 55.

[137] T. Sjöstrand, et al., *An introduction to PYTHIA 8.2*, Comput. Phys. Commun. **191** (2015) 159, arXiv:1410.3012 [hep-ph]. Cited on pages 42, 43, and 44.

[138] ATLAS Collaboration, *ATLAS Pythia 8 tunes to 7 TeV data*, Atl-phys-pub-2014-021, 2014, https://cds.cern.ch/record/1966419. Cited on pages 42, 43, and 44.

[139] R. D. Ball and Others, *Parton distributions with LHC data*, Nucl. Phys. B **867** (2013) 244, arXiv:1207.1303 [hep-ph]. Cited on pages 42, 43, and 44.

[140] M. Bähr and Others, *Herwig++ physics and manual*, Eur. Phys. J. C **58** (2008) 639, arXiv:0803.0883 [hep-ph]. Cited on page 43.

[141] J. Bellm and Others, *Herwig 7.0/Herwig++ 3.0 release note*, Eur. Phys. J. C **76** (2016) 196, arXiv:1512.01178 [hep-ph]. Cited on page 43.

[142] L. A. Harland-Lang, A. D. Martin, P. Motylinski, and R. S. Thorne, *Parton distributions in the LHC era: MMHT 2014 PDFs*, Eur. Phys. J. C **75** (2015) 204, arXiv:1412.3989 [hep-ph]. Cited on page 43.

[143] J. Alwall, et al., *The automated computation of tree-level and next-to-leading order differential cross sections, and their matching to parton shower simulations*, JHEP **07** (2014) 79, arXiv:1405.0301 [hep-ph]. Cited on pages 43 and 44.

[144] E. Re, *Single-top Wt-channel production matched with parton showers using the POWHEG method*, Eur. Phys. J. C **71** (2011) 1547, arXiv:1009.2450 [hep-ph]. Cited on page 43.

[145] S. Frixione, et al., *Single-top hadroproduction in association with a W boson*, JHEP **07** (2008) 29, arXiv:0805.3067 [hep-ph]. Cited on pages 43 and 55.

[146] R. Frederix, E. Re, and P. Torrielli, *Single-top t-channel hadroproduction in the four-flavour scheme with POWHEG and aMC@NLO*, JHEP **09** (2012) 130, arXiv:1207.5391 [hep-ph]. Cited on page 43.

[147] S. Alioli, P. Nason, C. Oleari, and E. Re, *NLO single-top production matched with shower in POWHEG: s- and t-channel contributions*, JHEP **09** (2009) 111, arXiv:0907.4076 [hep-ph]. Cited on page 43.

[148] L. Lönnblad, *Correcting the Colour-Dipole Cascade Model with Fixed Order Matrix Elements*, JHEP **05** (2002) 46, arXiv:0112284 [hep-ph]. Cited on page 44.

[149] L. Lönnblad and S. Prestel, *Matching tree-level matrix elements with interleaved showers*, JHEP **03** (2012) 19, arXiv:1109.4829 [hep-ph]. Cited on page 44.

[150] I. Doršner and A. Greljo, *Leptoquark toolbox for precision collider studies*, J. High Energy Phys. **2018** (2018), arXiv:1801.07641v2, http://arxiv.org/abs/1801.07641. Cited on page 44.

[151] M. Cacciari, G. P. Salam, and G. Soyez, *FastJet user manual*, Eur. Phys. J. C **72** (2012) 1896, arXiv:1111.6097 [hep-ph]. Cited on page 46.

[152] M. Cacciari, G. P. Salam, and G. Soyez, *The anti-k_t jet clustering algorithm*, JHEP **04** (2008) 63, arXiv:0802.1189 [hep-ph]. Cited on page 46.

[153] ATLAS Collaboration, *Reconstruction, Identification, and Calibration of hadronically decaying tau leptons with the ATLAS detector for the LHC Run 3 and reprocessed Run 2 data*, tech. rep., CERN, Geneva, 2022. https://cds.cern.ch/record/2827111. Cited on page 46.

[154] ATLAS Collaboration, *Electron reconstruction and identification in the ATLAS experiment using the 2015 and 2016 LHC proton–proton collision data at $\sqrt{s}$ = 13 TeV*, Eur. Phys. J. C **79** (2019) 639, arXiv:1902.04655 [hep-ex]. Cited on page 47.

[155] ATLAS Collaboration and M. Klein, *Official Isolation Working Points*, Feb, 2020. https://twiki.cern.ch/twiki/bin/view/Sandbox/MatthewKleinSandbox, last accessed: 2023-08-08. Cited on page 47.

[156] ATLAS Collaboration, *Muon reconstruction and identification efficiency in ATLAS using the full Run 2 pp collision data set at $\sqrt{s}$ = 13 TeV*, Eur. Phys. J. C **81** (2021) 578, arXiv:2012.00578 [hep-ex]. Cited on page 47.

[157] ATLAS Collaboration, *Electron and photon performance measurements with the ATLAS detector using the 2015–2017 LHC proton–proton collision data*, JINST **14** (2019) P12006, arXiv:1908.00005 [hep-ex]. Cited on page 47.

[158] ATLAS Collaboration, *Muon reconstruction performance of the ATLAS detector in proton–proton collision data at $\sqrt{s}$ = 13 TeV*, Eur. Phys. J. C **76** (2016) 292, arXiv:1603.05598 [hep-ex]. Cited on page 47.

[159] ATLAS Collaboration, *Jet energy scale and resolution measured in proton–proton collisions at $\sqrt{s}$ = 13 TeV with the ATLAS detector*, Eur. Phys. J. C **81** (2020) 689, arXiv:2007.02645 [hep-ex]. Cited on page 47.

[160] ATLAS Collaboration, *Tagging and suppression of pileup jets with the ATLAS detector*, Atlas-conf-2014-018, 2014, https://cds.cern.ch/record/1700870. Cited on page 47.

[161] ATLAS Collaboration, *ATLAS b-jet identification performance and efficiency measurement with $t\bar{t}$ events in pp collisions at $\sqrt{s}$ = 13 TeV*, Eur. Phys. J. C **79** (2019) 970, arXiv:1907.05120 [hep-ex]. Cited on page 47.

[162] ATLAS Collaboration, *Measurement of the c-jet mistagging efficiency in $t\bar{t}$ events using pp collision data at $\sqrt{s}$ = 13 TeV collected with the ATLAS detector*, Eur. Phys. J. C **82** (2021) 95, arXiv:2109.10627 [hep-ex]. Cited on page 47.

[163] ATLAS Collaboration, *Calibration of light-flavour b-jet mistagging rates using ATLAS proton–proton collision data at $\sqrt{s}$ = 13 $\sim$ TeV*, Atlas-conf-2018-006, 2018, https://cds.cern.ch/record/2314418. Cited on page 47.

[164] A. K. Swain and P. Konar, *Constrained $\sqrt{\hat{s}_{min}}$ and reconstructing with semi-invisible production at hadron colliders*, JHEP **03** (2015) 142, arXiv:1412.6624 [hep-ph]. Cited on page 48.

[165] P. Konar, K. Kong, K. T. Matchev, and M. Park, *RECO level $\sqrt{s}_{min}$ and subsystem $\sqrt{s}_{min}$: Improved global inclusive variables for measuring the new physics mass scale in E_T events at hadron colliders*, JHEP **06** (2011) 41, arXiv:1006.0653 [hep-ph]. Cited on page 48.

[166] A. Elagin, P. Murat, A. Pranko, and A. Safonov, *A New Mass Reconstruction Technique for Resonances Decaying to di-tau*, Nucl. Instrum. Meth. A **654** (2011) 481–489, arXiv:1012.4686 [hep-ex]. Cited on page 49.

[167] ATLAS Collaboration, *Performance of the ATLAS muon triggers in Run 2*, JINST **15** (2020) P09015, arXiv:2004.13447 [hep-ex]. Cited on page 51.

[168] ATLAS Collaboration, *Performance of electron and photon triggers in ATLAS during LHC Run 2*, Eur. Phys. J. C **80** (2020) 47, arXiv:1909.00761 [hep-ex]. Cited on page 51.

[169] ATLAS Collaboration, *The ATLAS Tau Trigger in Run 2*, Atlas-conf-2017-061, 2017, https://cds.cern.ch/record/2274201. Cited on page 51.

[170] *Search for resonant and non-resonant Higgs boson pair production in the $b\bar{b}\tau^+\tau^-$ decay channel using 13 TeV pp collision data from the ATLAS detector*, arXiv:2209.10910 [hep-ex]. Cited on page 54.

[171] ATLAS Collaboration, *Search for scalar leptoquarks in the $b\tau\tau$ final state in pp collisions at $\sqrt{s}$ = 13, TeV with the ATLAS detector*, Atlas-conf-2022-037, 2022, https://cds.cern.ch/record/2815283. Cited on page 54.

[172] J. Butterworth and Others, *PDF4LHC recommendations for LHC Run II*, J. Phys. G **43** (2016) 23001, arXiv:1510.03865 [hep-ph]. Cited on page 55.

[173] A. L. Read, *Presentation of search results: the CL_S technique*, J. Phys. G **28** (2002) 2693. Cited on page 60.

[174] G. Cowan, K. Cranmer, E. Gross, and O. Vitells, *Asymptotic formulae for likelihood-based tests of new physics*, Eur. Phys. J. C **71** (2011) 1554, arXiv:1007.1727 [physics.data-an]. Cited on page 60.

[175] L. Heinrich, M. Feickert, G. Stark, and K. Cranmer, *pyhf: pure-Python implementation of HistFactory statistical models*, J. Open Source Softw. **6** (2021) 2823, https://doi.org/10.21105/joss.02823. Cited on page 60.

[176] K. Cranmer, et al., *HistFactory: A tool for creating statistical models for use with RooFit and RooStats*, tech. rep., CERN, 2012. https://cds.cern.ch/record/1456844/. Cited on page 60.

[177] K. Cranmer and A. Held, *Building and steering binned template fits with cabinetry*, EPJ Web Conf. **251** (2021) 03067, https://www.epj-conferences.org/articles/epjconf/abs/2021/05/epjconf_chep2021_03067/epjconf_chep2021_03067.html. Cited on page 60.

[178] A. Held, *scikit-hep/cabinetry: design and steer profile likelihood fits - GitHub repository*, 2023. https://github.com/scikit-hep/cabinetry, last accessed: 2023-07-07. Cited on page 61.

[179] F. James and M. Roos, *Minuit - a system for function minimization and analysis of the parameter errors and correlations*, Comput. Phys. Commun. **10** (1975) 343–367. Cited on page 70.

[180] F. Faccio, et al., *Development of custom radiation-tolerant DCDC converter ASICs*, J. Instrum. **5** (2010) C11016, https://iopscience.iop.org/article/10.1088/1748-0221/5/11/C11016. Cited on page 76.

[181] DCDC Project, *DCDC project website*, 2022. http://cern.ch/project-DCDC-new, last accessed: 2023-06-20. Cited on page 76.

[182] NXP Semiconductors, *I2C-bus specification and user manual Rev. 7.0*, tech. rep., 2021. https://www.nxp.com/docs/en/user-guide/UM10204.pdf. Cited on page 76.

[183] J. Fonseca, et al., *lpGBT documentation*. 28. march ed., Mar, 2022. https://cds.cern.ch/record/2809058. Cited on pages 77, 78, 110, 112, 114, 116, 117, and 118.

[184] W. Zhang, et al., *Characterization and quality control test of a gigabit cable receiver ASIC (GBCR2) for the ATLAS Inner Tracker Detector upgrade*, J. Instrum. **16** (2021) P08013, https://iopscience.iop.org/article/10.1088/1748-0221/16/08/P08013. Cited on pages 78, 119, and 120.

[185] E. Hering, R. Martin, and M. Stohrer, *Taschenbuch der Mathematik und Physik*. Springer, 5th ed., 2009. http://dx.doi.org/10.1007/978-3-540-78684-9. Cited on page 82.

[186] DCDC Project, *bPOL2V5_V2.2 - Radiation tolerant 3.6W Synchronous Step-Down Buck DC/DC converter*, Datasheet. https://espace.cern.ch/

project-DCDC-new/SharedDocuments/bPOL2V5_V3.3datasheetrev3.pdf, last accessed: 2023-08-22. Cited on page 82.

[187] Fairchild Semiconductor, *CMOS, the Ideal Logic Family*, Application note, Jan, 1983. https://web.archive.org/web/20150109070537/https://www.fairchildsemi.com/application-notes/AN/AN-77.pdf, last accessed: 2023-08-22. Cited on page 82.

[188] S. Buso, G. Spiazzi, F. Faccio, and S. Michelis, *Comparison of dc-dc converter topologies for future SLHC experiments*, 2009 IEEE Energy Convers. Congr. Expo. (2009) 1775–1782, https://doi.org/10.1109/ECCE.2009.5316570. Cited on page 82.

[189] P. Horowitz and W. Hill, *The Art of Electronics*. Cambridge University Press, 3rd ed., 2015. https://www.cambridge.org/tw/9780521809269. Cited on page 83.

[190] O. Simoska, E. M. Gaffney, K. Lim, and R. Ahmad, *The Monitoring of Pixel System (MOPS) chip for the Detector Control System of the ATLAS ITk Pixel Detector*, J. Phys. Conf. Ser. **2374** (2022) 012094, https://iopscience.iop.org/article/10.1088/1742-6596/2374/1/012094. Cited on page 83.

[191] R. Ahmad, et al., *Second generation Monitoring of Pixel System (MOPS) chip for the Detector Control System (DCS) of the ATLAS ITk Pixel detector*, J. Instrum. **18** (2023) C04015, https://iopscience.iop.org/article/10.1088/1748-0221/18/04/C04015. Cited on page 83.

[192] W. P. J. Heubers, H. Boterenbrood, J. T. Van Es, and R. G. K. Hart, *CAN field bus for industrial-controls applications in high-energy physics experiments*, tech. rep., Mar, 1998. https://cds.cern.ch/record/685609. Cited on page 83.

[193] L. Franconi and A. O'Neill, *Pin-to-pin Mapping between PP0 and the FELIX card connectors in the Data Transmission Chain for the ATLAS ITk Pixel Detector (ATLAS internal)*, May, 2022. https://edms.cern.ch/document/2615470/2, last accessed: 2023-06-08. Cited on page 84.

[194] P. Moreira, *Ecole de microélectronique 2017 de l'IN2P3 (14-19 May 2017): Inside the lpGBT*, 2017. https://indico.in2p3.fr/event/14305/contributions/17786/, last accessed: 2023-06-22. Cited on page 103.

[195] T. T. Böhlen, et al., *The FLUKA Code: Developments and Challenges for High Energy and Medical Applications*, Nucl. Data Sheets **120** (2014) 211–214. Cited on page 103.

[196] ATLAS Collaboration, *Radiation Simulation Public Results*, 2019. https://twiki.cern.ch/twiki/bin/view/AtlasPublic/RadiationSimulationPublicResults, last accessed: 2023-05-30. Cited on page 103.

[197] J. Moreira and H. Wekmann, *An Engineer's Guide to Automated Testing of High-Speed Interfaces*. Artech, 2010. https://ieeexplore.ieee.org/document/9106079. Cited on pages 104 and 105.

[198] A. Blankman, *Understanding SDA III Jitter Calculation Methods*, tech. rep., LeCroy, Sep, 2012. https://teledynelecroy.com/doc/docview.aspx?id=7499. Cited on pages 104, 105, 106, and 107.

[199] B. Lerner and A. Lowenberger, *Understanding Jitter Requirements of PLL-Based Processors*, Tech. Rep. EE-261, Analog Devices, Jan, 2005. https://www.analog.com/media/en/technical-documentation/application-notes/EE-261.pdf. Cited on page 105.

[200] B. Analui, J. F. Buckwalter, and A. Hajimiri, *Data-dependent jitter in serial communications*, IEEE Trans. Microw. Theory Tech. **53** (2005) 3388–3397. Cited on page 105.

[201] Teledyne LeCroy, *SDA 816Zi-B oscilloscope*, https://teledynelecroy.com/oscilloscope/wavemaster-sda-dda-8-zi-b-oscilloscopes/sda-816zi-b, last accessed: 2023-06-27. Cited on page 105.

[202] A. Blankman, *Understanding SDA II Jitter Calculation Methods*, tech. rep., LeCroy, Jan, 2012. https://teledynelecroy.com/doc/docview.aspx?id=7499. Cited on pages 105, 106, and 107.

[203] Agilent Technologies, M. Müller, R. Stephens, and R. McHugh, *Total Jitter Measurement at Low Probability Levels, Using Optimized BERT Scan Method 2*, tech. rep., 2005. https://www.keysight.com/ch/de/assets/7123-1002/application-notes/5989-2933.pdf. Cited on pages 107 and 108.

[204] R. J. Barlow, *Statistics: A Guide to the Use of Statistical Methods in the Physical Sciences*, vol. 3. Wiley, 1991. Cited on page 108.

[205] N. Guettouche, et al., *The lpGBT production testing system*, J. Instrum. **17** (2022) C03040, https://iopscience.iop.org/article/10.1088/1748-0221/17/03/C03040. Cited on page 109.

[206] P. Moreira, *The lpGBT: a radiation tolerant ASIC for Data, Timing, Trigger and Control Applications in HL-LHC · Indico*, Sep, 2019. https://indico.cern.ch/event/799025/contributions/3486153/, last accessed: 2023-05-23. Cited on page 109.

[207] S. Biereigel, et al., *The lpGBT PLL and CDR Architecture, Performance and SEE Robustness*, PoS **TWEPP2019** (2020) 34. Cited on page 109.

[208] A. Ilg, *Novel Analysis Techniques and High-Speed Readout to Search for New Physics*. PhD thesis, University of Bern, Aug, 2021. https://cds.cern.ch/record/2779858. Cited on pages 109 and 122.

[209] C. Bissell and D. Chapman, *Digital Signal Transmission*. Cambridge University Press, 2nd ed., 1992. Cited on page 110.

[210] S. B. Huq and J. Goldie, *An Overview of LVDS Technology*, tech. rep., National Semiconductor, 1998. Cited on page 110.

[211] F. De Canio, et al., *Characterization of SLVS Driver and Receiver in a 65 nm CMOS Technology for High Energy Physics Applications*, PoS **TWEPP-17** (2018) 14. Cited on page 110.

[212] G. Traversi, et al., *Design of low-power, low-voltage, differential I/O links for High Energy Physics applications*, J. Instrum. **10** (2015) C01055, https://iopscience.iop.org/article/10.1088/1748-0221/10/01/C01055. Cited on page 110.

[213] S. B. Wicker and V. K. Bhargava, *Reed-Solomon Codes and Their Applications*. Wiley, 1999. https://ieeexplore.ieee.org/book/5264570. Cited on page 112.

[214] S. Cavaliere, *FEC coding for SuperB serial links: a preliminary study*, Mar, 2010. https://agenda.infn.it/event/2026/contributions/38890/, last accessed: 2023-05-15. Cited on page 112.

[215] Xilinix, *Aurora 64B/66B Protocol Specification - SP011 (v1.3)*, 2014. https://docs.xilinx.com/v/u/en-US/aurora_64b66b_protocol_spec_sp011, last accessed: 2023-06-28. Cited on page 113.

[216] D. B. Serrano, et al., *Embedded Monitoring and Control Interface technical specification rev 0.1*, Feb, 2020. https://indico.cern.ch/event/886532/sessions/339231/, last accessed: 2023-06-29. Cited on page 115.

[217] C. Chen, et al., *A gigabit transceiver for the ATLAS inner tracker pixel detector readout upgrade*, J. Instrum. **14** (2019) C07005—-C07005. Cited on page 119.

[218] C. Chen, et al., *1.28 and 5.12 Gbps multi-channel twinax cable receiver ASICs for the ATLAS Inner Tracker Pixel Detector upgrade*, Nucl. Instruments Methods Phys. Res. Sect. A Accel. Spectrometers, Detect. Assoc. Equip. **981** (2020) 164439. Cited on page 119.

[219] L. Zhang, et al., *The design and test results of A Giga-Bit Cable Receiver (GBCR) for the ATLAS Inner Tracker Pixel Detector*, J. Instrum. **18** (2023) C03005, https://iopscience.iop.org/article/10.1088/1748-0221/18/03/C03005. Cited on page 119.

[220] Teledyne LeCroy, *Test Happens - Teledyne LeCroy Blog: Continuous Time Linear Equalization*, Jul, 2018. https://blog.teledynelecroy.com/2018/07/continuous-time-linear-equalization.html, last accessed: 2023-06-29. Cited on page 119.

[221] J. Troska, L. Olanterä, and C. Soos, *The Versatile Link+ Application Note v1.6*, 2021. https://edms.cern.ch/project/CERN-0000149833, last accessed: 2023-05-31. Cited on page 121.

[222] Z. Zeng, et al., *LDQ10: a compact ultra low-power radiation-hard 4x10 Gb/s driver array*, J. Instrum. **12** (2017), http://dx.doi.org/10.1088/1748-0221/12/02/P02020. Cited on pages 119 and 120.

[223] J. Troska, *Versatile Link+ Technical Specification, part 2.1 - Versatile Link+ Transceiver (VTRx+)*, tech. rep., VL+ Project Team, CERN, Oct, 2019. https://espace.cern.ch/project-Versatile-Link-Plus/SitePages/Home.aspx. Cited on page 122.

[224] Python Software Foundation, *tkinter - Python interface to Tcl/Tk - Python 3.11.4 documentation*, https://docs.python.org/3/library/tkinter.html, last accessed: 2023-06-19. Cited on page 122.

[225] J. Anders, et al., *A facility for radiation hardness studies based on a medical cyclotron*, J. Instrum. **17** (2022). Cited on page 127.

[226] K. Moustakas, et al., *A Clock and Data Recovery Circuit for the ALTAS/CMS HL-LHC Pixel Front End Chip in 65 nm CMOS Technology*, Proc. Sci. **370** (2020) 046, https://pos.sissa.it/. Cited on page 127.

[227] M. Daas, et al., *BDAQ53, a versatile pixel detector readout and test system for the ATLAS and CMS HL-LHC upgrades*, Nucl. Instruments Methods Phys. Res. Sect. A Accel. Spectrometers, Detect. Assoc. Equip. **986** (2021) 164721. Cited on page 127.

[228] I. Siral, *itk-felix-sw / ic-over-netio - GitLab repository*, 2021. https://gitlab.cern.ch/itk-felix-sw/ic-over-netio, last accessed: 2023-06-19. Cited on page 128.

[229] R. Müller, et al., *optoboard_felix - GitLab repository*, 2023. https://gitlab.cern.ch/bat/optoboard_felix/, last accessed: 2023-08-22. Cited on page 128.

[230] T. Heim, *YARR - A PCIe based Readout Concept for Current and Future ATLAS Pixel Modules*, J. Phys. Conf. Ser. **898** (2017) 032053, https://iopscience.iop.org/article/10.1088/1742-6596/898/3/032053. Cited on page 128.

[231] N. L. Whallon, et al., *Upgrade of the YARR DAQ System for the ATLAS Phase-II Pixel Detector Readout Chip*, Proc. Sci. **313** (2018) 076, https://www.ohwr.org/projects/spec/wiki/wiki. Cited on page 128.

[232] R. Müller and ATLAS ITk Collaboration, *System tests of the ATLAS ITk planar and 3D pixel modules*, J. Instrum. **18** (2023) C03014, https://iopscience.iop.org/article/10.1088/1748-0221/18/03/C03014. Cited on pages 129, 131, and 133.

[233] R. Müller, *INSPIRE Publication Profile*, https://inspirehep.net/authors/2636084, last accessed: 2023-08-23. Cited on page 135.

[234] G. Brandt, et al., *DeMi - ATLAS ITk Pixel System Test Microservices*, https://demi.docs.cern.ch/, last accessed: 2023-08-24. Cited on page 136.

Acronyms

AC Alternate Current
AI Artificial Intelligence
ALICE A Large Ion Collider Experiment
ASIC Application-Specific Integrated Circuit
ATLAS A Toroidal LHC ApparatuS
AWG American Wire Gauge

BCM' Beam Conditions Monitor Prime
BDT Boosted Decision Tree
BERT Bit Error Rate Test
BoB breakout board
bPOL buck Point of Load
BSM Beyond Standard Model
BUJ Bounded Uncorrelated Jitter

CAN Controller Area Network
CDF Cumulative Density Function
CDR Clock Data Recovery
CERN Conseil Européen pour la Recherche Nucléaire
CLPS CERN Low Power Signaling
CML Current-Mode Logic
CMOS Complementary Metal-Oxide-Semiconductor
CMS Compact Muon Solenoid
CPT Continuous Phase Tracking
CR Coupled Ring
CSC Cathode Strip Chamber
CTLE Continous Time Linear Equaliser
CTP Central Trigger Processor

DAQ Data Acquisition
DC Direct Current
DCD Duty-Cycle Distortion
DCS Detector Control System
DDJ Data Dependent Jitter
DEC Decoder
DeSER De-Serialiser
DFT Data Feedthrough
DJ Deterministic Jitter
DLL Delay Locked Loop
DSCR De-Scrambler

EC End Caps
EC External Control
ECAL Electromagnetic Calorimeter
ECLK ePortClk
EF Event Filter
eLink Electrical Link
EMEC Electromagnetic End-cap Calorimeter
EMI electromagnetic interference
EOS End of Stave
EPRX ePortRx
EPTX ePortTx
Eq Equaliser

FCal Forward Calorimeter
FE Front End
FEC Forward Error Correction
FELIX FrontEnd LInk eXchange
FFT Fast Fourier Transform
FL Flat Layer
FLUKA FLUktuierende KAskade
FPGA Field Programmable Gate Array

GBCR Giga-Bit Cable Receiver

GEANT GEometry ANd Tracking
GUI Guided User Interface

HCAL Hadronic Calorimeter
HEC Hadronic End-cap Calorimeter
HEP High Energy Physics
HL-LHC High-Luminosity LHC
HLT High-Level Trigger

I2C Inter-Integrated Circuit
IBL Insertable B-Layer
IC Internal Control
ID Inner Detector
IL Inclined Layer
IP Interaction Point
IR Intermediate Ring
IS Inner System
ISI Inter-Symbol Interference
ITk Inner Tracker

JVT Jet Vertex Tagger

L Layer
L1 Level-1 trigger
L2 Level-2 trigger
LA Limiting Amplifier
LAr Liquid Argon
LEP Large Electron Positron Collider
LFV Lepton Flavour Violation
LHC Large Hadron Collider
LHCb Large Hadron Collider beauty
LINAC Linear Accelerator
LLS Loaded Local Supports
LM Latency Measurement
LO Leading Order
lpGBT Low Power Giga Bit Transceiver
LQ Leptoquark
LR Link Receiver
LS Long Shutdown
LU Lepton Universality
LVDS Low Voltage Differential Signaling

MC Monte Carlo
MDT Monitored Drift Tube
ME Matrix Elements
MET Missing Transverse Energy
MMC Missing Mass Calculator
MOPS Monitor of Pixel System
MS Muon Spectrometer
MSB Most Significant Bit
MTP Multi-fiber Termination Push-on
MUX Multiplexer

N^{3}LO Next-to-NNLO
NLO Next-to-leading Order
NNLO Next-to-next-to-leading Order

OB Outer Barrel
Ob-b Optoboard-b
Ob-a Optoboard-a
OS Opposite-Sign

PA Phase Aligner
PCB Printed Circuit Board
PCC Pixel Cluster Counting
PDF Parton Distribution Function
PDF Probability Density Function
PIN Positive Intrinsic Negative
PJ Periodic Jitter
PLL Phase-Locked Loop
PLR Pixel Luminosity Ring
PP Patch Panel
PRBS Pseudo Random Bit Sequence
PS Proton Synchroton
PS Power Supplies
PSB Proton Synchroton Booster

Q Quads
QCD Quantum Chromodynamics
QED Quantum Electrodynamics
QFT Quantum Field Theory
QR Quad Ring

R Rings
RAM Random Access Memory
RF Radio Frequency
RJ Random Jitter
RMS Root Mean Square

RNN Recurrent Neural Network
ROD Readout Driver
ROI Region of Interest
ROL Readout Link
ROM Read-Only Memory
RPC Resistive-Plate Chamber
RS Reed-Salomon

SC Slow Control
SCC Single Chip Card
SCR Scrambler
SCT SemiConductor Tracker
SDA Serial Data Analysis
SEU Single Event Upset
SLAC Stanford Linear Accelerator Center
SLVS Scalable Low Voltage Signaling
SM Standard Model
SMA SubMiniature version A
SMD Surface Mounted Device
SNR signal-to-noise ratio
SP Serial Powering
SPS Super Proton Synchroton
SS Same-Sign

T Triplets
TB Termination Board
TDAQ Trigger and Data Acquisition
TES τ_{had} Energy Scale
TGC Thin-Gap Chamber
TIA Transimpedance Amplifier
TID Total Ionisation Dose
TIE Time Interval Error
TJ Total Jitter
TOTEM TOTal cross section, Elastic scattering and diffraction dissociation Measurement at the LHC
TRT Transition Radiation Tracker
TTC Timing and Trigger Control
TTVA Track to Vertex Association

US Underground Structure
USA Underground Service ATLAS

VCSEL Vertical-Cavity Surface-Emitting laser
VEV Vacuum Expectation Value
VTRx+ Versatile Link Transceiver Plus

Appendix A

ITk Pixel Detector Layout Tables

Ring Types	Positions in z [mm]
Coupled Rings	293, 291, 322, 357, 396, 437, 486, 543, 604, 675, 749, 835, 925, 1026, 1142
R0.5 Rings	1103, 1229, 1359, 1503, 1665, 1846
R1 Rings	1272, 1403, 1553, 1721, 1909, 2120, 2357, 2621

Table A.1: Exact z positions for the rings in the ITk Pixel Inner System (after layout ATLAS-P2-ITK-23-00-00). Table taken from [102].

Ring Endcap	Positions in z [mm]	Split between half rings [mm]
R2	1145.5, 1249, 1365, 1492, 1633, 1789, 1961, 2151, 2361, 2593, 2850	11
R3	1145.5, 1297, 1473, 1676, 1910, 2180, 2491, 2850	11
R4	1145.5, 1277, 1427, 1597, 1789, 2007, 2253, 2533, 2850	11

Table A.2: Exact z positions for the rings in the ITk Pixel Outer Endcap (after layout ATLAS-P2-ITK-23-00-00). Table taken from [102].

Appendix B

ITk Pixel Detector Barrel and Ring DFT and Powering Assignment

For the explanation of how to read these figures see Figure 4.14.

B.1 Inner System

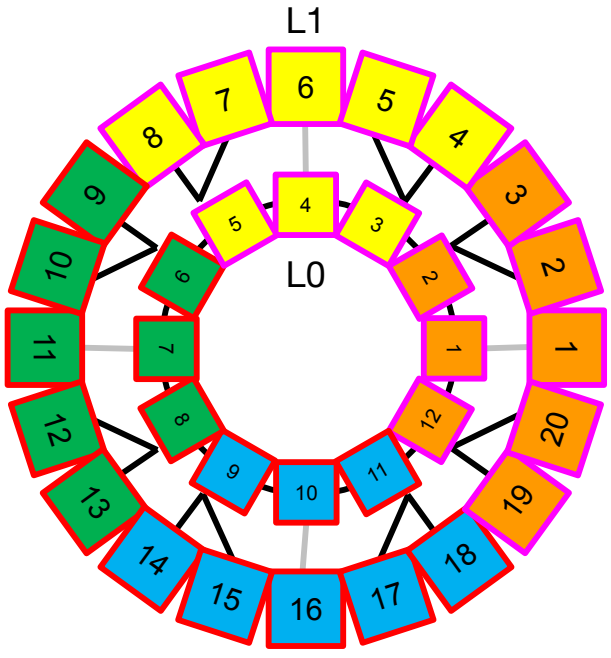

Figure B.1: Sketch of the IS L0L1 barrel.

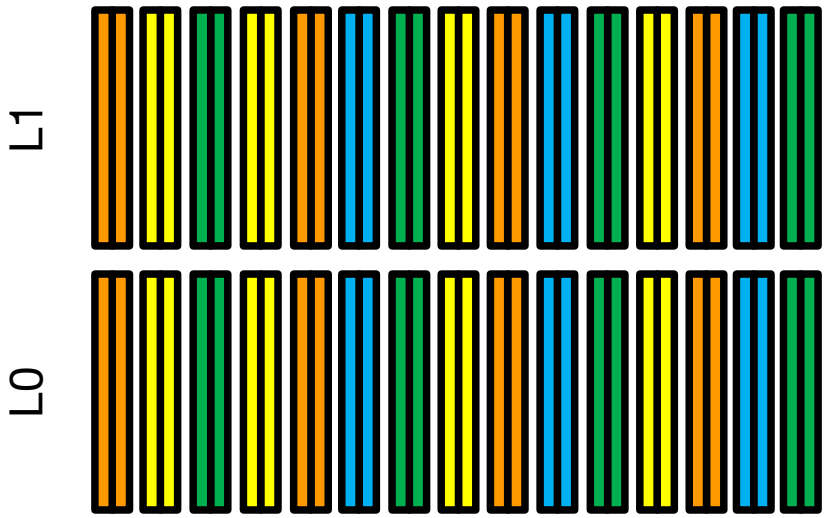

Figure B.2: Sketch of the IS L0L1 CR.

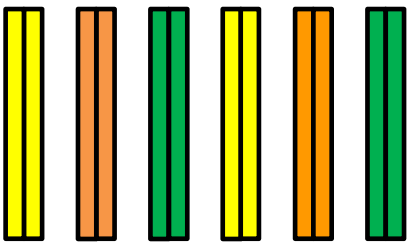

Figure B.3: Sketch of the IS IR.

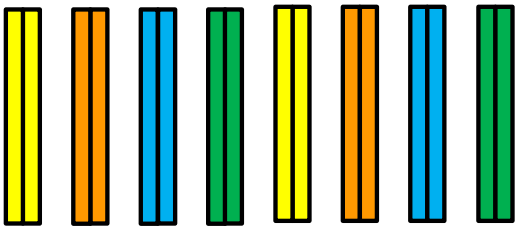

Figure B.4: Sketch of the IS QR.

B.2 Outer Barrel

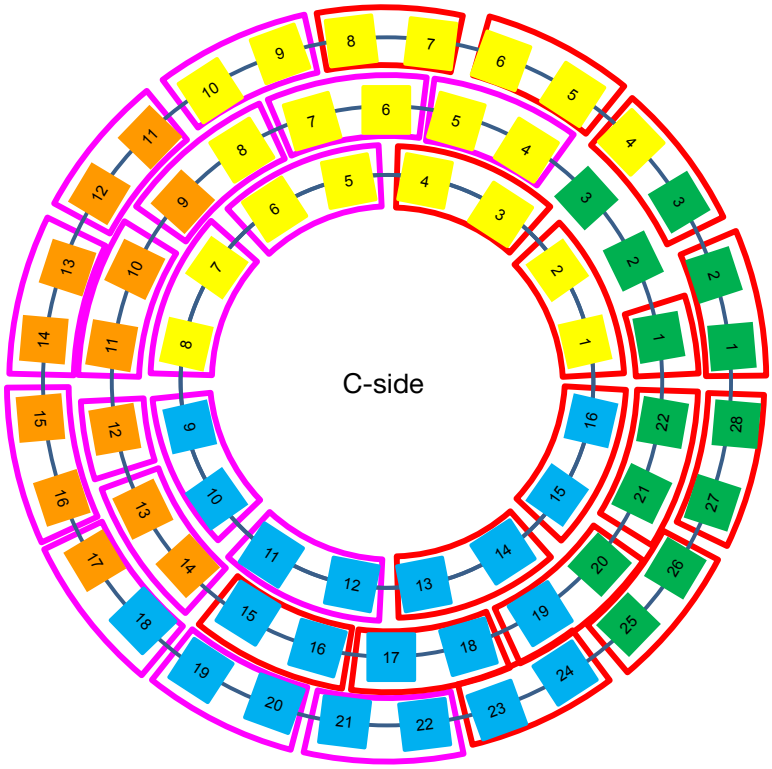

Figure B.5: Sketch of all OB layers on the ATLAS c-side.

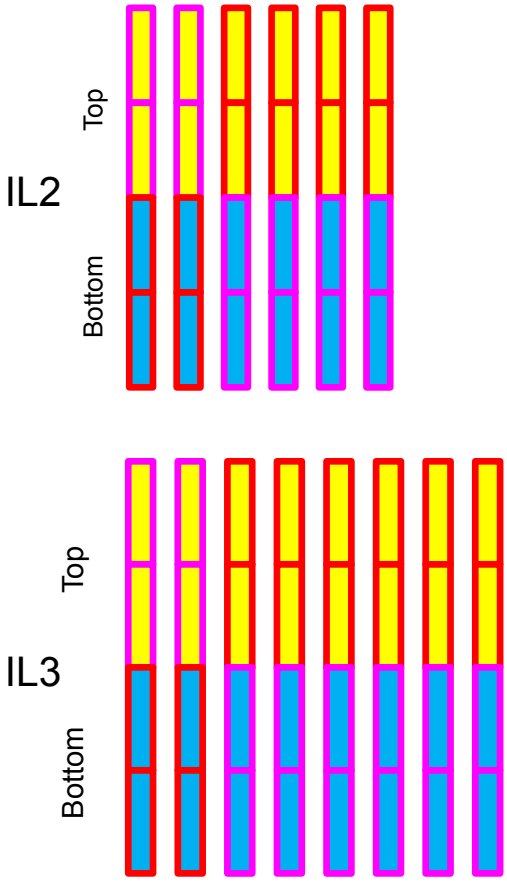

Figure B.6: Sketch of the OB IL2&3 rings on the ATLAS A-side.

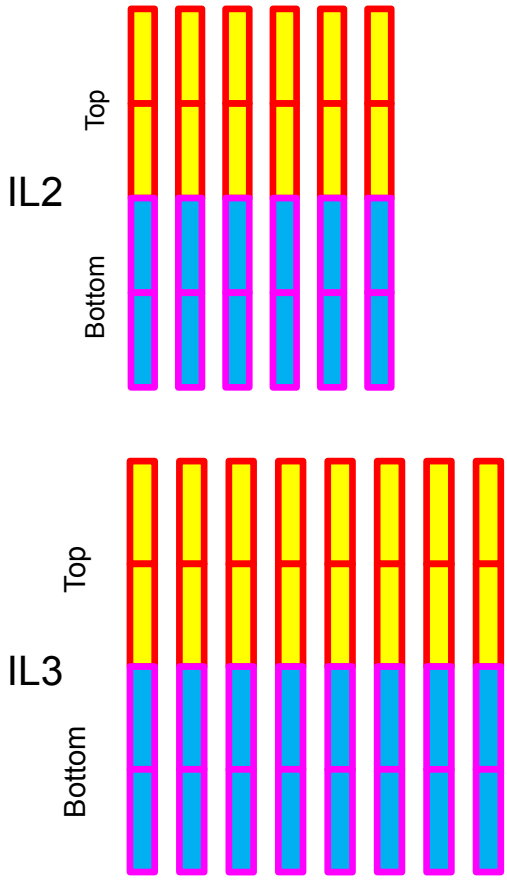

Figure B.7: Sketch of the OB IL2&3 rings on the ATLAS C-side.

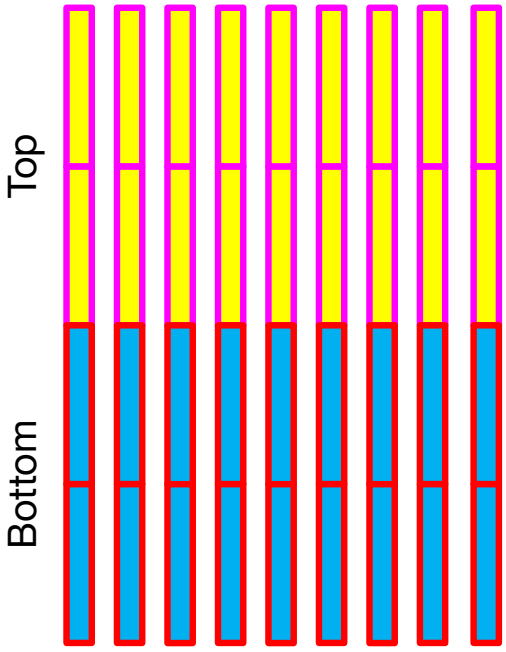

Figure B.8: Sketch of the OB IL4 rings.

B.3 End Caps

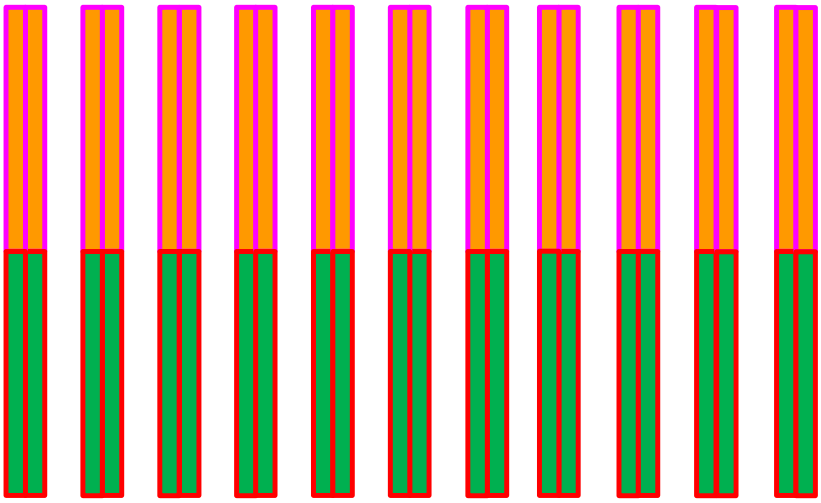

Figure B.9: Sketch of the EC L2 rings.

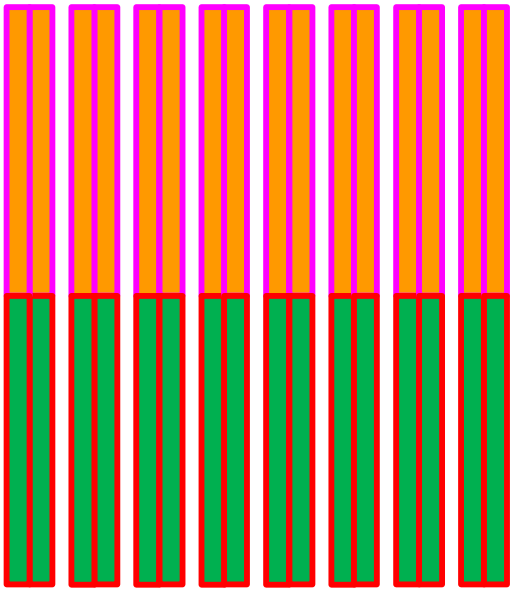

Figure B.10: Sketch of the EC L3 rings.

Appendix C

Optopanel Layouts

For the explanation of how to read these figures see Section 4.7.2.

C.1 ATLAS A side

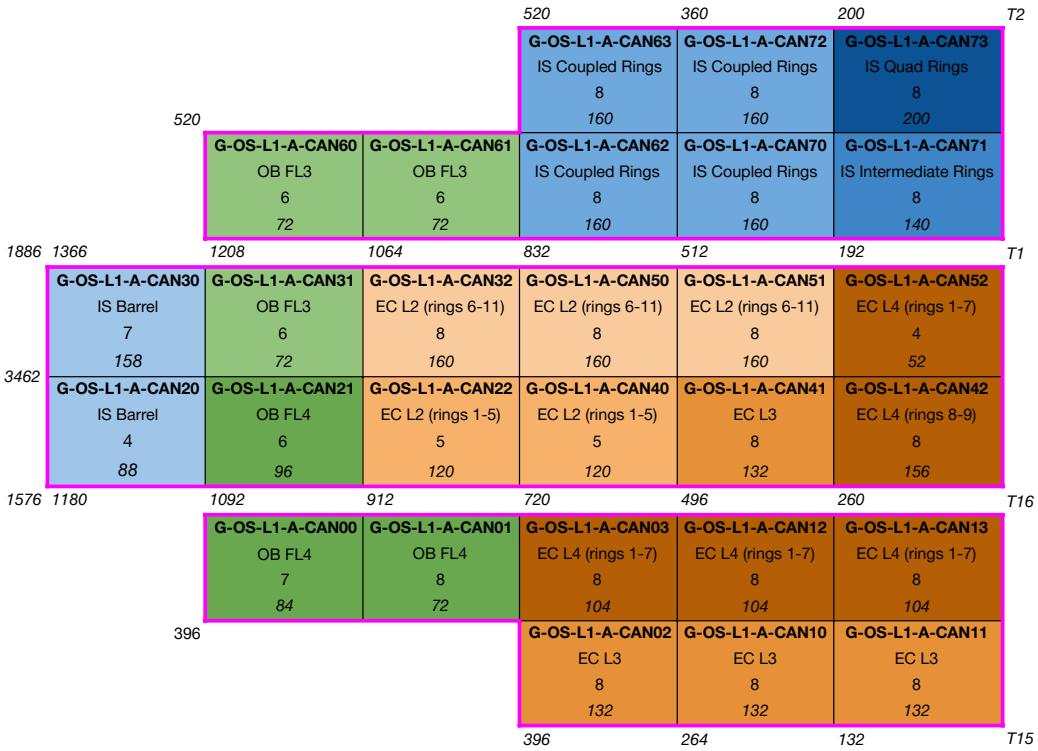

Figure C.1: Optobox distribution in the A-side sector 1 Optopanel (DFT a1-8). Each box represents an Optobox, its background colour is to distinguish the different layers. The Optobox ID is bold and the layer name is given below. The first number in each box is the amount of Optoboards and the italic number the amount of Twinax cables ending at that Optobox. The thicker, coloured border indicates the source of powering cavern.

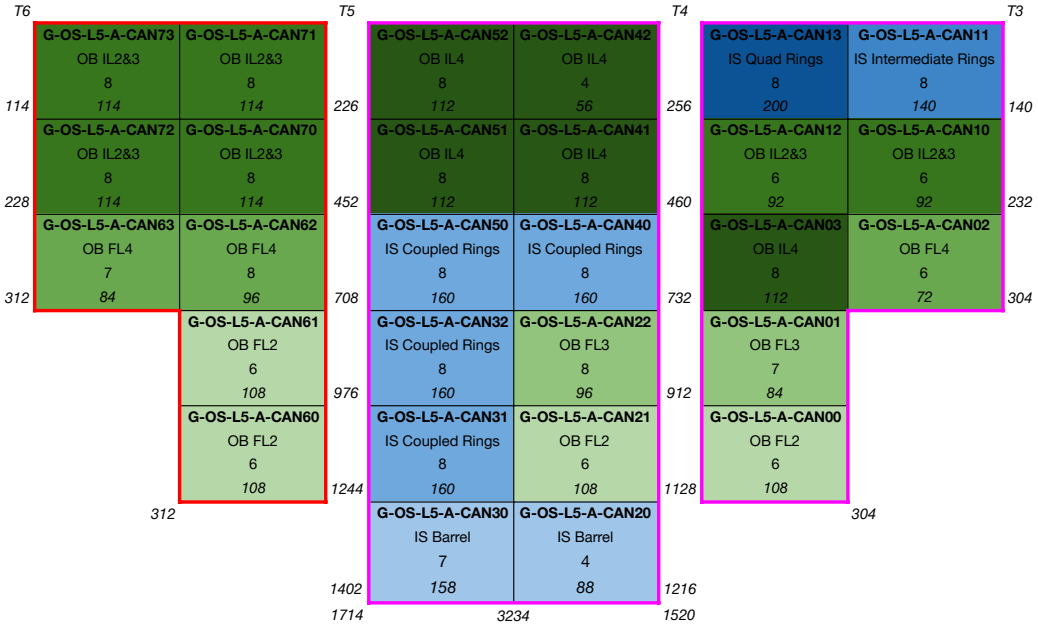

Figure C.2: Optobox distribution in the A-side sector 5 Optopanel (DFT a2-3). Each box represents an Optobox, its background colour is to distinguish the different layers. The Optobox ID is bold and the layer name is given below. The first number in each box is the amount of Optoboards and the italic number the amount of Twinax cables ending at that Optobox. The thicker, coloured border indicates the source of powering cavern.

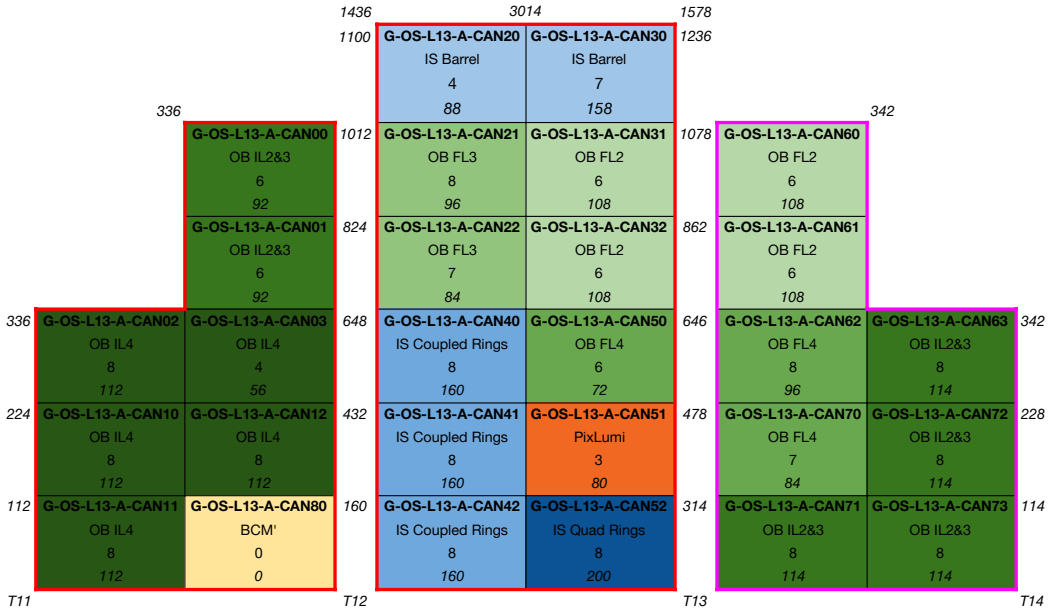

Figure C.3: Optobox distribution in the A-side sector 13 Optopanel (DFT a6-7). Each box represents an Optobox, its background colour is to distinguish the different layers. The Optobox ID is bold and the layer name is given below. The first number in each box is the amount of Optoboards and the italic number the amount of Twinax cables ending at that Optobox. The thicker, coloured border indicates the source of powering cavern.

C.2 ATLAS C side

Figure C.4: Optobox distribution in the C side sector 1 Optopanel (DFT c1-8). Each box represents an Optobox, its background colour is to distinguish the different layers. The Optobox ID is bold and the layer name is given below. The first number in each box is the amount of Optoboards and the italic number the amount of Twinax cables ending at that Optobox. The thicker, coloured border indicates the source of powering cavern.

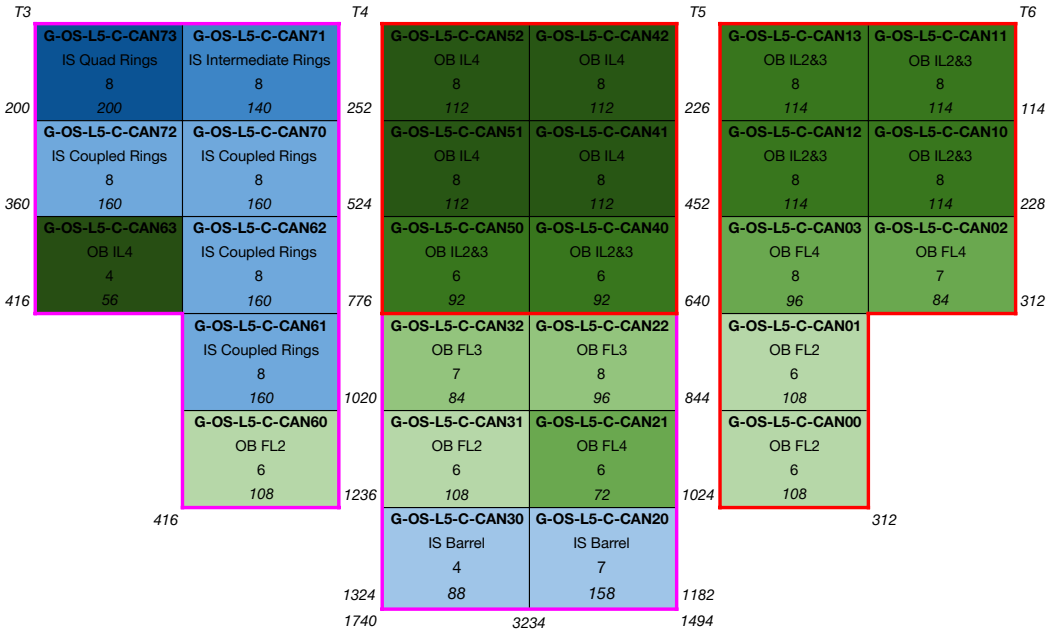

Figure C.5: Optobox distribution in the C side sector 5 Optopanel (DFT c2-3). Each box represents an Optobox, its background colour is to distinguish the different layers. The Optobox ID is bold and the layer name is given below. The first number in each box is the amount of Optoboards and the italic number the amount of Twinax cables ending at that Optobox. The thicker, coloured border indicates the source of powering cavern.

Figure C.6: Optobox distribution in the C side sector 9 Optopanel (DFT c4-5). Each box represents an Optobox, its background colour is to distinguish the different layers. The Optobox ID is bold and the layer name is given below. The first number in each box is the amount of Optoboards and the italic number the amount of Twinax cables ending at that Optobox. The thicker, coloured border indicates the source of powering cavern.

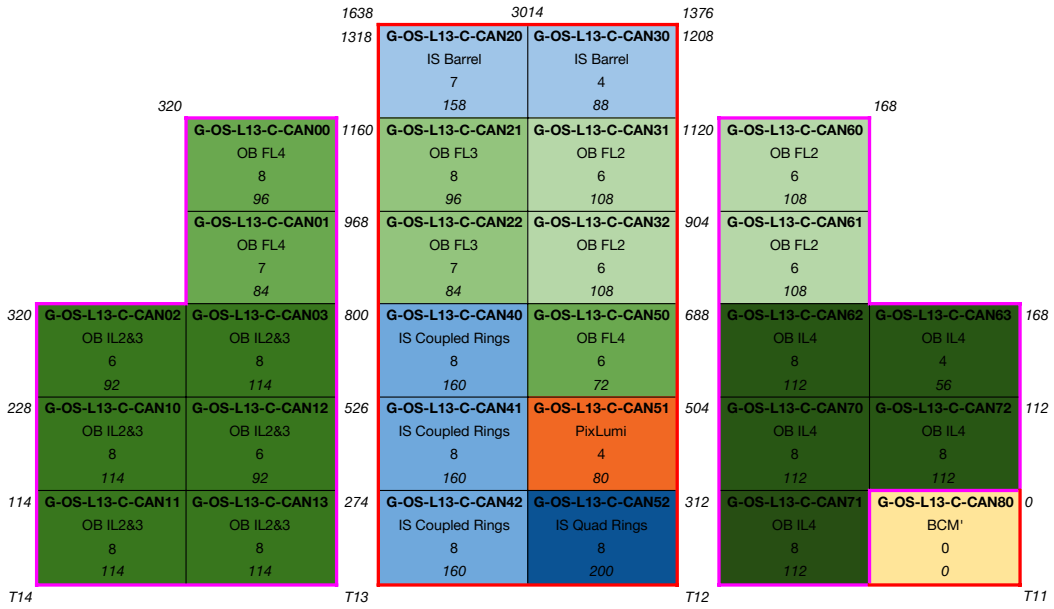

Figure C.7: Optobox distribution in the C side sector 13 Optopanel (DFT c6-7). Each box represents an Optobox, its background colour is to distinguish the different layers. The Optobox ID is bold and the layer name is given below. The first number in each box is the amount of Optoboards and the italic number the amount of Twinax cables ending at that Optobox. The thicker, coloured border indicates the source of powering cavern.

3396	3843	4146			
3224	4477	4343	5508	5374	
3968	4256	5609	5475	5374	5346
3504	4378	4464	3686	5443	5346
4908	5298	5505	5577	5443	
4507	5048	5443			

			5353	4831	3703
	5443	5577	5446	5153	4652
5346	5443	3686	4464	4378	3504
5346	5374	3324	3016	4256	3968
	5374	5508	4343	4477	3224
			4146	3843	3396

4339	4782	4878	5093	5306	5038
4947	5227	5131	5268	5261	5034
5262	5331	5234	5321	5642	5712
	5343	5577	5577	5651	
	5517	5517	5374	5517	
		5346	5346		

		5346	5346		
	5374	5443	5517	5517	
	5508	5577	5651	5651	
5391	5127	0	5508	5134	5262
5242	5368	4968	3580	5131	4814
5038	5098	5201	4718	5093	0

Table C.1: The lengths of the longest cables in millimetre that are terminated at each Optobox in the Optopanels of the ATLAS C side. The top two Optopanels from the left are sectors 1 (DFT c1-8) and 9 (DFT c4-5). The lower two Optopanels are sectors 5 (DFT c2-3) and 13 (DFT c6-7). The background colours represent the different layers of the corresponding subsystem.

Appendix D

Analysis

D.1 Systematics

D.1.1 List of Systematics

```
EG_RESOLUTION_ALL
EG_SCALE_ALL
EL_EFF_Iso_SIMPLIFIED_UncorrUncertaintyNP17
EL_EFF_Iso_SIMPLIFIED_UncorrUncertaintyNP8
EL_EFF_Reco_SIMPLIFIED_UncorrUncertaintyNP8
FT_EFF_Eigen_B_0
FT_EFF_Eigen_B_1
FT_EFF_Eigen_B_2
FT_EFF_Eigen_B_3
FT_EFF_Eigen_C_0
FT_EFF_Eigen_Light_0
FT_EFF_Eigen_Light_1
FT_EFF_Eigen_Light_2
FT_EFF_extrapolation
FT_EFF_extrapolation_from_charm
JET_EffectiveNP_Mixed2
JET_EffectiveNP_Modelling1
JET_EffectiveNP_Modelling2
JET_EffectiveNP_Modelling3
JET_EffectiveNP_Statistical2
JET_EtaIntercalibration_Modelling
JET_EtaIntercalibration_NonClosure_2018data
JET_EtaIntercalibration_TotalStat
JET_Flavor_Composition
JET_Flavor_Response
JET_JER_DataVsMC_MC16
JET_JER_EffectiveNP_1
JET_JER_EffectiveNP_10
JET_JER_EffectiveNP_11
JET_JER_EffectiveNP_12restTerm
JET_JER_EffectiveNP_2
```

```
JET_JER_EffectiveNP_3
JET_JER_EffectiveNP_4
JET_JER_EffectiveNP_5
JET_JER_EffectiveNP_6
JET_JER_EffectiveNP_7
JET_JER_EffectiveNP_8
JET_JER_EffectiveNP_9
JET_Pileup_OffsetMu
JET_Pileup_OffsetNPV
JET_Pileup_RhoTopology
MUON_EFF_ISO_STAT
MUON_EFF_ISO_SYS
MUON_EFF_RECO_STAT
MUON_EFF_RECO_SYS
MUON_EFF_TTVA_STAT
MUON_EFF_TTVA_SYS
MUON_SCALE
TAUS_TRUEELECTRON_EFF_ELEBDT_STAT
TAUS_TRUEHADTAU_EFF_ELEOLR_TOTAL
TAUS_TRUEHADTAU_EFF_RECO_TOTAL
TAUS_TRUEHADTAU_EFF_RNNID_1PRONGSTATSYSTPTGE40
TAUS_TRUEHADTAU_EFF_RNNID_3PRONGSTATSYSTPTGE40
TAUS_TRUEHADTAU_EFF_RNNID_HIGHPT
TAUS_TRUEHADTAU_EFF_RNNID_SYST
TAUS_TRUEHADTAU_EFF_TRIGGER_STATDATA161718
TAUS_TRUEHADTAU_EFF_TRIGGER_STATDATA2016
TAUS_TRUEHADTAU_EFF_TRIGGER_STATMC161718
TAUS_TRUEHADTAU_EFF_TRIGGER_STATMC2016
TAUS_TRUEHADTAU_EFF_TRIGGER_SYST161718
TAUS_TRUEHADTAU_EFF_TRIGGER_SYST2016
TAUS_TRUEHADTAU_SME_TES_DETECTOR
TAUS_TRUEHADTAU_SME_TES_INSITUEXP
TAUS_TRUEHADTAU_SME_TES_INSITUFIT
TAUS_TRUEHADTAU_SME_TES_MODEL_CLOSURE
TAUS_TRUEHADTAU_SME_TES_PHYSICSLIST
```

Listing D.1: Systematics used for the fitting results. Note: `JET_*` in the $Z \to \ell\ell$ samples and `JET_JER_EffectiveNP_4`, `JET_JER_DataVsMC_MC16` for W-jets samples have been removed for the $m_{\ell\ell}$ variable due to errors in the input files at the time of writing.

D.1.2 Impact of Uncertainties

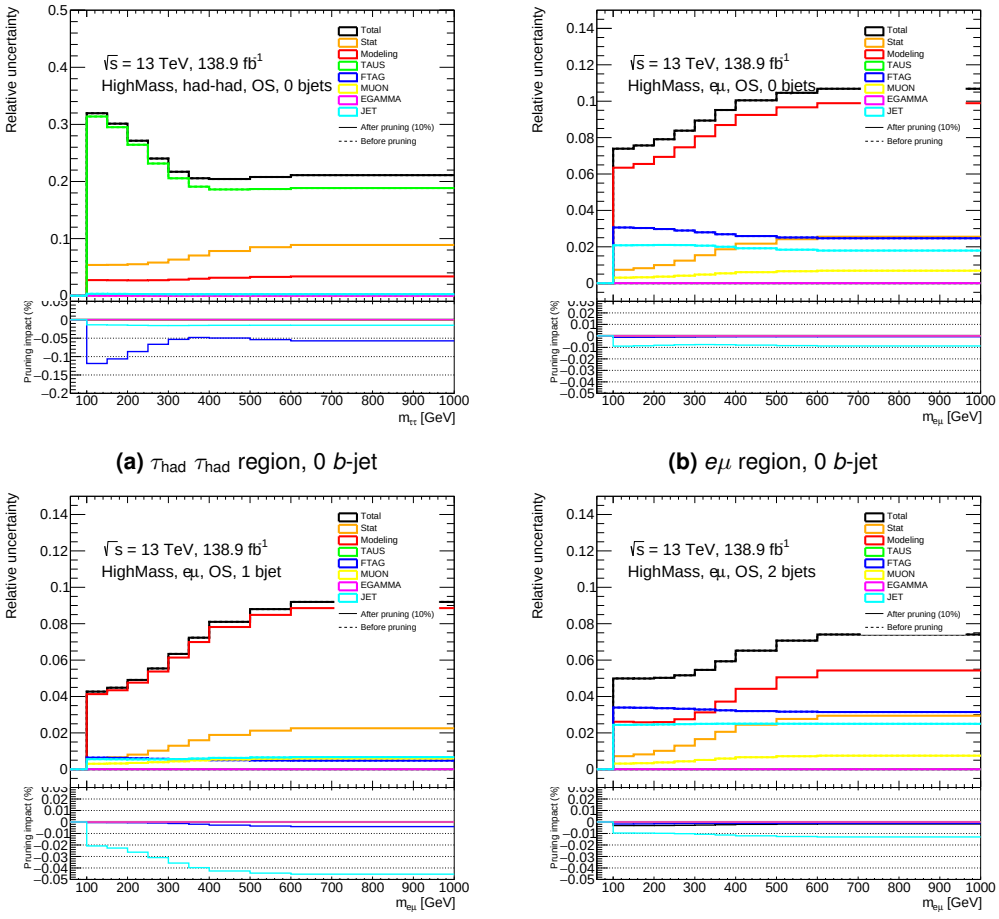

(a) $\tau_{\text{had}}\,\tau_{\text{had}}$ region, 0 *b*-jet

(b) $e\mu$ region, 0 *b*-jet

(c) $e\mu$ region, 1 *b*-jet

(d) $e\mu$ region, 2 *b*-jet

Figure D.1: Impact of relative uncertainties before and after pruning (upper pads) on the MC $m_{\ell\ell}$ distribution before the unfolding. Effects of pruning on the total and the experimental uncertainties (ratio pads).

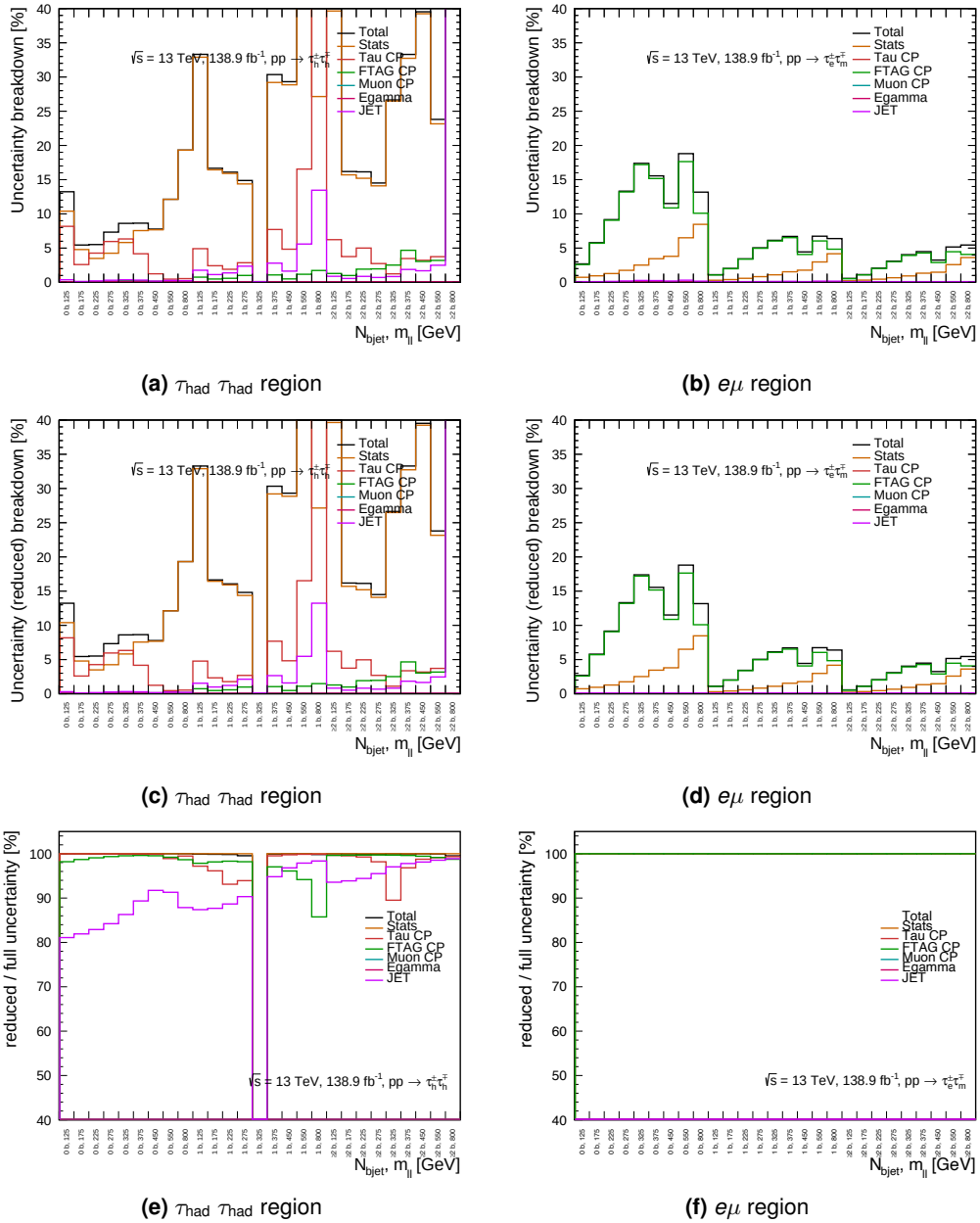

(a) $\tau_{\text{had}}\,\tau_{\text{had}}$ region **(b)** $e\mu$ region

(c) $\tau_{\text{had}}\,\tau_{\text{had}}$ region **(d)** $e\mu$ region

(e) $\tau_{\text{had}}\,\tau_{\text{had}}$ region **(f)** $e\mu$ region

Figure D.2: Relative uncertainties before pruning (upper row), after pruning (middle row), and ratio between the uncertainties before and after pruning (lower row) on the MC $m_{\ell\ell}$ distribution after the unfolding. (e) is identical to Figure 3.6. Note: (e) and (f) have added ATLAS disclaimer and moved x-axis label.

D.2 Data vs. Simulation Comparisons

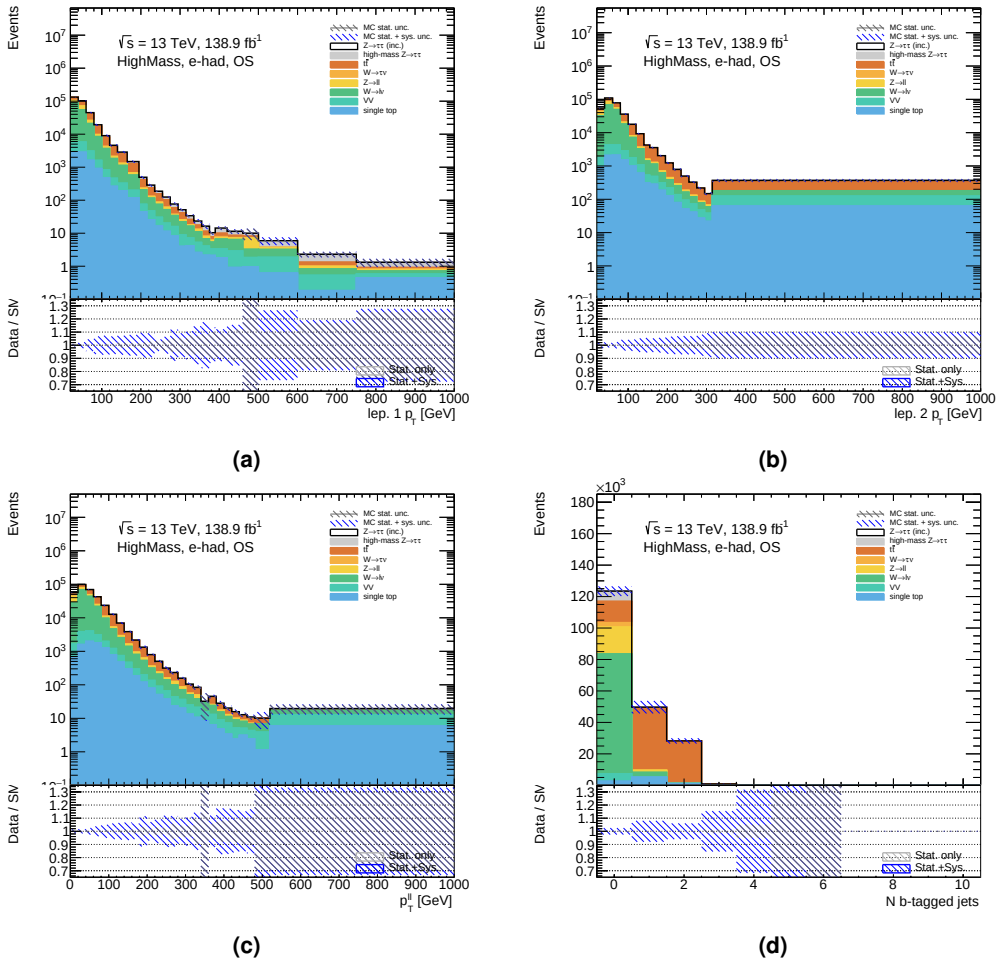

Figure D.3: MC simulation data for a number of kinematic quantities in the high-mass, opposite-sign, $e\tau_{\text{had}}$ region: (a) the leading τ_{had} $p_{\text{T}}^{\text{vis}}$, (b) the subleading τ_{had} $p_{\text{T}}^{\text{vis}}$, (c) the $p_{\text{T}}^{\text{vis}}$ of the $\tau_{\text{had}}\tau_{\text{had}}$ system, and (d) the *b*-jet multiplicity.

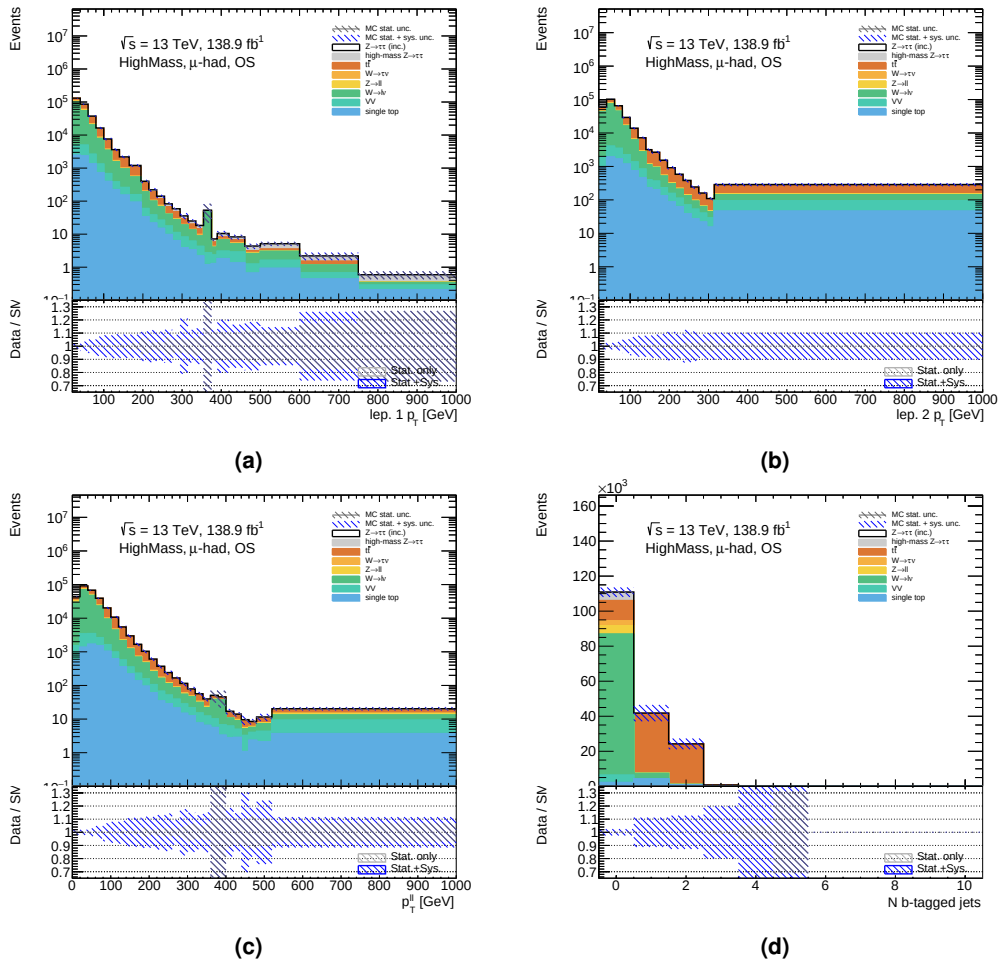

Figure D.4: MC simulation data for a number of kinematic quantities in the high-mass, opposite-sign, $\mu\tau_{\text{had}}$ region: (a) the leading τ_{had} $p_{\text{T}}^{\text{vis}}$, (b) the subleading τ_{had} $p_{\text{T}}^{\text{vis}}$, (c) the $p_{\text{T}}^{\text{vis}}$ of the $\tau_{\text{had}}\tau_{\text{had}}$ system, and (d) the *b*-jet multiplicity.

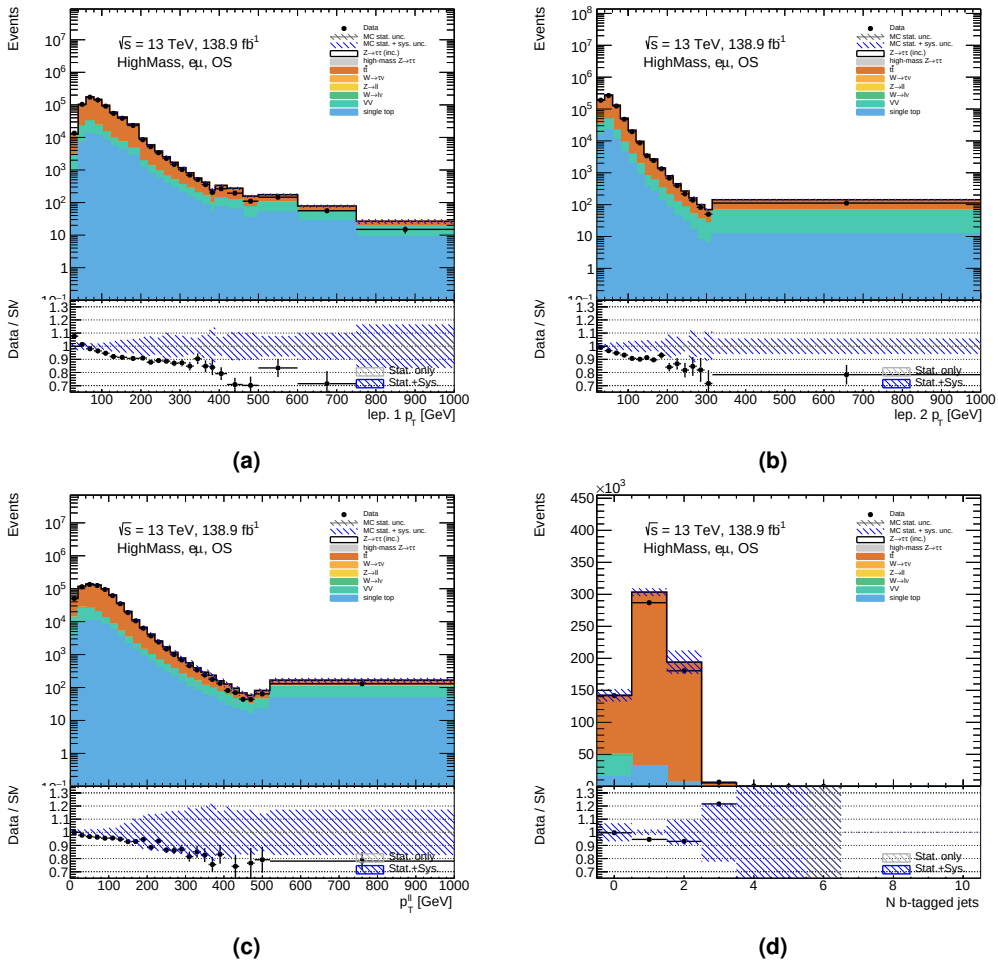

Figure D.5: Comparisons between MC simulation and collision data for a number of kinematic quantities in the high-mass, opposite-sign, $e\mu$ region: (a) the leading τ_{had} $p_{\text{T}}^{\text{vis}}$, (b) the subleading τ_{had} $p_{\text{T}}^{\text{vis}}$, (c) the $p_{\text{T}}^{\text{vis}}$ of the $\tau_{\text{had}}\tau_{\text{had}}$ system, and (d) the b-jet multiplicity.

D.3 Expected Leptoquark Yields

Tables D.1–D.2 show the expected event yields in the analysis signal regions for the SM processes considered in the analysis split by lepton channels and *b*-jet multiplicity.

Process	0 *b*-jet	1 *b*-jet	2+ *b*-jets
W-jets	938.76 $\pm$ 142.72	9.96 $\pm$ 2.28	1.01 $\pm$ 0.22
$Z \to \ell\ell$	14.49 $\pm$ 0.94	0.12 $\pm$ 0.04	0.00 $\pm$ 0.00
$Z \to \tau\tau$	2803.19 $\pm$ 148.26	67.18 $\pm$ 18.29	4.88 $\pm$ 1.90
VV	81.14 $\pm$ 6.94	3.71 $\pm$ 0.46	0.21 $\pm$ 0.04
single t	22.46 $\pm$ 4.71	32.34 $\pm$ 7.92	9.66 $\pm$ 2.44
$t\bar{t}$	76.16 $\pm$ 7.43	183.86 $\pm$ 14.60	117.47 $\pm$ 8.25
Total	3936.18 $\pm$ 63.38	297.16 $\pm$ 29.86	133.23 $\pm$ 8.03
Asimov data	3936	297	133

Table D.1: Predicted event yields in the analysis $\tau_{\text{had}}\,\tau_{\text{had}}$ opposite-sign signal regions for the $m_{\text{T}}^{\text{total}}$ 1.5 TeV mass point.

Process	0 *b*-jet	1 *b*-jet	2+ *b*-jets
W-jets	5004.13 ± 942.00	167.25 ± 34.35	6.71 ± 3.04
$Z \to \ell\ell$	341.91 ± 18.33	16.89 ± 0.99	0.55 ± 0.07
$Z \to \tau\tau$	3492.47 ± 183.75	68.06 ± 4.69	5.33 ± 1.00
VV	28891.63 ± 1013.98	601.11 ± 38.64	24.46 ± 2.08
single t	10075.32 ± 2243.00	16532.62 ± 3979.70	3557.94 ± 920.35
$t\bar{t}$	50430.63 ± 2438.82	136551.67 ± 3991.50	95077.16 ± 982.18
Total	98236.09 ± 317.79	153937.61 ± 397.98	98672.15 ± 314.94
Asimov data	98236	153937	98672

Table D.2: Predicted event yields in the analysis $e\mu$ opposite-sign signal regions for the $m_{\text{T}}^{\text{total}}$ 1.5 TeV mass point.

D.4 Pure BSM and Pure Interference Terms

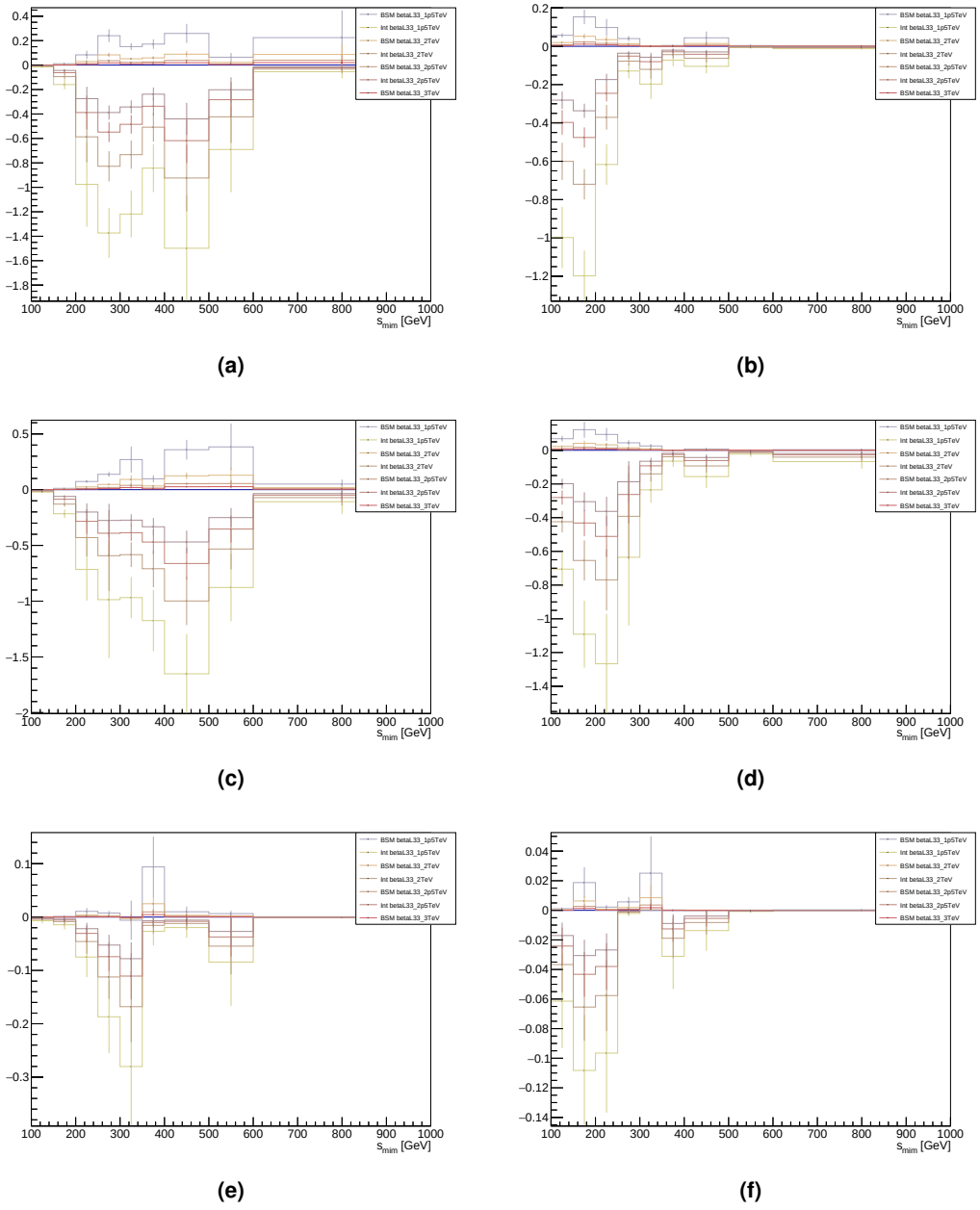

Figure D.6: Signal events of the high mass opposite sign τ_{had} τ_{had} (left side plots) and $e\mu$ (right side plots) regions for the $m_{\text{T}}^{\text{total}}$ variable.

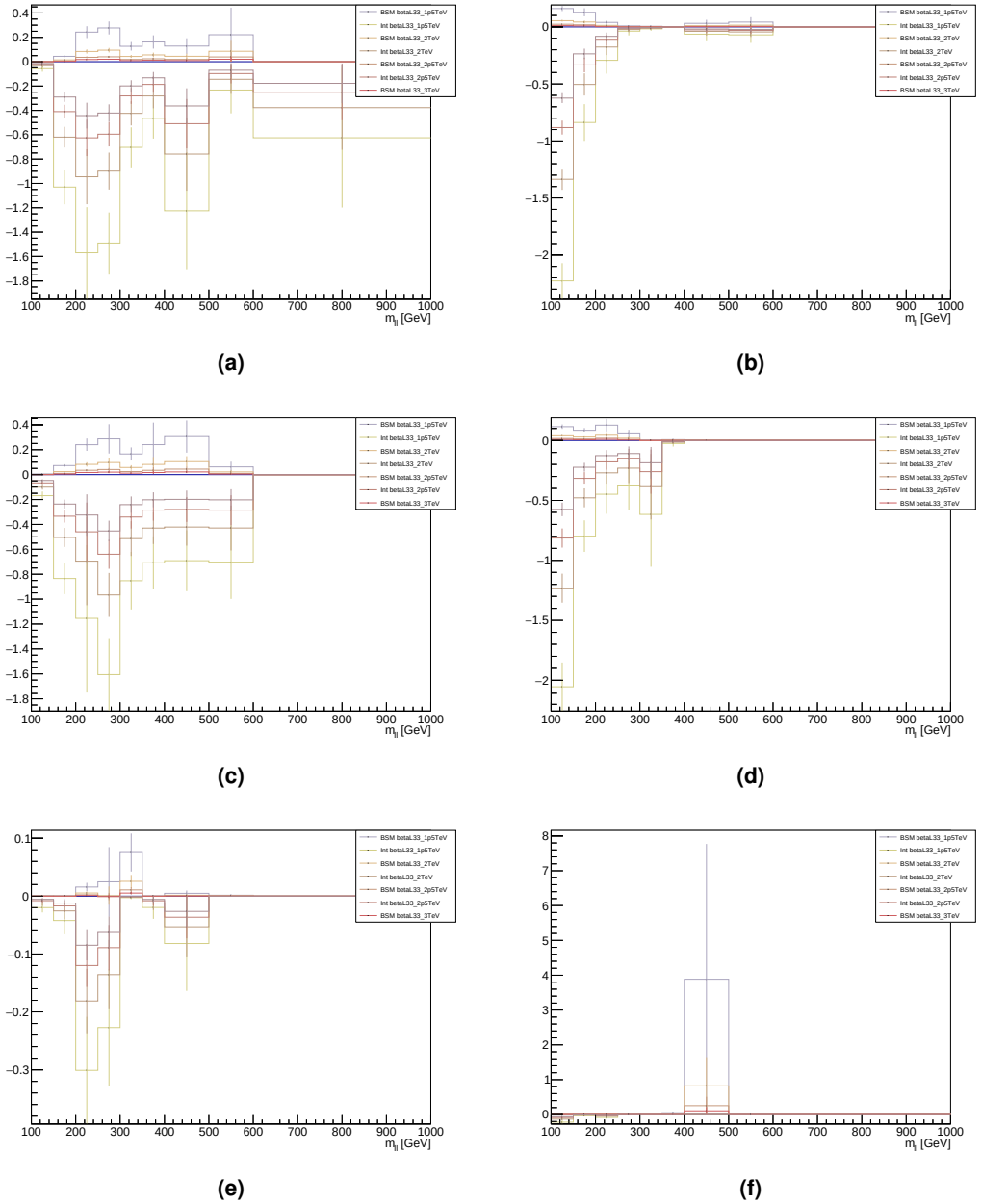

Figure D.7: Signal events of the high mass opposite sign τ_{had} τ_{had} (left side plots) and $e\mu$ (right side plots) regions for the $m_{\text{T}}^{\text{total}}$ variable.

D.5 Post-fitting Control Plots

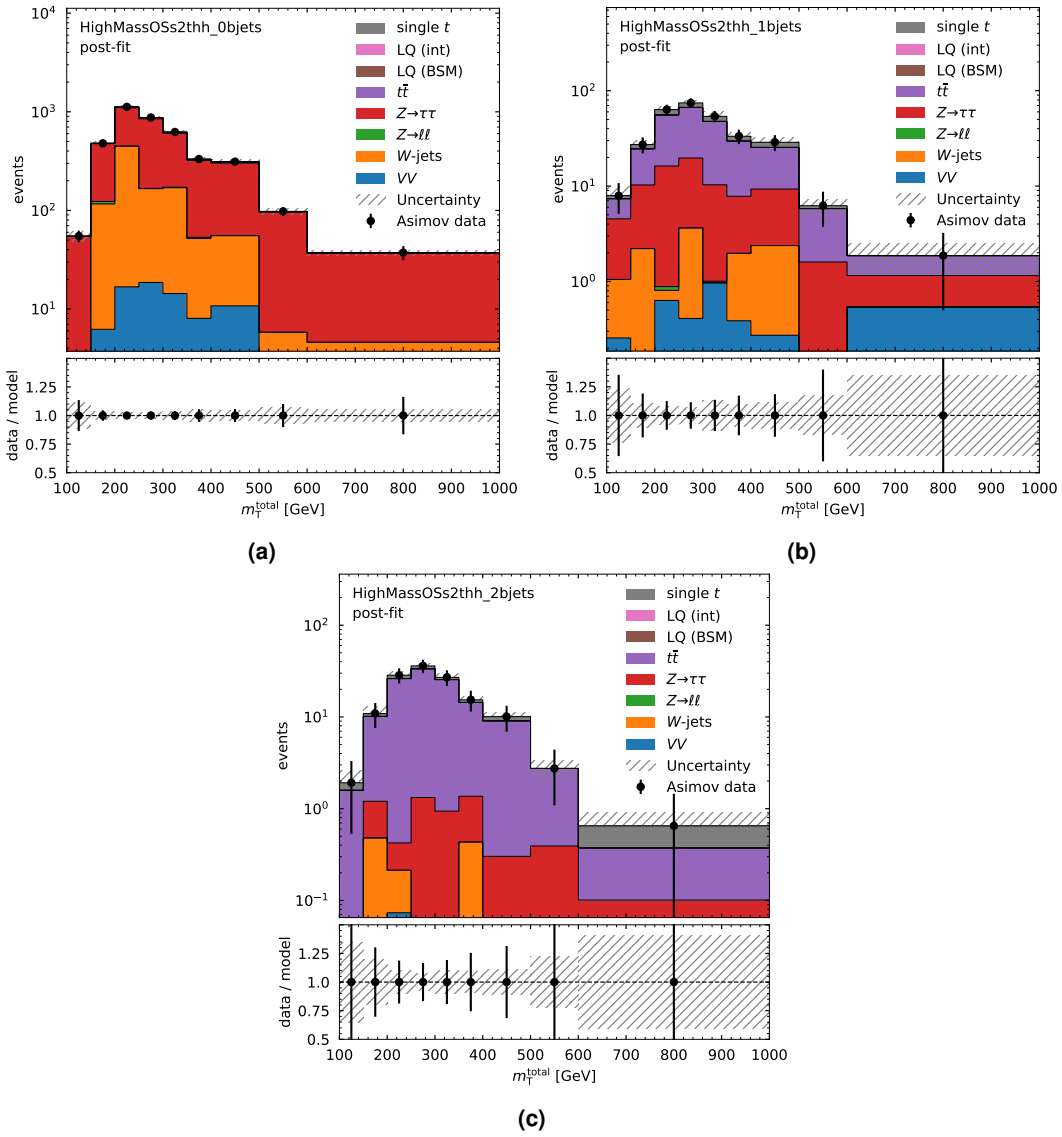

Figure D.8: Post-fit distributions of the di-lepton $m_{\mathrm{T}}^{\mathrm{total}}$ in high-mass, opposite-sign $\tau_{\mathrm{had}}\tau_{\mathrm{had}}$ region for the $\beta_L^{b\tau} = 1$, $m_{\mathrm{LQ}} = 2$ TeV fit. Distributions are shown (a) in the 0, (b) 1, and (c) 2+ b-jet multiplicity regions after the fit is performed. Uncertainties include the process modelling and cross section uncertainties described in Section 3.4.

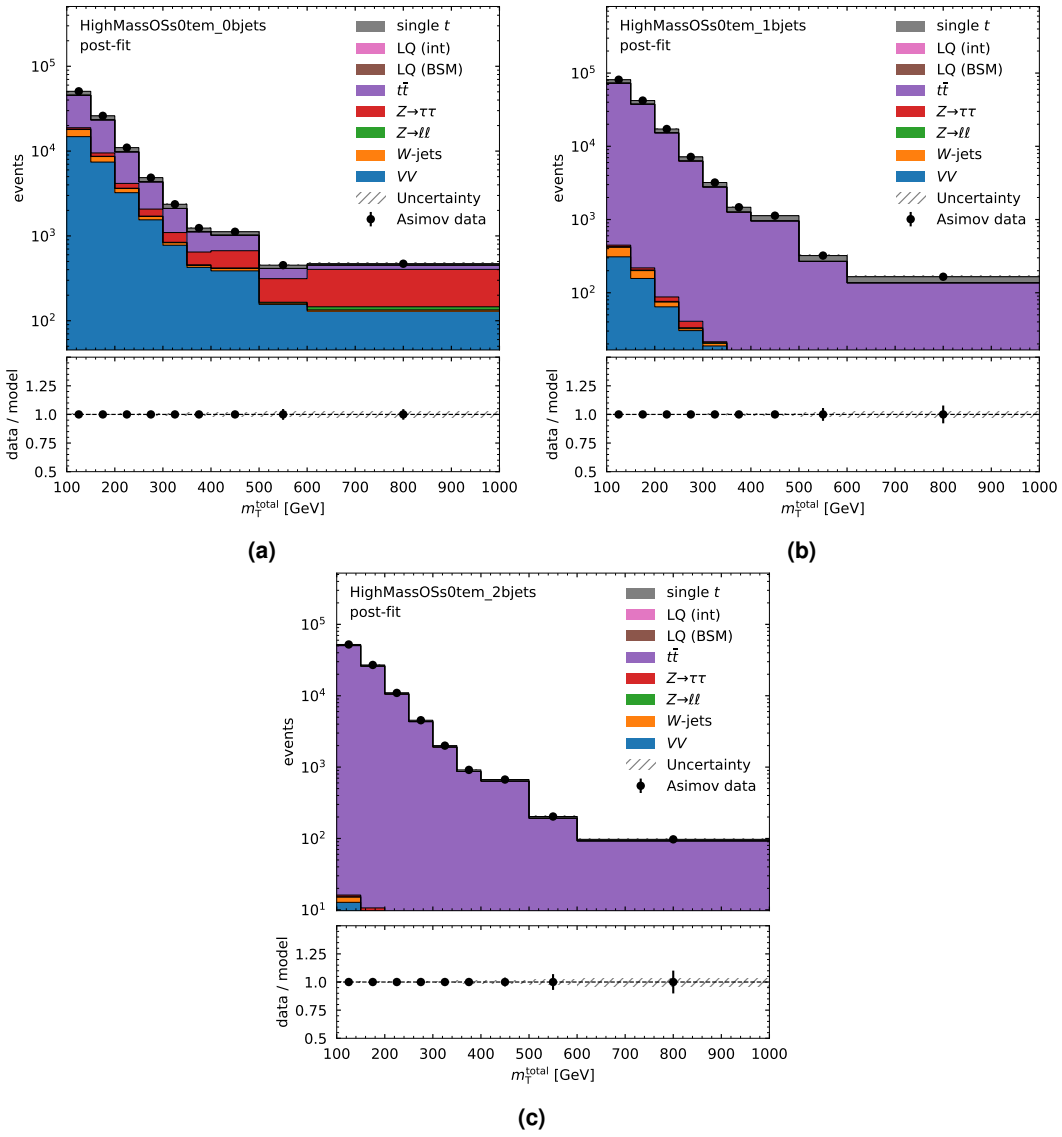

Figure D.9: Post-fit distributions of the di-lepton $m_{\mathrm{T}}^{\mathrm{total}}$ in high-mass, opposite-sign $e\mu$ region for the $\beta_L^{b\tau} = 1$, $m_{\mathrm{LQ}} = 2\,\mathrm{TeV}$ fit. Distributions are shown (a) in the 0, (b) 1, and (c) 2+ b-jet multiplicity regions after the fit is performed. Uncertainties include the process modelling and cross section uncertainties described in Section 3.4.

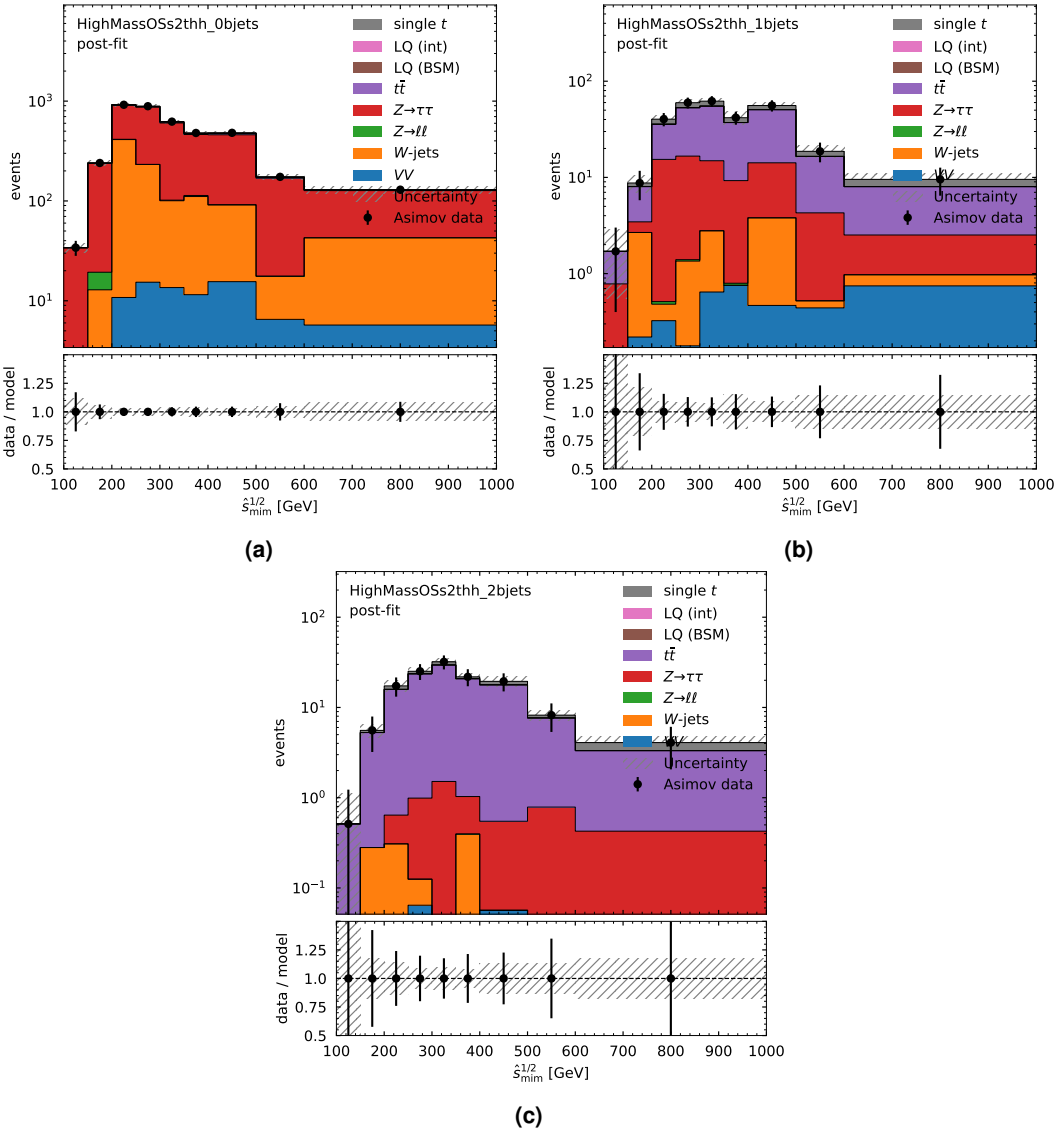

Figure D.10: Post-fit distributions of the di-lepton $\hat{s}^{1/2}_{\text{mim}}$ in high-mass, opposite-sign $\tau_{\text{had}}\tau_{\text{had}}$ region for the $\beta_L^{b\tau} = 1$, $m_{\text{LQ}} = 2$ TeV fit. Distributions are shown (a) in the 0, (b) 1, and (c) 2 b-jet multiplicity regions after the fit is performed. Uncertainties include the process modelling and cross section uncertainties described in Section 3.4.

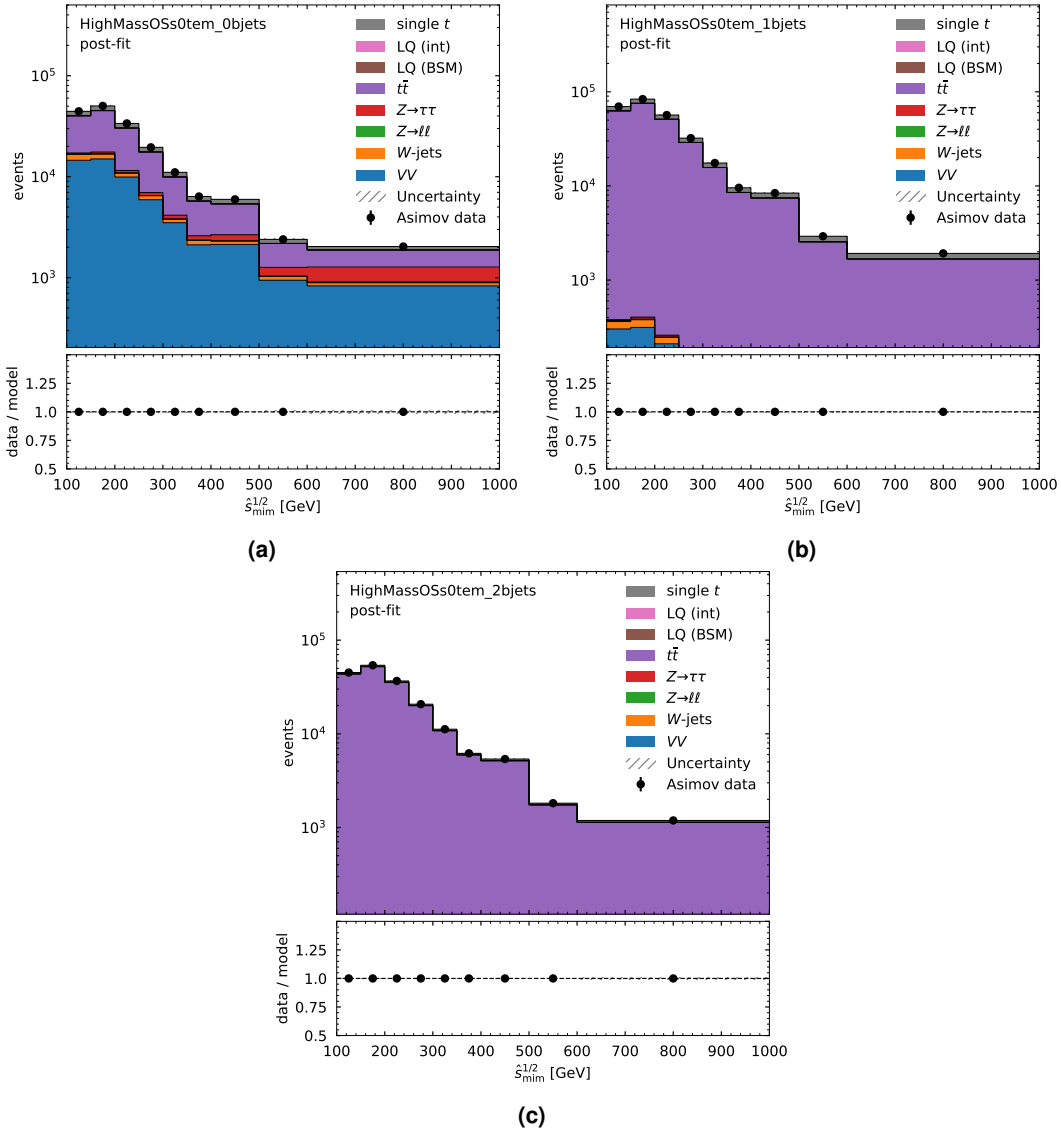

Figure D.11: Post-fit distributions of the di-lepton $\hat{s}^{1/2}_{\mathrm{mim}}$ in high-mass, opposite-sign $e\mu$ region for the $\beta_L^{b\tau} = 1$, $m_{\mathrm{LQ}} = 2\,\mathrm{TeV}$ fit. Distributions are shown (a) in the 0, (b) 1, and (c) 2 b-jet multiplicity regions after the fit is performed. Uncertainties include the process modelling and cross section uncertainties described in Section 3.4.

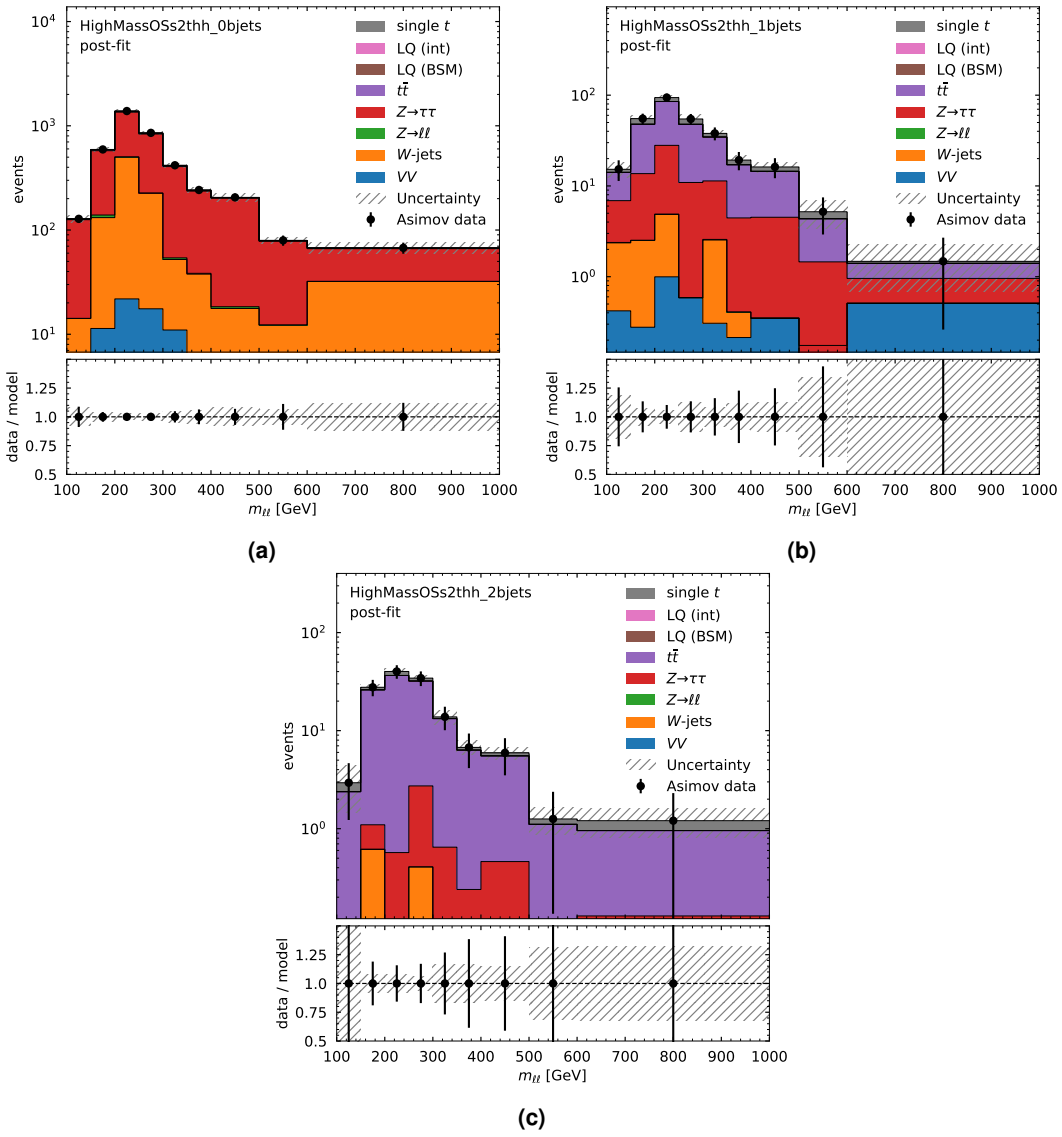

Figure D.12: Post-fit distributions of the di-lepton $m_{\ell\ell}$ in high-mass, opposite-sign $\tau_{\text{had}}\tau_{\text{had}}$ region for the $\beta_L^{b\tau} = 1$, $m_{\text{LQ}} = 2\,\text{TeV}$ fit. Distributions are shown (a) in the 0, (b) 1, and (c) 2 b-jet multiplicity regions after the fit is performed. Uncertainties include the process modelling and cross section uncertainties described in Section 3.4.

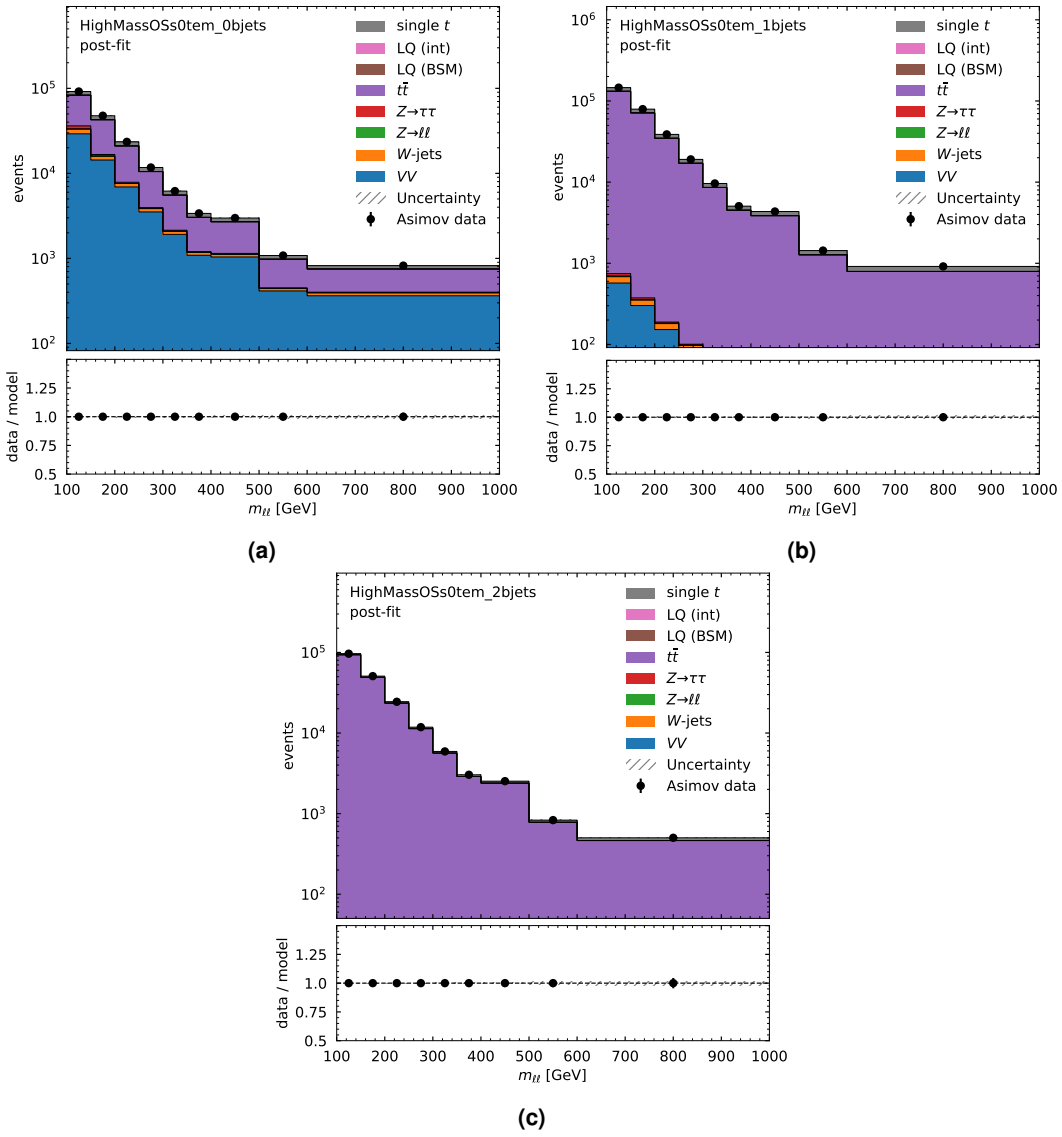

Figure D.13: Post-fit distributions of the di-lepton $m_{\ell\ell}$ in high-mass, opposite-sign $e\mu$ region for the $\beta_L^{b\tau} = 1$, $m_{\text{LQ}} = 2\,\text{TeV}$ fit. Distributions are shown (a) in the 0, (b) 1, and (c) 2 b-jet multiplicity regions after the fit is performed. Uncertainties include the process modelling and cross section uncertainties described in Section 3.4.

D.6 Pull Plots

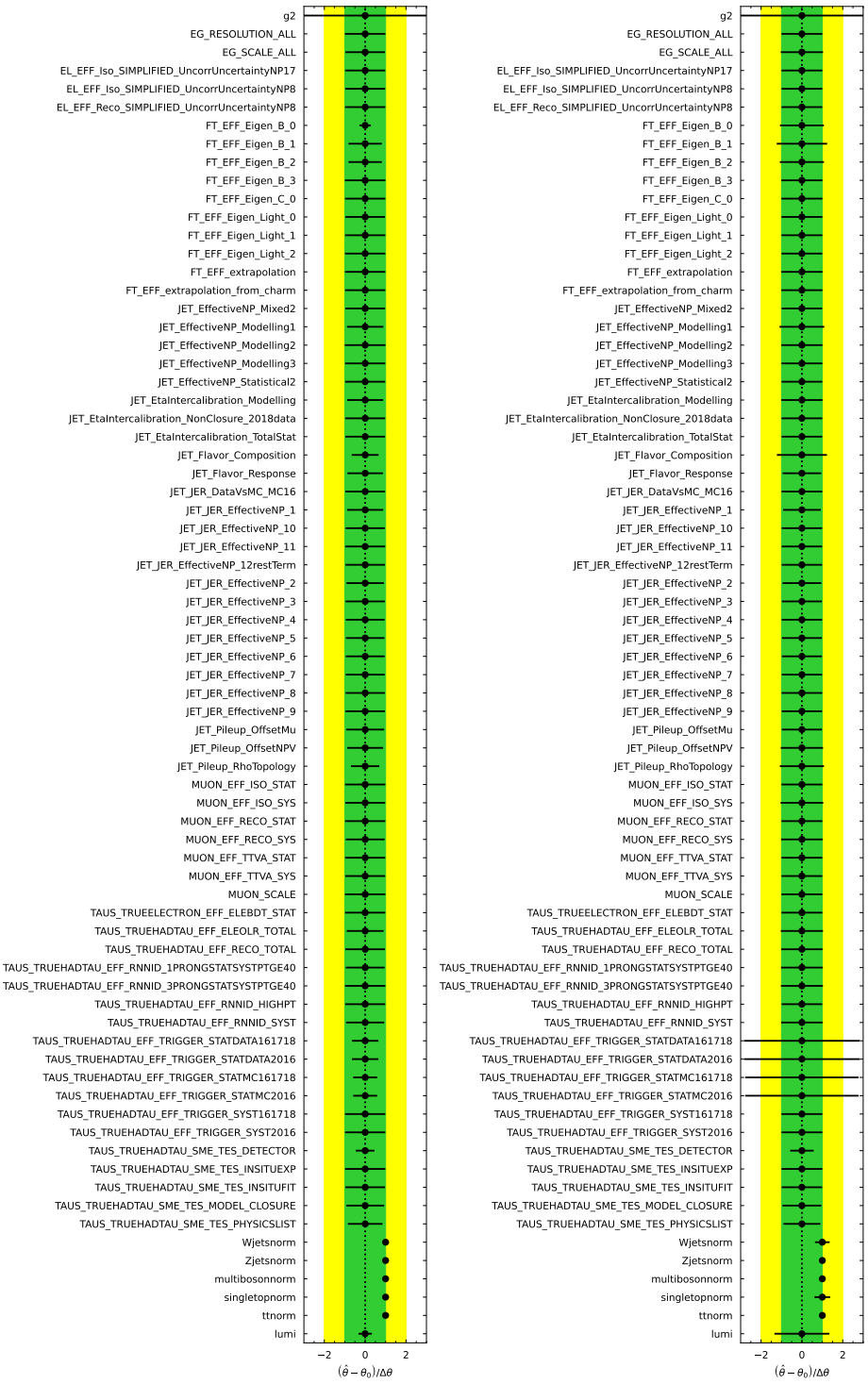

(a) $m_{\mathrm{LQ}} = 1.5\,\mathrm{TeV}$. **(b)** $m_{\mathrm{LQ}} = 2\,\mathrm{TeV}$.

Figure D.14: Pull plots of the $s_{\mathrm{mim}}^{1/2}$ variable.

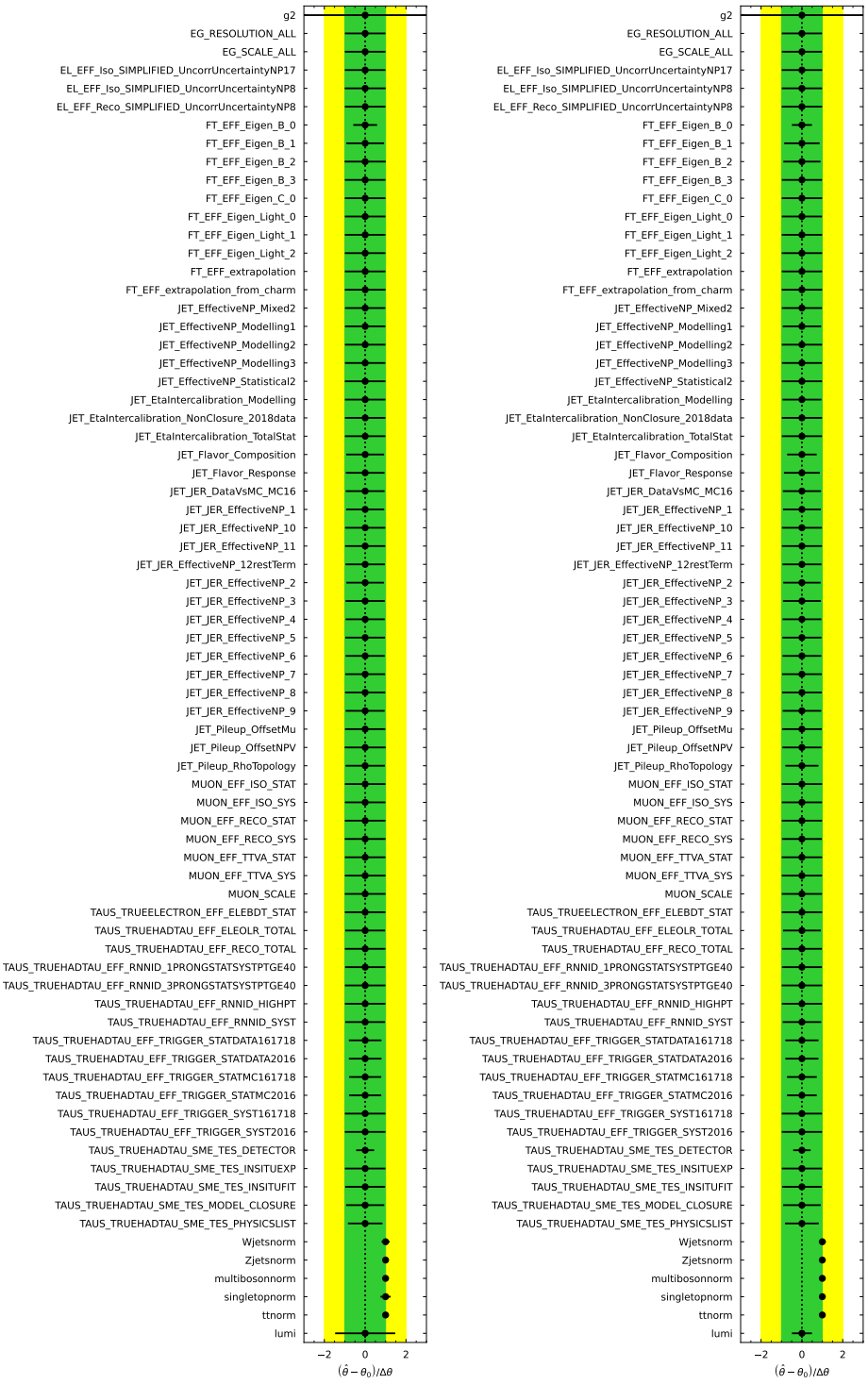

(a) m_{LQ} = 1.5 TeV. **(b)** m_{LQ} = 2 TeV.

Figure D.15: Pull plots of the $m_{\mathrm{T}}^{\mathrm{total}}$ variable.

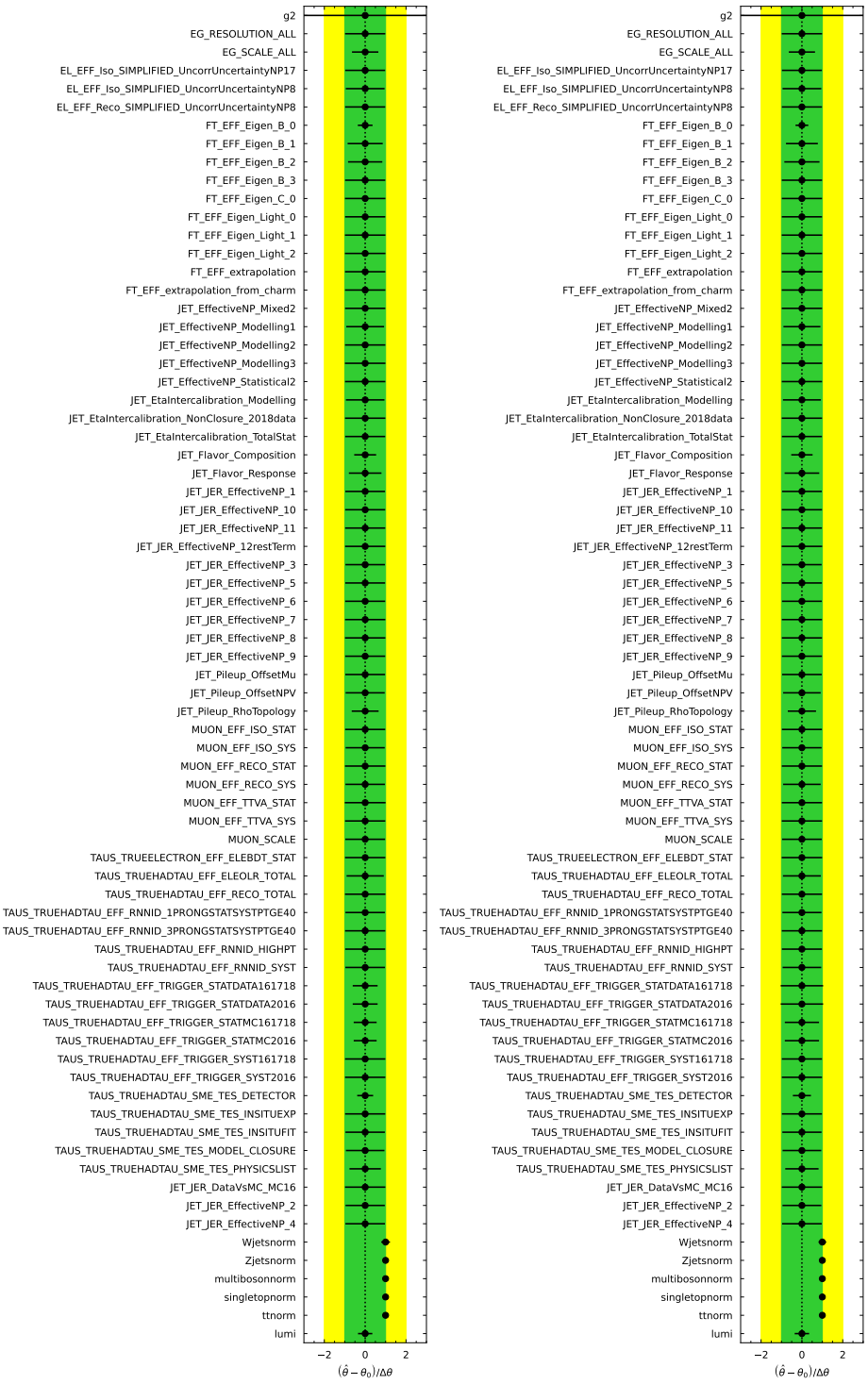

(a) m_{LQ} = 1.5 TeV. **(b)** m_{LQ} = 2 TeV.

Figure D.16: Pull plots of the $m_{\ell\ell}$ variable.

Declaration of consent

on the basis of Article 18 of the PromR Phil.-nat. 19

Name/First Name:	Müller Roman
Registration Number:	13-913-652
Study program:	PhD in Physics
	Bachelor ☐ Master ☐ Dissertation ☑
Title of the thesis:	Detector Development and Analysis Techniques for Finding Leptoquarks with the ATLAS Detector at the LHC
Supervisor:	Prof. Dr. Michele Weber

I declare herewith that this thesis is my own work and that I have not used any sources other than those stated. I have indicated the adoption of quotations as well as thoughts taken from other authors as such in the thesis. I am aware that the Senate pursuant to Article 36 paragraph 1 litera r of the University Act of September 5th, 1996 and Article 69 of the University Statute of June 7th, 2011 is authorized to revoke the doctoral degree awarded on the basis of this thesis.
For the purposes of evaluation and verification of compliance with the declaration of originality and the regulations governing plagiarism, I hereby grant the University of Bern the right to process my personal data and to perform the acts of use this requires, in particular, to reproduce the written thesis and to store it permanently in a database, and to use said database, or to make said database available, to enable comparison with theses submitted by others.

Bern, 04.09.2023

Place/Date

Signature